X-ray Intensity Correlation Spectroscopy from Fluid Surfaces

- Theory and Experiment -

Tuana Ghaderi

A thesis submitted in fulfillment
of the requirements for the degree of
Doctor of Natural Sciences in the subject of
Physics

Universität Dortmund

March 2006

Declaration

I hereby declare that this submission is my own work and that, to the best of my knowledge and belief, it contains no material previously published or written by another person nor material which to a substantial extent has been accepted for the award of any other degree or diploma of the University, except where due acknowledgement has been made in the text.

Tuana Ghaderi
March 16, 2006

Abstract

Thesis advisors
Sunil K. Sinha
Metin Tolan

Author
Tuana Ghaderi

X-ray Intensity Correlation Spectroscopy from Fluid Surfaces

X-ray intensity correlation spectroscopy (XICS) is a coherent X-ray scattering technique, which enables the investigation of dynamic properties of matter by analyzing the temporal correlations among intensities scattered by the studied material. This novel technique has been intensively applied in the last decade in order to examine the temporal and lateral correlation properties of fluid surfaces.

Although, intensity correlation experiments are qualitatively well understood, present theoretical interpretations fail to explain XICS data from some well known fluid surfaces, such as water and glycerol. We believe that the discrepancies, between the theoretical predictions for the intensity correlation function and the experimental results, are due to some idealized assumptions with regard to the coherence of the X-ray beam, as well as the instrumental resolution.

This thesis is mainly concerned with the derivation of the intensity correlation function for surface sensitive X-ray intensity correlation experiments including the effects of partial coherence and instrumental resolution. In order to derive the intensity correlation function the theoretical approach is based in this work on the statistical properties of the fluid surface and the scattered electric field. A scalar wave equation for the electric X-ray field is derived to determine the field expressions from time fluctuating and inhomogeneous media. The therefrom obtained field formulas are used to derive systematically field correlation functions and intensity correlation functions. The accuracy of the field expressions and the deduced correlation functions are restricted to the first Born approximation. Within this accuracy, we have provided intensity correlation functions that are applicable to charge scattering from fluid surfaces under the conditions of arbitrary spatial coherence and instrumental resolution. In addition, far and near field scattering conditions, i.e. Fraunhofer and Fresnel conditions, are rigorously incorporated in the theoretical intensity correlation functions.

The experimental part in thesis is dedicated to the analysis of XICS measurements from hexane and water surfaces. The data analysis is based in parts on the intensity correlation function which is derived in the theoretical part

of this work. We have convincingly illustrated that the conventionally used intensity correlation function is generally not suitable to analyze XICS experiments. In contrast to the conventionally used intensity correlation formula, we have obtained very good agreement between our theoretical intensity correlation function and the experimental results from hexane. This work may therefore be of general interest to scientists who make use of XICS or other scattering techniques using partially coherent X-ray beams.

Acknowledgments

I would like to thank all the people who encouraged and supported me during the undertaking of this research.

Firstly, I would like to thank my supervisors, Prof. Dr. Sunil K. Sinha and Prof. Dr. Metin Tolan. Their support, encouragement, guidance and expertise has proved invaluable.

I would like to thank Dr. Christian Gutt, Dr. Michael Sprung and Zhang Jiang for many useful discussions regarding X-ray scattering and physics in general. I thankfully acknowledge their valuable assistance in setting up the X-ray scattering experiments at the European Synchrotron Radiation Facility in France and at the Advanced Photon Source in the USA.

I would like to thank my family and friends. Their support, encouragement and friendship will always be treasured. My greatest debt and heartfelt thanks goes to my wonderful parents, Arian and Shirin. They have been an inspiration throughout my life.

I save the last special thanks for Tülin, she has stood by me through the most difficult times of this process, offering her unconditional love and support. You are an inspiration, thank you.

Contents

Chapter 1

Introduction

X-ray scattering has a long history of significant contributions to widely varying fields of scientific study. The scientific progress and outcome from X-ray scattering experiments has always been closely related to the availability and improvements of high brilliance synchrotron sources. Since the insertion of undulators and wigglers in synchrotron facilities so-called 3rd generation synchrotron sources are available, which produce a partially coherent X-ray beam. This significant improvement of synchrotron sources has substantially enriched conventional X-ray scattering experiments by many new types of coherent X-ray scattering techniques. For instance, a number of laser light experiments, such as holography, intensity correlation spectroscopy, phase contrast imaging etc., can nowadays be implemented with partially coherent X-rays for optically opaque materials and, in principle, with even higher spatial resolution. Due to these promising advantages much effort has been put into the design of scattering experiments using coherent X-rays in the last few years [65].

This thesis concerns exploiting the partial coherence of synchrotron radiation in order to carry out X-ray intensity correlation spectroscopy (XICS) experiments from fluid surfaces. Such experiments, which are also known as X-ray photon correlation spectroscopy (XPCS), promise exciting new insights into dynamical phenomena in condensed matter, occurring on shorter length scales than can be reached in dynamical light scattering (DLS). Specifically, the partially coherent illumination of a random surface height distribution yields a random interference pattern, which is referred to as a *speckle pattern*. This speckle pattern changes in time, if the surface height distribution undergoes different states in time. The intensity correlation spectroscopy method reveals the characteristic times of the sample via time correlation of the scattered intensity in the speckle pattern. The basic ideas of XICS experiments from dynamic surfaces are schematically illustrated in Fig. 1.1. It is conventionally assumed that the time dependent part of the resultant intensity correlation

signal $G_2(\tau)$ is essentially related to the surface height correlation function $\widetilde{C}_{zz}(\tau)$ of the sample via

$$G_2(\tau) \propto |\widetilde{C}_{zz}(\tau)|^2 \,, \tag{1.1}$$

where τ represents the correlation time. The measurement of the intensity correlation signal at different wave vector transfers eventually yields the dynamic properties of the surface at different length scales. The intensity correlation signal is, in a broader sense, also related to the intermediate scattering function [96, 66]. (A detailed discussion is given in chapter 5.)

Although, the above concepts appear plausible for surface sensitive XICS experiments, some experiments from relatively well understood fluid surfaces could not be interpreted by formulas that are essentially of the same form as eq. (1.1) [36, 85]. The most obvious discrepancy between eq. (1.1) and the experimental results in Ref.[36, 85] is the observation of a heterodyne intensity correlation signal, which refers to a linear relation between $G_2(\tau)$ and $\widetilde{C}_{zz}(\tau)$.

This thesis shows that the consideration of partial coherence and finite instrumental resolution are of central importance for the interpretation of XICS experiments from fluid surfaces. It is demonstrated that the influences of partial coherence and finite instrumental resolution can, for instance, lead to the observation of heterodyne intensity correlation signals. In the experimental part of this work we present XICS experiments on hexane and water surfaces. The interpretation of the intensity correlation signal from both liquids depend vitally on the consideration of coherence and resolution effects. In order to account for these effects we have derived a formula for the intensity correlation function, which allows, in contrast to conventional formulas, a reasonable interpretation of our XICS experiments.

The structure of the thesis and a short description of the content in each chapter is given below.

Chapter 2 summarizes the statistical properties of fluctuating fluid surfaces. Some central predictions from the *capillary wave model* and the *density functional theory* for fluid surfaces are in detail discussed. Static and dynamic surface height correlation functions are derived for low and high viscosity fluids. The provided surface height correlation functions are continuously used throughout this thesis to interpret the surface scattering experiments.

Chapter 3 presents the established description of elastic X-ray scattering from rough surfaces. Some approximation methods for constructing the specularly scattered X-ray intensity and the diffusely scattered counterpart are discussed in detail. A number of relations between the scattered X-ray intensity and the

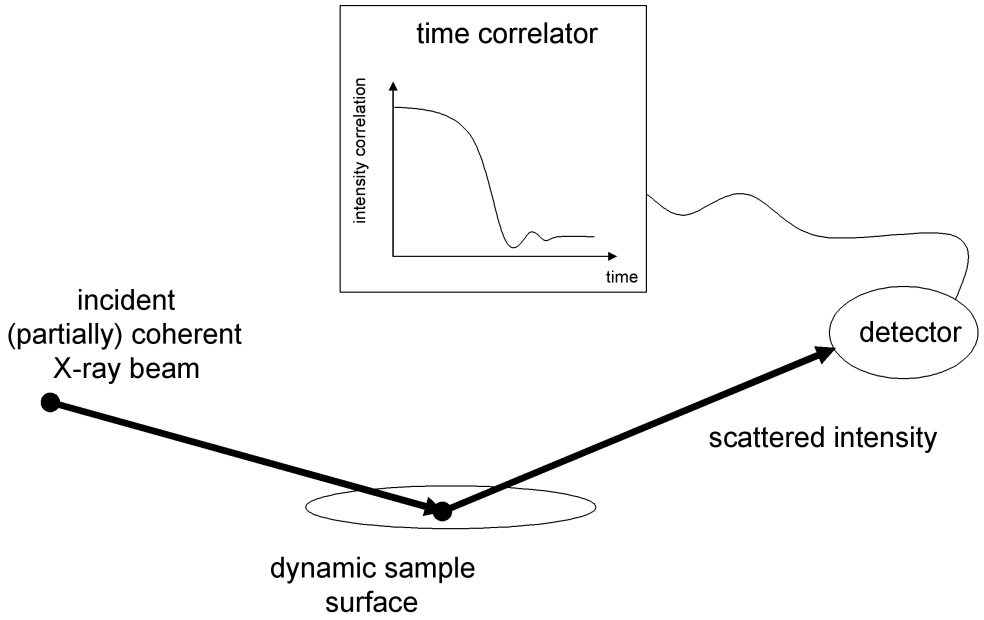

Figure 1.1: Schematic illustration of XICS experiments from dynamic surfaces. A coherent or at least partially coherent X-ray beam is scattered from a temporally fluctuating surface. The scattered intensity distribution yields a speckle-like interference pattern, which equally changes in time. The detection and time correlation of the scattered intensity reveals dynamic properties of the sample surface under study. The probed length scale from the sample surface depends on the detection position of the intensity correlation signal.

static surface height correlation function are provided. Furthermore, we have eliminated an unphysical singularity in the conventional intensity formulas for surface scattering. The conditions for Fraunhofer and Fresnel scattering situations are finally explored.

Chapter 4 is concerned with conditions of partial coherence in X-ray scattering experiments from static media. The propagation, diffraction and scattering of partial coherent X-rays are discussed in terms of mutual coherence functions. The diffraction of partially coherent X-rays from a square slit is explained in detail. This demonstration example is used as a guidance to develop scattering formulas from more complicated systems. The mutual coherence function for surface scattering conditions is constructed and examined for a variety of experimental situations. Surface sensitive scattering conditions are discussed in particular.

Chapter 5 presents a theoretical description of surface sensitive XICS experiments from fluid surfaces. The proposed intensity correlation function is based on statistical properties of the fluid surface, as well as the scattered fields. The conditions of partial coherence, instrumental resolution, and Fresnel scattering are accounted for in the discussion. The predictions of this intensity correlation function are finally compared with the conventionally used formula.

Chapter 6 presents surface sensitive XICS measurements from hexane and water. The data analysis was performed with the conventionally used intensity correlation function, as well as with the formula which is proposed in chapter 5. By using the latter formula for hexane, we have obtained reasonable results for the surface tension and the kinetic viscosity. In contrast to these results, the data analysis with the commonly used intensity correlation function yielded values for kinetic viscosities which are several times larger for both liquids.

Chapter 7 summarizes the main findings of this thesis. A discussion on future research based on this work is given as conclusion.

Chapter 2

Structure of Liquid-Vapor Interfaces

The challenging problem in equilibrium theories of liquid-vapor interfaces is to explain the density profile in the interfacial region, and to incorporate the role of surface tension, as well as the viscosity from a molecular point of view. The first approach to this problem was developed for ideal liquids (viscosity free) by Van der Waals, almost one century ago. The mean-field, or Van der Waals theory of interfaces, introduces a laterally flat intrinsic density profile that changes gradually from the mass density of the liquid $\varrho_l(z)$ into the vapor density $\varrho_v(z)$. Here, the z-direction is taken normal to the interfacial zone. The intrinsic interfacial width σ_i between the phases is related to the bulk density fluctuations and deduced from the bulk correlation length ℓ_b. Within this theory, long-range fluctuations in the liquid-vapor interface occur only if the temperature T approaches the critical temperature T_c, at which the bulk correlation length and intrinsic interfacial width diverges as $\ell_b, \sigma_i \sim (T_c - T)^{-\bar{\nu}}$, with the critical exponent $\bar{\nu}$ [80, 43, 105].

A second model for liquid-vapor interfaces takes long-range interfacial fluctuation into account for temperatures far below T_c. This model was proposed by Buff, Lovett, and Stillinger [14]. Based on the theory of classical hydrodynamic Buff et al. introduced a sharp liquid-vapor interface, which is displaced from its equilibrium position due to the thermal excitations of capillary waves. In this so-called capillary wave model, bulk fluctuations are entirely ignored and the interfacial width is obtained from the integral over all thermally excited capillary waves. The excited capillary wavelengths span from ℓ_b to the surface correlation length ℓ_s, which is apart from a factor of $\sqrt{2}$, identical to the so-called capillary length $a_c = \sqrt{2\gamma/(g \triangle\varrho)} = \sqrt{2}\ell_s$, hence ℓ_s is typically a macroscopic length [31, 27, 80]. Here γ is the macroscopic surface tension, g the gravitational constant, and $\triangle\varrho = \varrho_l - \varrho_v$ is the difference in the (bulk)

mass densities between the liquid and vapor phases. The picture, which has emerged from numerous theoretical and experiment efforts, is that short-range bulk fluctuations give rise to the formation of an intrinsic interface profile which experiences long-range capillary wave fluctuations at a scale larger than ℓ_b. In more recent theoretical works, using microscopic density functional theory for inhomogeneous ideal liquids, both types of fluctuations has been incorporated into a theory for liquid-vapor interfaces [63, 70].

In the following sections, some particular properties of liquid-vapor interfaces are briefly recapitulated, which are predicted from classical hydrodynamic and the density functional theory. The emphasis will be on the static and dynamic surface height correlation function, which plays a central role in the calculation of X-ray scattering cross-sections from liquid surfaces.

2.1 Hamiltonian Formalism for Liquid-Vapor Interfaces

The interfacial profile predicted by the phenomenological capillary wave model can be obtained from the hydrodynamic theory of incompressible ideal liquids, in combination with the theory of classical statistical mechanics. To summarize the main assumptions and predictions made in this model, the Hamiltonian formalism for liquid surfaces is used in the following section, which has been chiefly developed by V. E. Zakharov [110], J. M. Miles [64] and L. J. F. Broer [12]. The benefit of the Hamiltonian formalism is that it naturally fits in the more rigorous analysis of K. R. Mecke, M. Napiorkowski and S. Dietrich [63, 70], which is based on the density functional theory.

2.1.1 Capillary Wave Model

The central assumption in the capillary wave model is the incompressibility condition of the fluid. This requirement states - in contrast to the Van der Waals model - that bulk density fluctuations are negligible in the formation of the interfacial profile. If in addition to the requirement of incompressibility, the liquid is free from rotational flows and ideally friction free, then one can readily deduce the predictions of the capillary wave model from a hydrodynamical standpoint.

The hydrodynamical treatment of surface waves for an ideal homogeneous liquid that fills a square basin of finite depth d, is here recapitulated. WE assume that the only forces acting on the liquid are gravitational and capillary forces. The coordinate system is chosen such that the undisturbed surface coincides with a $(x, y)-$plane, see Fig.2.1. The $z-$axis is pointing away from

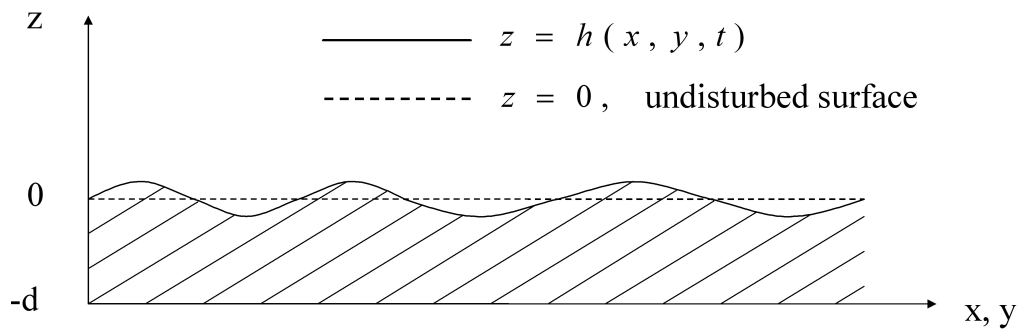

Figure 2.1: Schematic illustration of the local surface displacement $h(x, y, t)$ and the coordinate system.

the undisturbed surface, and perturbations from the equilibrium height $z = 0$ are described by the height displacement function $h = h(\boldsymbol{r}, t)$, where $\boldsymbol{r} = (x, y)$. Furthermore, the surface is considered to be almost flat, in the sense that the wave amplitudes are small compared to their wavelength, i.e. $qh \ll 1$, where $q = (q_x^2 + q_y^2)^{1/2}$ is the modulus of the surface in-plane wave vector $\boldsymbol{q} = (q_x, q_y)$. With these conditions, the equations of motion for a stream in an ideal liquid of finite depth can be expressed in the following form [67, 47]

$$\Delta\Phi = 0\,, \qquad h(\boldsymbol{r}, t) \geq z \geq -d \tag{2.1a}$$

$$\frac{\partial\Phi}{\partial z} = 0\,, \qquad z = -d \tag{2.1b}$$

$$\frac{\partial h}{\partial t} = \frac{1}{\varrho_l}\frac{\partial\Phi}{\partial z}\,, \qquad z = h(\boldsymbol{r}, t) \tag{2.1c}$$

$$\frac{\partial\Phi}{\partial t} = -\varrho_l\, gh + \gamma\Delta_{\parallel}h\,, \qquad z = h(\boldsymbol{r}, t) \tag{2.1d}$$

where $\Phi = \varrho_l\phi(\boldsymbol{r}, z, t)$ with ϱ_l being the liquid mass density and $\phi(\boldsymbol{r}, z, t)$ the velocity potential. γ is the surface tension and $\Delta_{\parallel}$ is the 2-dimensional Laplace operator with respect to the (x, y)-directions. A solution for streams inside the fluid volume can be obtained from Laplace's eq. (2.1a) under the restrictions from the surface boundary conditions (2.1c) and (2.1d), as well as the ground boundary condition (2.1b). Eq. (2.1c) describes the kinetic surface boundary condition, and describes (2.1d) the dynamic surface condition, in which the vapor mass density has been neglected. Laterally periodic boundary conditions are demanded at a distance L, i.e. $h(x, y, t) = h(x + L, y + L, t)$ and $\Phi(x, y, z, t) = \Phi(x + L, y + L, z, t)$, with $L = A^{1/2}$ being the linear dimension of the square interface of area A.

As it has been shown in Ref.[64, 12, 110], the surface boundary conditions

(2.1c,d) are equivalent to the canonical equations

$$\frac{\partial h(\boldsymbol{r},t)}{\partial t} = \frac{\delta \mathcal{H}}{\delta \Psi(\boldsymbol{r},t)}\,, \qquad \frac{\partial \Psi(\boldsymbol{r},t)}{\partial t} = -\frac{\delta \mathcal{H}}{\delta h(\boldsymbol{r},t)}\,, \tag{2.2}$$

whereas the height displacement function $h(\boldsymbol{r},t)$ refers to the generalized coordinate and

$$\Psi(\boldsymbol{r},t) = \Phi(\boldsymbol{r},z,t)|_{z=h(\boldsymbol{r},t)}. \tag{2.3}$$

defines the generalized momentum. $\delta\mathcal{H}/\delta h$ and $\delta\mathcal{H}/\delta\Psi$ are functional derivatives of the Hamiltonian density $\mathcal{H}$. In an ideal fluid, the total energy of the system is conserved and, accordingly, the Hamiltonian density can be constructed from the sum of the kinetic energy density $\mathcal{T}$ and the potential density $\mathcal{V}$ of the system, viz.

$$H = \int_A \mathcal{H}\; d^2r = \int_A (\mathcal{T}+\mathcal{V})\; d^2r\,, \tag{2.4a}$$

$$\mathcal{T} = \frac{1}{2\varrho_l}\int_{-d}^{h} (\nabla\Phi)^2 dz = \frac{1}{2\varrho_l}\Psi\frac{\partial\Phi}{\partial z}\bigg|_{z=h}\,, \tag{2.4b}$$

$$\mathcal{V} = \frac{1}{2}\varrho_l g h^2 + \frac{1}{2}\gamma|\nabla_\parallel h|^2. \tag{2.4c}$$

In eq. (2.4a) H denoted the Hamiltonian function, which is identical to the total energy of the system. The two terms in the potential density describe the energy needed to disturb the surface from its equilibrium height. For a disturbed surface the first term corresponds to the energy gain in the gravitational field, and the second term results from capillary forces which work against an extension in surface area. By solving the boundary value problem for the Laplace equation (2.1a), one can eliminate the Φ dependence in the kinetic energy and express with eq. (2.3) the Hamiltonian by h and Ψ only. In that sense h and Ψ fully define the fluid dynamics at the surface.

Next, it will be useful to introduce the Fourier series for h, Ψ and Φ by the relations

$$h(\boldsymbol{r},t) = \sum_{\boldsymbol{q}} \widetilde{h}(\boldsymbol{q},t)\, e^{i\boldsymbol{q}\cdot\boldsymbol{r}}\,, \qquad \widetilde{h}(0,t) = 0 \tag{2.5a}$$

$$\Psi(\boldsymbol{r},t) = \sum_{\boldsymbol{q}} \widetilde{\Psi}(\boldsymbol{q},t)\, e^{i\boldsymbol{q}\cdot\boldsymbol{r}}\,, \qquad \widetilde{\Psi}(0,t) = 0 \tag{2.5b}$$

$$\Phi(\boldsymbol{r},z,t) = \sum_{\boldsymbol{q}} \widetilde{\Phi}(\boldsymbol{q},z,t)\, e^{i\boldsymbol{q}\cdot\boldsymbol{r}}\,, \qquad \widetilde{\Phi}(0,z,t) = 0 \tag{2.5c}$$

where the Fourier coefficients satisfy the conditions $\widetilde{h}^*(\boldsymbol{q},t) = \widetilde{h}(-\boldsymbol{q},t)$, $\widetilde{\Psi}^*(\boldsymbol{q},t) = \widetilde{\Psi}(-\boldsymbol{q},t)$ and $\widetilde{\Phi}^*(\boldsymbol{q},z,t) = \widetilde{\Phi}(-\boldsymbol{q},z,t)$, since $h(\boldsymbol{r},t)$, $\Psi(\boldsymbol{r},t)$ and $\Phi(\boldsymbol{r},z,t)$

are real quantities. From the boundary value problem for Laplace's equation (2.1a) one then finds the relation $\widetilde{\Phi}(\boldsymbol{q}, z, t) = (\cosh q(z+d)/\cosh qd)\widetilde{\Psi}(\boldsymbol{q}, t)$ at $z = h(\boldsymbol{r}, t)$. By using this relation in eq. (2.5c), the surface conditions (2.1c,d) yield

$$\frac{\partial \widetilde{h}(\boldsymbol{q}, t)}{\partial t} = \frac{1}{\varrho_l} q \tanh qd \; \widetilde{\Psi}(\boldsymbol{q}, t)\,, \tag{2.6a}$$

$$\frac{\partial \widetilde{\Psi}(\boldsymbol{q}, t)}{\partial t} = -\left(\varrho_l\, g + \gamma \boldsymbol{q}^2\right) \widetilde{h}(\boldsymbol{q}, t)\,, \tag{2.6b}$$

for $qh(\boldsymbol{r}, t) \ll 1$ and $h \ll d$. The dispersion relation for capillary-gravity waves can next be obtained by decoupling the above two equation into two linear differential equations, which respectively have the solutions

$$\widetilde{h}(\boldsymbol{q}, t) = \widetilde{h}(\boldsymbol{q})\, e^{-i\omega(q)t}\,, \qquad \widetilde{\Psi}(\boldsymbol{q}, t) = \widetilde{\Psi}(\boldsymbol{q})\, e^{-i\omega(q)t}\,, \tag{2.7}$$

The explicit form for $\omega(q)$ is nothing else than the dispersion relation for capillary-gravity waves in shallow waters:

$$\omega(q) = \omega_s(q)\sqrt{\tanh qd}\,, \tag{2.8}$$

with

$$\omega_s(q) = \sqrt{gq + \frac{\gamma q^3}{\varrho_l}}\,, \tag{2.9}$$

being the dispersion relation for an infinitely deep liquid. In most practical situations eq. (2.9) sufficiently describes the dispersion relation for surface wavelengths that are small compared to a finite depth d. The gravitational and capillary contribution to the dispersion relation (2.9) are of equal magnitude at the characteristic wave vector value

$$q_g = \sqrt{\frac{\varrho_l g}{\gamma}} = \frac{1}{\ell_s}\,, \tag{2.10}$$

For wave vector numbers above the so-called gravitational cutoff q_g the dispersion properties are essentially caused by capillary forces, see Fig.2.2. Also important is the inverse relation between the gravitational cutoff and the surface correlation length ℓ_s [31, 27].

Another quantity of interest is the Hamiltonian function H in terms of $\widetilde{h}$ and $\widetilde{\Psi}$. By using the Fourier representation for Φ and the above mentioned expression for $\widetilde{\Phi}$, one finds the approximation

$$\left.\frac{\partial \Phi}{\partial z}\right|_{z=h} \approx \sum_{\boldsymbol{q}} (q \tanh qd)\, \widetilde{\Psi}(\boldsymbol{q}, t)\, e^{i\boldsymbol{q}\cdot\boldsymbol{r}}\,, \tag{2.11}$$

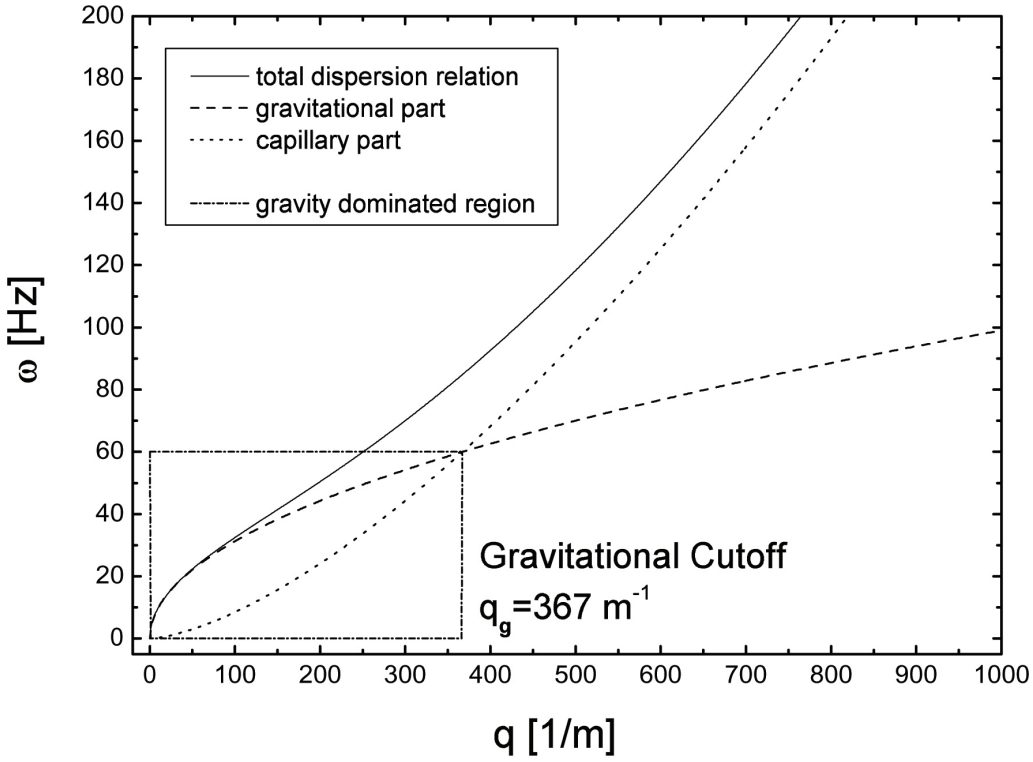

Figure 2.2: Dispersion relation of capillary gravity waves on a water surface at room temperature. For a surface tension of $\gamma = 0.0727$ Nm^{-1} and mass density of $\varrho_l = 1000$ kg/m^3 the gravitational cutoff for water yields $q_g = 367$ m^{-1}.

which partially contributes to the kinetic energy density (2.4b). With (2.11) and the equations (2.5a), (2.5b) and (2.7), the Hamiltonian function (2.4a) yields

$$H = \frac{1}{2}\sum_{\boldsymbol{q}}\sum_{\boldsymbol{q'}}\left(\frac{1}{\varrho_l} q \tanh qd\ \widetilde{\Psi}(\boldsymbol{q},t)\widetilde{\Psi}(\boldsymbol{q'},t) + (\varrho_l g + \gamma \boldsymbol{q}\cdot\boldsymbol{q'})\,\widetilde{h}(\boldsymbol{q},t)\widetilde{h}(\boldsymbol{q'},t)\right) \times \int_A d^2 r e^{i(\boldsymbol{q}+\boldsymbol{q'})\cdot\boldsymbol{r}}. \tag{2.12}$$

Due to the laterally periodic boundary conditions the allowed values for $\boldsymbol{q}$ and $\boldsymbol{q'}$ are multiples of $\pm 2\pi/L$. Accordingly, the integral in (2.12) fulfills the orthogonality relation

$$\frac{1}{A}\int_A d^2 r\ e^{i(\boldsymbol{q}+\boldsymbol{q'})\cdot\boldsymbol{r}} = \delta^2(\boldsymbol{q}+\boldsymbol{q'})\,, \tag{2.13}$$

where $\delta^2(\boldsymbol{q}+\boldsymbol{q'}) = \delta(q_x+q'_x)\delta(q_y+q'_y)$ is a 2-dimensional delta function. With (2.13), one finally obtains the Hamiltonian for a system of decoupled harmonic

oscillators in the following form

$$\begin{aligned}\widetilde{H} &= \sum_{\boldsymbol{q}} \widetilde{H}\Big[\widetilde{\Psi}(\boldsymbol{q}), \widetilde{h}(\boldsymbol{q})\Big] \\ &= \frac{1}{2} A \sum_{\boldsymbol{q}} \left(\frac{1}{\varrho_l} q \tanh qd \left|\widetilde{\Psi}(\boldsymbol{q})\right|^2 + \left(\varrho_l g + \gamma \boldsymbol{q}^2\right) \left|\widetilde{h}(\boldsymbol{q})\right|^2 \right). \end{aligned} \tag{2.14}$$

In order to obtain the interfacial roughness σ_{cw} due to thermally excited capillary wave, $h(\boldsymbol{q}, t)$ is next treated as a random variable, which obeys the statistical requirements of ergodicity, spatial homogeneity and isotropy [32, 58]. In the statistical sense, the surface roughness can then be defined as the mean-squared deviation

$$\sigma_{cw}^2 = \langle h(\boldsymbol{r}, t) h(\boldsymbol{r}, t) \rangle = \sum_{\boldsymbol{q}} \sum_{\boldsymbol{q'}} \langle \widetilde{h}(\boldsymbol{q}, t) \widetilde{h}(\boldsymbol{q'}, t) \rangle \, e^{i(\boldsymbol{q}+\boldsymbol{q'})\cdot \boldsymbol{r}} \,, \tag{2.15}$$

where the brackets denote an ensemble or time average, and the mean equilibrium height is located at $\langle h(\boldsymbol{r}, t) \rangle = 0$. According to the above statistical requirements for $h(\boldsymbol{r}, t)$, it follows that σ_{cw} is independent of time and space, which implies the following conditions for the right-hand side of eq. (2.15) [58]

$$\langle \widetilde{h}(\boldsymbol{q}, t) \widetilde{h}(\boldsymbol{q'}, t) \rangle = \langle \widetilde{h}(-\boldsymbol{q}, t) \widetilde{h}(-\boldsymbol{q'}, t) \rangle = 0 \tag{2.16}$$

$$\langle \widetilde{h}(\boldsymbol{q}, t) \widetilde{h}(-\boldsymbol{q'}, t) \rangle = \langle \widetilde{h}(-\boldsymbol{q}, t) \widetilde{h}(\boldsymbol{q'}, t) \rangle = \langle \left|\widetilde{h}(\boldsymbol{q'})\right|^2 \rangle \delta^2(\boldsymbol{q} - \boldsymbol{q'}) \,. \tag{2.17}$$

Hence, the surface roughness, or correspondingly the interfacial width σ_{cw}, can be evaluated from

$$\sigma_{cw}^2 = \sum_{\boldsymbol{q}} \langle \left|\widetilde{h}(\boldsymbol{q})\right|^2 \rangle \,. \tag{2.18}$$

The average values $\langle \left|\widetilde{h}(\boldsymbol{q})\right|^2 \rangle$ per $\boldsymbol{q}-$mode yield with eq. (2.14), (2.10) and the Maxwell-Boltzmann statistic the roughness expression per $\boldsymbol{q}-$mode

$$\begin{aligned} \langle \left|\widetilde{h}(\boldsymbol{q})\right|^2 \rangle &= \frac{\iint d\widetilde{h}(\boldsymbol{q}) d\widetilde{\Psi}(\boldsymbol{q}) \; |\widetilde{h}(\boldsymbol{q})|^2 \; e^{-\widetilde{H}\left(\widetilde{\Psi}(\boldsymbol{q}), \widetilde{h}(\boldsymbol{q})\right)/k_B T}}{\iint d\widetilde{h}(\boldsymbol{q}) d\widetilde{\Psi}(\boldsymbol{q}) \; e^{-\widetilde{H}\left(\widetilde{\Psi}(\boldsymbol{q}), \widetilde{h}(\boldsymbol{q})\right)/k_B T}} \\ &= \frac{\int_0^\infty d\widetilde{h}(\boldsymbol{q}) \; \widetilde{h}^2(\boldsymbol{q}) \; e^{-\frac{A}{2k_B T}(q_g^2 + q^2)\widetilde{h}^2(\boldsymbol{q})}}{\int_0^\infty d\widetilde{h}(\boldsymbol{q}) \;\; e^{-\frac{A}{2k_B T}(q_g^2 + q^2)\widetilde{h}^2(\boldsymbol{q})}} \\ &= \frac{k_B T}{A\gamma} \frac{1}{q_g^2 + \boldsymbol{q}^2} \,, \end{aligned} \tag{2.19}$$

where k_B is the Boltzmann constant. With (2.18), the capillary wave roughness can be expressed as a double sum over all $\boldsymbol{q} = (q_x, q_y)$ modes or alternatively

as a single sum over $q = |\boldsymbol{q}|$, viz.

$$\sigma_{cw}^2 = \sum_{q>0} \frac{k_B T}{A\gamma} \frac{1}{q_g^2 + q^2} \,. \tag{2.20}$$

In (2.20) the summation starts from the lowest value $q = 2\pi/L$ to the upper cutoff q_{max}, which serves as truncation of the continuous (hydrodynamic model) medium. The upper cutoff is customarily estimated to be inversely proportional to the bulk correlation length [80], but it has also been taken to be inversely proportional to the intermolecular spacings [22, 99]. In the limit $A \to \infty$ expression (2.20) yields the key formula of the capillary wave model:

$$\sigma_{cw}^2 = \frac{k_B T}{2\pi\gamma} \int_0^{q_{max}} dq \; \frac{q}{q_g^2 + q^2} = \frac{k_B T}{4\pi\gamma} \ln\left(1 + \frac{q_{max}^2}{q_g^2}\right) . \tag{2.21}$$

Eq. (2.21) can be derived from (2.20) by using the limit relation $\sum_{\boldsymbol{q}>0} \to A/(2\pi)^2 \int d^2q$. Due to the requirement of statistical isotropy, one can furthermore transform the integral into polar coordinates, which eventually leads to expression (2.21). The fraction q_{max}/q_g may alternatively be replaced by $2\pi\ell_s/\ell_b$, which describes the ratio between the short-range bulk and long-range surface correlation length. For temperatures far below T_c, a rough estimate for the bulk correlation length $\ell_b \approx d_m$ is commonly deduced from the mean molecular diameter d_m [27, 22, 99]. Note that eq. (2.21) would lead to a logarithmical singularity for the surface width, if the upper wave vector cutoff is not being introduced.

2.1.2 Effective Interface Hamiltonian

It may be readily seen that the interfacial roughness can effectively be determined by the potential energy of the Hamiltonian function eq. (2.4a). Accordingly, one may derive the interfacial roughness at once by constructing an effective interface Hamiltonian $H[h(\boldsymbol{r})]$, which describes the cost in energy to deform the flat interface into a given rippled configuration. From this standpoint, one obtains the result of the previous section by constructing the so-called "drumhead" Hamiltonian [39, 43]

$$H_{dh}[h(\boldsymbol{r})] = \frac{1}{2} \int_A d^2r \; \triangle\varrho \, g h^2(\boldsymbol{r}) + \gamma \int_A d^2r \left(\sqrt{1 + |\nabla_\parallel h(\boldsymbol{r})|^2} - 1\right) , \tag{2.22}$$

which eventually yields with the following gradient expansion

$$\sqrt{1 + |\nabla_\parallel h(\boldsymbol{r})|^2} = 1 + \frac{1}{2}|\nabla_\parallel h(\boldsymbol{r})|^2 + \mathcal{O}\left(|\nabla_\parallel h(\boldsymbol{r})|^4\right) . \tag{2.23}$$

the "capillary wave" effective Hamiltonian of Buff et al. [14, 8, 27, 80]

$$H_{cw}[h(\boldsymbol{r})] = \frac{1}{2}\int_A d^2r\ \triangle\varrho\, g h^2(\boldsymbol{r}) + \frac{\gamma}{2}\int_A d^2r\ |\nabla_{\parallel} h(\boldsymbol{r})|^2. \tag{2.24}$$

Evidently, eq. (2.24) yields (regardless of the small difference $\triangle\varrho = \varrho_l - \varrho_v$) the same statistical properties for liquid surfaces as eq. (2.4). By using the above formal approach, one can conveniently study a variety of surfaces by constructing the effective interfacial Hamiltonian of the system.

Effective interface Hamiltonians that yield in their normal coordinates a Gaussian form for the Maxwell-Boltzmann weighting factor, i.e. $e^{-\widetilde{H}[\widetilde{h}(\boldsymbol{q})]/k_BT}$, represent the class of Hamiltonians in the so-called Gaussian approximation. Due to their simplicity and structural similarity with the capillary wave Hamiltonian, these types of effective interface Hamiltonians play an important role in the statistical analysis of liquid surfaces. Among the most important phenomenological Hamiltonians in the Gaussian approximation is the Helfrich Hamiltonian, which is of the form [38, 24, 62]

$$H_H[h(\boldsymbol{r})] = \frac{1}{2}\int_A d^2r\ \triangle\varrho\, g h^2 + \frac{1}{2}\int_A d^2r\ \left\{\gamma|\nabla_{\parallel} h(\boldsymbol{r})|^2 + \kappa\left(\Delta_{\parallel} h(\boldsymbol{r})\right)^2\right\}, \tag{2.25}$$

where κ is the bending rigidity modulus. Helfrich's Hamiltonian takes into account the curvature dependence of the surface energy, whereas the capillary wave Hamiltonian assigns the same surface energy to all configurations which have equal total area. In the normal mode representation eq. (2.25) can be arranged such that it resembles the effective capillary wave Hamiltonian, hence

$$\widetilde{H}_H\left[\widetilde{h}(\boldsymbol{q})\right] = \frac{1}{(2\pi)^2}\int d^2q\ \frac{1}{2}\left(\triangle\varrho\, g + \gamma(q)\boldsymbol{q}^2\right)\left|\widetilde{h}(\boldsymbol{q})\right|^2, \tag{2.26}$$

where now $\gamma(q)$ denotes a q-dependent surface tension

$$\gamma(q) = \gamma + \kappa q^2\,, \tag{2.27}$$

which reduces at large length scales, i.e. $q \to 0$, to the macroscopic surface tension γ. Although the surface tension γ and the bending rigidity κ remain phenomenological constants, the Helfrich Hamiltonian makes the important prediction that the effectively measured surface tension is a function of length scales, i.e. $1/q$.

Despite the fact that the phenomenological effective Hamiltonians uncover important properties of liquid vapor interfaces, such as long-range surface correlations below T_c, they fail to include bulk fluctuations or to provide a microscopic picture of the surface tension. In order to incorporate the predictions

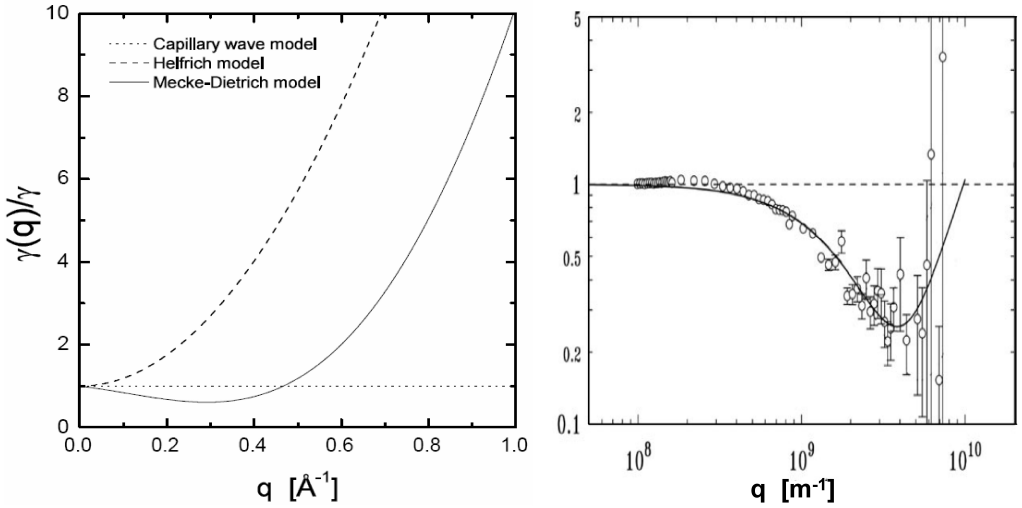

Figure 2.3: Surface tension as a function of q. Left: Comparison of Mecke-Dietrich's model of surface tension (solid curve) with the phenomenological capillary wave theory (dotted curve) and the Helfrich theory (dashed curve). The phenomenological Helfrich theory does not yield a specific value for κ/γ. Here, it is chosen such that this ratio has the value of the one predicted by Mecke-Dietrich's theory for large q, i.e. $\kappa/\gamma = 0.74 C_H^2 \ell_b^2 (1/2 + (\ell_b/d_m)^2)$. The parameters are $C_H = 0.1$, $d_m = 2$Å and $\ell_b = 5 d_m$. Right: Experimental confirmation of the reduction of surface tension on a water surface at room temperature [30]. The solid curve has been obtained from Mecke-Dietrich's theory for the parameters: $C_H = 0.35$, $d_m = 10$Å and $\ell_b = d_m/3$ [23].

of the capillary wave model into the traditional Van der Waals model of interfaces, R. Evans formulated a density functional theory for inhomogeneous simple (mono molecular) liquids. The theory describes short-range density-density fluctuation in the bulk, as well as long-range surface fluctuation at a liquid-vapor interface [27, 28]. This approach was first adopted by M. Napiorkowski & S. Dietrich [70] to construct an effective surface Hamiltonian which is based on a microscopic picture of the liquid. In a further improved version of the density functional approach, K. R. Mecke & S. Dietrich [63] derived an effective Hamiltonian that contains the capillary wave Hamiltonian as a limit result. Furthermore, it yields a $q-$dependent surface tension, which is essentially determined by the molecule diameter d_m and the bulk correlation length ℓ_b. After a subtle calculation, these authors obtain, in the Gaussian approxi-

mation, the following effective Hamiltonian in its normal mode representation

$$\widetilde{H}_{MD}\Big[\widetilde{h}(\boldsymbol{q})\Big] = \frac{1}{(2\pi)^2}\int d^2q\ \frac{1}{2}\Big\{\triangle\varrho\, g\left(1-2C_H(q\ell_b)^2\right)+\gamma(q)\boldsymbol{q}^2\Big\}\big|\widetilde{h}(\boldsymbol{q})\big|^2, \tag{2.28}$$

where the parameter C_H is a weight for the curvature corrections of the density profile for thermally exited capillary waves. C_H is limited between $0 < C_H < 0.5$, but it is not further specified in this theory. The surface tension $\gamma(q)$ in eq. (2.28) decreases from its macroscopic value at $q = 0$ due to the effect of attractive long-range forces, reaches a minimum, and then increases $\propto q^2$ at large q, due to the distortion of the density profile when the surface is bent [62]. An approximate formula for the surface tension takes the form [63]

$$\begin{aligned}\frac{\gamma(q)}{\gamma} = &\left(2-C_H(q\ell_b)^2\right)\frac{\widetilde{w}(qd_m)}{(qd_m)^2}+0.74C_H^2\left(\frac{1}{2}+\left(\frac{\ell_b}{d_m}\right)^2\widetilde{w}(qd_m)\right)(q\ell_b)^2\\ &+\mathcal{O}\left((qd_m)^4\right),\end{aligned} \tag{2.29}$$

with $\widetilde{w}(x) = 1-(1+x)e^{-x}$. In the limit $q\to\infty$, Mecke & Dietrich's theory predicted the following limiting expression for the surface tension [63]

$$\gamma(q\to\infty) = \kappa\, q^2\,. \tag{2.30}$$

Eq. (2.29) holds in the so-called product approximation, which comprises the condition $\ell_b \gg d_m$. However, it is argued that the maximum error in the product approximation is less than 10% even for $\ell_b \gtrapprox d_m$ [63, 69]. Expression (2.29) yields the same limit result as the effective Helfrich surface tension (2.27), and eq. (2.29) reduces for $(q\ell_b)^2 \ll 1$ to the capillary wave result. A comparison between the three surface tension models is shown in Fig.2.3 (left). The formation of a minimum in the surface tension appear to has been experimentally confirmed by surface sensitive X-ray scattering techniques for several liquids [30, 69, 50]. The experimental result for a water surface at room temperature is given in Fig.2.3 (right). It should be noted that the theoretically predicted and experimentally observed reduction in surface tension appears for relatively large $\boldsymbol{q} = (q_x, q_y)$ values (of the order $10^9\mathrm{m}^{-1}$). Hence, if the maximum experimental q values are smaller than ca. $1/\ell_b$, one may readily use the capillary wave model. This will be in particular the case for X-ray reflectively experiments, where $\boldsymbol{q}$ is experimentally set to be zero. The same conclusion may be drawn from the effective Mecke-Dietrich Hamiltonian (2.28) for $(q\ell_b)^2 \ll 1$. In summary, the Mecke-Dietrich theory of surfaces appears to reveal some fundamentally new properties of fluid surfaces at atomic length scales, which is, however, up to now controversially debated in the scientific

community. With respect to time dependent surface properties, it should acknowledged that a time dependent density fluctuation theory for surfaces is not developed at the present time. Hence, the understanding of dynamic surface properties is ordinarily deduced from linear response theories of classical hydrodynamic [10, 53, 40, 41].

2.2 Surface Height Correlation Function

In comparison to surface microscopy techniques, such as Scanning Tunneling Microscope (STM) and Atomic Force Microscopy (AFM), surface sensitive X-ray scattering techniques provide statistical information from a relatively large surface area which can extend to several hundreds of square microns [99]. The statistical characterization of surface structures, in terms of height correlation functions, allow a relatively direct and systematic analysis of X-ray scattering data and play, therefore, a central role in the theoretical calculation of scattering cross sections from rough surfaces. In this section the static and dynamic height correlation functions are derived for some specific liquid surfaces, which are of interest for this work.

2.2.1 Static Height Correlation Function

The static height correlation function $C_{zz}(\boldsymbol{r}, \boldsymbol{r'})$ describes the lateral correlation between two spatially separated height displacements on a surface. In analogy to the mean-squared roughness definition (2.15) one finds for the height correlation function

$$C_{zz}(\boldsymbol{r}, \boldsymbol{r'}) = \langle h(\boldsymbol{r}, t) h(\boldsymbol{r'}, t) \rangle = \sum_{\boldsymbol{q}} \sum_{\boldsymbol{q'}} \langle \widetilde{h}(\boldsymbol{q}, t) \widetilde{h}(\boldsymbol{q'}, t) \rangle \, e^{i(\boldsymbol{q}\cdot\boldsymbol{r} + \boldsymbol{q'}\cdot\boldsymbol{r'})} \,, \tag{2.31}$$

Based on the demanded statistical properties for the random height displacements $h(\boldsymbol{r}, t)$ (see section 2.1.1) it follows with eq. (2.16) and (2.17) that the height correlation function is spatially only a function of the separation $\boldsymbol{r'} - \boldsymbol{r}$. Hence, eq. (2.31) becomes

$$C_{zz}(\boldsymbol{r'} - \boldsymbol{r}) = \sum_{\boldsymbol{q}} \langle |\widetilde{h}(\boldsymbol{q})|^2 \rangle \, e^{i\boldsymbol{q}\cdot(\boldsymbol{r'} - \boldsymbol{r})} \,. \tag{2.32}$$

In addition to the spatial dependence, eq. (2.31) and (2.15) require the following two general properties

$$C_{zz}(\boldsymbol{r'} - \boldsymbol{r}) = C_{zz}(\boldsymbol{r} - \boldsymbol{r'}) \,, \tag{2.33}$$

$$\sigma^2 = C_{zz}(\boldsymbol{r'} - \boldsymbol{r})\big|_{\boldsymbol{r'} - \boldsymbol{r} = 0} \,, \tag{2.34}$$

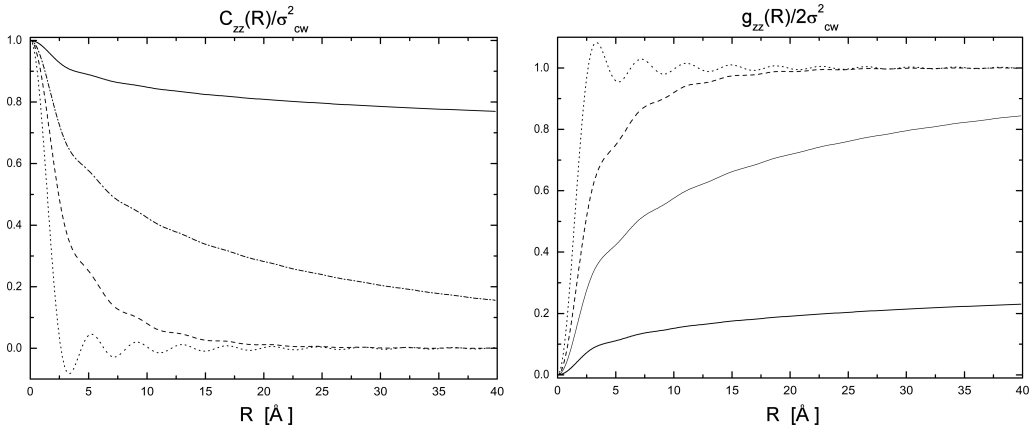

Figure 2.4: Normalized static height correlation function $C_{zz}(R)/\sigma_{cw}^2$ as a function of R. Left: Normalized height correlation for a water surface at room temperature (solid line); the correlations lengths are $\ell_s = 2.7$mm and $\ell_b \approx 2r_m$, with the mean molecular radius $r_m(\mathbf{H_2O}) = 1.92$Å [11]. The q_{max} cutoff, inherent to the capillary wave model, is taken to be $q_{max} = 2\pi/\ell_b$. The height correlation decays as the surface correlation length decreases; three arbitrary cases are illustrated: $q_g = q_{max}/100$ (dash-dotted line), $q_g = q_{max}/10$ (dashed line) and $q_g = q_{max}$ (dotted line). Right: Illustration of the normalized height-difference correlation function for the same values used in the left plot.

where the condition (2.34) defines the maximum value for height correlation function. In the continuous limit, expression (2.32) transforms into the integral expression

$$C_{zz}(\boldsymbol{R}) = \frac{1}{(2\pi)^2} \int d^2q \; \widetilde{C}_{zz}(\boldsymbol{q})\, e^{i\boldsymbol{q}\cdot\boldsymbol{R}}, \tag{2.35}$$

where $\boldsymbol{R} = \boldsymbol{r'} - \boldsymbol{r}$ and $\widetilde{C}_{zz}(\boldsymbol{q})$ is the reciprocal space height correlation function, which takes for the capillary wave model the following form

$$\widetilde{C}_{zz}(\boldsymbol{q}) = \frac{k_B T}{\gamma} \frac{1}{\boldsymbol{q}^2 + q_g^2}\,. \tag{2.36}$$

The real space expression for the height correlation function can be evaluated

by transforming integral (2.35) into polar coordinates, which yields

$$C_{zz}(R) = \frac{k_B T}{2\pi\gamma} \int_0^{q_{max}} dq \; \frac{q}{q^2 + q_g^2} \, J_0(qR) \,, \tag{2.37}$$

$$= \frac{k_B T}{4\pi\gamma} \left(\frac{q_{max}}{q_g} \right)^2 \times \sum_{k=0}^{\infty} \frac{(-1)^k}{\Gamma[1+k]} \, {}_2F_1\Big[1, 1+k; 2+k; -q_{max}^2/q_g^2\Big] \left(\frac{q_{max} R}{2} \right)^{2k} , \tag{2.38}$$

where $R = (x^2 + y^2)^{1/2}$, and $J_0(qR)$ represents the Bessel function of the first kind. By performing the integral (2.37), with the sum representation for the Bessel function [33], one finds the result (2.38), where ${}_2F_1[1, 1+k; 2+k; -q_{max}^2/q_g^2]$ is the regularized hypergeometric function and $\Gamma[1+k]$ is the Gamma function. Eq. (2.38) does satisfy the symmetry condition (2.33) as well as

$$\sigma_{cw}^2 = C_{zz}(R)\big|_{R=0} \,. \tag{2.39}$$

Note that the sharp cutoff in (2.37) leads to oscillation in the height correlation function, see Fig.2.4. Another quantity, that is of interest in the calculation of scattering cross sections from surfaces is the static height-difference correlation function $g_{zz}(\boldsymbol{R})$ [90]:

$$g_{zz}(\boldsymbol{r}' - \boldsymbol{r}) = \Big\langle \big(h(\boldsymbol{r}', t) - h(\boldsymbol{r}, t) \big)^2 \Big\rangle \,, \tag{2.40}$$

which can easily be reduced to the radial height-difference correlation function for liquid surfaces

$$g_{zz}(R) = 2 \left(\sigma_{cw}^2 - C_{zz}(R) \right) . \tag{2.41}$$

The spatial behavior of the radial height correlation function (2.38) and the height-difference correlation function (2.41) are illustrated in Fig.2.4.

It is worth mentioning that the commonly used height correlation function is derived from (2.37) for the limit $q_{max} \to \infty$ [81, 6, 22, 99]. In that case one finds [33]

$$C_{zz}(R) = \frac{k_B T}{2\pi\gamma} \int_0^{\infty} dq \; \frac{q}{q^2 + q_g^2} \, J_0(qR) \,, \tag{2.42}$$

$$= \frac{k_B T}{2\pi\gamma} K_0(q_g R) \,, \tag{2.43}$$

where $K_0(q_g R)$ is the modified Bessel function of the second kind. The relatively simple result of eq. (2.43) has some useful properties with regard to the calculation of scattering functions, see section 3.2. However, due to the limit

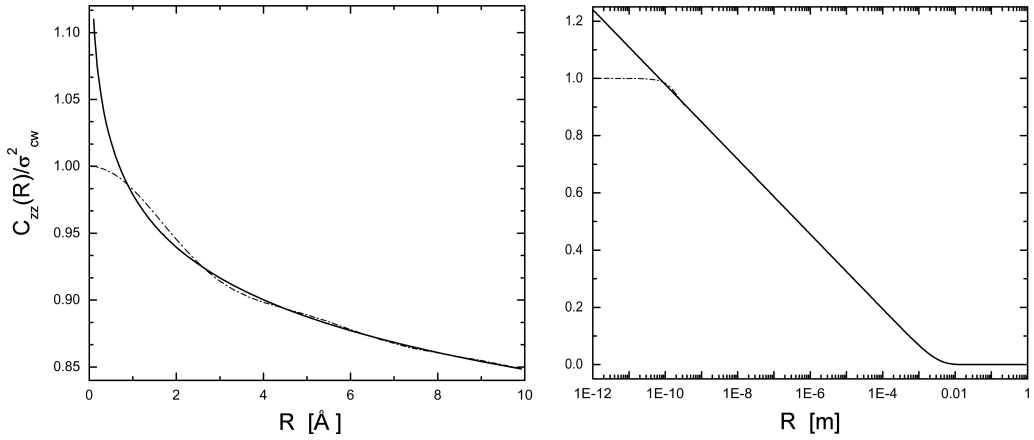

Figure 2.5: Normalized static height correlation function $C_{zz}(R)/\sigma_{cw}^2$ as a function of R. Comparison between eq. (2.43) (continuous line) and eq. (2.38) (dash-dotted line). The normalized height correlation functions are obtained by using the material constants for water at room temperature. q_{max} is taken to be $q_{max} = \pi/r_m$, where $r_m = 1.92$Å. Left: For short distances, the main difference appears at $R = 0$. Right: In the limit $R \gg \ell_b$, eq. (2.43) is in good agreement with the exact solution for the height correlation function (2.38).

$\lim_{R\to 0} K_0(q_g R) \to \infty$ the condition (2.39) is obviously not satisfied and, correspondingly, the theoretical scattering functions that are derived from (2.43) contain singularities in reciprocal space. A comparison between eq .(2.38) and (2.43) is shown in Fig.2.5.

2.2.2 Dynamic Height Correlation Function

The static height correlation functions of the previous section are only applicable to static scattering experiments from liquid surface. In time resolved (surface sensitive) experiments such as dynamical light scattering (DLS), or X-ray intensity correlation spectroscopy (XICS), the measured quantity is, however, related to the dynamic height correlation function, which is in general defined as

$$C_{zz}(\boldsymbol{r}, \boldsymbol{r'}, t, t') = \langle h(\boldsymbol{r}, t) h(\boldsymbol{r'}, t') \rangle \,. \tag{2.44}$$

With the statistical properties of the height displacement function $h(\boldsymbol{r}, t)$, see section 2.1.1, the autocorrelation function $C_{zz}(\boldsymbol{r}, \boldsymbol{r'}, t, t')$ reduces to a function which depends only on spatial and time differences [58, 32]. Accordingly, the dynamic height correlation function can, henceforth, be written as

$$C_{zz}(\boldsymbol{r'} - \boldsymbol{r}, t' - t) = \langle h(\boldsymbol{r}, t) h(\boldsymbol{r'}, t') \rangle \,, \tag{2.45}$$

and, moreover, it obeys the following conditions

$$C_{zz}(\boldsymbol{r'}-\boldsymbol{r},t'-t) = C_{zz}(\boldsymbol{r}-\boldsymbol{r'},t-t')\,, \tag{2.46}$$

$$C_{zz}(\boldsymbol{r'}-\boldsymbol{r}) = C_{zz}(\boldsymbol{r'}-\boldsymbol{r},t'-t)\big|_{t'-t=0}\,, \tag{2.47}$$

$$\sigma^2 = C_{zz}(\boldsymbol{r'}-\boldsymbol{r},t'-t)\big|_{\boldsymbol{r'}-\boldsymbol{r}=0,t'-t=0}\,. \tag{2.48}$$

In order to obtain a specific expression for the dynamic height correlation function, it will be useful to use the Wiener-Khintchine theorem, which relates the autocorrelation function of stationary random processes and the power spectrum of these fluctuations, by a conventional Fourier transform [58]. Using the Wiener-Khintchine theorem in combination with eq (2.35), one can derive the dynamic height correlation function from

$$C_{zz}(\boldsymbol{R},\tau) = \frac{1}{(2\pi)^3}\iint d\omega\, d^2q\; S_{zz}(\boldsymbol{q},\omega)\, e^{i(\boldsymbol{q}\cdot\boldsymbol{R}-\omega\tau)}\,, \tag{2.49}$$

where $\boldsymbol{R}=\boldsymbol{r'}-\boldsymbol{r}$, $\tau=t'-t$ and $S_{zz}(\boldsymbol{q},\omega)$ represents the power spectrum of thermal surface displacements.

Explicit expressions for the surface spectrum $S_{zz}(\boldsymbol{q},\omega)$ have been deduced from linear response theory by several authors [10, 53, 40, 41]. In the limiting case of deep liquids, as considered in this work, the surface spectrum $S_{zz}(\boldsymbol{q},\omega)$ for an incompressible fluid with arbitrary viscosity is given by

$$S_{zz}(\boldsymbol{q},\omega) = \frac{2k_BT}{\omega}\,\mathrm{Im}\left[\frac{q/\varrho_l}{\omega_s^2(q)-(\omega+i2\nu\boldsymbol{q}^2)^2-4\nu^2\boldsymbol{q}^4(1-\omega/\nu\boldsymbol{q}^2)^{1/2}}\right], \tag{2.50}$$

where ν is the kinematic viscosity. The depth dependance is in The Fourier transform of eq. (2.50) is a nontrivial task and, therefore, it is only solved below for special cases. For a highly viscous liquid eq. (2.50) can be approximated by a Lorentzian curve, which peaks at $\omega=0$ with a half width at half maximum (HWHM) of $\Gamma_h(q)=\gamma q/(2\nu\varrho_l)$. In the low viscosity case the surface spectrum yields two equally spaced sharp peaks at $\omega=\pm\omega_s(q)$ with a HWHM of $\Gamma_l(\boldsymbol{q})=2\nu\boldsymbol{q}^2$. Here the subscribes h and l denote the limits for high and low viscosity liquids, respectively.

A. Height correlation function for low viscosity liquids

In the low viscosity limit the general surface spectrum eq. (2.50) simplifies to [41]

$$S_{zz}(\boldsymbol{q},\omega) = 2k_BT\frac{q}{\varrho_l}\frac{2\Gamma_l(\boldsymbol{q})}{(\omega^2-\omega_s^2(q))^2+(2\omega\Gamma_l(\boldsymbol{q}))^2}\,, \tag{2.51}$$

with

$$\Gamma_l(\boldsymbol{q}) = 2\nu\boldsymbol{q}^2\,. \tag{2.52}$$

The above expression can be used to derive the height correlation function of propagating capillary waves. By performing the Fourier transform with respect to ω we find [33]

$$\widetilde{C}_{zz}(\boldsymbol{q},\tau) = \frac{k_B T}{\gamma}\frac{1}{\boldsymbol{q}^2+q_g^2}\, e^{-\Gamma_l(\boldsymbol{q})\tau}\left[\cos\left(\omega_s(q)\tau\sqrt{1-\left(\Gamma_l(\boldsymbol{q})/\omega_s(q)\right)^2}\right)\right. \\ \left. +\frac{\Gamma_l(\boldsymbol{q})}{\omega_s(q)\sqrt{1-\left(\Gamma_l(\boldsymbol{q})/\omega_s(q)\right)^2}}\sin\left(\omega_s(q)\tau\sqrt{1-\left(\Gamma_l(\boldsymbol{q})/\omega_s(q)\right)^2}\right)\right], \tag{2.53}$$

where we used the trigonometric relations $\sin(\arccos\alpha) = (1-\alpha^2)^{1/2}$ and $\sin 2\alpha = 2\sin\alpha\cos\alpha$. A useful approximation is obtained, if the condition $\Gamma_l(\boldsymbol{q})/\omega_s(q) \ll 1$ is satisfied in the range of experimental wave vector transfers. Eq. (2.53) then simplifies to

$$\widetilde{C}_{zz}(\boldsymbol{q},\tau) \approx \frac{k_B T}{\gamma}\frac{1}{\boldsymbol{q}^2+q_g^2}\cos\left(\omega_s(q)\tau\right)\, e^{-\Gamma_l(\boldsymbol{q})\tau}\,, \quad \text{for} \;\; \Gamma_l(\boldsymbol{q})/\omega_s(q) \ll 1\,. \tag{2.54}$$

For the discussion of surface sensitive XICS the reciprocal space expression (2.54) is in fact sufficient enough, as will be shown later. Note that the solutions (2.53) and (2.54) hold only for $\tau \geq 0$. The corresponding real-space expression to (2.54) can be expressed in a series form; however, its usability is questionable and, therefore, it is left out of the discussion.

B. Height correlation function for high viscosity liquids

For a liquid with high viscosity the surface spectrum $S_{zz}(\boldsymbol{q},\omega)$ takes the form of a Lorentzian curve, viz.

$$S_{zz}(\boldsymbol{q},\omega) = 2k_B T\frac{1}{\gamma\boldsymbol{q}^2}\frac{\Gamma_h(q)}{\omega^2+\Gamma_h^2(q)\left(1+q_g^2/\boldsymbol{q}^2\right)^2}\,, \tag{2.55}$$

where

$$\Gamma_h(q) = \frac{\gamma}{2\nu\varrho_l}\,q\,. \tag{2.56}$$

The half width at half maximum is essentially determined by $\Gamma_h(q)$ and additionally broadened by a term that contains the gravitational cutoff. For typical experimental $q-$values, the contribution of q_g gives a negligible correction to the width of $S_{zz}(\boldsymbol{q},\omega)$ and is, therefore, often omitted [41]. With the surface

spectrum (2.55) one can easily calculate the height correlation function for high viscosity liquids, which yields [33]

$$\widetilde{C}_{zz}(\boldsymbol{q},\tau) = \frac{k_B T}{\gamma}\frac{1}{\boldsymbol{q}^2+q_g^2}\, e^{-\Gamma_h(q)\tau(1+q_g^2/\boldsymbol{q}^2)}\,, \qquad \text{for} \quad \tau \geq 0\,. \tag{2.57}$$

It is worth noting that eq. (2.54) and (2.57) reduce to the static height correlation function for $\tau = 0$, i.e. they obey the condition (2.47).

Chapter 3

Elastic X-Ray Scattering From Rough Surfaces

The interaction of electromagnetic waves with material interfaces is a classical discipline in scattering theory. Among the first descriptions one may count Snell's law of refraction and the Fresnel formulas of reflection and transmission, which apply to the interaction of electromagnetic waves at a perfectly smooth surface [9]. Since these classical works of Snell and Fresnel, the analysis of surface scattering from smooth, structured and rough surface has been the object of theoretical and experimental studies of a large body of work, which contains the description of surface scattering of long wavelength radar waves, visible light, down to X-ray wavelengths [7, 5, 104, 99, 22].

With the growing number of X-ray synchrotron radiation sources, surface scattering has been rediscovered as a powerful experimental tool and increasingly used to investigate surface properties, down to the atomic-scale. For X-ray wavelengths, the interaction of electromagnetic wave with matter is mainly determined by the electron charges in the scatterer. Although there are many phenomena associated with the interaction, here we will only consider those related to elastic Thompson scattering. Since we are not concerned with absorption and emission processes, the quantum theory of photon-electron scattering will not be needed and, hence, the scattered intensity expressions can be readily obtained from Maxwell's field equations.

In this section, we will relate the statistical properties of rough surface to the scattered X-ray intensity. The scattering process will henceforth be describe within the scalar theory of electromagnetic wave scattering. In view of the discussion on quasi-elastic scattering, some of the derivations and results in this chapter will later serve us as a reference.

3.1 Basic Principles

According to the classic description of scattering, one can determine the scattered intensity from the modulus square of the scattered electric field. In order to derive the explicit expression for the scattered electric field, we will consider throughout this work a nonmagnetic, isotropic and homogenous scatterer. In that case, the propagation of the electric field can be described by the (scalar) Helmholtz equation [9], namely

$$\Delta\widetilde{U}(\mathbf{r},\omega_0) + k_0^2 n^2(\mathbf{r},\omega_0)\widetilde{U}(\mathbf{r},\omega_0) = 0 \ . \tag{3.1}$$

where k_0 is the free-space wave number and ω_0 is the frequency of the field at the observation point $\mathbf{r} = (\boldsymbol{r}, z)$ with $\boldsymbol{r} = (x, y)$. $\widetilde{U}(\mathbf{r},\omega_0)$ is a complex scalar representation for the electric field and $n(\mathbf{r},\omega)$ is the refractive index, which characterizes the optical properties of scatterer in the occupied volume V as well as the exterior volume V_R, such as $n(\mathbf{r},\omega_0) = 1$ takes the vacuum value for $\mathbf{r} \in V_R$. To specify the response characteristics of the index of refraction in the hard X-ray limit, it is sufficient to use the classical formulas, viz.

$$n^2(\mathbf{r},\omega_0) = 1 + 4\pi\chi(\mathbf{r},\omega_0) \ , \qquad \text{for} \quad \mathbf{r} \in V \tag{3.2}$$

where, in the Drude model [42], the dielectric susceptibility $\chi(\mathbf{r},\omega_0)$ is described as

$$\chi(\mathbf{r},\omega_0) = r_e c^2 N \sum_j \ \frac{f_j}{\omega_j^2 - \omega_0^2 - i\gamma_j\omega_0}. \tag{3.3}$$

In eq. (3.3) the constants r_e and c represent the classical electron radius and the speed of light, respectively. N is the number of molecules per unit volume with Z electrons per molecule. The resonance frequencies ω_j of the electrons are weighted by the oscillation strength f_j, which gives the number of electrons per resonance frequency and, thus, f_j obeys the sum rule $\Sigma_j f_j = Z$. γ_j is a phenomenological damping constant [42]. For X-ray frequencies far beyond any resonance frequency one finds for (3.2)

$$n^2(\mathbf{r},\omega_0) = 1 - 4\pi r_e \rho(\mathbf{r})\frac{c^2}{\omega_0^2} \ , \tag{3.4}$$

which simplifies, with the expansion $\sqrt{1-x} \approx 1 - x/2$, to the form

$$n(\mathbf{r},\omega_0) = 1 - \delta(\mathbf{r},\omega_0) \ , \tag{3.5}$$

with

$$\delta(\mathbf{r},\omega_0) = 2\pi r_e \rho(\mathbf{r})\frac{c^2}{\omega_0^2} \ . \tag{3.6}$$

Here $\rho(\mathbf{r})$ is the number of electrons per unit volume. The dispersion term $\delta(\mathbf{r},\omega_0)$ is zero in vacuum and is, otherwise, a small positive quantity of the order of 10^{-6} (for X-ray wavelengths). Due to the negative sign in (3.5), the index of refraction in matter is always smaller than in vacuum. Hence, at grazing incident angles below the critical angle $\alpha_c \approx \sqrt{2\delta(\mathbf{r},\omega_0)}$, the negative sign leads to the phenomenon of external total reflection in contrast to the analogous phenomenon of total internal reflection for visible light [99]. Corrections to expression (3.5) contain an addition absorption term $\beta(\mathbf{r},\omega_0)$, and the proper atomic scattering factor $f_p = f_p^0 + f_p'(\omega_0) + if_p''(\omega_0)$ of each component p of the scattering material, so that in general, $n(\mathbf{r},\omega_0)$ yields the expression [99]

$$n(\mathbf{r},\omega_0) = 1 - \delta(\mathbf{r},\omega_0) + i\beta(\mathbf{r},\omega_0) \ , \tag{3.7}$$

with the dispersion and absorption terms

$$\delta(\mathbf{r},\omega_0) = 2\pi r_e \rho(\mathbf{r}) \frac{c^2}{w_0^2} \sum_p \frac{f_p^0 + f_p'(\omega_0)}{Z} \ , \tag{3.8a}$$

$$\beta(\mathbf{r},\omega_0) = 2\pi r_e \rho(\mathbf{r}) \frac{c^2}{w_0^2} \sum_p \frac{f_p''(\omega_0)}{Z} = \frac{c}{2\omega_0}\mu(\mathbf{r}) \ , \tag{3.8b}$$

where $\mu(\mathbf{r})$ represents the linear absorption length.

Next we will give the formal solution for the electric field in a scattering experiment. The finding of a rigorous solutions for the Helmholtz equation including the proper boundary conditions is a classic problem in diffraction optics and, generally, a difficult mathematical task [93]. A simpler and widely accepted approach to the solution of (3.1) is based on integral equations for $\widetilde{U}(\mathbf{r},\omega)$. In order to derive the needed integral equations it will be useful to express eq. (3.1) in form of Schrödinger's equation

$$\Delta\widetilde{U}(\mathbf{r},\omega_0) + k_0^2\widetilde{U}(\mathbf{r},\omega_0) = -4\pi\widetilde{F}(\mathbf{r},\omega_0)\widetilde{U}(\mathbf{r},\omega_0) \ , \tag{3.9}$$

where

$$\widetilde{F}(\mathbf{r},\omega_0) = \frac{\omega_0^2}{c^2}\,\chi(\mathbf{r},\omega_0) \ , \tag{3.10}$$

is called the optical potential of the medium. The wave number k_0 is represented in (3.10) by $\omega_0/c = k_0$. For values $\mathbf{r} \in V_R$ the optical potential obeys the condition $\widetilde{F}(\mathbf{r},\omega_0) = 0$, which is in accordance with the demanded vacuum value for the index of refraction outside of V, see Fig.3.1. The Green's function $G(\mathbf{r},\mathbf{r}',\omega_0)$ associated with the Helmholtz operator $(\Delta + k_0^2)$ satisfies the equation

$$(\Delta + k_0^2)G(\mathbf{r},\mathbf{r}',\omega_0) = -4\pi\delta^3(\mathbf{r}-\mathbf{r}') \ . \tag{3.11}$$

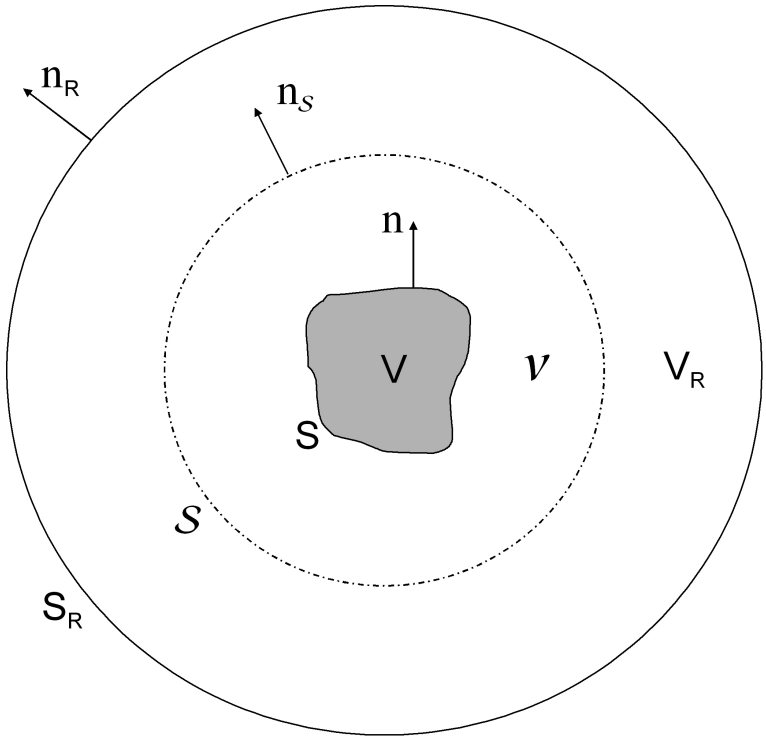

Figure 3.1: Illustration of the notation for potential scattering expressions and surface scattering expressions (Kirchhoff integral formulation). The exterior volume V_R is for simplicity definition by a sphere S_R of radius R (note, that $V \nsubseteq V_R$). The arbitrary volume $\mathcal{V}$ can coincide either with the volume V or with V_R. The volumes V, $\mathcal{V}$ and V_R are respectively bounded by the surfaces S, $\mathcal{S}$ and S_R. The normal unit vectors $\mathbf{n}$, $\mathbf{n}_{\mathcal{S}}$ and $\mathbf{n}_R$ point outwards to the surfaces S, $\mathcal{S}$ and S_R, respectively.

By using Green's integral theorem and eqs. (3.9) and (3.11) one finds the following integral equation [103]

$$\int_{\mathcal{V}} \widetilde{U}(\mathbf{r}',\omega_0)\delta^3(\mathbf{r}-\mathbf{r}')d^3\mathrm{r}' = \int_{\mathcal{V}} G(\mathbf{r},\mathbf{r}',\omega_0)\widetilde{F}(\mathbf{r}',\omega_0)\widetilde{U}(\mathbf{r}',\omega_0)d^3\mathrm{r}' - \frac{1}{4\pi}\int_{\mathcal{S}}\left[\widetilde{U}(\mathbf{r}',\omega_0)\frac{\partial G(\mathbf{r},\mathbf{r}',\omega_0)}{\partial \mathbf{n}_{\mathcal{S}}} - G(\mathbf{r},\mathbf{r}',\omega_0)\frac{\partial \widetilde{U}(\mathbf{r}',\omega_0)}{\partial \mathbf{n}_{\mathcal{S}}}\right] d\mathcal{S}\,, \tag{3.12}$$

where the volume $\mathcal{V}$ coincides either with the volume V or with V_R. The derivatives $\partial/\partial\mathbf{n}_{\mathcal{S}}$ denote differentiations along the outward normal to the surface $\mathcal{S}$, which bounds the domain $\mathcal{V}$. Depending on the choice of domain $\mathcal{V}$ and position of the observation point $\mathbf{r}$ one obtains four possible solutions for

the integral equation (3.12) [71]:

1. $\mathcal{V} = V$ and $\mathbf{r} \in V$ (in that case $\mathbf{r}$ is denoted by $\mathbf{r}_<$)

$$\widetilde{U}(\mathbf{r}_<, \omega_0) = \int_V G(\mathbf{r}_<, \mathbf{r}', \omega_0)\widetilde{F}(\mathbf{r}', \omega_0)\widetilde{U}(\mathbf{r}', \omega_0)d^3\mathrm{r}' \\ -\frac{1}{4\pi}\int_S \left[\widetilde{U}(\mathbf{r}', \omega_0)\frac{\partial G(\mathbf{r}_<, \mathbf{r}, \omega_0)}{\partial \mathbf{n}} - G(\mathbf{r}_<, \mathbf{r}', \omega_0)\frac{\partial \widetilde{U}(\mathbf{r}', \omega_0)}{\partial \mathbf{n}}\right] dS\,, \tag{3.13}$$

2. $\mathcal{V} = V$ and $\mathbf{r} \in V_R$ (in that case $\mathbf{r}$ is denoted by $\mathbf{r}_>$)

$$0 = \int_V G(\mathbf{r}_>, \mathbf{r}', \omega_0)\widetilde{F}(\mathbf{r}', \omega_0)\widetilde{U}(\mathbf{r}', \omega_0)d^3\mathrm{r}' \\ -\frac{1}{4\pi}\int_S \left[\widetilde{U}(\mathbf{r}', \omega_0)\frac{\partial G(\mathbf{r}_>, \mathbf{r}', \omega_0)}{\partial \mathbf{n}} - G(\mathbf{r}_>, \mathbf{r}', \omega_0)\frac{\partial \widetilde{U}(\mathbf{r}', \omega_0)}{\partial \mathbf{n}}\right] dS\,, \tag{3.14}$$

3. $\mathcal{V} = V_R$ and $\mathbf{r} \in V$

$$0 = \frac{1}{4\pi}\int_S \left[\widetilde{U}(\mathbf{r}', \omega_0)\frac{\partial G(\mathbf{r}_<, \mathbf{r}', \omega_0)}{\partial \mathbf{n}} - G(\mathbf{r}_<, \mathbf{r}', \omega_0)\frac{\partial \widetilde{U}(\mathbf{r}', \omega_0)}{\partial \mathbf{n}}\right] dS \\ -\lim_{R\to\infty}\frac{1}{4\pi}\int_{S_R} \left[\widetilde{U}(\mathbf{r}', \omega_0)\frac{\partial G(\mathbf{r}_<, \mathbf{r}', \omega_0)}{\partial \mathbf{n}_R} - G(\mathbf{r}_<, \mathbf{r}', \omega_0)\frac{\partial \widetilde{U}(\mathbf{r}', \omega_0)}{\partial \mathbf{n}_R}\right] dS\,, \tag{3.15}$$

4. $\mathcal{V} = V_R$ and $\mathbf{r} \in V_R$

$$\widetilde{U}(\mathbf{r}_>, \omega_0) = \frac{1}{4\pi}\int_S \left[\widetilde{U}(\mathbf{r}', \omega_0)\frac{\partial G(\mathbf{r}_>, \mathbf{r}', \omega_0)}{\partial \mathbf{n}} - G(\mathbf{r}_>, \mathbf{r}', \omega_0)\frac{\partial \widetilde{U}(\mathbf{r}', \omega_0)}{\partial \mathbf{n}}\right] dS \\ -\lim_{R\to\infty}\frac{1}{4\pi}\int_{S_R} \left[\widetilde{U}(\mathbf{r}', \omega_0)\frac{\partial G(\mathbf{r}_>, \mathbf{r}', \omega_0)}{\partial \mathbf{n}_R} - G(\mathbf{r}_>, \mathbf{r}', \omega_0)\frac{\partial \widetilde{U}(\mathbf{r}', \omega_0)}{\partial \mathbf{n}_R}\right] dS\,. \tag{3.16}$$

Next, let the field $\widetilde{U}(\mathbf{r}, \omega_0)$ be expressed as the sum of the incident field $\widetilde{U}_i(\mathbf{r}, \omega_0)$ and the scattered field $\widetilde{U}_s(\mathbf{r}, \omega_0)$, namely

$$\widetilde{U}(\mathbf{r}, \omega_0) = \widetilde{U}_i(\mathbf{r}, \omega_0) + \widetilde{U}_s(\mathbf{r}, \omega_0)\ . \tag{3.17}$$

By using the above field representation (3.17) and also Sommerfeld's radiation condition, one obtains in the limit $R \to \infty$ the following result for the surface integral over S_R [75, 76]:

$$\widetilde{U}_i(\mathbf{r},\omega_0) = -\lim_{R\to\infty}\frac{1}{4\pi}\int_{S_R}\left[\widetilde{U}(\mathbf{r}',\omega_0)\frac{\partial G(\mathbf{r},\mathbf{r}',\omega_0)}{\partial \mathbf{n}_R} - G(\mathbf{r},\mathbf{r}',\omega_0)\frac{\partial \widetilde{U}(\mathbf{r}',\omega_0)}{\partial \mathbf{n}_R}\right] dS. \tag{3.18}$$

With eq. (3.18) the four possible integral solutions can be reformulated as [76, 106]

1. $\mathcal{V} = V$ and $\mathbf{r} \in V$

$$\widetilde{U}(\mathbf{r}_<,\omega_0) = \widetilde{U}_i(\mathbf{r}_<,\omega_0) + \int_V G(\mathbf{r}_<,\mathbf{r}',\omega_0)\tilde{F}(\mathbf{r}',\omega)\widetilde{U}(\mathbf{r}',\omega_0)d^3\mathrm{r}', \tag{3.19}$$

2. $\mathcal{V} = V$ and $\mathbf{r} \in V_R$

$$\widetilde{U}(\mathbf{r}_>,\omega_0) = \widetilde{U}_i(\mathbf{r}_>,\omega_0) + \int_V G(\mathbf{r}_>,\mathbf{r}',\omega_0)\widetilde{F}(\mathbf{r}',\omega_0)\widetilde{U}(\mathbf{r}',\omega_0)d^3\mathrm{r}', \tag{3.20}$$

3. $\mathcal{V} = V_R$ and $\mathbf{r} \in V$

$$\widetilde{U}_i(\mathbf{r}_<,\omega_0) = -\frac{1}{4\pi}\int_S\left[\widetilde{U}(\mathbf{r}',\omega_0)\frac{\partial G(\mathbf{r}_<,\mathbf{r}',\omega_0)}{\partial \mathbf{n}} - G(\mathbf{r}_<,\mathbf{r}',\omega_0)\frac{\partial \widetilde{U}(\mathbf{r}',\omega_0)}{\partial \mathbf{n}}\right] dS, \tag{3.21}$$

4. $\mathcal{V} = V_R$ and $\mathbf{r} \in V_R$

$$\widetilde{U}(\mathbf{r}_>,\omega_0) = \widetilde{U}_i(\mathbf{r}_>,\omega_0) + \frac{1}{4\pi}\int_S\left[\widetilde{U}(\mathbf{r}',\omega_0)\frac{\partial G(\mathbf{r}_>,\mathbf{r}',\omega_0)}{\partial \mathbf{n}} - G(\mathbf{r}_>,\mathbf{r}',\omega_0)\frac{\partial \widetilde{U}(\mathbf{r}',\omega_0)}{\partial \mathbf{n}}\right] dS. \tag{3.22}$$

The first two relations (3.19) and (3.20) are the usual integral equations for potential scattering. Eq. (3.21) represents an extinction theorem, which expresses the cancelation of the incident field at every point inside the optical potential. A detail discussion on the physical meaning of the extinction theorem can be found in Refs.[71, 106]. The last integral equation (3.22) is a Kirchhoff integral formulation of scattering. In order to evaluate the exterior field $\widetilde{U}(\mathbf{r}_>,\omega_0)$, one can use (3.20) or (3.22). In eq. (3.20) the mathematical and physical problem lies in finding the adequate optical potential of the scatterer, while the

Kirchhoff integral formulation (3.22) requires the determination of the boundary values of the field at the scattering surface. For historical reasons, the Kirchhoff integral formulation is used in the description of radar and light scattering from surfaces. The conventionally used field boundary conditions are described within the Beckmann-Kirchhoff theory of surface scattering. For further readings on this approach see the classical work of P. Beckmann and A. Spizzichino [7] or also Refs.[5, 104, 71]. Although both eqs. (3.20) and (3.22) are equivalent approaches to describe the scattering process, it is customary in the field of surface X-ray scattering to use the integral equation for potential scattering. A comprehensive description based on the potential scattering formulation is given by S. K. Sinha et al. [90]. In the following sections we will use integral equation (3.20) to derive the scattered field or, respectively, the scattered intensity.

3.2 Surface Scattering in First Born Approximation

In this section we will use the integral equation for potential scattering (3.20) to describe surface scattering from statistical rough surfaces in the first Born approximation. Most results in this section follow to a great extent S. K. Sinha's work on X-ray and neutron scattering from rough surfaces [89, 90].

In order to derive the scattered intensity, one can first substitute eq. (3.17) into (3.20), which gives the following result for a weakly scattering medium

$$\widetilde{U}_s(\mathbf{r},\omega_0) = \int_V G(\mathbf{r},\mathbf{r}',\omega_0)\widetilde{F}(\mathbf{r}',\omega_0)\widetilde{U}_i(\mathbf{r}',\omega_0)d^3\mathrm{r}' \,. \tag{3.23}$$

The above field equation gives the first Born approximation for the scattered field. The assumption of a weak scatterer is based on the fact that the X-ray index of refraction is, for most materials, very close to the vacuum value. Conclusively, the optical potential $\widetilde{F}(\mathbf{r}',\omega_0)$ itself takes in the X-ray limit values very close to zero. However, the omitted field term $\widetilde{U}_s(\mathbf{r},\omega_0)$ in the integrant of (3.23) takes significant value for incident angles close to the critical angle α_c, or below α_c. In this regime close to total external reflection the first Born approximation will consequently breakdown. We will address corrections to formula (3.23) at a later stage.

Next, one can use the outgoing free-space Green's function of the Helmholtz operator $(\Delta + k_0^2)$, namely [9, 42]

$$G(\mathbf{r},\mathbf{r}',\omega_0) = \frac{e^{ik_0|\mathbf{r}-\mathbf{r}'|}}{|\mathbf{r}-\mathbf{r}'|} \,, \qquad \text{with} \quad k_0 = \omega_0/c \,. \tag{3.24}$$

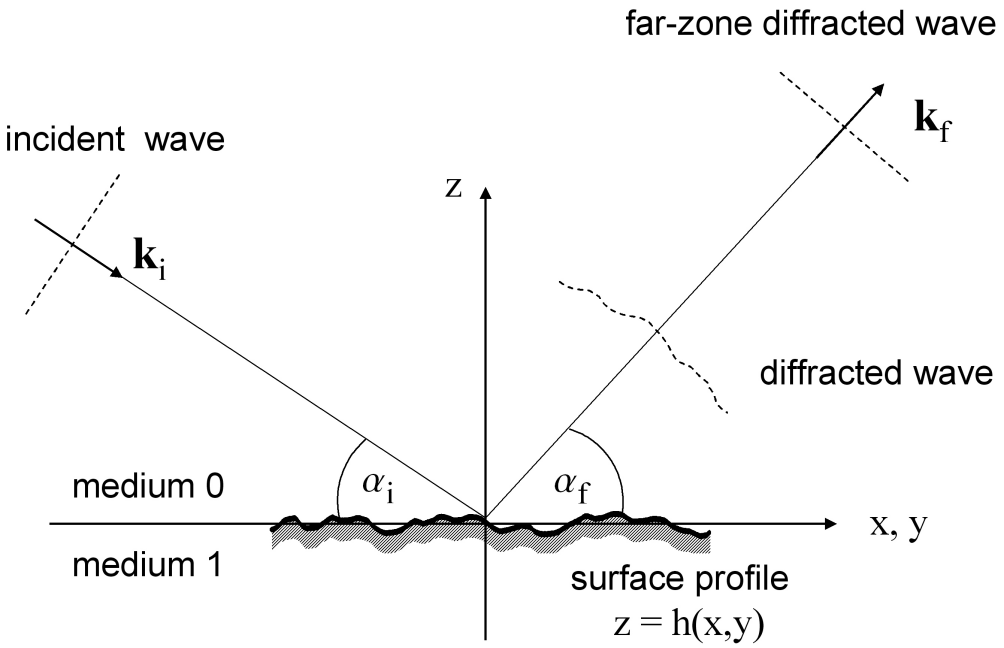

Figure 3.2: Schematic illustration of the scattering geometry for surface scattering. $\mathbf{k}_\mathrm{i}$ and α_i represents the mean incident wave vector and angle, respectively. Similarly, $\mathbf{k}_\mathrm{f}$ and α_f stand for the mean outgoing wave vector and angle. The transmitted wave into medium 1 is not considered here. The interface is defined by the interfacial zone of medium 0 (vapor atmosphere) and medium 1 (liquid phase).

If the detection point $\mathbf{r}$ is placed far from the scattering position $\mathbf{r}'$, we can approximate $|\mathbf{r}-\mathbf{r}'|$ by

$$\begin{aligned} |\mathbf{r}-\mathbf{r}'| &= \sqrt{\mathrm{r}^2 - 2\mathbf{r}\cdot\mathbf{r}' + \mathrm{r}'^2} = \mathrm{r}\sqrt{1 - 2\hat{\mathbf{r}}\cdot\left(\frac{\mathbf{r}'}{\mathrm{r}}\right) + \left(\frac{\mathbf{r}'}{\mathrm{r}}\right)^2}\,, \\ &\approx \mathrm{r} - \hat{\mathbf{r}}\cdot\mathbf{r}' + \mathcal{O}\left((\mathbf{r}'/\mathrm{r})^2\right)\,, \end{aligned} \tag{3.25}$$

and hence

$$G(\mathbf{r},\mathbf{r}',\omega_0) \approx \frac{e^{ik_0\mathrm{r}}}{\mathrm{r}}\; e^{-i\mathbf{k}_\mathrm{f}\cdot\mathbf{r}'}\,, \qquad \text{where}\;\; \mathbf{k}_\mathrm{f} = k_0\hat{\mathbf{r}}\,, \tag{3.26}$$

denotes the outgoing wave vector. If, furthermore, the radiating (point) source is far away from the scattering volume, one can describe the incident field by a plane wave

$$\widetilde{U}_i(\mathbf{r}',\omega_0) = \widetilde{U}_{0i}\; e^{i\mathbf{k}_\mathrm{i}\cdot\mathbf{r}'}\,, \tag{3.27}$$

where the incident amplitude $\widetilde{U}_{0i} = \sqrt{I_0}$ is proportional to the square-root of the incident intensity I_0, and $\mathbf{k}_\mathrm{i}$ is the incident wave vector, see Fig.3.2. Note, that the far-zone condition for the source is only required for divergently emitting sources. Thus, for some source type one may use the plane wave representation (3.23) regardless of source-sample distance, e.g. laser-type sources.

With the far-zone Green's function (3.26) and the incident plane wave representation (3.27) one finally obtains the scattered field in the so-called plane wave first Born approximation (PWBA):

$$\widetilde{U}_s(\mathbf{r},\omega_0) = \widetilde{U}_{0s}(\mathbf{q})\,\frac{e^{ik_0\mathrm{r}}}{\mathrm{r}}\,, \tag{3.28}$$

where $\widetilde{U}_{0s}(\mathbf{q})$ defines the scattering amplitude of the outgoing spherical wave, namely

$$\widetilde{U}_{0s}(\mathbf{q}) = \widetilde{U}_{0i}\int_V \widetilde{F}(\mathbf{r}',\omega_0)\,e^{-i\mathbf{q}\cdot\mathbf{r}'}\,d^3\mathrm{r}', \tag{3.29}$$

with

$$\mathbf{q} = \mathbf{k}_\mathrm{f} - \mathbf{k}_\mathrm{i}\,, \tag{3.30}$$

being the wave vector transfer. Eq. (3.29) can finally be used to express the scattered intensity as

$$I_s(\mathbf{r},\omega_0) = \left|\widetilde{U}_s(\mathbf{r},\omega_0)\right|^2, \tag{3.31}$$

$$= \frac{I_0}{\mathrm{r}^2}\left|\int_V \widetilde{F}(\mathbf{r}',\omega_0)\,e^{-i\mathbf{q}\cdot\mathbf{r}'}\,d^3\mathrm{r}'\right|^2, \tag{3.32}$$

$$= \frac{I_0}{\mathrm{r}^2}\,r_e^2\left|\int_V \rho(\mathbf{r}')\,e^{-i\mathbf{q}\cdot\mathbf{r}'}\,d^3\mathrm{r}'\right|^2, \tag{3.33}$$

where the representation (3.33) follows from eq. (3.10) in combination with (3.2) and (3.4). Alternatively, one may define the intensity of the spherical wave as $I_s(\mathbf{q}) \equiv \left|\widetilde{U}_{0s}(\mathbf{q})\right|^2$. To exhibit the connection of expression (3.33) to other formal description of elastic scattering we give here the relations to the differential scattering cross section $d\sigma/d\Omega$ [3]

$$\frac{d\sigma}{d\Omega} = \frac{\mathrm{r}^2\left|\widetilde{U}_s(\mathbf{r},\omega_0)\right|^2}{\left|\widetilde{U}_i(\mathbf{r},\omega_0)\right|^2} = \left|\frac{\widetilde{U}_{0s}(\mathbf{q})}{\widetilde{U}_{0i}}\right|^2 = r_e^2\left|\int_V \rho(\mathbf{r}')\,e^{-i\mathbf{q}\cdot\mathbf{r}'}\,d^3\mathrm{r}'\right|^2. \tag{3.34}$$

Although, the analysis in this work will be mainly based on intensity expressions one can equally find analog formulas in terms of the differential scattering cross section.

In order to arrive at the formal description of scattering from rough surfaces, we will next specify the functional form and the statistical properties of the electron density $\rho(\mathbf{r})$. For this purpose we first rewrite (3.33) in the following form

$$\langle I_s(\mathbf{r},\omega_0)\rangle = \left\langle \widetilde{U}_s^*(\mathbf{r},\omega_0)\widetilde{U}_s(\mathbf{r},\omega_0)\right\rangle \tag{3.35}$$

$$= \frac{I_0}{\mathrm{r}^2}\, r_e^2 \iint_V \langle \rho(\mathbf{r}_1')\rho(\mathbf{r}_2')\rangle\, e^{-i\mathbf{q}\cdot(\mathbf{r}_2'-\mathbf{r}_1')}\, d^3\mathrm{r}_1' d^3\mathrm{r}_2' \;, \tag{3.36}$$

where the bracket denote an ensemble average over the intensity measured by the detector. By taking the ensemble average, we take into account, that the spatial fluctuations of the electron density and, consequently, the scattered intensity is averaged out in scattering experiments. The averaging can experimentally result from a large illuminated scattering volume, finite detector area, partial coherence of the incident electric field, etc.. It is worth mentioning that the averaging mechanism due to a large illuminated sample volume comprises a valuable advantage, since it reveals useful statistical information over a large segment of the scatterer. Unfortunately, the statistical information are always folded with instrumental resolution and effects of partial coherence [91].

The model that we propose here is based on some statistical conditions for the electron density fluctuations, as well as its spatial distribution. The distribution of the liquid is, for simplicity, considered to be of infinite depth but truncated in the positive z-direction at the height h, where $h = h(\boldsymbol{r}')$ is a randomly changing function of the surface position $\boldsymbol{r}'$. The electron density distribution along the $\boldsymbol{r}' = (x', y')$ coordinates are considered to be of finite extent in both directions, which will be denoted below by a limited integration over the surface area A, see expression (3.43). On top of the liquid surface we will think of a vapor atmosphere, which is similarly extended to an infinite height. The influences of the vapor atmosphere on the height displacements $h(\boldsymbol{r}')$ is assumed to be negligible, so that the spatial properties of the height function are essentially determined by the liquid.

For a convenient formulation of the electron density $\rho(\boldsymbol{r}', z')$, in terms of its mean equilibrium value $\bar{\rho}$ plus the deviation $\triangle\rho(\boldsymbol{r}', z')$ from it, we will consider $\rho(\boldsymbol{r}', z')$ as the electron density function of the entire z-space. Then $\bar{\rho}$ represents the arithmetical average of the mean equilibrium values from the liquid and the vapor atmosphere, which are represented by $\bar{\rho}_l$ and $\bar{\rho}_v$, respectively. The deviation of the electron density $\triangle\rho(\boldsymbol{r}', z')$ from its mean value $\bar{\rho}$ is assumed to be maximal at the liquid-vapor interface region. In other words, the inherent bulk electron density fluctuations in the liquid and vapor atmosphere are neglected in this model. The mathematical formulation

for the electron density distribution is then

$$\rho(\boldsymbol{r}', z') = \bar{\rho} + \triangle\rho(\boldsymbol{r}', z') \tag{3.37}$$

$$= \bar{\rho} + \triangle\bar{\rho}\left[\frac{1}{2} - \mathrm{H}(z' - h(\boldsymbol{r}'))\right], \tag{3.38}$$

$$= \bar{\rho}_l\big[1 - \mathrm{H}(z' - h(\boldsymbol{r}'))\big], \qquad \text{for } \bar{\rho}_l \gg \bar{\rho}_v, \tag{3.39}$$

where $\bar{\rho} = (\bar{\rho}_l + \bar{\rho}_v)/2$, $\triangle\bar{\rho} = \bar{\rho}_l - \bar{\rho}_v$ and $\mathrm{H}(z' - h(\boldsymbol{r}'))$ is the Heaviside function. Eq. (3.38) states that the deviations from the mean electron density appear at the height position $h(\boldsymbol{r}')$ with a magnitude of $\pm\triangle\bar{\rho}/2$. In the approximated model (3.39), we have replaced the electron density $\bar{\rho}_v$ by zero, which correspondingly yields the vacuum index of refraction $n(\boldsymbol{r}', z' > h(\boldsymbol{r}'), \omega_0) \approx 1$. [1]

By using the electron density model (3.39) for the entire z-space, which yet comprises the finite distribution of the liquid, one can readily extent the z-integrations in expression (3.36) from minus to plus infinity. With eq. (3.39) the z-integrations in expression (3.36) yield

$$\iint_{-\infty}^{\infty} dz_1' dz_2' \, \langle \rho(\boldsymbol{r}_1', z_1')\rho(\boldsymbol{r}_2', z_2')\rangle \, e^{-iq_z(z_2' - z_1')} = \frac{\bar{\rho}_l^2}{q_z^2} \left\langle e^{-iq_z(h_2 - h_1)} \right\rangle , \tag{3.40}$$

where $h_1 = h(\boldsymbol{r}_1')$ and $h_2 = h(\boldsymbol{r}_2')$.

Next, we demand that the random realizations of the height displacements are, in the ensemble average, symmetrically distributed above and below the mean equilibrium $\bar{h}$ at the origin $z = 0$. This symmetrical distribution of the height displacements is explicitly characterized by a Gaussian probability function. In addition, we assume that h_1 and h_2 are statistically dependent from each other for arbitrary spatial differences. Conclusively, the ensemble average on the right hand side of eq. (3.40) can be evaluated with the bivariate

[1] In order to model a liquid with finite depth d, one may add the term $\bar{\rho}_l\big[\mathrm{H}(z' + d) - 1\big]$ to the right hand side of eq. (3.39). The z-integration for this second term yields

$$\bar{\rho}_l \int_{-\infty}^{\infty} dz' \, \big[\mathrm{H}(z' + d) - 1\big] e^{iq_z z'} = \bar{\rho}_l \frac{i}{q_z} e^{iq_z d} .$$

The above integral determines an addition contribution to the scattered field from the bottom interface at $z = -d$. The scattering from that interface is ignored in this work. A justification for omitting this term, is often based on the X-ray absorption inside the scattered [3, 89]. If the depth is sufficiently large and q_z is treated as a weakly imaginary quantity, then the intensity of the X-ray beam reduces effectively to zero as it penetrates to the bottom interface. Based on these physical arguments, we will use eq. (3.39) to describe surface scattering.

Gaussian probability function, which leads to the relations

$$\left\langle e^{-iq_z(h_2-h_1)} \right\rangle = e^{-q_z^2 g_{zz}(\boldsymbol{r}_2'-\boldsymbol{r}_1')/2} \tag{3.41}$$

$$= e^{-q_z^2\left(\sigma^2 - C_{zz}(\boldsymbol{r}_2'-\boldsymbol{r}_1')\right)} . \tag{3.42}$$

A prove for the above relations is given in Appendix A. After substituting the relation (3.41) into (3.40) one finds the following expression for the mean intensity

$$\langle I_s(\mathbf{r},\omega_0)\rangle = \frac{I_0}{\mathrm{r}^2}\left(\frac{r_e\bar{\rho}_l}{q_z}\right)^2 e^{-q_z^2\sigma^2} \iint_A e^{q_z^2 C_{zz}(\boldsymbol{r}_2'-\boldsymbol{r}_1')}\, e^{-i\boldsymbol{q}\cdot(\boldsymbol{r}_2'-\boldsymbol{r}_1')}\, d^2r_1' d^2r_2' , \tag{3.43}$$

$$= \frac{I_0}{\mathrm{r}^2}\left(\frac{r_e\bar{\rho}_l}{q_z}\right)^2 e^{-q_z^2\sigma^2} A \int_A e^{q_z^2 C_{zz}(\boldsymbol{R})}\, e^{-i\boldsymbol{q}\cdot\boldsymbol{R}}\, d^2R , \tag{3.44}$$

$$= \frac{I_0}{\mathrm{r}^2}(r_e\bar{\rho}_l)^2 A\, S(\mathbf{q}) , \tag{3.45}$$

where $\boldsymbol{R} = \boldsymbol{r}_2' - \boldsymbol{r}_1'$ and the function $S(\mathbf{q})$ in eq. (3.45) is defined as [90]

$$S(\mathbf{q}) \equiv \frac{e^{-q_z^2\sigma^2}}{q_z^2} \int_A e^{q_z^2 C_{zz}(\boldsymbol{R})}\, e^{-i\boldsymbol{q}\cdot\boldsymbol{R}}\, d^2R . \tag{3.46}$$

With eq. (3.46) we can eventually relate the statistical properties of rough surfaces with the elastically scattered intensity in X-ray surface scattering experiments. The mathematical problems of determining the scattered intensity is essentially constrained to the evaluation of $S(\mathbf{q})$. Since the function $S(\mathbf{q})$ plays a central role, we will address it in the following discussions as the (surface) scattering function.

Following the analysis of Ref.[90], we can next breakup the scattering function into a specular reflected part $S_{\mathrm{spec}}(\mathbf{q})$ and a diffusely $S_{\mathrm{diff}}(\mathbf{q})$ scattered component, viz.

$$S(\mathbf{q}) = S_{\mathrm{spec}}(\mathbf{q}) + S_{\mathrm{diff}}(\mathbf{q}) , \tag{3.47}$$

where

$$S_{\mathrm{spec}}(\mathbf{q}) = \frac{e^{-q_z^2\sigma^2}}{q_z^2} \int_A e^{-i\boldsymbol{q}\cdot\boldsymbol{R}}\, d^2R , \tag{3.48}$$

and

$$S_{\mathrm{diff}}(\mathbf{q}) = \frac{e^{-q_z^2\sigma^2}}{q_z^2} \int_A \left(e^{q_z^2 C_{zz}(\boldsymbol{R})} - 1\right) e^{-i\boldsymbol{q}\cdot\boldsymbol{R}}\, d^2R . \tag{3.49}$$

By using eqs. (3.48) and (3.49) one obtains some useful, decoupled formulas for specular and diffuse scattering.

A. Reflectivity from Rough Surfaces

The specular scattered contribution to the scattering function yields

$$\begin{aligned} S_{\text{spec}}(\mathbf{q}) &= \frac{e^{-q_z^2\sigma^2}}{q_z^2} \int_{-\infty}^{\infty} \mathcal{G}(\boldsymbol{R})\; e^{-i\boldsymbol{q}\cdot\boldsymbol{R}}\, d^2R\;, \\ &= \frac{e^{-q_z^2\sigma^2}}{q_z^2}\; \widetilde{\mathcal{G}}(\boldsymbol{q})\,, \end{aligned} \tag{3.50}$$

here $\mathcal{G}(\boldsymbol{R})$ stands for a truncation function which takes the finite sample area A into account, and $\widetilde{\mathcal{G}}(\boldsymbol{q})$ denotes its Fourier transformed form. For a sufficiently large surface area A one may approximately describe $\widetilde{\mathcal{G}}(\boldsymbol{q})$ by a Dirac delta function, viz.

$$S_{\text{spec}}(\mathbf{q}) \simeq \frac{e^{-q_z^2\sigma^2}}{q_z^2}\; 4\pi^2\delta^2(\boldsymbol{q}) = \frac{1}{(r_e\bar{\rho}_l)^2 A} \left(\frac{d\sigma}{d\Omega}\right)_{\text{spec}}\;, \tag{3.51}$$

where we have demanded, that the plane wave condition, i.e. $\sqrt{A} \ll \mathrm{r}$, is still fulfilled. With eq. (3.51) one can finally determine the reflectivity $\mathcal{R}$ from a rough surface as [90]

$$\mathcal{R}(q_z) = \frac{1}{A\sin\alpha_{\mathrm{i}}} \int d\Omega \left(\frac{d\sigma}{d\Omega}\right)_{\text{spec}}\;, \qquad \text{with}\;\; d\Omega = \frac{dq_x dq_y}{k_0^2 \sin\alpha_{\mathrm{f}}}\,, \tag{3.52}$$

$$= \frac{(r_e\bar{\rho}_l)^2}{k_0^2 \sin^2\alpha_{\mathrm{i}}} \iint dq_x dq_y\; S_{\text{spec}}(q_x, q_y, q_z)\,, \qquad \text{for}\;\; \alpha_{\mathrm{f}} = \alpha_{\mathrm{i}}\,, \tag{3.53}$$

$$= \frac{(4\pi r_e\bar{\rho}_l)^2}{q_z^4}\; e^{-q_z^2\sigma^2}\;, \qquad \text{with}\;\; q_z = 2k_0\sin\alpha_{\mathrm{i}}\,. \tag{3.54}$$

The integration over $d\Omega$ or respectively $dq_x dq_y$ takes the finite detection area into account. It is worth noting, that eq. (3.54) can equally be derived from (3.50), if we consider a point detector, and thereby ignore the resolution effect of the detector. After some simple modifications of (3.54) in combination with (3.2) one further finds the following reflectivity expression [3]

$$\mathcal{R}(q_z) = \left(\frac{q_c}{2q_z}\right)^4 e^{-q_z^2\sigma^2}\,, \tag{3.55}$$

where

$$q_c = 2k_0^2 \sin\alpha_c\,, \tag{3.56}$$

is the critical wave vector transfer. The critical angle can be determined from the mean dispersion constant $\bar{\delta}(\omega_0)$ by using the relation

$$\alpha_c \approx \sqrt{2\bar{\delta}(\omega_0)} = \sqrt{4\pi r_e\bar{\rho}_l \frac{c^2}{\omega_0^2}}\,. \tag{3.57}$$

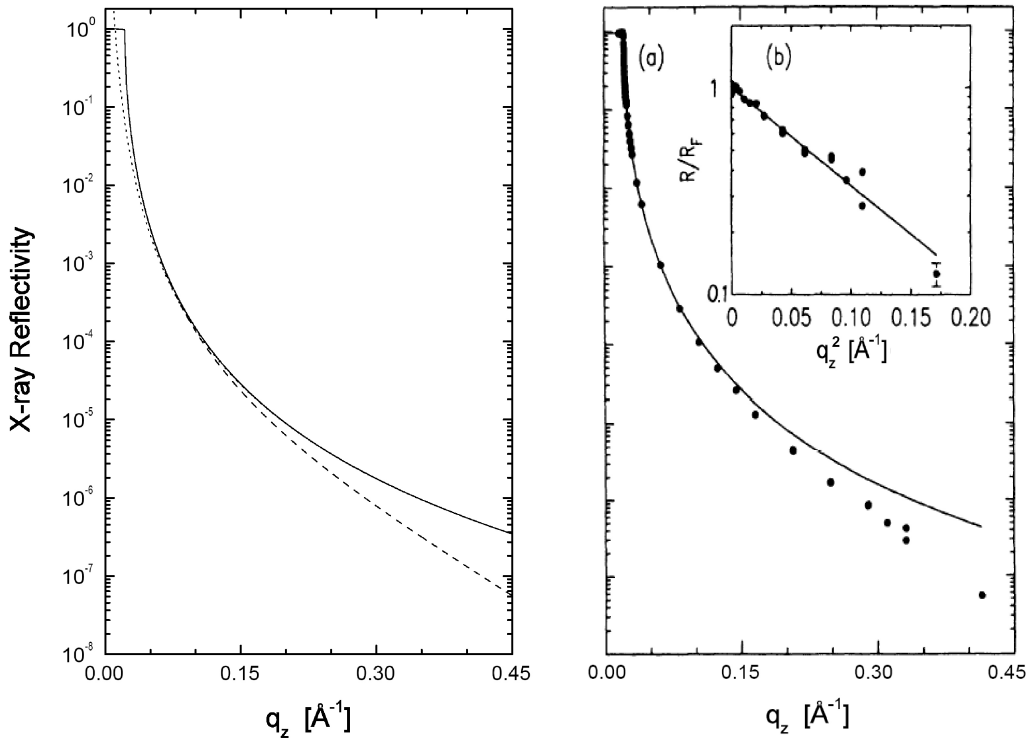

Figure 3.3: Left: Theoretical reflectivity curves for water at $T = 20°\mathrm{C}$. The solid curve is the Fresnel reflectivity $\mathcal{R}_F(q_z)$, see eq. (3.59). The dotted curve represents the reflectivity formula (3.55) with $\sigma = 0$Å. Eq. (3.55) diverges for $q_z \to 0$. The dash curve is reflectivity eq. (3.58) with $\sigma = 3$Å. Right: The right figure shows reflectivity data from a water surface at $T = 20°\mathrm{C}$ [11]. A surface roughness of 3.3Å has been determined from a fit with eq. (3.58).

Eqs. (3.54) and (3.55) represent reflectivity formulas in the first Born approximation. Evidently, the first term in (3.55) (and (3.54)) holds only in the large q_z limit, due to the divergence at $q_z = 0$. The first term is known as Porod's law of reflection from smooth surfaces, which is in agreement with the Fresnel theory of reflection for large incident angles [90]. In order to correct eq. (3.55) in the region $q_z \to 0$, it is customary to replace the Porod's law by Fresnel's reflectivity formula $\mathcal{R}_F(q_z)$, hence

$$\mathcal{R}(q_z) = \mathcal{R}_F(q_z)\; e^{-q_z^2\sigma^2}\,, \tag{3.58}$$

with the Fresnel reflectivity [6]

$$\mathcal{R}_F(q_z) = \left| \frac{q_z - \sqrt{q_z^2 - q_c^2}}{q_z + \sqrt{q_z^2 - q_c^2}} \right|^2 . \tag{3.59}$$

In order to include absorption effects, one can evaluate the critical wave vector transfer in eq. (3.59) with the following expression for the critical angle

$$\alpha_c \approx \sqrt{2\bar{\delta}(\omega_0) + 2\bar{\beta}(\omega_0)} = \sqrt{4\pi r_e \bar{\rho}_l \frac{c^2}{\omega_0^2} + \frac{c}{\omega_0}\bar{\mu}_l}\,, \tag{3.60}$$

where $\bar{\mu}_l$ represents the mean linear absorption length in the liquid.

The second term in (3.58) (and (3.55)) takes the surface roughness σ into account. The modification of the Fresnel reflectivity by this term is similar to the Debye-Waller factor encountered in calculating the intensity of Bragg reflections from crystal in which the atoms are vibrating about their mean positions [89]. A comparison between eqs. (3.58), (3.55) and the Fresnel formula (3.59) is shown in Fig.3.3. The right side in Fig.3.3 shows an experimental reflectivity curve from a water surface. A surface roughness of 3.3Å has been determined from a fit with eq. (3.58). For more details see Ref.[11].

In the derivation of the reflectivity formula (3.58) it was demanded that the height function be a Gaussian random variable. If this assumption is avoided, one finds the following reflectivity formula [89, 3]

$$\mathcal{R}(q_z) = \mathcal{R}_F(q_z) \left| \frac{1}{\bar{\rho}_l} \int dz' \, \frac{\partial \rho(z')}{\partial z'} \, e^{iq_z z'} \right|^2 . \tag{3.61}$$

Eq. (3.61) is preferably used for the analysis of reflectivity data from multilayer films. Besides this, eq. (3.61) can be used to reconstruct the electron density profile along the z-direction. A systematic investigation of eq. (3.61) and other reflectivity formulas, such as the Paratt formula, can be found in Ref.[49, 99, 3].

B. Diffuse Scattering from Rough Surfaces

Reflectivity experiments allow one to probe surface roughness and, in principle, to reconstruct the electron density profile in the z-direction. Additional sample information can be obtained by performing off-specular measurements of the diffusely scattered intensity. Such experiments can reveal the surface morphology, as well as the correlation length in the surface plane, i.e. in the (x, y)-directions. Some straightforward conclusions can be drawn from the diffuse part of the scattering function (3.49), if the product $q_z^2 C_{zz}(\boldsymbol{R})$ is small compared to one. In this limit, eq. (3.49) may be replaced by

$$S_{\text{diff}}(\mathbf{q}) = e^{-q_z^2\sigma^2} \int_{-\infty}^{\infty} C_{zz}(\boldsymbol{R}) \mathcal{G}(\boldsymbol{R}) \; e^{-i\boldsymbol{q}\cdot\boldsymbol{R}} d^2R \;, \qquad \text{for} \;\; q_z^2 C_{zz}(\boldsymbol{R}) \ll 1, \tag{3.62}$$

$$= e^{-q_z^2\sigma^2} \int_{-\infty}^{\infty} \widetilde{C}_{zz}(\boldsymbol{q}') \widetilde{\mathcal{G}}(\boldsymbol{q} - \boldsymbol{q}') \, d^2q' \;, \tag{3.63}$$

In eq. (3.63) we have made use of the convolution theorem for Fourier transformation. If next $\widetilde{\mathcal{G}}(\boldsymbol{q})$ is approximated by a delta function, one finds

$$S_{\text{diff}}(\boldsymbol{q}, q_z) = e^{-q_z^2\sigma^2}\widetilde{C}_{zz}(\boldsymbol{q}) \ . \tag{3.64}$$

According to expression (3.64), the off-specular part of the scattered intensity is simply determined by the functional form of the surface height correlation function in **q**-space. In the idealized case of a perfectly smooth surface, i.e. $\sigma^2 = \widetilde{C}_{zz}(\boldsymbol{q}) = 0$, the diffusely scattered intensity becomes zero. Another simple, but conceptually interesting conclusion can be drawn from expression (3.64) for surfaces with nonzero roughness and long-range surface correlations. Under these circumstances the surface height correlation function $C_{zz}(\boldsymbol{R})$ can essentially be described by a constant over a large range in $\boldsymbol{R}$. Evidently, such real-space behavior leads to a height correlation function in **q**-space, which is similar to a delta function. Hence, in the strict limit

$$\lim_{\ell_s\to\infty} S_{\text{diff}}(\boldsymbol{q}, q_z) \propto e^{-q_z^2\sigma^2}\delta^2(\boldsymbol{q}) \ , \tag{3.65}$$

the entire diffuse intensity it squeezed into the specular direction. For that reason, it is customary in the analysis of reflectivity data, to distinguish between a true-reflectivity and a diffuse-reflectivity, which is in particular encountered for liquid surfaces [22].

C. Closed-Form Solution for Specular and Diffuse Scattering, without cutoff

In order to obtain closed-form expression for the specular and diffuse part of the scattering function, we turn to formula (3.46), which we rewrite as

$$S(\mathbf{q}) = \frac{e^{-q_z^2\sigma^2}}{q_z^2}\int_{-\infty}^{\infty}\mathcal{G}_e(\boldsymbol{R})\, e^{q_z^2 C_{zz}(\boldsymbol{R})}\, e^{-i\boldsymbol{q}\cdot\boldsymbol{R}}\, d^2R \ , \tag{3.66}$$

where $\mathcal{G}_e(\boldsymbol{R})$ represents an effective truncation function. Depending on the experimental conditions, $\mathcal{G}_e(\boldsymbol{R})$ may take into account the finite sample surface, the finite illuminated sample area (beam footprint on the sample) or the finite coherence length of the X-ray beam. To evaluate expression (3.66) we turn to polar-coordinates

$$S(\mathbf{q}) = \frac{2\pi}{q_z^2}\, e^{-q_z^2\sigma^2}\int_0^{\infty}\mathcal{G}_e(R)\, e^{q_z^2 C_{zz}(R)}\, R\, J_0(qR)\, dR \ , \tag{3.67}$$

and represent $\mathcal{G}_e(R)$ by a Gaussian function

$$\mathcal{G}_e(R) = e^{-R^2/2\triangle R^2} \ , \tag{3.68}$$

where the physical meaning of the Gaussian width $\triangle R$ depends on the effective experimental cutoff. The solution of eq. (3.67) for liquid surfaces requires in the capillary wave model to use the height correlation function (2.38). However, the use of eq. (2.38) is practically not feasible, we therefore make use of an approximated form of eq. (2.43), namely [90, 81, 6]

$$\begin{aligned} C_{zz}(R) &= \frac{k_B T}{2\pi\gamma} K_0(q_g R)\,, \\ &\approx -\frac{B}{2}\left[\gamma_E + \ln\left(\frac{q_g R}{2}\right)\right], \qquad \text{for } \; q_g R \lesssim 1\;, \end{aligned} \tag{3.69}$$

where $\gamma_E \approx 0.5772$ is the Euler constant and $B = k_B T/\pi\gamma$. Approximation (3.69) holds for most liquids (with $q_g \sim 300 - 1000\mathrm{m}^{-1}$), if the integral (3.67) over R is effectively truncated by $\triangle R$ at values around a few millimeters or less. Using the approximation (3.69) in (3.67) yields the following scattering function [33]

$$\begin{aligned} S(\mathbf{q}) &= \frac{2\pi}{q_z^2}\, e^{-q_z^2(\sigma^2 + B\gamma_E/2)} \int_0^\infty e^{-R^2/2\triangle R^2} e^{-\eta \ln(q_g R/2)} R\, J_0(qR)\, dR\,, \\ &= \frac{2\pi}{q_z^2}\left(\frac{2}{q_g}\right)^{\eta} e^{-q_z^2(\sigma^2 + B\gamma_E/2)} \int_0^\infty e^{-R^2/2\triangle R^2} R^{1-\eta}\, J_0(qR)\, dR\,, \\ &= \frac{2\pi}{q_z^2}\triangle R^2 \left(\frac{\sqrt{2}}{q_g \triangle R}\right)^{\eta} e^{-q_z^2(\sigma^2 + B\gamma_E/2)} \\ &\quad \times \Gamma\left[1-\eta/2\right]\, {}_1F_1\Big[1-\eta/2; 1; -q^2\triangle R^2/2\Big]\,, \\ &= \frac{2\pi}{q_z^2}\, \frac{e^{-q_z^2\sigma_{\mathrm{eff}}^2}}{\triangle q^2}\, \Gamma\left[1-\eta/2\right]\, {}_1F_1\Big[1-\eta/2; 1; -q^2/2\triangle q^2\Big]\,, \end{aligned} \tag{3.70}$$

with

$$\eta = q_z^2 B/2\,, \tag{3.71}$$

$$\triangle q = 1/\triangle R\,, \tag{3.72}$$

$$\sigma_{\mathrm{eff}}^2 = \sigma^2 + \frac{1}{2} B\gamma_E - \frac{1}{2} B\, \ln\left(\sqrt{2}\triangle q/q_g\right). \tag{3.73}$$

Eq. (3.73) defines an effective roughness, which takes experimental resolution effects into account. The function ${}_1F_1[1-\eta/2; 1; -q^2/2\triangle q^2]$ is the Kummer function [33]. Closed-form solutions, such as eq. (3.70), were first derived by Sinha et al. [90] and are widely used to analyze scattering data from liquid surfaces.

D. Closed-Form Solution for Specular and Diffuse Scattering, with cutoff

Although, expression (3.70) describes the resolution dependent specular and diffuse scattering function from liquid surfaces, it holds only for $\eta < 2$. As $\eta = q_z^2 k_B T/2\pi\gamma$ reaches values close to 2, the Gamma function in (3.70) becomes singular. For instance, reflectivity formulas that were deduced from the specular part of the above scattering function, namely

$$S_{\rm spec}(0, q_z) = \frac{2\pi}{q_z^2} \frac{e^{-q_z^2\sigma_{\rm eff}^2}}{\triangle q^2} \Gamma\left[1 - \eta/2\right]. \tag{3.74}$$

equally contain the Gamma function term and, hence, a singularity [81, 86, 99]. We believe that the appearance of this singularity is due to the choice of the height correlation function (3.69), which itself contains a singularity at $R = 0$. An alternative solution to eq. (3.70) can be found, if we introduce the integral limit $r_{min} = 2\pi/q_{max}$ to truncate the singularity in the integration over R. Hence, we seek a solution for the following scattering function

$$S(\mathbf{q}) = \frac{2\pi}{q_z^2} \left(\frac{2}{q_g}\right)^{\eta} e^{-q_z^2(\sigma^2 + B\gamma_E/2)} \int_{r_{min}}^{\infty} e^{-R^2/2\triangle R^2} R^{1-\eta} J_0(qR)\, dR. \tag{3.75}$$

The above integral can be solved by using the sum expression for the Bessel function $J_0(qR)$, one then finds [33]

$$\begin{aligned} S(\mathbf{q}) &= \frac{2\pi}{q_z^2} \left(\frac{2}{q_g}\right)^{\eta} e^{-q_z^2(\sigma^2 + B\gamma_E/2)} \sum_{j=0}^{\infty} \frac{(-1)^j}{j!\Gamma[1+j]} \left(\frac{q}{2}\right)^{2j} \int_{r_{min}}^{\infty} R^{1-\eta+2j} e^{-R^2/2\triangle R^2} dR, \\ &= \frac{2\pi}{q_z^2} \left(\frac{2}{q_g}\right)^{\eta} e^{-q_z^2(\sigma^2 + B\gamma_E/2)} \\ &\quad \times \sum_{j=0}^{\infty} \frac{(-1)^j}{j!\Gamma[1+j]} \left(\frac{q}{2}\right)^{2j} \left(\triangle R^2 \left(\frac{1}{\sqrt{2}\triangle R}\right)^{\eta-2j} \Gamma\left[1 - \frac{\eta}{2} + j; \frac{r_{min}^2}{2\triangle R^2}\right]\right), \\ &= \frac{2\pi}{q_z^2} \frac{e^{-q_z^2\sigma_{\rm eff}^2}}{\triangle q^2} \sum_{j=0}^{\infty} \frac{(-1)^j}{j!\Gamma[1+j]} \Gamma\left[1 - \frac{\eta}{2} + j; 2\pi^2 \frac{\triangle q^2}{q_{max}^2}\right] \left(\frac{q^2}{2\triangle q^2}\right)^j, \end{aligned} \tag{3.76}$$

where $\Gamma[1 - \eta/2 + j; \triangle q^2/2q_{max}^2]$ is the incomplete Gamma function, which reduces to the complete Gamma function for $q_{max} \to \infty$. To arrive at a scattering formula, which is formally similar to eq. (3.70), we replace the incomplete Gamma function by

$$\Gamma[a, x] = \Gamma[a] + \big(\Gamma[a, z] - \Gamma[a]\big), \tag{3.77}$$

which leads to

$$S(\mathbf{q}) = \frac{2\pi}{q_z^2}\,\frac{e^{-q_z^2\sigma_{\rm eff}^2}}{\triangle q^2}\Bigg\{\sum_{j=0}^{\infty}\frac{\Gamma[1-\eta/2+j]}{j!\Gamma[1+j]}\left(-\frac{q^2}{2\triangle q^2}\right)^j + \sum_{j=0}^{\infty}\frac{1}{j!\Gamma[1+j]} \times\left(\Gamma\left[1-\frac{\eta}{2}+j;2\pi^2\frac{\triangle q^2}{q_{max}^2}\right]-\Gamma\left[1-\frac{\eta}{2}+j\right]\right)\Bigg\}. \tag{3.78}$$

On using the definition for the Pochhammer symbol [33]

$$(a)_n = a(a+1)\cdots(a+n-1) = \frac{\Gamma[a+n]}{\Gamma[a]}\,, \tag{3.79}$$

one finds the following representation for the two Gamma functions in the first sum of eq. (3.78), viz.

$$\frac{\Gamma[1-\eta/2+j]}{\Gamma[1+j]} = \Gamma[1-\eta/2]\frac{(1-\eta/2)_j}{(1)_j}\,. \tag{3.80}$$

With (3.80) and the definition for the Kummer function [33]

$${}_1F_1\big[a;b;z\big] = \sum_{j=0}^{\infty}\frac{(a)_j z^j}{(b)_j j!} \tag{3.81}$$

one eventually finds

$$S(\mathbf{q}) = \frac{2\pi}{q_z^2}\,\frac{e^{-q_z^2\sigma_{\rm eff}^2}}{\triangle q^2}\Bigg\{\Gamma[1-\eta/2]\,{}_1F_1\big[1-\eta/2;1;-q^2/2\triangle q^2\big] + \sum_{j=0}^{\infty}\frac{1}{j!\Gamma[1+j]} \times\left(\Gamma\left[1-\frac{\eta}{2}+j;2\pi^2\frac{\triangle q^2}{q_{max}^2}\right]-\Gamma\left[1-\frac{\eta}{2}+j\right]\right)\left(-\frac{q^2}{2\triangle q^2}\right)^j\Bigg\}. \tag{3.82}$$

Eq. (3.82) differs from the previous result (3.70) by the sum term. As $q_{max}\to\infty$ the difference between the incomplete and complete Gamma function in (3.82) becomes zero, and eq. (3.82) reduces to (3.70). Next we separate the $j=0$ sum term and rewrite eq. (3.82) as

$$S(\mathbf{q}) = \frac{2\pi}{q_z^2}\,\frac{e^{-q_z^2\sigma_{\rm eff}^2}}{\triangle q^2}\Gamma[1-\eta/2]\Big({}_1F_1\big[1-\eta/2;1;-q^2/2\triangle q^2\big]-1\Big) + \frac{2\pi}{q_z^2}\,\frac{e^{-q_z^2\sigma_{\rm eff}^2}}{\triangle q^2}\Gamma\big[1-\eta/2;2\pi^2\triangle q^2/q_{max}^2\big] + f(q,q_z)\,, \tag{3.83}$$

where

$$f(q,q_z) = \frac{2\pi}{q_z^2}\,\frac{e^{-q_z^2\sigma_{\rm eff}^2}}{\triangle q^2}\sum_{j=1}^{\infty}\frac{1}{j!\Gamma[1+j]} \times\left(\Gamma\left[1-\frac{\eta}{2}+j;\frac{2\pi^2\triangle q^2}{q_{max}^2}\right]-\Gamma\left[1-\frac{\eta}{2}+j\right]\right)\left(-\frac{q^2}{2\triangle q^2}\right)^j. \quad (3.84)$$

Using eq. (3.83) and ${}_1F_1[a;b;0]=1$, one easily finds for $q=0$ the following expression for the specular part of the scattering function

$$S_{\rm spec}(0,q_z) = \frac{2\pi}{q_z^2}\,\frac{e^{-q_z^2\sigma_{\rm eff}^2}}{\triangle q^2}\,\Gamma\big[1-\eta/2;2\pi^2\triangle q^2/q_{max}^2\big], \quad (3.85)$$

which is nonsingular at $\eta=2$.

Without going into the details of the calculation, see Ref.[81, 6, 99, 72], we give here a reflectivity formula, which can be deduced from the scattering function $S_{\rm spec}(0,q_z)$ without the r_{min} cutoff, namely

$$\mathcal{R}(q_z) = \mathcal{R}_{\rm F}(q_z)\; e^{-q_z^2\sigma_{\rm eff}^2}\frac{1}{\sqrt{\pi}}\Gamma\left[(1-\eta)/2\right], \quad (3.86)$$

where $\sigma_{\rm eff}^2$ can be expressed as

$$\sigma_{\rm eff}^2 = \sigma_i^2 + \frac{B}{2}\ln\left(\frac{2q_{max}}{q_z\triangle\alpha_{\rm f}}\right). \quad (3.87)$$

In eq. (3.87), an intrinsic roughness has been taken into account by σ_i. The capillary wave roughness σ_{cw} as well as resolution corrections to it are given by the second term in (3.87). Evidently, eq. (3.86) contains a singularity at $\eta=1$, which makes its application impossible for large q_z-values, due to the q_z-dependents of $\eta = q_z^2B/2$. If $B/2$ reaches values around $B/2\approx 4\text{Å}^2$, the Gamma function becomes singular at $q_z\approx 0.5\text{Å}^{-1}$. This problem was first noticed in an reflectivity experiment on normal alkanes $CH_3-[CH_2]_18-CH_3$, performed by B. M. Ocko et al. [72]. The actual $B/2$-value in this experiment is 4.4Å^2, which leads to a singularity at $q_z\approx 4.75\text{Å}^{-1}$. To avoid problems, due to the Gamma function, the term $\Gamma[(1-\eta)/2]/\sqrt{\pi}$ was omitted in the data analysis [72], see Fig.3.4. It is worth recognizing, that in a number of other reflectivity experiments the Gamma singularity appeared far beyond the experimental q_z-range and, for that reason, the application of the full reflectivity expression (3.86) has not led to any difficulties in the analysis [81, 86].

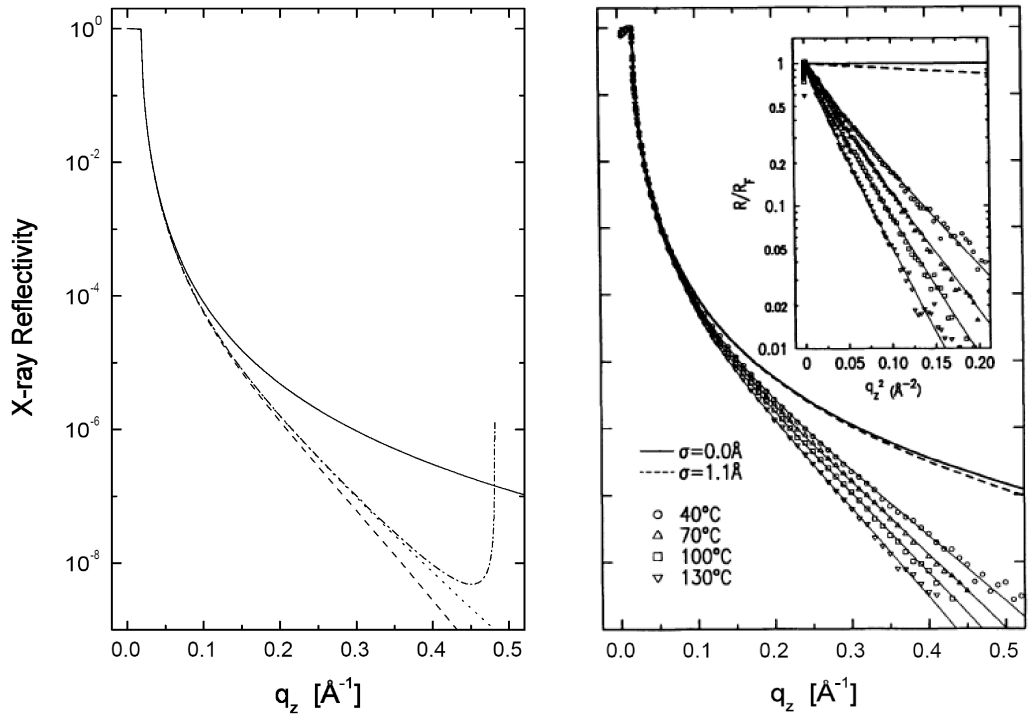

Figure 3.4: Left: Theoretical reflectivity curves for $CH_3 - [CH_2]_1 8 - CH_3$ at $T = 130°$C. The solid curve is the Fresnel reflectivity $\mathcal{R}_F(q_z)$, see eq. (3.59). The dash-dotted curve represents the cutoff free reflectivity formula (3.86), which becomes singular at $q_z \approx 4.75\text{Å}^{-1}$. The dash curve is obtained from eq. (3.86) without the term $\Gamma[(1-\eta)/2]/\sqrt{\pi}$; which is the formula used in Ref.[72]. The dotted curve results from eq. (3.88), which contains a cutoff. Right: The right figure shows actual reflectivity data from $CH_3 - [CH_2]_1 8 - CH_3$ at $T = 40, 70, 100$ and 130°C [72].

In Fig.3.4 we give a comparison between the reflectivity formula used in Ref.[72], the cutoff free formula (3.86), and the following expression

$$\mathcal{R}(q_z) = \mathcal{R}_F(q_z)\; e^{-q_z^2\sigma_{\text{eff}}^2} \frac{1}{\sqrt{\pi}} \Gamma\left[(1-\eta)/2; 2\pi^2 (q_z \triangle\alpha_{\text{f}}/2)^2/q_{max}^2\right], \qquad (3.88)$$

which takes the $r_{min} = 2\pi/q_{max}$ cutoff into account. The reflectivity curves in Fig.3.4 are plotted with the experimental parameters used in Ref.[72], i.e $T = 130°$C, $\sigma = 1.1$Å, $q_{max} \approx 4.4\text{Å}^{-1}$, $\gamma \approx 0.0205$ Nm^{-1}, $\lambda_0 = 1.53$Å and $\alpha_{\text{f}} = 3.3$ mrad. Eq.(3.88) overlaps with the reflectivity formula used by Ocko et al., if $q_{max} \approx 4.4\text{Å}^{-1}$ is replaced by $q_{max} \approx 1.57\text{Å}^{-1}$, which corresponds to a molecular radius of approximately 2Å.

3.3 Distorted Wave Born Approximation

The first Born approximation gives a fairly accurate description of surface scattering experiments with scattering angles $\alpha_\mathrm{i} \gg \alpha_c$ and $\alpha_\mathrm{f} \gg \alpha_c$. However, for grazing-angle scattering experiments close to the critical α_c, the accuracy of the first Born approximation is not sufficient to explain the phenomenon of total external reflection or the appearance of the so-called Yoneda peak [109]. In order to overcome the shortcoming of the first Born approximation one can apply improved approximation techniques, such as the Wentzel-Kramers-Brillouin method (WKB), [49, 113, 112, 111] or the distorted wave Born approximation (DWBA) [90, 94, 102, 95, 78, 83, 25, 26]. In the following we will briefly discuss the approximation technique, which is given by the more popular DWBA method. To arrive at the distorted wave approximation, the optical potential $\widetilde{F}(\mathbf{r}', \omega_0)$ is written as

$$\widetilde{F}(\mathbf{r}', \omega_0) = \widetilde{F}_1(\mathbf{r}', \omega_0) + \widetilde{F}_2(\mathbf{r}', \omega_0)\,, \tag{3.89}$$

where $\widetilde{F}_1(\mathbf{r}', \omega_0)$ is, at this moment, an arbitrary part of the optical potential, and $\widetilde{F}_2(\mathbf{r}', \omega_0)$ is a small perturbation. After substituting (3.89) into eq. (3.20) one finds

$$\begin{aligned} \widetilde{U}(\mathbf{r}, \omega_0) &= \widetilde{U}_i(\mathbf{r}, \omega_0) + \int_V d^3\mathrm{r}'\; G(\mathbf{r}, \mathbf{r}', \omega_0)\widetilde{F}_1(\mathbf{r}', \omega_0)\widetilde{U}(\mathbf{r}', \omega_0) \\ &\quad + \int_V d^3\mathrm{r}'\; G(\mathbf{r}, \mathbf{r}', \omega_0)\widetilde{F}_2(\mathbf{r}', \omega_0)\widetilde{U}(\mathbf{r}', \omega_0)\,. \end{aligned} \tag{3.90}$$

The DWBA method now consists in replacing the field $\widetilde{U}(\mathbf{r}', \omega_0)$ in both integrals on the right-hand side of (3.90) by the distorted wave $\widetilde{U}_1(\mathbf{r}, \omega_0)$, which satisfies [102]

$$\widetilde{U}_1(\mathbf{r}, \omega_0) = \widetilde{U}_i(\mathbf{r}, \omega_0) + \int_V d^3\mathrm{r}'\; G(\mathbf{r}, \mathbf{r}', \omega_0)\widetilde{F}_1(\mathbf{r}', \omega_0)\widetilde{U}_1(\mathbf{r}', \omega_0)\,. \tag{3.91}$$

Hence, eq. (3.90) becomes

$$\begin{aligned} \widetilde{U}(\mathbf{r}, \omega_0) = \widetilde{U}_i(\mathbf{r}, \omega_0) &+ \int_V d^3\mathrm{r}' G(\mathbf{r}, \mathbf{r}', \omega_0)\widetilde{F}(\mathbf{r}', \omega_0)\widetilde{U}_i(\mathbf{r}', \omega_0) \\ &+ \int_V d^3\mathrm{r}' G(\mathbf{r}, \mathbf{r}', \omega_0)\widetilde{F}(\mathbf{r}', \omega_0) \int_V d^3\mathrm{r}'' G(\mathbf{r}', \mathbf{r}'', \omega_0)\widetilde{F}_1(\mathbf{r}'', \omega_0)\widetilde{U}_1(\mathbf{r}'', \omega_0). \end{aligned} \tag{3.92}$$

Eq. (3.92) reveals, that the DWBA approach is a simplified version of the second order Born approximation, which however still takes multiple scattering

events into account. By making, once more, use of expression (3.91) one can easily reduce (3.92) to

$$\widetilde{U}(\mathbf{r},\omega_0) = \widetilde{U}_1(\mathbf{r},\omega_0) + \int_V d^3\mathrm{r}'\; G(\mathbf{r},\mathbf{r}',\omega_0)\widetilde{F}_2(\mathbf{r}',\omega_0)\widetilde{U}_1(\mathbf{r}',\omega_0)\,, \tag{3.93}$$

which represents the field solution in the so-called first-order distorted wave Born approximation [102, 25]. In order to evaluate eq. (3.93), the optical potential $\widetilde{F}_1(\mathbf{r}',\omega_0)$ is chosen such that it describes a surface in absence of roughness, i.e.

$$\widetilde{F}_1(\mathbf{r}',\omega_0) = \begin{cases} 0\,, & \text{if } z' > 0\,, \\ k_0^2(1-n^2(\mathbf{r}',\omega_0))\,, & \text{if } z' < 0\,. \end{cases} \tag{3.94}$$

The field $\widetilde{U}_1(\mathbf{r}',\omega_0)$ then yields the unperturbed solution consisting of the incident, reflected and refracted wave, viz. [90, 89]

$$\widetilde{U}_1(\mathbf{r}',\omega_0) = \widetilde{U}_{0i}\; e^{i\boldsymbol{k}_\mathrm{i}\cdot\boldsymbol{r}'} \begin{cases} e^{-ik_{\mathrm{i},z}z'} + \boldsymbol{r}(\alpha_\mathrm{i})\; e^{ik_{\mathrm{i},z}z'}\,, & \text{if } z' > 0, \\ \boldsymbol{t}(\alpha_\mathrm{i})\; e^{-ik^t_{\mathrm{i},z}z'}\,, & \text{if } z' < 0\,, \end{cases} \tag{3.95}$$

where $\boldsymbol{k}_\mathrm{i}$ and $\boldsymbol{r}'$ are the in-plane components of $\mathbf{k}_\mathrm{i}$ and $\mathbf{r}'$, respectively. $k_{\mathrm{i},z} = k_0 \sin\alpha_\mathrm{i}$ is the z-component of the wave vector outside the medium, and $k^t_{\mathrm{i},z} = n(\mathbf{r},\omega_0)k_0\sin\alpha_{\mathrm{t},i} = k_0(n^2(\mathbf{r},\omega_0) - \cos^2\alpha_\mathrm{i})^{1/2}$ inside the medium, where $\alpha_{\mathrm{t},i}$ the refraction angle. The coefficients $\boldsymbol{r}(\alpha_\mathrm{i})$ and $\boldsymbol{t}(\alpha_\mathrm{i})$ are the Fresnel reflection and transmission coefficients, respectively

$$\boldsymbol{r}(\alpha_\mathrm{i}) = \frac{\sin\alpha_\mathrm{i} - \sqrt{n^2(\mathbf{r}',\omega_0) - \cos^2\alpha_\mathrm{i}}}{\sin\alpha_\mathrm{i} + \sqrt{n^2(\mathbf{r}',\omega_0) - \cos^2\alpha_\mathrm{i}}}\,, \tag{3.96a}$$

$$\boldsymbol{t}(\alpha_\mathrm{i}) = \frac{2\sin\alpha_\mathrm{i}}{\sin\alpha_\mathrm{i} + \sqrt{n^2(\mathbf{r}',\omega_0) - \cos^2\alpha_\mathrm{i}}}\,. \tag{3.96b}$$

Eq. (3.96a) can easily be expressed as a function of q_z and related to the Fresnel reflectivity by $\mathcal{R}_F(q_z) = |\boldsymbol{r}(q_z)|^2$, see eq. (3.59). Similarly, one can formulate the Fresnel transmissivity as $\mathcal{T}(q_z) = |\boldsymbol{t}(q_z)|^2 = |2q_z/(q_z + (q_z^2 - q_c^2)^{1/2})|^2$.

Next one needs to solve the remaining integral term in eq. (3.93), which takes the actual surface roughness into account. The optical potential $\widetilde{F}_2(\mathbf{r}',\omega_0)$ may then be defined as [90]

$$\widetilde{F}_2(\mathbf{r}',\omega_0) = \begin{cases} k_0^2(1-n^2(\mathbf{r}',\omega_0))\,, & \text{if } 0 < z' < h(\boldsymbol{r}') \text{ and } 0 < h(\boldsymbol{r}')\,, \\ -k_0^2(1-n^2(\mathbf{r}',\omega_0))\,, & \text{if } 0 > z' > h(\boldsymbol{r}') \text{ and } 0 > h(\boldsymbol{r}')\,, \\ 0\,, & \text{elsewhere}\,. \end{cases} \tag{3.97}$$

The perturbation $\widetilde{F}_2(\mathbf{r}', \omega_0)$ describes a thin surface layer of partly positive thickness $h(\boldsymbol{r}')$ for $h(\boldsymbol{r}') > 0$, and negative thickness for $h(\boldsymbol{r}') < 0$. Due to the choice of $\widetilde{F}_1(\mathbf{r}', \omega_0)$ and $\widetilde{F}_2(\mathbf{r}', \omega_0)$, it follows that the integral term in eq. (3.93) accounts for a randomly scattered field $\widetilde{U}_2(\mathbf{r}, \omega_0)$ from the rough surface, hence

$$\begin{aligned} \widetilde{U}_2(\mathbf{r}, \omega_0) &= \widetilde{U}(\mathbf{r}, \omega_0) - \widetilde{U}_1(\mathbf{r}, \omega_0)\,, \\ &= \int_V d^3\mathrm{r}'\; G(\mathbf{r}, \mathbf{r}', \omega_0)\widetilde{F}_2(\mathbf{r}', \omega_0)\widetilde{U}_1(\mathbf{r}', \omega_0)\,. \end{aligned} \tag{3.98}$$

The Green's function in (3.98) can be determined from eq. (3.11), where the vacuum wave number k_0 has to be replaced by $n(\mathbf{r}', \omega_0)k_0$. As it has been shown in Ref.[94], the Green's function yields

$$G(\mathbf{r}, \mathbf{r}', \omega_0) \approx e^{-i\boldsymbol{k}_\mathrm{f}\cdot\boldsymbol{r}'}\; \frac{e^{ik_0\mathrm{r}}}{\mathrm{r}} \begin{cases} e^{-ik_{\mathrm{f},z}z'} + \boldsymbol{r}(\alpha_\mathrm{f})\; e^{ik_{\mathrm{f},z}z'}\,, & \text{if } z' > 0. \\ \\ \boldsymbol{t}(\alpha_\mathrm{f})\; e^{-ik^t_{\mathrm{f},z}z'}\,, & \text{if } z' < 0\,, \end{cases} \tag{3.99}$$

Since $G(\mathbf{r}, \mathbf{r}', \omega_0)$ and $\widetilde{U}_1(\mathbf{r}', \omega_0)$, as well as their first derivatives must all be continuous at the surface, one may approximate for even $z' > 0$ the Green's function and the distorted wave by their expressions for $z' < 0$. By using the analytic continuations of $G(\mathbf{r}, \mathbf{r}', \omega_0)$ and $\widetilde{U}_1(\mathbf{r}', \omega_0)$ in region $z' < 0$, one finds the following compact result for (3.98):

$$\begin{aligned} \widetilde{U}_2(\mathbf{r}, \omega_0) &= \widetilde{U}_{0i}\frac{e^{ik_0\mathrm{r}}}{\mathrm{r}}\boldsymbol{t}(\alpha_\mathrm{i})\boldsymbol{t}(\alpha_\mathrm{f})k_0^2(1 - n^2(\mathbf{r}, \omega_0))\iint_A d^2r'\, e^{-i\boldsymbol{q}\cdot\boldsymbol{r}'}\int_0^{h(\boldsymbol{r}')} dz'\, e^{-iq^t_z z'}, \\ &= \widetilde{U}_{0i}\frac{e^{ik_0\mathrm{r}}}{\mathrm{r}}\boldsymbol{t}(\alpha_\mathrm{i})\boldsymbol{t}(\alpha_\mathrm{f})k_0^2(1 - n^2(\mathbf{r}, \omega_0))\frac{i}{q^t_z} \\ &\quad \times\iint_A d^2r'\, e^{-i\boldsymbol{q}\cdot\boldsymbol{r}'}\Big(e^{-iq^t_z h(\boldsymbol{r}')} - 1\Big), \end{aligned} \tag{3.100}$$

where $q^t_z = k^t_{\mathrm{i},z} + k^t_{\mathrm{f},z}$ is the z-component of the wave vector transfer in the medium. On using expression (3.100), one finds the same scattering amplitude which was derived by Sinha et al., compare with eq. (4.38) in Ref.[90]. The scattering amplitude in Ref.[90] is, however, deduced from a "time reversed" field , which is similar to the Green' function eq. (3.99). (The equivalence between the two different DWBA approaches has been discussed in Ref.[95].)

With the eqs. (3.95) and (3.100), one can eventually derive the scattering function in the distorted wave Born approximation. The details are omitted here, and we give only a key formula, which reveals a fruitful relation between the scattering function in the DWBA and PWBA, namely [89, 90]

$$S^{\mathrm{DWBA}}(\mathbf{q}) = |\boldsymbol{t}(\alpha_\mathrm{i})|^2|\boldsymbol{t}(\alpha_\mathrm{f})|^2 S^{\mathrm{PWBA}}(\mathbf{q})\,, \qquad \text{where } \mathbf{q} = (\boldsymbol{q}, q^t_z)\,. \tag{3.101}$$

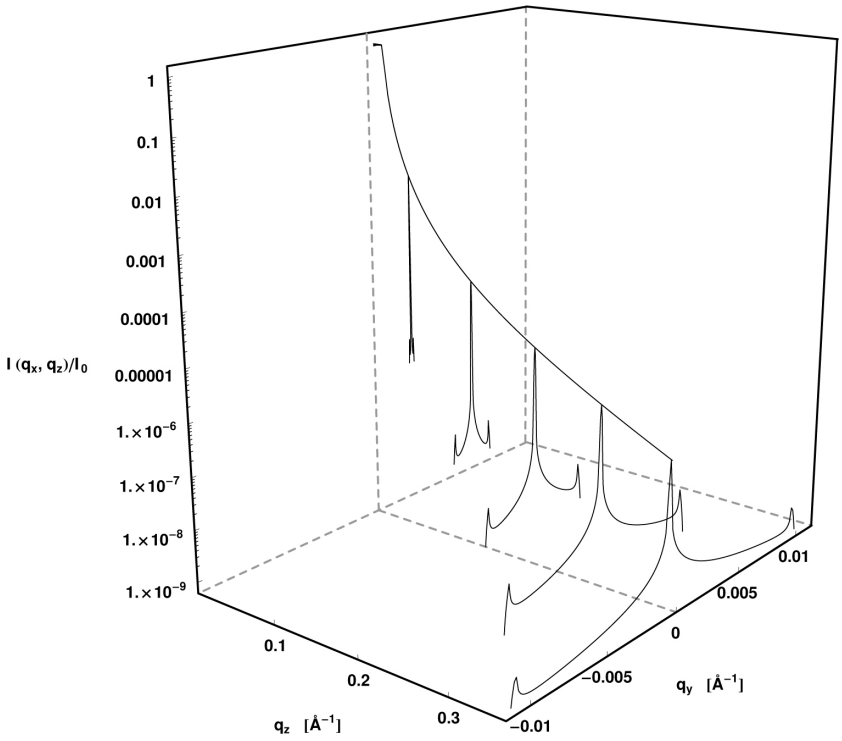

Figure 3.5: Specular and diffuse intensity from a water surface. Simulation of $\langle I(q_y, q_z)\rangle/I_0$ with the material constant of water; see eq. (3.103). At $q_y = 0$, $\langle I(0, q_z)\rangle/I_0$ describes the behavior of a reflectivity curve. In fact, it reduces to the reflectivity eq. (3.86) [81]. For fixed $q_z = 0.05, 0.125, 0.2, 0.275$ and 0.35Å^{-1} the q_y-dependence yields a maximum at the specular position $q_y = 0$, whereas its width is determined by $\triangle q_x$ resolution. Outside the resolution of the specular peak, eq. (3.103) decays as power law: $\langle I(q_y, q_z = \text{fixed})\rangle \propto q_y^{\eta-1}$ [99]. The power law behavior ends into the two side peak at $\alpha_\text{i} = \alpha_c$ and $\alpha_\text{f} = \alpha_c$, respectively. These peaks are referred to as the Yoneda-Peaks [109].

Here $S^{\text{PWBA}}(\mathbf{q})$ represents the scattering function in the plane-wave first Born approximation. Hence, one can essentially use the scattering function given in the previous section by replacing q_z with q_z^t. For instant, the diffuse part of the scattering function transforms to [90]

$$S_{\text{diff}}^{\text{PWBA}}(\boldsymbol{q}, q_z^t) = \frac{e^{-|q_z^t|^2\sigma^2}}{|q_z^t|^2} \int_A \left(e^{|q_z^t|^2 C_{zz}(\boldsymbol{R})} - 1\right) e^{-i\boldsymbol{q}\cdot\boldsymbol{R}} d^2R\,, \tag{3.102}$$

which then determines the $S_{\text{diff}}^{\text{DWBA}}(\mathbf{q})$ by multiplying eq. (3.102) with the transmission function $|\boldsymbol{t}(\alpha_\text{i})|^2$ and $|\boldsymbol{t}(\alpha_\text{f})|^2$. Since $q_z^t \simeq q_z$, if only α_i or α_f is large compared to the critical angle α_c, we can even replace eq. (3.102) to a good

approximation by (3.49). Based on this approximation, one finds the following in-plane intensity expression (i.e. $q_x = 0$), viz. [81, 99, 6]

$$\begin{aligned}\langle I(q_y, q_z)\rangle \quad \propto \quad & I_0 |\boldsymbol{t}(\alpha_\mathrm{i})|^2 |\boldsymbol{t}(\alpha_\mathrm{f})|^2 \left|\frac{q_c}{2q_z}\right|^4 e^{-q_z^2\sigma_\mathrm{eff}^2} \\ & \times \frac{1}{\sqrt{\pi}}\,\Gamma\left[\frac{1-\eta}{2}\right] {}_1F_1\left[\frac{1-\eta}{2}; \frac{1}{2}; -\frac{q_y^2}{2\triangle q_y^2}\right], \end{aligned} \tag{3.103}$$

where $q_c = 2k_0(1 - n^2(\mathbf{r}, \omega_0))1/2$ is here a complex quantity. Eq. (3.103) can be derived from the scattering function eq. (3.66), see for details Ref.[6, 81]. In Fig.3.5, a simulation of (3.103) is shown for a variate of q_y and q_z values. The plots are generated with the material constant of water at $T = 20°\mathrm{C}$.

3.4 Fresnel Effects

The discussion in the previous sections was based on the far field approximation, which is also referred to the Fraunhofer limit, or Fraunhofer condition. The Fraunhofer limit is, generally speaking, achieved if the wavelength λ_0 of the radiated field is much larger compared to the ratio between sample dimensions and source-sample distance, as well as the detector-sample distance [9]. According to this limits, one can approximate a spherical outgoing wave from a points source by a plane wave at the sample position. Similarly, one may describe the scattered field at the detector position as well by a plane wave. Although the plane wave approximation is an appealing concept, it is questionable whether the approximations are satisfied for X-ray scattering experiments. In a number of theoretical papers by Sinha et al. [91] and M. Tolan et al. [100, 101, 99] it has been argued, that Fraunhofer conditions and the assumption of perfect coherence are not fulfilled in current X-ray scattering experiments. In order to find field expressions that go beyond the plane wave approximation, we will next sketch the derivation of the field in the so-called Fresnel limit, also known as the near field approximation.

In actual X-ray scattering experiments the wavelength λ_0 is most likely a fixed parameter, and a plane wave condition may, therefore, only be realized by increasing the distances between the sample and the source, and the detector. With regard to the pre-sample far field condition, we will consider below an incident plane wave, regardless of the source-sample distance. This treatment may be readily justified for X-ray beams with negligible divergence, which are, for instance, generated by synchrotron sources.

To model the scattered field beyond the Fraunhofer limit, we will expanded

expression (3.25) to the second order, so that

$$\begin{aligned} k_0|\mathbf{r}-\mathbf{r}'| &= k_0\mathrm{r} - \mathbf{k}_\mathrm{f}\cdot\mathbf{r}' + \frac{k_0}{2\mathrm{r}}\left[\mathbf{r}'^2 - (\hat{\mathbf{r}}\cdot\mathbf{r}')^2\right] + \mathcal{O}\left(k_0(\mathbf{r}'/\mathrm{r})^3\right) \\ &= k_0\mathrm{r} - \mathbf{k}_\mathrm{f}\cdot\mathbf{r}' + \frac{1}{2k_0\mathrm{r}}\left(\mathbf{k}_\mathrm{f}\times\mathbf{r}'\right)^2 + \mathcal{O}\left(k_0(\mathbf{r}'/\mathrm{r})^3\right)\,, \end{aligned} \tag{3.104}$$

where the quadratic term in (3.104) takes near field condition into account. In this so-called Fresnel limit, one easily finds the following expression for the scattered field in the first Born approximation:

$$\widetilde{U}_s(\mathbf{r},\omega_0) = -r_e\sqrt{I_0}\,\frac{e^{ik_0\mathrm{r}}}{\mathrm{r}}\int_V d^3\mathrm{r}'\;\rho(\mathrm{r}')\;e^{i(\mathbf{k}_\mathrm{f}\times\mathbf{r}')^2/(2k_0\mathrm{r})}\;e^{-i\mathbf{q}\cdot\mathbf{r}'}\,. \tag{3.105}$$

which reduces to the Fraunhofer limit, if

$$\left|\frac{1}{2k_0\mathrm{r}}\left(\mathbf{k}_\mathrm{f}\times\mathbf{r}'\right)^2\right|_{max} \ll 1\,. \tag{3.106}$$

In reflectively experiments the outgoing wave vector $\mathbf{k}_\mathrm{f}$ can be written as $\mathbf{k}_\mathrm{f} = k_0(0,\cos\alpha_\mathrm{i},\sin\alpha_\mathrm{i})$, and thus the above condition reduces to

$$\begin{aligned} \lambda_0 &\gg \pi\left|\frac{1}{\mathrm{r}}\left(x'^2 + (z'\cos\alpha_\mathrm{i} - y'\sin\alpha_\mathrm{i})^2\right)\right|_{max}\,, \\ &\gg \pi\left|\frac{1}{\mathrm{r}}\left(x'^2 + y'^2 + z'^2\right)\right|_{max}\,, \end{aligned} \tag{3.107}$$

where we have used the Cauchy-Schwarz inequality in the second line. Eq. (3.107) reveals that the Fraunhofer limit can hardly be obtained for X-ray wave length. For example, if $\lambda = 1$Å and the sample-detector distance r is about two meters (which may be the case for most X-ray laboratories), then the Fraunhofer limit is only fulfilled for a relatively small scattering volume, with a maximum linear dimension of several microns. To evaluate eq. (3.105) for the specular reflected field, we will consider absorption inside the liquid (see discussion in section 3.2), and a perfectly smooth surface, i.e. $h(\boldsymbol{r}) = 0$. The maximum surface area shall be determined by a Gaussian truncation function, where the full width $\triangle L$ at $1/e$ defines the linear dimensions of the surface area, i.e. $\triangle L \approx \sqrt{A/8}$. Hence, the specularly scattered field in the Fresnel limit may be obtained from

$$\begin{aligned} \widetilde{U}_s(\mathbf{r},\omega_0) = -r_e\bar{\rho}_l\sqrt{I_0}\,\frac{e^{ik_0\mathrm{r}}}{\mathrm{r}} &\int_{-\infty}^{\infty} dx'\; e^{-\frac{x'^2}{2\triangle L^2}}\; e^{i\frac{k_0}{2\mathrm{r}}x'^2}\; e^{-iq_x x'} \\ \times &\int_{-\infty}^{\infty} dy'\; e^{-\frac{y'^2}{2\triangle L^2}}\; e^{i\frac{q_z^2}{8k_0\mathrm{r}}y'^2}\; e^{-i\frac{q_z}{2\mathrm{r}}\sqrt{1-\frac{q_z^2}{4k_0^2}}\;z'y'}\; e^{-iq_y y'} \\ \times &\int_{-\infty}^{\infty} dz'\;(1-H(z'))\; e^{i\frac{k_0}{2\mathrm{r}}\left(1-\frac{q_z^2}{4k_0^2}\right)z'^2}\; e^{-iq_z z'}\,, \end{aligned} \tag{3.108}$$

where we have eliminated trigonometric functions by their relations to $q_z = 2k_0 \sin\alpha_\mathrm{i}$. The solution for (3.108) can be written as

$$\begin{aligned}\widetilde{U}_s(\mathbf{r},\omega_0) &= r_e\bar{\rho}_l\sqrt{I_0}\,\frac{e^{ik_0\mathrm{r}}}{\mathrm{r}}\,\frac{(2\pi)^{3/2}\,e^{-\frac{q_x^2}{2\triangle q_x^2}}e^{-\frac{q_y^2}{2\triangle q_y^2}}e^{-i\frac{Q_z^2}{2\triangle q_z^2}}}{\triangle q_x\triangle q_y\triangle q_z} \\ &\quad\times\left\{\frac{e^{-i3\pi/4}}{2}+\frac{1}{\sqrt{2}}\mathcal{F}\left[\frac{Q_z}{\sqrt{\pi}\triangle q_z}\right]\right\},\end{aligned} \tag{3.109}$$

with

$$\triangle q_x = \frac{1}{\triangle L}\sqrt{1-ik_0\frac{\triangle L^2}{\mathrm{r}}}\,, \tag{3.110}$$

$$\triangle q_y = \frac{1}{\triangle L}\sqrt{1-i\frac{q_z^2}{4k_0}\frac{\triangle L^2}{\mathrm{r}}}\,, \tag{3.111}$$

$$\triangle q_z = \sqrt{\frac{k_0}{\mathrm{r}}\left(1-\frac{q_z^2}{4k_0^2}\right)\left(1+i\frac{q_z^2}{4k_0}\frac{1}{\mathrm{r}\triangle q_y^2}\right)}\,, \tag{3.112}$$

$$Q_z = q_z\left(1-i\frac{q_y}{2\,\mathrm{r}\triangle q_y^2}\sqrt{1-\frac{q_z^2}{4k_0^2}}\right). \tag{3.113}$$

The function $\mathcal{F}[x] = \mathcal{C}(x) + i\mathcal{S}(x)$ represents the Fresnel function, which can be decomposed in the Fresnel cosine integral $\mathcal{C}(x)$ and Fresnel sine integral $\mathcal{S}(x)$ [33]. Eq. (3.109) can next be used to evaluate a reflectivity formula for an perfectly smooth surface in the Fresnel limit. According to the discussion in section 3.2, one finds in the case of point detection

$$\mathcal{R}(q_z) \propto \frac{(4\pi r_e\bar{\rho}_l)^2}{q_z^2}\left|\frac{e^{-i\frac{q_z^2}{2\triangle q_z^2}}}{\triangle q_x\triangle q_y\triangle q_z}\left\{\frac{e^{-i3\pi/4}}{2}+\frac{1}{\sqrt{2}}\mathcal{F}\left[\frac{q_z}{\sqrt{\pi}\triangle q_z}\right]\right\}\right|^2. \tag{3.114}$$

In Fig.3.6 a comparison between (3.114) and (3.59) is shown for a fixed sample area of $A = 0.01\mathrm{mm}^2$ and sample-detector distances of $\mathrm{r} = 0.1, 1$ and 10m. The plot illustrates that the reflectivity formula (3.114) decays faster than (3.59) as q_z increases and r decreases. However, for small q_z Fresnel effects appear to have no influence on the reflectivity curve.

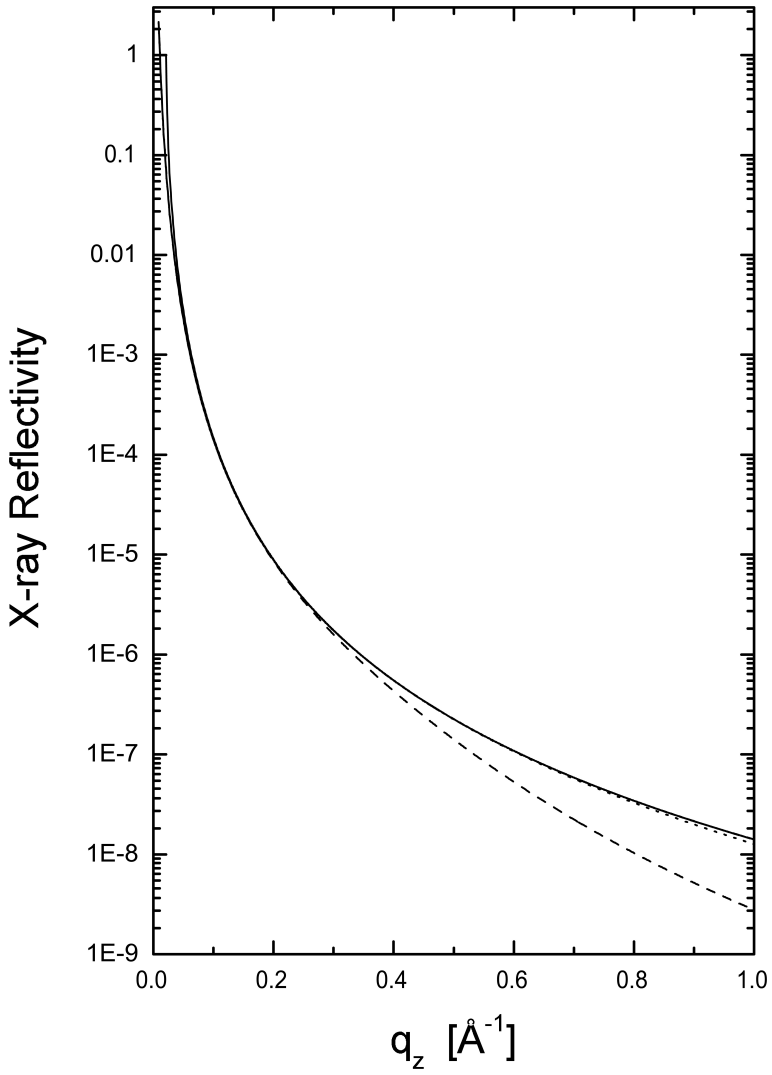

Figure 3.6: Theoretical reflectivity curves under near field conditions. Left: Theoretical reflectivity curves from a perfectly smooth surface with the material constants of water at $T = 20°\mathrm{C}$. The solid curve is the Fresnel reflectivity $\mathcal{R}_F(q_z)$, see eq. (3.59). The dash curve is obtained from eq. (3.114) with r = 0.1m, $A = 0.01\mathrm{mm}^2$ and $\lambda = 1\text{Å}$. The dotted curve denotes the case r = 1m. The reflectivity curve for r = 10m reduces to $(q_c/2q_z)^4$, which overlaps with eq. (3.59) for $q_z \gg q_c$.

Chapter 4

Effects of Partial Coherence

With the advent of third-generation synchrotron sources, a partially coherent X-ray beam is provided, which has made it possible to preform many new types of coherent scattering experiments. Although, most coherent X-ray scattering techniques has been adopted from laser light techniques, it is worthwhile emphasizing that the response of matter at X-ray wavelength can be fundamentally different from optical wavelength. For instance, a number of innovative laser experiments, such as holography, photon correlation spectroscopy, phase contrast imaging etc., can be implemented with X-rays for optically opaque materials and, in principle, with even higher spatial resolution. Due to these promising advantages much effort has been put into the design of coherent X-ray experiments in the last few years. However, the data analysis is customarily based on laser light scattering theories. It is, for example, prevalently assumed that the Fraunhofer limit is fulfilled and the conditions of partial coherence are ignored.

In order to understand the influence of partial coherence in X-ray intensity correlation spectroscopy experiments from liquid surfaces (see chapter 5) we will provide in the following chapter a formal analysis on effects of partial coherence in scattering experiments. We will, in particular, discuss the propagation of a partially coherent X-ray beam and its diffraction from a square slit, as well as the scattering from an arbitrary static scatterer in the Fresnel limit. Furthermore, we will address the question, whether effects of partial coherence can be taken into account by means of convolution formulas, as is customary in the theoretical description of instrumental resolution effects [99]. For a general and extensive analysis on partial coherence see the book by Mandel and Wolf [58], and Goodman [32]. A comprehensive analysis on partial coherence and Fresnel effect in X-ray experiments from deterministic media can be found in a work by Sinha, Tolan and Gibaud [91]. Theoretical studies on scattering from spatially random media with partially coherent fields are also discussed in a

series of papers by Wolf, Foley and Gori [107, 29, 108].

4.1 Temporal and Spatial Coherence

The emitted electromagnetic field of any optical source is associated with irregular fluctuations in space and time. In its broadest sense, optical coherence theory is concerned with the statistical description of the fluctuations, and optical coherence phenomena may be said to be manifestations of correlations between them [57]. The degree of correlation between the field fluctuations, at two space-time points, can be theoretically characterized in terms of mutual coherence functions and experimentally determined from interference experiments [9, 58, 57]. The classical experiments to observe the spatial and temporal coherence of optical fields are Young's double pinhole interference experiment and Michelson interferometer experiment, respectively [32]. In both interference experiments the essential influences of partial coherence are revealed in the reduced visibility of the fringe patterns formed in these experiments.

The term temporal coherence addresses the degree of self-correlation of an optical beam after a given time delay $\triangle t$. In interferometer experiments the time delay is realized by first dividing a beam in two beams. In a second step the beams are reuniting after a path delay $\triangle l = c\triangle t$ has been introduced between them. If the path difference is sufficiently small, so that the time delay between the two beam is smaller than the coherence time τ_c, one observes a fringe pattern as the beams superimpose. The visibility of the fringe pattern decreases if the time delay $\triangle t = \triangle l/c$ increases beyond the coherence time ξ_t. In general, interference fringes will only be observed if

$$\triangle t \leq \tau_c \sim 1/\triangle\nu \ , \tag{4.1}$$

where the coherence time is inversely related to the bandwidth $\triangle\nu$ of the field [9]. Corresponding to the coherence time τ_c, one can also estimate the formation of fringes from the longitudinal coherence length ξ_l, which is defined as [9]

$$\xi_l = c\,\tau_c \sim c/\triangle\nu = \lambda_0^2/\triangle\lambda, \tag{4.2}$$

where $\triangle\lambda$ represents the wavelength spread of the field. The longitudinal coherence length for synchrotron X-ray beams is enhanced by monochromator crystals, which yield in most cases a coherence length of several microns [99].

To characterize the degree of spatial correlation at two points in space, one speaks of the transverse coherence length ξ_t of a field, which may be simplest measured from the fringe visibility in Young's double pinhole interference experiment. Remarkably, the transverse coherence length of a field can increase

as the field propagates away from the radiating source. For an incoherent source the transverse coherence length increase as

$$\xi_t \sim \lambda_0 L/s, \tag{4.3}$$

where L denotes the distance to the incoherent source of linear spatial extent s. Eq. (4.3) can be used to estimate the minimum transverse coherence length at the sample position (placed at a distances L away from the radiating source). In the theory of optical coherence, the alterations of field correlation at a given distance from the source position are comprehensively described by propagation laws of correlation, e.g. by the van Cittert-Zernike theorem [9, 58].

4.2 Diffraction of Partially Coherent X-rays from a Plane Aperture

In this section we will examine the theoretical diffraction pattern from a square aperture including the effects of partially coherence and the conditions of the Fresnel approximation. The results may be of practical use, since in most coherent X-ray experiments square aperture are used to control the coherence of the beam. The intensity pattern will be determined from the van Cittert-Zernike theorem, and the source will be described by a Gaussian Schell-model source. Due to the simplicity of the experimental arrangement, slit interference experiments may be easily used to determine the transverse coherence length from the visibility of the fringe pattern. By taking the partial coherence of the synchrotron source into account, we believe that the analysis of diffraction patterns could provide a better estimate for the transverse coherence length, than given by eq. (4.3).

4.2.1 The van Cittert-Zernike Propagation Law

We consider here a finite and planar source area. The propagation of field correlations from the source plane towards a detection plane can then be described by the van Cittert-Zernike propagation law [58]

$$J_o(\eta_1, \zeta_1; \eta_2, \zeta_2) = \iiiint_{\mathcal{S}} J_s(u_1, v_1; u_2, v_2) \frac{e^{i\bar{k}_0(S_2 - S_1)}}{S_1 S_2} \, \bar{\Lambda}^*_{s1} \bar{\Lambda}_{s2} \, du_1 dv_1 du_2 dv_2 \,, \tag{4.4}$$

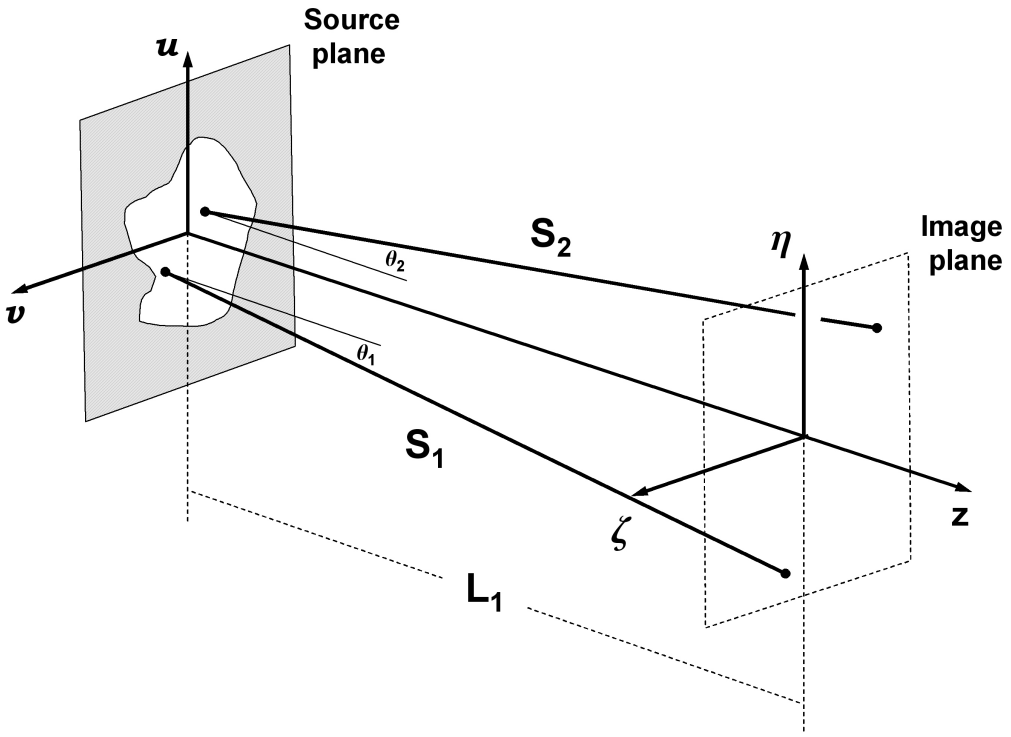

Figure 4.1: Illustration of the notation for radiating partially coherent source.

where

$$J_s(u_1, v_1; u_2, v_2) = \langle U^*(u_1, v_1, t) U(u_2, v_2, t) \rangle \,, \tag{4.5}$$

$$J_o(\eta_1, \zeta_1; \eta_2, \zeta_2) = \langle U^*(\eta_1, \zeta_1, t) U(\eta_2, \zeta_2, t) \rangle \,, \tag{4.6}$$

are *mutual intensity functions* on the source $\mathcal{S}$ and the detection domain $\mathcal{O}$, respectively. $\bar{k}_0$ denotes the mean wave number in free space and the distances S_1, S_2 are illustrated in Fig.4.1. The van Cittert-Zernike propagation law holds for strictly monochromatic sources, as well as for quasi-monochromatic conditions, i.e. the time delay $\triangle t$ between the fields on the detection domain must be smaller than one over the bandwidth of the source. Note that quasi-monochromatic conditions are, in general, best fulfilled for field distributions close to the optical axis. The mean inclination terms are given by $\bar{\Lambda}^*_{s1} = -i(\bar{k}_0/2\pi)\cos\theta_1$ and $\bar{\Lambda}_{s2} = i(\bar{k}_0/2\pi)\cos\theta_2$. If the angles of radiation θ_1 and θ_2 are sufficiently small, one can use the approximation

$$\frac{\bar{\Lambda}^*_{s1}\bar{\Lambda}_{s2}}{S_1 S2} \approx \left(\frac{\bar{k}_0}{2\pi L_1}\right)^2 \,, \tag{4.7}$$

and hence eq. (4.4) yields

$$J_o(\eta_1,\zeta_1;\eta_2,\zeta_2) \approx \left(\frac{\bar{k}_0}{2\pi L_1}\right)^2 \iiiint_{\mathcal{S}} J_s(u_1,v_1;u_2,v_2)\; e^{i\bar{k}_0(S_2-S_1)}\; du_1 dv_1 du_2 dv_2\,. \tag{4.8}$$

Eq. (4.8) describes the propagation of mutual coherence from a source plane towards an image plane. The transverse coherence length on the image plane can be probed by placing a slit at the position of the image plane. The resulting interference pattern can eventually be analyzed to extract the transverse coherence length. The intensity function $I_d(x,y) = J_d(x,y;x,y)$ on the detection plane may be determined from the mutual intensity function $J_o(\zeta_1,\eta_1;\zeta_2,\eta_2)$ by applying again the van Cittert-Zernike propagation law, hence

$$I_d(x,y) = \iiiint_{\mathcal{O}} J_o(\eta_1,\zeta_1;\eta_2,\zeta_2)\; \frac{e^{i\bar{k}_0(R_2-R_1)}}{R_1R_2}\bar{\Lambda}^*_{r1}\bar{\Lambda}_{r2}\; d\eta_1 d\zeta_1 d\eta_2 d\zeta_2\;, \tag{4.9}$$

or approximately

$$I_d(x,y) \approx \left(\frac{\bar{k}_0}{2\pi L_2}\right)^2 \iiiint_{\mathcal{O}} J_o(\eta_1,\zeta_1;\eta_2,\zeta_2)\; e^{i\bar{k}_0(R_2-R_1)}\; d\eta_1 d\zeta_1 d\eta_2 d\zeta_2\;, \tag{4.10}$$

where $J_o(\eta_1,\zeta_1;\eta_2,\zeta_2)$ can be obtained from eq. (4.8). Expression (4.10) yields the diffracted intensity pattern at the image plane, which depends with (4.8) on the coherence properties and spatial dilatation of the source. The entire diffraction geometry and notation is illustrated in Fig.4.2.

4.2.2 Gaussian Schell-Model Source

To model a partially coherent source we will consider a Gaussian Schell-model source. A source of this kind can generate a partially coherent field, whose radiant intensity has appreciable values only within a cone of narrow solid angle, i.e. it can generate a beam, which is referred to as a Gaussian Schell-model beam. The explicit mathematical form of the source mutual intensity function $J_s(u_1,v_1;u_2,v_2)$ is defined as [82, 58]

$$J_s(u_1,v_1;u_2,v_2) = \sqrt{I_s(u_1,v_1)}\sqrt{I_s(u_2,v_2)}\,j_s(u_2-u_1;v_2-v_1)\,, \tag{4.11}$$

where the source intensity distributions $I_s(u_1,v_1), I_s(u_2,v_2)$ and their mutual correlations $j_s(u_2-u_1;v_2-v_1)$ are all described by Gaussian functions. Hence,

$$\sqrt{I_s(u_1,v_1)} = \sqrt{I_0}\; e^{-u_1^2/4s_x^2}\; e^{-v_1^2/4s_y^2}\,, \tag{4.12a}$$

$$\sqrt{I_s(u_2,v_2)} = \sqrt{I_0}\; e^{-u_2^2/4s_x^2}\; e^{-v_2^2/4s_y^2}\,, \tag{4.12b}$$

$$j_s(u_2-u_1;v_2-v_1) = e^{-(u_2-u_1)^2/2\xi_{tx}^2}\; e^{-(v_2-v_1)^2/2\xi_{ty}^2}\,, \tag{4.12c}$$

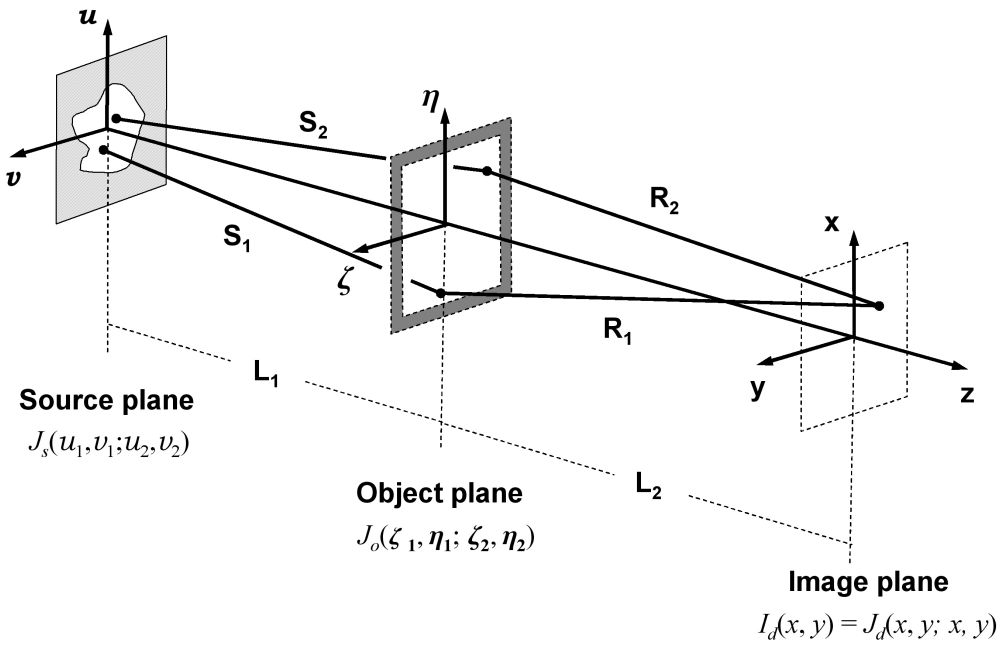

Figure 4.2: Diffraction of partially coherent X-rays from a plane aperture. Illustration of the diffraction geometry and notation.

here ξ_{tx} and ξ_{ty} are the vertical and horizontal transverse coherence lengths, and s_x and s_y define the vertical and horizontal source size, respectively. With the substitutions

$$a_x = 1/4s_x^2 + 1/2\xi_{tx}^2 \ , \qquad a_y = 1/4s_y^2 + 1/2\xi_{ty}^2 \ , \tag{4.13a}$$

$$b_x = 1/2\xi_{tx}^2 \ , \qquad b_y = 1/2\xi_{ty}^2 \ , \tag{4.13b}$$

eq. (4.11) takes the form

$$J_s(u_1, v_1; u_2, v_2) = I_0 \ e^{-\left(a_x u_1^2 + a_x u_2^2 - 2b_x u_1 u_2\right)} e^{-\left(a_y v_1^2 + a_y v_2^2 - 2b_y v_1 v_2\right)}. \tag{4.14}$$

Next, we approximated the distances S_1 and S_2 by expanding them in $u_{1,2}/L_1$, $v_{1,2}/L_1$, $\zeta_{1,2}/L_1$ and $\eta_{1,2}/L_1$, one then finds in second order (Fresnel limit)

$$S_1 = \sqrt{(\eta_1 - u_1)^2 + (\zeta_1 - v_1)^2 + L_1^2} \approx L_1 + \frac{1}{2L_1}\left[(\eta_1 - u_1)^2 + (\zeta_1 - v_1)^2\right], \tag{4.15a}$$

$$S_2 = \sqrt{(\eta_2 - u_2)^2 + (\zeta_2 - v_2)^2 + L_1^2} \approx L_1 + \frac{1}{2L_1}\left[(\eta_2 - u_2)^2 + (\zeta_2 - v_2)^2\right]. \tag{4.15b}$$

Substituting (4.15a,b) and (4.14) into (4.8) yields

$$\begin{aligned} J_o(\eta_1,\zeta_1;\eta_2,\zeta_2) = I_0 \left(\frac{\kappa_1}{\pi}\right)^2 e^{i\kappa_1\left[(\eta_2^2-\eta_1^2)+(\zeta_2^2-\zeta_1^2)\right]} \\ \times \iint_{-\infty}^{\infty} \left(e^{-(a_x+i\kappa_1)u_1^2} e^{-i(i2b_x u_2 - 2\kappa_1\eta_1)u_1}\right) \\ \times \left(e^{-(a_x-i\kappa_1)u_2^2} e^{-i2\kappa_1\eta_2 u_2}\right) du_1 du_2 \\ \times \iint_{-\infty}^{\infty} \left(e^{-(a_y+i\kappa_1)v_1^2} e^{-i(i2b_y v_2 - 2\kappa_1\zeta_1)v_1}\right) \\ \times \left(e^{-(a_y-i\kappa_1)v_2^2} e^{-i2\kappa_1\zeta_2 v_2}\right) dv_1 dv_2 \,, \end{aligned} \tag{4.16}$$

where we have made use of the substitution

$$\kappa_1 = \frac{\bar{k}_0}{2L_1} \,. \tag{4.17}$$

In eq. (4.16) the integral limits has been extended over all space, since the source domain $\mathcal{S}$ is implicitly included in the Gaussian Schell-model source. Eq. (4.16) can be solved with the help of the following integral solution [33]

$$\int_{-\infty}^{\infty} dx\; e^{-c^2x^2} e^{-iqx} = \frac{\sqrt{\pi}}{c}\; e^{-q^2/4c^2} \,, \qquad \mathrm{Re}[c] > 0 \,. \tag{4.18}$$

On using (4.18) in eq. (4.16) one finds, after a long but straightforward simplification, the following mutual intensity function on the object plane

$$J_o(\eta_1,\zeta_1;\eta_2,\zeta_2) = \sqrt{I_o(\eta_1,\zeta_1)}\sqrt{I_o(\eta_2,\zeta_2)}\; j_o(\eta_2-\eta_1;\zeta_2-\zeta_1)\; \phi(\eta_1,\eta_2;\zeta_1,\zeta_2). \tag{4.19}$$

Evidently, the solution of the van Cittert-Zernike propagation law yields again a Gaussian Schell-model source, which is however modified by a phase term $\phi(\eta_1,\eta_2;\zeta_1,\zeta_2)$. The explicit expressions for the right hand side of eq. (4.19) are:

$$\sqrt{I_o(\zeta_1,\eta_1)} = \sqrt{I_0\; \frac{s_x s_y}{\Sigma_x\Sigma_y}}\; e^{-\eta_1^2/4\Sigma_x^2}\; e^{-\zeta_1^2/4\Sigma_y^2} \,, \tag{4.20a}$$

$$\sqrt{I_o(\zeta_2,\eta_2)} = \sqrt{I_0\; \frac{s_x s_y}{\Sigma_x\Sigma_y}}\; e^{-\eta_2^2/4\Sigma_x^2}\; e^{-\zeta_2^2/4\Sigma_y^2} \,, \tag{4.20b}$$

$$g_o(\zeta_2-\zeta_1;\eta_2-\eta_1) = e^{-(\eta_2-\eta_1)^2/2\Xi_{tx}^2}\; e^{-(\zeta_2-\zeta_1)^2/2\Xi_{ty}^2} \,, \tag{4.20c}$$

$$\phi(\zeta_1,\zeta_2;\eta_1,\eta_2) = e^{i\kappa_1(1-s_x^2/\Sigma_x^2)(\eta_2^2-\eta_1^2)}\; e^{i\kappa_1(1-s_y^2/\Sigma_y^2)(\zeta_2^2-\zeta_1^2)}. \tag{4.20d}$$

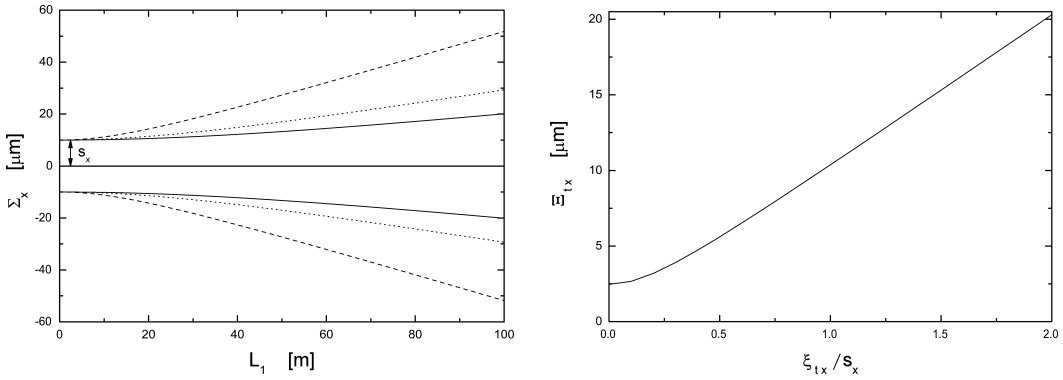

Figure 4.3: Properties of a Gaussian Schell-model beam. Left: Simulation of the Gaussian Schell-model beam waist Σ_x for an X-ray energy of $E = 8\text{keV}$. The solid curves illustrate the divergence of the beam for $\xi_{tx}/s_x = 2$. The beam divergence increases with distance L_1 and decreasing source coherence ξ_{tx}, which is for $\xi_{tx}/s_x = 1$ (dotted curve), and for $\xi_{tx}/s_x = 0.5$ (dashed curve). Right: The transverse coherence length Ξ_{tx} at a distance $L_1 = 1m$ increases with the source coherence ξ_{tx}. However, for a completely incoherent source the minimum value of Ξ_{tx} is proportional to $L_1/\bar{k}_0 s_x \approx 2.5\mu\text{m}$, for $s_x = 10\mu\text{m}$, $E = 8\text{keV}$ and $L_1 = 1\text{m}$.

The transverse coherence length $\Xi_{tx,ty}$ and the width $\Sigma_{x,y}$ on the object plane are

$$\Sigma_x = \sqrt{\frac{1+\left(a_x^2-b_x^2\right)/\kappa_1^2}{4(a_x-b_x)}} = \sqrt{s_x^2+\left(\frac{L_1}{\bar{k}_0}\right)^2\left(\frac{1}{4s_x^2}+\frac{1}{\xi_{tx}^2}\right)}\,, \tag{4.21a}$$

$$\Sigma_y = \sqrt{\frac{1+\left(a_y^2-b_y^2\right)/\kappa_1^2}{4(a_y-b_y)}} = \sqrt{s_y^2+\left(\frac{L_1}{\bar{k}_0}\right)^2\left(\frac{1}{4s_y^2}+\frac{1}{\xi_{ty}^2}\right)}\,, \tag{4.21b}$$

$$\Xi_{tx} = \sqrt{\frac{1+\left(a_x^2-b_x^2\right)/\kappa_1^2}{2b_x}} = \sqrt{\xi_{tx}^2\left[1+\left(\frac{L_1}{2\bar{k}_0 s_x^2}\right)^2\right]+\left(\frac{L_1}{\bar{k}_0 s_x}\right)^2}\,, \tag{4.21c}$$

$$\Xi_{ty} = \sqrt{\frac{1+\left(a_y^2-b_y^2\right)/\kappa_1^2}{2b_y}} = \sqrt{\xi_{ty}^2\left[1+\left(\frac{L_1}{2\bar{k}_0 s_y^2}\right)^2\right]+\left(\frac{L_1}{\bar{k}_0 s_y}\right)^2}\,, \tag{4.21d}$$

The intensity distribution $I_o(\zeta,\eta) = J_o(\eta,\zeta;\eta,\zeta)$ on the object plane is described by a Gaussian function. The width $\Sigma_{x,y}$ of this Gaussian function increases with the distance L_1 from the source, furthermore it depends on the transverse coherence length $\xi_{tx,ty}$ on the source plane. The quantity $\Sigma_{x,y}$ can be

interpreted as the beam waist. The transverse coherence properties on the object plane is as well describe by a Gaussian function, i.e. by $g_o(\zeta_2-\zeta_1;\eta_2-\eta_1)$. It is worth noting, that for $\xi_{tx,ty} \to 0$ the transverse coherence length $\Xi_{tx,ty}$ at $z = L_1$ reduces to the transverse coherence formula (4.3), which refers to the coherence formula for incoherent sources. In Fig.4.3 we illustrated the functional behavior of Ξ_{tx} as a function of ξ_{tx}, and Σ_x as a function of ξ_{tx}, L_1. A comprehensive discussion on Gaussian Schell-model sources and beams is given in Ref.[58, 71, 32].

4.2.3 The Diffraction Solution

With solution (4.19) we can next solve integral (4.10). We consider again Fresnel conditions, i.e. the distances R_1 and R_2 become

$$R_1 \approx L_2 + \frac{1}{2L_2}\left[(x-\eta_1)^2 + (y-\zeta_1)^2\right], \tag{4.22a}$$

$$R_2 \approx L_2 + \frac{1}{2L_2}\left[(x-\eta_2)^2 + (y-\zeta_2)^2\right]. \tag{4.22b}$$

With (4.22a,b) and the substitution

$$\kappa_2 = \frac{\bar{k}_0}{2L_2}\,, \tag{4.23}$$

one finds the following representation for integral (4.10):

$$I_d(x,y) = \left(\frac{\kappa_2}{\pi}\right)^2 \iiiint_{\mathcal{O}} d\eta_1 d\zeta_1 d\eta_2 d\zeta_2 \; J_o(\eta_1,\zeta_1;\eta_2,\zeta_2) \times e^{i\kappa_2\left[(\eta_2^2-\eta_1^2)-2(\eta_2-\eta_1)x\right]} \; e^{i\kappa_2\left[(\zeta_2^2-\zeta_1^2)-2(\zeta_2-\zeta_1)y\right]}\,. \tag{4.24}$$

The above integral can be simplest solved by expressing $J_o(\eta_1,\zeta_1;\eta_2,\zeta_2)$ as

$$J_o(\eta_1,\zeta_1;\eta_2,\zeta_2) = \mathcal{J}_1(\eta_1,\eta_2)\mathcal{J}_2(\zeta_1,\zeta_2)\,, \tag{4.25a}$$

where

$$\mathcal{J}_1(\eta_1,\eta_2) = \sqrt{I_0}\,\frac{s_x}{\Sigma_x}\; e^{-(\eta_1^2+\eta_2^2)/4\Sigma_x^2}\; e^{-(\eta_2-\eta_1)^2/2\Xi_{tx}^2}\; e^{i\kappa_1(1-s_x^2/\Sigma_x^2)(\eta_2^2-\eta_1^2)}\,, \tag{4.25b}$$

$$\mathcal{J}_2(\zeta_1,\zeta_2) = \sqrt{I_0}\,\frac{s_y}{\Sigma_y}\; e^{-(\zeta_1^2+\zeta_2^2)/4\Sigma_y^2}\; e^{-(\zeta_2-\zeta_1)^2/2\Xi_{ty}^2}\; e^{i\kappa_1(1-s_y^2/\Sigma_y^2)(\zeta_2^2-\zeta_1^2)}\,. \tag{4.25c}$$

Since $J_o(\eta_1, \zeta_1; \eta_2, \zeta_2)$ decouples into a (η_1, η_2) and (ζ_1, ζ_2) depending term, we can rewrite integral (4.24) itself in a decoupled form, hence

$$I_d(x, y) = \mathcal{I}_d(x)\mathcal{I}_d(y) \ , \tag{4.26a}$$

where

$$\mathcal{I}_d(x) = \frac{\kappa_2}{\pi} \iint_{\mathcal{O}_x} \mathcal{J}_1(\eta_1, \eta_2)\ e^{i\kappa_2\left[(\eta_2^2-\eta_1^2)-2(\eta_2-\eta_1)x\right]}\ d\eta_1 d\eta_2 \ , \tag{4.26b}$$

$$\mathcal{I}_d(y) = \frac{\kappa_2}{\pi} \iint_{\mathcal{O}_y} \mathcal{J}_2(\zeta_1, \zeta_2)\ e^{i\kappa_2\left[(\zeta_2^2-\zeta_1^2)-2(\zeta_2-\zeta_1)y\right]}\ d\zeta_1 d\zeta_2 \ . \tag{4.26c}$$

If the object area $\mathcal{O}$ has a square shape, we can consider $\mathcal{I}_d(x)$ and $\mathcal{I}_d(y)$ as independent slit solutions for the diffraction pattern in the x and y direction, respectively. Since, the integrals (4.26b) and (4.26b) are of the same mathematical form, we can confine the ongoing discussion to eq.(4.26b). In order to solve integral (4.26b) in combination with (4.25b), let us first introduce explicit integral limits, hence

$$\begin{aligned}\mathcal{I}_d(x) = \sqrt{I_0}\ \frac{\kappa_2 s_x}{\pi\Sigma_x} \\ &\times \int_{-w_x/2}^{w_x/2} d\eta_1\ e^{-\left[1/4\Sigma_x^2+1/2\Xi_{tx}^2+i\left(\kappa_1(1-s_x^2/\Sigma_x^2)+\kappa_2\right)\right]\eta_1^2}\ e^{i2\kappa_2 x\eta_1} \\ &\times \int_{-w_x/2}^{w_x/2} d\eta_2\ e^{-\left[1/4\Sigma_x^2+1/2\Xi_{tx}^2-i\left(\kappa_1(1-s_x^2/\Sigma_x^2)+\kappa_2\right)\right]\eta_2^2}\ e^{-i\left(2\kappa_2 x+i\eta_1/\Xi_{tx}^2\right)\eta_2} \ ,\end{aligned} \tag{4.27}$$

where w_x represents the total width of the slit opening. At next, it will be useful to introduce the following set of substitutions

$$A_x = 1/4\Sigma_x^2 + 1/2\Xi_{tx}^2 \ , \tag{4.28a}$$

$$B_x = 1/2\Xi_{tx}^2 \ , \tag{4.28b}$$

$$C_x^2 = A_x + i\left(\kappa_1(1 - s_x^2/\Sigma_x^2) + \kappa_2\right) , \tag{4.28c}$$

We can then express (4.27) as

$$\begin{aligned}\mathcal{I}_d(x) = \sqrt{I_0}\ \frac{\kappa_2 s_x}{\pi\Sigma_x} \int_{-w_x/2}^{w_x/2} d\eta_1\ e^{-C_x^2\eta_1^2}\ e^{i2\kappa_2 x\eta_1} \\ \times \int_{-w_x/2}^{w_x/2} d\eta_2\ e^{-(C_x^*)^2\eta_2^2}\ e^{-i(2\kappa_2 x+i2B_x\eta_1)\eta_2} \ ,\end{aligned} \tag{4.29}$$

where the asterisk denotes the complex conjugate of C_x^2. The integration over η_2 can be solved with [33]

$$\int_a^b dx\ e^{-c^2x^2}\ e^{-iqx} = \frac{\sqrt{\pi}}{2c}\ e^{-q^2/4c^2}\left[\mathrm{erf}\left(bc + i\frac{q}{2c}\right) - \mathrm{erf}\left(ac + i\frac{q}{2c}\right)\right], \quad (4.30)$$

where $\mathrm{erf}(x)$ is the error function. Using the above integral result in (4.29) gives

$$\begin{aligned}\mathcal{I}_d(x) = \sqrt{\frac{I_0}{4\pi}}\ \frac{\kappa_2 s_x}{C_x^*\Sigma_x}\ e^{-(\kappa_2 x/C_x^*)^2} \\ \times \int_{-w_x/2}^{w_x/2} d\eta_1\ e^{-\left(C_x^2-(B_x/C_x^*)^2\right)\eta_1^2}\ e^{i\left[2\kappa_2 x\left(1-B_x/(C_x^*)^2\right)\right]\eta_1} \\ \times\left[\mathrm{erf}\left(\frac{w_x}{2}C_x^* + i\frac{\kappa_2 x}{C_x^*} - \frac{B_x}{C_x^*}\eta_1\right) - \mathrm{erf}\left(-\frac{w_x}{2}C_x^* + i\frac{\kappa_2 x}{C_x^*} - \frac{B_x}{C_x^*}\eta_1\right)\right].\end{aligned} \quad (4.31)$$

To express eq. (4.31) in a mathematically uncomplicated form, we introduce a final set of substitutions, namely

$$\mathcal{I}_0(x) = \sqrt{\frac{I_0}{4\pi}}\ \frac{\kappa_2 s_x}{C_x^*\Sigma_x}\ e^{-(\kappa_2 x/C_x^*)^2}\ , \quad (4.32a)$$

$$\alpha_+(x) = \frac{w_x}{2}C_x^* + i\frac{\kappa_2 x}{C_x^*}\ , \quad (4.32b)$$

$$\alpha_-(x) = -\frac{w_x}{2}C_x^* + i\frac{\kappa_2 x}{C_x^*}\ , \quad (4.32c)$$

$$\beta = -B_x/C_x^* \quad (4.32d)$$

$$\gamma^2 = C_x^2 - (B_x/C_x^*)^2\ , \quad (4.32e)$$

$$Q(x) = 2x\kappa_2\left(1 - B_x/(C_x^*)^2\right)\ , \quad (4.32f)$$

and

$$K(x,\eta_1) = \left[\mathrm{erf}(\alpha_+(x) + \beta\eta_1) - \mathrm{erf}(\alpha_-(x) + \beta\eta_1)\right]\ e^{-\gamma^2\eta_1^2}. \quad (4.32g)$$

Integral (4.31) then simplifies to

$$\mathcal{I}_d(x) \ = \ \mathcal{I}_0(x)\int_{-w_x/2}^{w_x/2} K(x,\eta_1)\ e^{iQ(x)\eta_1}\ d\eta_1\,. \quad (4.33)$$

The above integral can be used for numerical simulation. An analytical solution can be found by evaluating (4.33) with the Taylor series of $K(x,\eta_1)$, viz.

$$K(x,\eta_1) \ = \ \sum_{n=0}^{\infty} a_n(x)\eta_1^n\,, \quad (4.34)$$

where the coefficients $a_n(x)$ can be determined from the $n's$ derivative of $K^{(n)}(x,\eta_1)$ at $\eta_1 = 0$. With the Taylor series of $K(x,\eta_1)$ eq. (4.33) yields

$$\mathcal{I}_d(x) \;=\; \mathcal{I}_0(x)\sum_{n=0}^{\infty} a_n(x)\int_{-w_x/2}^{w_x/2} \eta_1^n\; e^{iQ(x)\eta_1}\; d\eta_1\,, \tag{4.35}$$

where the simplified integral on the right hand side of (4.35) has an analytical solution of the form [33]

$$\int_{-a}^{a} dx\; x^n e^{iqx} = \frac{\Gamma[1+n, iaq] - \Gamma[1+n, -iaq]}{(-iq)^{1+n}}\;. \tag{4.36}$$

With the above equation and the identity $\Gamma[\alpha, x] = \Gamma[\alpha] - (x^\alpha/\alpha){}_1F_1[\alpha;\alpha+1;-x]$, one finds for $\mathcal{I}_d(x)$ the following sum solution

$$\begin{aligned}\mathcal{I}_d(x) &= \mathcal{I}_0(x)\sum_{n=0}^{\infty} a_n(x)\frac{\Gamma[1+n, iw_xQ(x)/2] - \Gamma[1+n, -iw_xQ(x)/2]}{(-iQ(x))^{1+n}}\\ &= \mathcal{I}_0(x)\sum_{n=0}^{\infty}\frac{a_n(x)(w_x/2)^{1+n}}{1+n}\;\Big[{}_1F_1[1+n;2+n;iw_xQ(x)/2]\\ &\quad -(-1)^{1+n}{}_1F_1[1+n;2+n;-iw_xQ(x)/2]\Big]\,,\end{aligned} \tag{4.37}$$

with

$$\begin{aligned}a_n(x) &= \left.\frac{K^{(n)}(x,\eta_1)}{n!}\right|_{\eta_2=0}\\ &= \frac{1}{n!}\left(\Big[\mathrm{erf}(\alpha_+(x)+\beta\eta_1) - \mathrm{erf}(\alpha_-(x)+\beta\eta_1)\Big]\; e^{-\gamma^2\eta_1^2}\right)^{(n)}\Bigg|_{\eta_1=0}\,.\end{aligned} \tag{4.38}$$

The partial derivatives in eq. (4.38) can be evaluated by rewrite $a_n(x)$ in the form

$$\begin{aligned}a_n(x) &= \frac{1}{n!}\left[\Big(\mathrm{erf}(\alpha_+(x)+\beta\eta_1)e^{-\gamma^2\eta_1^2}\Big)^{(n)} - \Big(\mathrm{erf}(\alpha_-(x)+\beta\eta_1)e^{-\gamma^2\eta_1^2}\Big)^{(n)}\right]_{\eta_1=0}\\ &= \sum_{m=0}^{n}\frac{1}{(n-m)!m!}\left.\frac{\partial^m e^{-\gamma^2\eta_1^2}}{\partial\eta_1^m}\right|_{\eta_1=0}\\ &\quad\times\left(\frac{\partial^{n-m}\mathrm{erf}(\alpha_+(x)+\beta\eta_1)}{\partial\eta_1^{n-m}} - \frac{\partial^{n-m}\mathrm{erf}(\alpha_-(x)+\beta\eta_1)}{\partial\eta_1^{n-m}}\right)\Bigg|_{\eta_1=0}\,,\end{aligned} \tag{4.39}$$

where we have made use of the binomial formula [13]. For the partial derivatives in (4.39) one finds the following representations

$$\left.\frac{\partial^m e^{-\gamma^2\eta_1^2}}{\partial\eta_1^m}\right|_{\eta_1=0} = \frac{(1+(-1)^m)}{2}\frac{m!}{(m/2)!}\;(i\gamma)^m\;, \tag{4.40a}$$

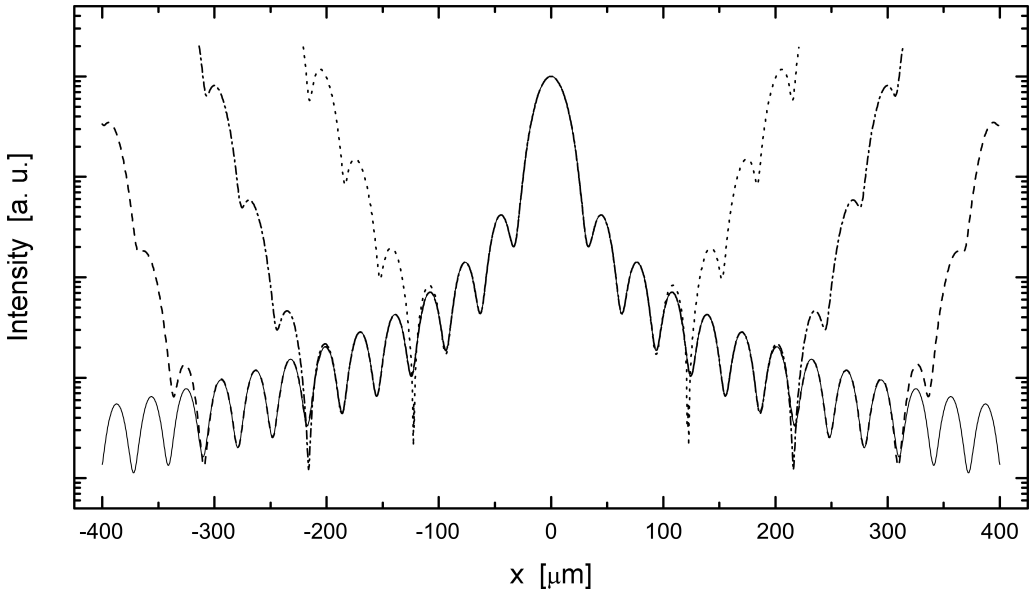

Figure 4.4: Simulations of slit diffraction patterns with the parameters: $E =$ 8keV, $L_1 = 2$m, $L_2 = 2$m, $w_x = 10\mu$m, $s_x = 10\mu$m and $\xi_{tx} = 10\mu$m. The solid curve represents the numerical solution of integral (4.35). The other curves are obtained from eq. (4.37). Dotted curve: A convergence range of $x_{max} = 100\mu$m requires $N_{min} = 10$, i.e. beyond 100μm the Taylor solution disagrees with integral (4.35). Dash-Dotted curve: A convergence range of $x_{max} = 200\mu$m requires $N_{min} = 20$. Dashed curve: A convergence range of $x_{max} = 300\mu$m requires $N_{min} = 30$. N_{min} has been determined from the inequality (4.42).

and [1]

$$\left.\frac{\partial^{n-m}\mathrm{erf}(\alpha_\pm(x)+\beta\eta_1)}{\partial\eta_1^{n-m}}\right|_{\eta_1=0} = (2\beta)^{n-m}(\alpha_\pm(x))^{1-(n-m)} \times {}_2F_2\left[\frac{1}{2},1;1-\frac{n-m}{2},\frac{3-(n-m)}{2};-(\alpha_\pm(x))^2\right], \tag{4.40b}$$

where ${}_2F_2[\alpha_1,\alpha_2;\beta_1,\beta_2;z]$ is the regularized hypergeometric function. Using the fact, that only even values of m contribute in (4.40a) leads eventually to the following expression for the coefficients

$$a_n(x) = \sum_{m=0}^{n} \frac{(i\gamma)^{2m}(2\beta)^{n-2m}}{(n-2m)!m!} \times \left\{ (\alpha_+(x))^{1+2m-n} {}_2F_2\left[\frac{1}{2}, 1; 1+m-\frac{n}{2}, m+\frac{3-n}{2}; -(\alpha_+(x))^2\right] - (\alpha_-(x))^{1+2m-n} {}_2F_2\left[\frac{1}{2}, 1; 1+m-\frac{n}{2}, m+\frac{3-n}{2}; -(\alpha_-(x))^2\right] \right\}. \tag{4.41}$$

For practical use of solution (4.37) it is necessary to exscind the sum after the nth order of the Taylor series. The smallest sub-sum, with N_{min} order, may be numerically found from the following inequality:

$$\limsup_{N \to N_{min}} \left| 1 - \frac{\sum_{n=0}^{N} a_n(x)(w_x/2)^n}{K(x, w_x/2)} \right|_{x=x_{max}} \leq 1, \qquad \text{for } \infty > N > N_{min} \ . \tag{4.42}$$

Here x_{max} defines the maximum range of convergence on the image plane and lim sup denotes the *supremum limit*. With inequality (4.42) one obtains, for a demanded convergence range up to x_{max}, the minimum order in the Taylor series, which is denoted by N_{min}. An example for the convergence range is illustrated in Fig.4.4

In Fig.4.5 a simulation of the far-field diffraction pattern from a slit is shown for four conditions of coherence. The corresponding square slit diffraction patterns are given in Fig.4.6. The near-field diffraction pattern from a slit is shown in Fig.4.7. Note that in the Fresnel limit the intensity is reduced around $x = 0\mu$m. Near-field effects of this kind are further discussed in Ref.[93, 37], see e.g. the discussion on the *Poisson's Spot*. The square slit diffraction patterns under Fresnel conditions are shown in Fig.4.8.

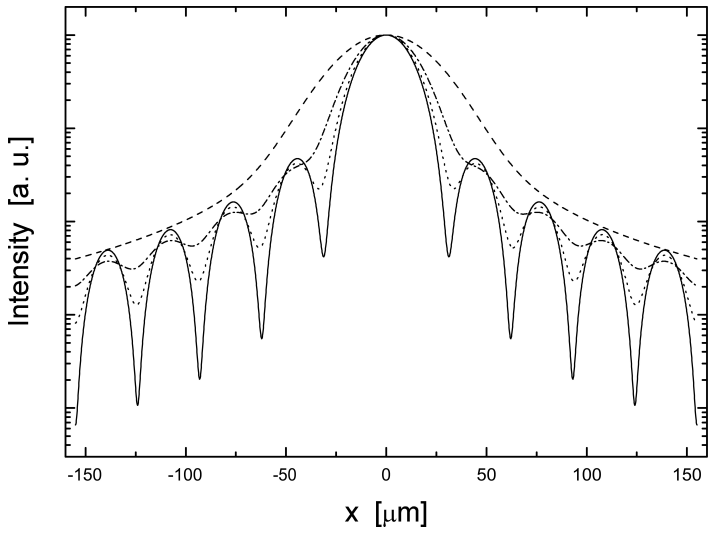

Figure 4.5: Theoretical diffraction pattern from a slit in the Fraunhofer limit. The parameters in the simulation are: $E = 8\text{keV}$, $L_1 = 2\text{m}$, $L_2 = 2\text{m}$, $w_x = 10\mu\text{m}$, $s_x = 20\mu\text{m}$ and $\xi_{tx} = 1, 5, 10\mu\text{m}$ and $40\mu\text{m}$. The solid curve shows the solution for $\xi_{tx} = 40\mu\text{m}$. The visibility of the diffraction pattern decreases as the source coherence decreases. The dotted curve represents the case $\xi_{tx} = 10\mu\text{m}$, the dash-dotted refers to $\xi_{tx} = 5\mu\text{m}$ and the dashed curve refers to $\xi_{tx} = 1\mu\text{m}$.

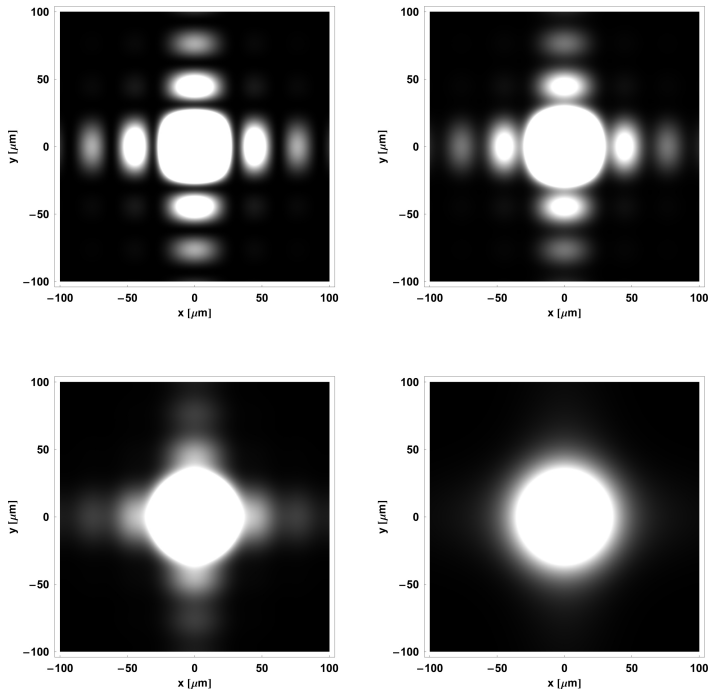

Figure 4.6: Illustration of the effect of decreasing transverse coherence length on the diffraction pattern from a square slit (from left to right, and from top to bottom). The parameter of the simulation are the same as in Fig.4.5.

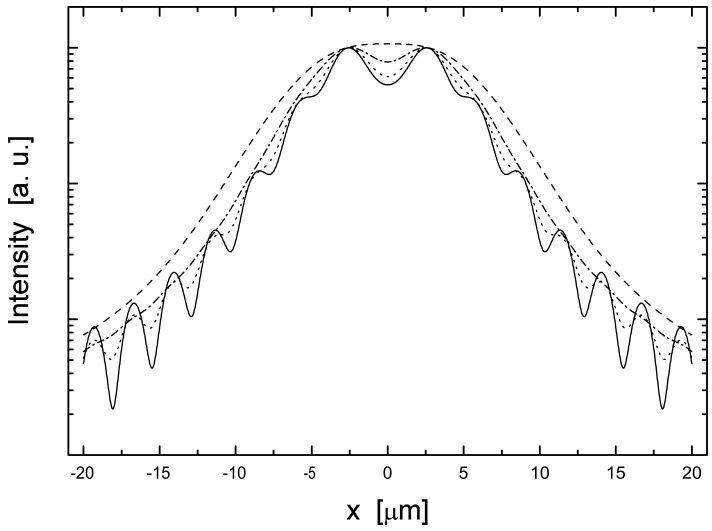

Figure 4.7: Theoretical diffraction pattern from a slit in the Fresnel limit. The parameters in the simulation are: $E = 8\text{keV}$, $L_1 = 2\text{m}$, $L_2 = 0.25\text{m}$, $w_x = 15\mu\text{m}$, $s_x = 20\mu\text{m}$ and $\xi_{tx} = 1, 5, 10\mu\text{m}$ and $40\mu\text{m}$. The solid curve shows the solution for $\xi_{tx} = 40\mu\text{m}$. The visibility of the diffraction pattern decreases as the source coherence decreases. The dotted curve represents the case $\xi_{tx} = 10\mu\text{m}$, the dash-dotted refers to $\xi_{tx} = 5\mu\text{m}$ and the dashed curve refers to $\xi_{tx} = 1\mu\text{m}$.

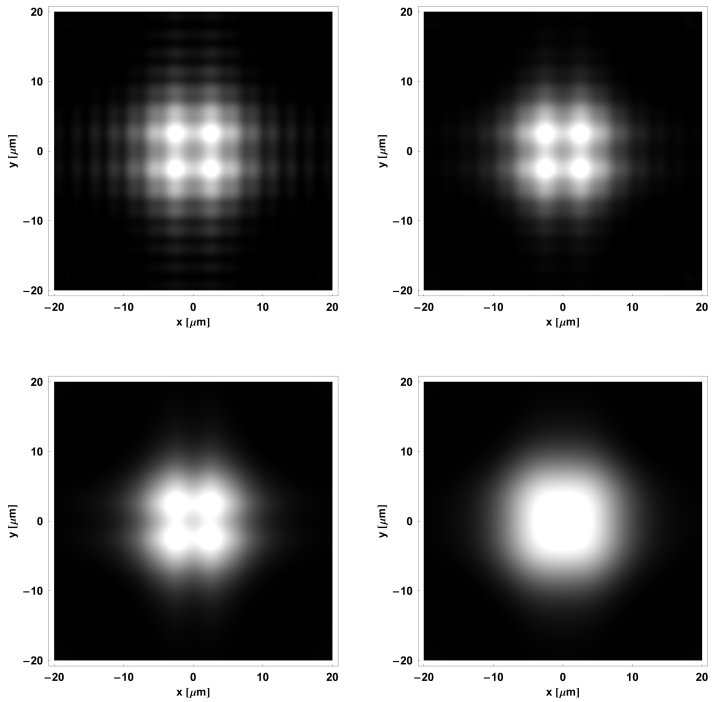

Figure 4.8: Illustration of the effect of decreasing transverse coherence length on the diffraction pattern from a square slit (from left to right, and from top to bottom). The parameter of the simulation are the same as in Fig.4.7.

In summary, the effect of partial coherence leads to a reduced visibility of the fringe pattern from a plane aperture. The contrast reduction affects the Fraunhofer diffraction pattern, as well as the Fresnel diffraction pattern in a qualitatively same manner. Note that for sufficiently poor source coherence, it is nearly impossible to distinguish the Fraunhofer diffraction pattern from the Fresnel pattern. It seems plausible, that the effects of partial coherence may be simplest describes by means of the convolution theorem for Fourier transformations. For instance, one may express the intensity distribution $\mathcal{I}_d(x)$ in the Fraunhofer limit as

$$\mathcal{I}_d(x) \propto \int_{-\infty}^{\infty} dX \; \mathfrak{S}(X-x) \; \widetilde{T}^2(X) \; , \tag{4.43}$$

where $\widetilde{T}(X) \sim \sin(Xw_x)/(Xw_x)$ is the Fourier transform of the *pupil function* from a simple slit [9], and $\mathfrak{S}(X)$ is some at this moment arbitrary function, which however takes into account the resolution and coherence effects of the source. Since the slit diffraction pattern from an ideal point source yields the intensity distribution which is proportional to $(\sin(Xw_x)/(Xw_x))^2$, we may readily rewrite eq. (4.43) as [32, 52]

$$\mathcal{I}_d(x) \propto \int_{-\infty}^{\infty} dX \; \mathfrak{S}(X-x) \; \mathcal{I}_{coh}(X) \; , \tag{4.44}$$

where the coherent intensity distribution $\mathcal{I}_{coh}(X) \propto \widetilde{T}^2(X)$ refers to the solution form a point source, which is in fact the simplest realization of a fully coherent source. Eventually, eq. (4.44) describes the diffracted intensity distribution in terms of convoluting the coherent point source solution $\mathcal{I}_{coh}(X)$ with a source function $\mathfrak{S}(X)$, which accounts for the actual source size and coherence length. Similarly, we may obtain the Fresnel diffraction pattern from [45, 46]

$$\mathcal{I}_d(x) \propto \int_{-\infty}^{\infty} dX \; \mathfrak{S}(X-x) \; \mathcal{I}_{coh}^{Fres}(X) \; , \tag{4.45}$$

where the coherent intensity distribution in the Fresnel limit is $\mathcal{I}_{coh}^{Fres}(X) \propto |\widetilde{T}^{Fres}(X)|^2$ with $\widetilde{T}^{Fres}(X) \sim [\mathrm{erf(X-w_x-i(X-w_x))-erf(X+w_x-i(X+w_x))}]$. Evidently, eqs. (4.44) and (4.45) allow a relatively simple formulation and, moreover, interpretation of the diffraction pattern form a partially coherent beam. A justification for the convolution formulas (4.44) and (4.45) can however only be obtained, if the radiating source is completely incoherent, i.e. $J_s(u_1, v_1; u_2, v_2) = \sqrt{I_s(u_1, v_1)}\sqrt{I_s(u_2, v_2)}\delta^2(u_2 - u_1; v_2 - v_1)$ where $\delta^2(u_2 - u_1; v_2 - v_1)$ is a two dimensional delta function. For that reason, one can not take it for granted, that effects of partial coherence can be, in general, incorporated into the diffraction solution by means of simple convolution formulas like (4.44) and (4.45).

We like to show next, that a convolution formula can in deed be found for even partially coherent conditions. For this purpose, we rewrite eq. (4.26b) as

$$\mathcal{I}_d(x) = \iint_{-\infty}^{\infty} T(\eta_1)T(\eta_2)\mathcal{J}_F(\eta_1,\eta_2)\ e^{-i2\kappa_2 x(\eta_2-\eta_1)}\ d\eta_1 d\eta_2\ , \tag{4.46}$$

where $T(\eta)$ represents the pupil function (truncation function)

$$T(\eta) = H(w_x/2 - |\eta|)\ , \tag{4.47}$$

and let

$$\mathcal{J}_F(\eta_1,\eta_2) = \frac{\kappa_2}{\pi}\mathcal{J}_1(\eta_1,\eta_2)\ e^{i\kappa_2(\eta_2^2-\eta_1^2)} \tag{4.48}$$

defines a general resolution function, which takes Fresnel and partial coherence effects into account. Next, we replace the pupil functions in eq. (4.46) by their Fourier transformation, which we represent as

$$T(\eta_1) = \int_{-\infty}^{\infty} \widetilde{T}^*(\widetilde{\eta}_1)e^{-i\eta_1\widetilde{\eta}_1}d\widetilde{\eta}_1\ , \tag{4.49}$$

$$T(\eta_2) = \int_{-\infty}^{\infty} \widetilde{T}(\widetilde{\eta}_2)e^{i\eta_2\widetilde{\eta}_2}d\widetilde{\eta}_2\ . \tag{4.50}$$

Substituting the above formulas in (4.46) yields

$$\begin{aligned}\mathcal{I}_d(x) = &\iint_{-\infty}^{\infty} d\widetilde{\eta}_1 d\widetilde{\eta}_2\ \widetilde{T}^*(\widetilde{\eta}_1)\widetilde{T}(\widetilde{\eta}_2)\\ &\times\iint_{-\infty}^{\infty} d\eta_1 d\eta_2\ \mathcal{J}_F(\eta_1,\eta_2)\ e^{-i(\widetilde{\eta}_1-2\kappa_2 x)\eta_1}\ e^{i(\widetilde{\eta}_2-2\kappa_2 x)\eta_2}\ .\end{aligned} \tag{4.51}$$

The integration over η_1, η_2 leads, after a straightforward calculation to, a Gaussian Schell-model with the new arguments $\widetilde{\eta}_1$ and $\widetilde{\eta}_2$. Hence, eq. (4.51) becomes

$$\mathcal{I}_d(x) = \iint_{-\infty}^{\infty} d\widetilde{\eta}_1 d\widetilde{\eta}_2\ \widetilde{T}^*(\widetilde{\eta}_1)\widetilde{T}(\widetilde{\eta}_2)\widetilde{\mathcal{J}}_F(\widetilde{\eta}_1 - 2\kappa_2 x, \widetilde{\eta}_2 - 2\kappa_2 x)\ , \tag{4.52}$$

with

$$\begin{aligned}\widetilde{\mathcal{J}}_F(\widetilde{\eta}_1 - 2\kappa_2 x, \widetilde{\eta}_2 - 2\kappa_2 x) = \widetilde{J}_0\ &e^{-(\widetilde{\eta}_1-2\kappa_2 x)^2/2\triangle\widetilde{\eta}_1^2}\ e^{-(\widetilde{\eta}_2-2\kappa_2 x)^2/2\triangle\widetilde{\eta}_2^2}\\ &\times e^{-[(\widetilde{\eta}_2-2\kappa_2 x)-(\widetilde{\eta}_1-2\kappa_2 x)]^2/2\triangle\widetilde{\eta}_{1,2}^2}\ ,\end{aligned} \tag{4.53}$$

and

$$\widetilde{J}_0 = \sqrt{I_0}\ \frac{\kappa_2 s_x}{\Sigma_x \sqrt{(C_x C_x^*)^2 - B_x}}\ , \tag{4.54a}$$

$$\triangle\widetilde{\eta}_1 = \sqrt{2\frac{(C_x C_x^*)^2 - B_x^2}{(C_x^*)^2 - B_x}}\ , \tag{4.54b}$$

$$\triangle\widetilde{\eta}_2 = \sqrt{2\frac{(C_x C_x^*)^2 - B_x^2}{C_x^2 - B_x}}\ , \tag{4.54c}$$

$$\triangle\widetilde{\eta}_{1,2} = \sqrt{2((C_x C_x^*)^2 - B_x^2)/B_x}\ . \tag{4.54d}$$

Eq. (4.52) presents a convolution integral under the conditions of partial coherence. Simplifications of (4.52) obviously depend on the approximations that are made for the generalized resolution function $\widetilde{\mathcal{J}}_F(\widetilde{\eta}_1, \widetilde{\eta}_2)$. It should be noted, that the two convolution integrals in (4.52) are coupled due to the third exponential function in (4.51), or in other words due to the bivariate Gaussian structure of eq. (4.53). The coupling part in $\widetilde{\mathcal{J}}_F(\widetilde{\eta}_1, \widetilde{\eta}_2)$ vanishes in the coherent limit, i.e. $B_x = 1/2\Xi_{tx}^2 \to 0$, and eq. (4.52) then simplifies to the modulus squared of a single convolution integral, which resembles the conventional intensity expression for diffraction solutions at a slit [9].

4.3 Scattering of Partially Coherent X-rays from Arbitrary Media

The scattering of partially coherent X-rays from matter is in a general manner comparable to the previous discussion on diffraction from apertures. In principle, any interference pattern produced by arbitrary structures, such as optical gratings or rough surfaces, yield an intensity distribution that contains information from the static structure of the scatterer, as well as the integrated coherence properties of the electromagnetic source. In the previous section we have presupposed, that the shape of the aperture is known, which therefore enabled us to focus on the effects on partial coherence and Fresnel conditions. In scattering experiments the situation is however more complicated, in the sense that the structure of the scatterer is the subject of investigation, thus it is usually unknown. Due to this addition lack of knowledge, the interpretation of the interference pattern is evidently more complicated, e.g. a random electron density distribution yields a complicated random interference pattern, which is referred to as a speckle pattern. In order to extract the structural properties of the scatterer from such a random interference pattern, some foreknowledge

is required with regard to the coherence and resolution characteristic of the electromagnetic source.

In this section we will discuss the scattering of X-rays from matter including the effects of resolution and partial coherence of the radiating source. In analogy to the van Cittert-Zernike theorem, we will provide propagation formulas for field correlation, which undergo a scattering process within the accuracy of the first Born approximation.

4.3.1 Generalized van Cittert-Zernike Propagation Law

The van Cittert-Zernike propagation law (4.4) holds for quasi-monochromatic conditions. If the experimental conditions are such, that the radiating source can not be treated as a quasi-monochromatic source, then one has to consider the actual spectral distribution of the source fields, as well as their correlations. A convenient description of propagating field correlations for non-quasi-monochromatic conditions can be obtained with the help of the Huygens-Fresnel principle [58]. Using this principle yields for the radiating field from a source [9]

$$\widetilde{U}(\mathbf{r},\omega_0) = \int_A \widetilde{U}(\boldsymbol{a},\omega_0)\ \frac{e^{ik_0 R_a}}{R_a}\ \Lambda(\omega_0)\ d^2a\ , \tag{4.55}$$

where $\boldsymbol{a}$ represents the position vector on the source area A, R_a is the distance between a source and a detection point at $\mathbf{r}$. $\Lambda(\omega_0)$ is the inclination factor at the source plane. Next, we assume that the frequency dependence of the inclination factor can be ignored and essentially be replaced by $\bar{\Lambda} = \Lambda(\bar{\omega}_0)$, where $\bar{\omega}_0$ shall be the mean frequency of outgoing field $\widetilde{U}(\boldsymbol{a},\omega_0)$. Under these circumstance we can easily formulated eq.(4.55) in the time domain by taking the Fourier transform on both sides of (4.55), hence

$$U(\mathbf{r},t) = \int_A \frac{U(\boldsymbol{a},t-R_a/c)}{R_a}\ \bar{\Lambda}\ d^2a\ , \tag{4.56}$$

where $U(\boldsymbol{a},t-R_a/c)$ results from

$$U(\boldsymbol{a},t-R_a/c) = 2\int_0^\infty U(\boldsymbol{a},\omega_0)\ e^{-i\omega_0(t-R_a/c)}\ d\omega_0\ . \tag{4.57}$$

The negative frequency part in the Fourier transformations are omitted, i.e. the fields in the time domain refer to the complex analytic representation of the (real) fields [32, 9, 58]. Such modified Fourier transformations are customarily used in optical coherence theory to represent a real non-monochromatic field $U^{(r)}(\mathbf{r},t)$ by a complex analytic signal $U(\mathbf{r},t) = [U^{(r)}(\mathbf{r},t) + iU^{(i)}(\mathbf{r},t)]/2$ [91,

59]. Let us now take the complex conjugate of eq.(4.56), viz.

$$U^*(\mathbf{r}_1, t_1) = \int_A \frac{U^*(\boldsymbol{a}_1, t - R_{a_1}/c)}{R_{a_1}} \; \bar{\Lambda}_1^* \; d^2a_1 \; , \tag{4.58}$$

where the subscribed was introduced to distinguish the field $U^*(\mathbf{r}_1, t_1)$ from a second field

$$U(\mathbf{r}_2, t_2) = \int_A \frac{U(\boldsymbol{a}_2, t - R_{a_2}/c)}{R_{a_2}} \; \bar{\Lambda}_2 \; d^2a_2 \; . \tag{4.59}$$

By multiplying the eqs. (4.58) and (4.59) and taking the time average, one finds

$$\Gamma\left(\mathbf{r}_1, \mathbf{r}_2, t_1, t_2\right) = \iint_{\mathcal{A}} \frac{\Gamma_a\left(\boldsymbol{a}_1, \boldsymbol{a}_2, t_1 - R_{a_1}/c, t_2 - R_{a_2}/c\right)}{R_{a_1} R_{a_2}} \; \bar{\Lambda}_1^* \bar{\Lambda}_2 \; d^2a_1 d^2a_2 \; , \tag{4.60}$$

where

$$\Gamma(\mathbf{r}_1, \mathbf{r}_2, t_1, t_2) = \langle U^*(\mathbf{r}_1, t_1) U(\mathbf{r}_2, t_2) \rangle \, , \tag{4.61}$$

$$\Gamma_a\left(\boldsymbol{a}_1, \boldsymbol{a}_2, t_1 - R_{a_1}/c, t_2 - R_{a_2}/c\right) = \langle U^*(\boldsymbol{a}_1, t_1 - R_{a_1}/c) U(\boldsymbol{a}_2, t_2 - R_{a_2}/c) \rangle \, , \tag{4.62}$$

represent *mutual coherence functions* one the detection and source plane, respectively. (The mutual coherence function reduces to the mutual intensity function for $t_1 = t_2$, i.e $\Gamma(\mathbf{r}_1, \mathbf{r}_2, t_1, t_1) = J(\mathbf{r}_1, \mathbf{r}_2)$.) If the fields at source plane are stationary fluctuation quantities, it follows that the correlation function $\Gamma_a\left(\boldsymbol{a}_1, \boldsymbol{a}_2, t_1 - R_{a_1}/c, t_2 - R_{a_2}/c\right)$ depends on its two time arguments only through the time difference $\tau = t_2 - t_1$ [58]. Since the relationship between the field $U(\mathbf{r}, t)$ and the $U(\boldsymbol{a}, t - R_a/c)$ is linear, the same is true for the field correlation function $\Gamma(\mathbf{r}_1, \mathbf{r}_2, t_1, t_2)$. Under these conditions one can replace eq.(4.60) by

$$\Gamma\left(\mathbf{r}_1, \mathbf{r}_2, \tau\right) = \iint_{\mathcal{A}} \frac{\Gamma_a\left(\boldsymbol{a}_1, \boldsymbol{a}_2, \tau - (R_{a_2} - R_{a_1})/c\right)}{R_{a_1} R_{a_2}} \; \bar{\Lambda}_1^* \bar{\Lambda}_2 \; d^2a_1 d^2a_2 \; . \tag{4.63}$$

The above propagation formula is a generalization of the van Cittert-Zernike propagation law [58]. Eq. (4.63) can easily be reduced to the Cittert-Zernike propagation law, if τ is set to be zero and the fields at the source plane are represented by a quasi-monochromatic field, i.e $U(\boldsymbol{a}, t) = U_0(\boldsymbol{a}) e^{-i\bar{\omega}_0 t}$, where $U_0(\boldsymbol{a})$ represents the field amplitude.

A more general propagation law than eq. (4.63) can be directly deduced from (4.56), namely [58]

$$W(\mathbf{r}_1, \mathbf{r}_2, \omega_0) = \iint_{\mathcal{A}} W_a(\boldsymbol{a}_1, \boldsymbol{a}_2, \omega_0) \; \frac{e^{ik_0(R_{a_2} - R_{a_1})}}{R_{a_1} R_{a_2}} \; \Lambda_1^*(\omega_0) \Lambda_2(\omega_0) \; d^2a_1 d^2a_2 \; , \tag{4.64}$$

where the *cross-spectral density functions*

$$\langle \widetilde{U}^*(\mathbf{r}_1,\omega_0)\widetilde{U}(\mathbf{r}_2,\omega_0')\rangle = W(\mathbf{r}_1,\mathbf{r}_2,\omega_0)\delta(\omega_0-\omega_0')\,, \tag{4.65}$$

$$\langle \widetilde{U}^*(\boldsymbol{a}_1,\omega_0)\widetilde{U}(\boldsymbol{a}_2,\omega_0')\rangle = W_a(\boldsymbol{a}_1,\boldsymbol{a}_2,\omega_0)\delta(\omega_0-\omega_0')\,, \tag{4.66}$$

define the correlations between the spectral amplitudes of any particular frequency component ω_0 of the field vibrations at the two points on the detector plane and source plane, respectively. A relation between the mutual coherence functions and the cross-spectral density function can be established on the Wiener-Khintchine theorem, which states that the time correlation function and the spectral density function form a Fourier transform pair [58]:

$$\Gamma(\mathbf{r}_1,\mathbf{r}_2,\tau) = \frac{1}{2\pi}\int_0^\infty W(\mathbf{r}_1,\mathbf{r}_2,\omega_0)\; e^{-i\omega_0\tau}\; d\omega_0\;, \tag{4.67}$$

$$W(\mathbf{r}_1,\mathbf{r}_2,\omega_0) = \int_{-\infty}^\infty \Gamma(\mathbf{r}_1,\mathbf{r}_2,\tau)\; e^{i\omega_0\tau}\; d\tau. \tag{4.68}$$

Note, that with eq. (4.67) and (4.64) one can readily derive the propagation law (4.63) for mutual coherence, if the inclination factors in eq. (4.64) are approximated by their mean values $\bar{\Lambda}_1$ and $\bar{\Lambda}_2$. The propagation laws (4.63) and (4.64) are both of central importance in the description of partially coherent sources and beams. In the continuing discussion, we will use the above propagation laws to describe the incident partially coherence beam in scattering experiments.

4.3.2 Propagation of Field Correlations from a Scatterer

Next, we discuss a propagation formula for field correlation, that undergo a scattering process from an arbitrary media. In analogy to the previous section, we will first derive a propagation formula for mutual coherence function, which is essentially based on a scattered field express in its first Born approximation, viz.

$$\widetilde{U}_s(\mathbf{r},\omega_0) = -r_e\int_V \rho(\mathbf{r}')\widetilde{U}_i(\mathbf{r}',\omega_0)\frac{e^{ik_0R}}{R}\; d^3\mathrm{r}'\;, \tag{4.69}$$

where $R = |\mathbf{r}-\mathbf{r}'|$ denotes the distance between a position in the scatterer $\mathbf{r}'$ and a detection point $\mathbf{r}$, the notation is illustrated in Fig. 4.9. Eq. (4.69) can be obtained by solving the inhomogeneous Helmholtz equation (3.9) in the first Born approximation, see section 3. From eq. (4.69) we can next deduce a field equation in the time domain, which may take the form

$$U_s(\mathbf{r},t) = -r_e\int_V\; \rho(\mathbf{r}')\;\frac{U_i(\mathbf{r}',t-R/c)}{R}\; d^3\mathrm{r}'\;. \tag{4.70}$$

The fields in the time domain are again considered as complex analytical representations of the real fields. If furthermore, the incident field $U_i(\mathbf{r}', t - R/c)$ is a stationary fluctuating quantity, one can readily deduce the following propagation formula

$$\Gamma_s(\mathbf{r}_1, \mathbf{r}_2, \tau) = r_e^2 \iint_V \rho(\mathbf{r}'_1)\rho(\mathbf{r}'_2)\, \frac{\Gamma_i\left(\mathbf{r}'_1, \mathbf{r}'_2, \tau - (R_2 - R_1)/c\right)}{R_1 R_2}\, d^3\mathrm{r}'_1 d^3\mathrm{r}'_2\,, \quad (4.71)$$

where

$$\Gamma_s(\mathbf{r}_1, \mathbf{r}_2, \tau) = \langle U_s^*(\mathbf{r}_1, t_1) U_s(\mathbf{r}_2, t_2)\rangle\,, \quad (4.72)$$

$$\Gamma_i\left(\mathbf{r}'_1, \mathbf{r}'_2, \tau - (R_2 - R_1)/c\right) = \langle U_i^*(\mathbf{r}'_1, t_1 - R_1/c) U_i(\mathbf{r}'_2, t_2 - R_2/c)\rangle\,. \quad (4.73)$$

Here $\Gamma_i\left(\mathbf{r}'_1, \mathbf{r}'_2, \tau - (R_2 - R_1)/c\right)$ is the retarded incident mutual coherence function at the scatterer and $\Gamma_s(\mathbf{r}_1, \mathbf{r}_2, \tau)$ represents the resulting fields correlations after the scattering process.

Up to now we have assumed that the scattering medium was deterministic, in the sense, that the spatial distribution of the electron density is, in principle, strictly known. Let us now assume, instead, that the electron density distribution of the scatterer are only characterized by random functions of position. An example of such media would be a rough surface, amorphous glass, or stochastic fractal structures. A meaningful measure for the observable intensity $I_s(\mathbf{r}) = \Gamma_s(\mathbf{r}, \mathbf{r}, 0)$ in an X-ray scattering experiment may then be obtained, by taking an ensemble average over the different realizations of the electron density, i.e. eq. (4.71) may be replaced by

$$\Gamma_s(\mathbf{r}_1, \mathbf{r}_2, \tau) = r_e^2 \iint_V C_{\rho\rho}(\mathbf{r}'_1, \mathbf{r}'_2)\, \frac{\Gamma_i\left(\mathbf{r}'_1, \mathbf{r}'_2, \tau - (R_2 - R_1)/c\right)}{R_1 R_2}\, d^3\mathrm{r}'_1 d^3\mathrm{r}'_2\,, \quad (4.74)$$

where

$$C_{\rho\rho}(\mathbf{r}'_1, \mathbf{r}'_2) = \langle \rho(\mathbf{r}'_1)\rho(\mathbf{r}'_2)\rangle\,, \quad (4.75)$$

represents the (static) electron density correlation function.

The propagation formula (4.71) was implicitly used by S. K. Sinha and M. Tolan to investigate the theoretical effects of partial coherence in X-ray diffraction experiments from crystals, periodic surface structures, as well as rough surfaces [91, 100]. Eq. (4.74) resembles a propagation formula, which was introduced by Wolf et al. [108]. In their original work, a slightly more general formula, than eq. (4.74), was given in the frequency-space domain, i.e in terms of cross-spectral density function. Both propagation formulas (4.71) and (4.74) provide useful starting points to determine the scattered intensity $I_s(\mathbf{r}) = \Gamma_s(\mathbf{r}, \mathbf{r}, 0)$ within the accuracy of the first Born approximation.

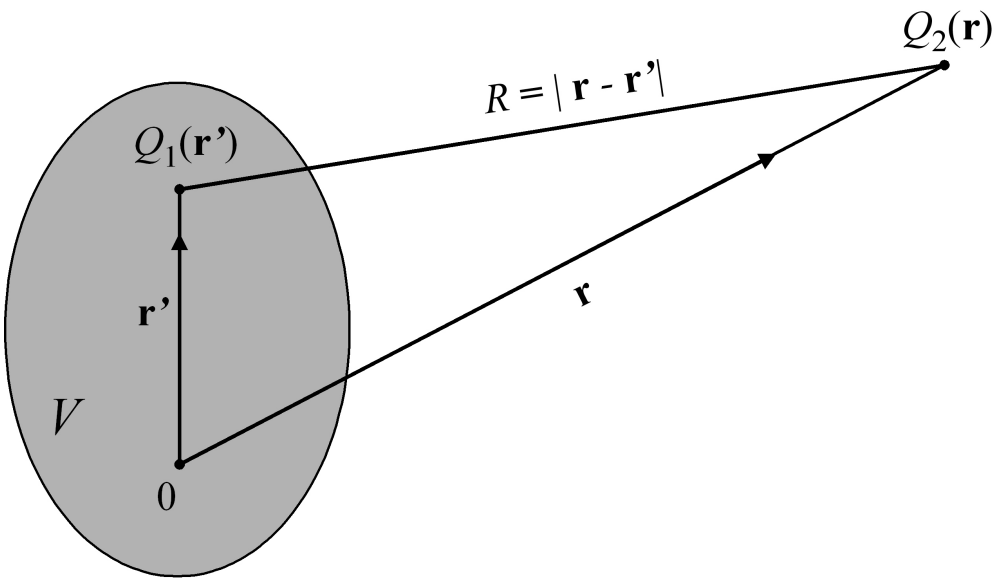

Figure 4.9: Schematic illustrating of the scattering geometry. $Q_1(\mathbf{r}')$ represents a point inside the scattering volume V and $Q_2(\mathbf{r})$ denotes a the detection point of the scattered field.

A. Remarks on Coherent, Incoherent and Partially Coherent Scattering Conditions

Whether equation (4.71) or (4.74) can be expressed in form of a convolution integral in reciprocal space, depends evidently on the choice for the incident mutual coherence function. We will briefly examine this question by considering a quasi-monochromatic incident plane wave of the form

$$U_i(\mathbf{r}', t) = U_{0i}(\mathbf{r}')\ e^{i(\mathbf{k}_i \cdot \mathbf{r}' - \bar{\omega}_0 t)}\ , \tag{4.76}$$

where the exponential function describes a plane wave with a mean incident direction $\mathbf{k}_i = \bar{k}_0 \hat{\mathbf{k}}_i$ and an average frequency of $\bar{\omega}_0 = c\bar{k}_0$. The fluctuating amplitude $U_{0i}(\mathbf{r}')$ of the field refers to a relatively slow changing envelope function in space. With eq. (4.76) one arrives at the following representation for the incident mutual coherence function:

$$\Gamma_i(\mathbf{r}'_1, \mathbf{r}'_2, \tau - (R_2 - R_1)/c) = J_i(\mathbf{r}'_1, \mathbf{r}'_2) e^{i\mathbf{k}_i \cdot (\mathbf{r}'_2 - \mathbf{r}'_1)} e^{-i\bar{\omega}_0(\tau - (R_2 - R_1)/c)}\ , \tag{4.77}$$

where $J_i(\mathbf{r}'_1, \mathbf{r}'_2)$ represents the mutual intensity function of the incident field amplitudes. In order to specify the path distances $R_1 = |\mathbf{r} - \mathbf{r}'_1|$ and $R_2 = |\mathbf{r} - \mathbf{r}'_2|$, we consider the Fresnel limit. Hence, with eq. (3.104) and (3.30) one finds

$$\Gamma_i(\mathbf{r}'_1, \mathbf{r}'_2, \tau - (R_2 - R_1)/c) = J_i(\mathbf{r}'_1, \mathbf{r}'_2) \mathrm{f}_b^*(\mathbf{r}'_1) \mathrm{f}_b(\mathbf{r}'_2) e^{-i\bar{\omega}_0 \tau} e^{-i\mathbf{q} \cdot (\mathbf{r}'_2 - \mathbf{r}'_1)}\ , \tag{4.78}$$

where the (after-sample) Fresnel corrections are incorporated by the function $f_b(\mathbf{r}')$, viz.

$$\mathrm{f}_b(\mathbf{r}') = e^{i(\mathbf{k}_\mathrm{f}\times\mathbf{r}')^2/(2\bar{k}_0\mathrm{r})} . \tag{4.79}$$

The intensity expression $I_s(\mathbf{r}) = \Gamma_s(\mathbf{r},\mathbf{r},0)$ can be found by substituting eq. (4.78) into (4.71), hence

$$I_s(\mathbf{r}) = \left(\frac{r_e}{\mathrm{r}}\right)^2 \iint_V \rho(\mathbf{r}'_1)\rho(\mathbf{r}'_2)\; J_i(\mathbf{r}'_1,\mathbf{r}'_2)\mathrm{f}^*_b(\mathbf{r}'_1)\mathrm{f}_b(\mathbf{r}'_2)\; e^{-i\mathbf{q}\cdot(\mathbf{r}'_2-\mathbf{r}'_1)}\; d^3\mathrm{r}'_1 d^3\mathrm{r}'_2 \;, \tag{4.80}$$

where we have approximated the path lengths R_1 and R_2 in the denominate by r. Eq. (4.80) can be written in a more compact form, if we make use of the definition $\rho_{_F}(\mathbf{r}) \equiv \rho(\mathbf{r})\mathrm{f}_b(\mathbf{r})$, which is refereed to as the *Fresnel electron density* [91]. With this definition, eq. (4.80) finally yields

$$I_s(\mathbf{r}) = \left(\frac{r_e}{\mathrm{r}}\right)^2 \iint_V \rho^*_{_F}(\mathbf{r}'_1)\rho_{_F}(\mathbf{r}'_2)J_i(\mathbf{r}'_1,\mathbf{r}'_2)\; e^{-i\mathbf{q}\cdot(\mathbf{r}'_2-\mathbf{r}'_1)}\; d^3\mathrm{r}'_1 d^3\mathrm{r}'_2 \;. \tag{4.81}$$

Although we have assumed quasi-monochromatic incident fields, we have obtained with eq. (4.81) a relatively simply formula, which can be used to examine the effects of spatial coherence. In order to discuss different spatial coherence conditions, we will consider in the following a Gaussian-Schell model for the incident mutual intensity function, i.e. $J_i(\mathbf{r}'_1,\mathbf{r}'_2) = \sqrt{I_i(\mathbf{r}'_1)}\sqrt{I_i(\mathbf{r}'_2)}j_i(\mathbf{r}'_2-\mathbf{r}'_1)$.

In the *incoherent limit*, the coherence factor $j(\mathbf{r}'_2-\mathbf{r}'_1)$ may be modeled by a 3-dimensional delta function. Eq. (4.81) then reduces to

$$I_s(\mathbf{r}) \propto \left(\frac{r_e}{\mathrm{r}}\right)^2 \int_V \rho^2(\mathbf{r}')I_i(\mathbf{r}')\; d^3\mathrm{r}' \;. \tag{4.82}$$

The above equation reveals, that the observable scattered intensity $I_s(\mathbf{r})$ is proportional to a continuous summation over that faction of the incident intensity, which falls within the sample volume V. The electron density players only the role of a weighting function and is independent from Fresnel correlations. The scattered intensity $I_s(\mathbf{r} = \mathrm{r}\hat{\mathbf{k}}_\mathrm{f})$ in not enhanced in any particular direction, but symmetrically decreases in strength with $1/\mathrm{r}^2$, i.e as an outgoing spherical wave. On using the *Parseval theorem* for Fourier transformations, one can alternatively express eq. (4.82) as [13]

$$I_s(\mathbf{r}) \propto \left(\frac{r_e}{\mathrm{r}}\right)^2 \int_{-\infty}^{\infty} \left|\widetilde{\rho}(\mathbf{q})\widetilde{\mathcal{G}}(\mathbf{q})\right|^2 d^3\mathrm{q} \;, \tag{4.83}$$

where $\widetilde{\mathcal{G}}(\mathbf{q})$ represents here the Fourier transform of the field truncation function $\sqrt{I_i(\mathbf{r}')}$.

To arrive at an intensity expression in the *coherent limit*, we may replace the coherence factor $j_i(\mathbf{r}'_2 - \mathbf{r}'_1)$ by one. If furthermore the integral in (4.81) is effectively truncated by the illuminated sample volume (i.e. by $\sqrt{I_i(\mathbf{r}')}$), we can readily extend the integration limits in (4.81) to infinity, and write

$$I_s(\mathbf{r}) = \left(\frac{r_e}{\mathrm{r}}\right)^2 \left| \int_{-\infty}^{\infty} \rho_{_F}(\mathbf{r}') \sqrt{I_i(\mathbf{r}')}\; e^{-i\mathbf{q}\cdot\mathbf{r}'} d^3\mathrm{r}' \right|^2 . \tag{4.84}$$

The above integral can be expressed as a convolution integral, viz.

$$I_s(\mathbf{r}) = \left(\frac{r_e}{\mathrm{r}}\right)^2 \left| \int_{-\infty}^{\infty} \widetilde{\rho}_{_F}(\mathbf{q}')\, \widetilde{\mathcal{G}}(\mathbf{q} - \mathbf{q}')\, d^3\mathrm{q}' \right|^2 . \tag{4.85}$$

The above two integrals will give rise to interference phenomena, due to the modulus squared outside the integral. The convolution integral (4.85) simply states a blurring of the Fresnel electron density distribution in q-space, which results from the truncation of the real-space Fourier integral.

In the *partially coherent case*, one may arrive at a convolution integral of the form

$$I_s(\mathbf{r}) = \left(\frac{r_e}{\mathrm{r}}\right)^2 \iint_{-\infty}^{\infty} \widetilde{\rho}^*_{_F}(\mathbf{q}_1) \widetilde{\rho}_{_F}(\mathbf{q}_2)\, \widetilde{J}(\mathbf{q} - \mathbf{q}_1, \mathbf{q} - \mathbf{q}_2)\, d^3\mathrm{q}_1 d^3\mathrm{q}_2 \,, \tag{4.86}$$

where $\widetilde{J}(\mathrm{q}_1, \mathrm{q}_2)$ is the Fourier transform of the incident mutual intensity. With a Gaussian-Schell model one can show, that $\widetilde{J}(\mathbf{q}_1, \mathbf{q}_2)$ takes the form of a bivariate Gaussian function, see chapter 4.2.3. Hence, the double convolutions in eq. (4.86) are coupled, and can therefore not be simplified to expressions like (4.85).

B. Remarks on Speckle Patterns

It is worth noting that the propagation formula (4.71) can be used to simulate the formation of speckle patterns from inhomogeneous media, whereas eq. (4.74) yields only the mean intensity distribution. An interesting theoretical analysis of random speckle patterns from rough surfaces was, for instance, given by M. Tolan et al. [100, 99]. In this study, the theoretical intensity distribution was derived from eq. (4.71) for different random surface morphologies with, however, identical statistical properties of the surface height distribution. After a subtle calculation, these authors provide several theoretical curves of the specularly scattered intensity distribution from a nearly coherent Gaussian-Schell beam under Fresnel conditions, see Fig.4.10. The calculated distributions illustrate q_y-scans of the reflected intensity for a smooth surface

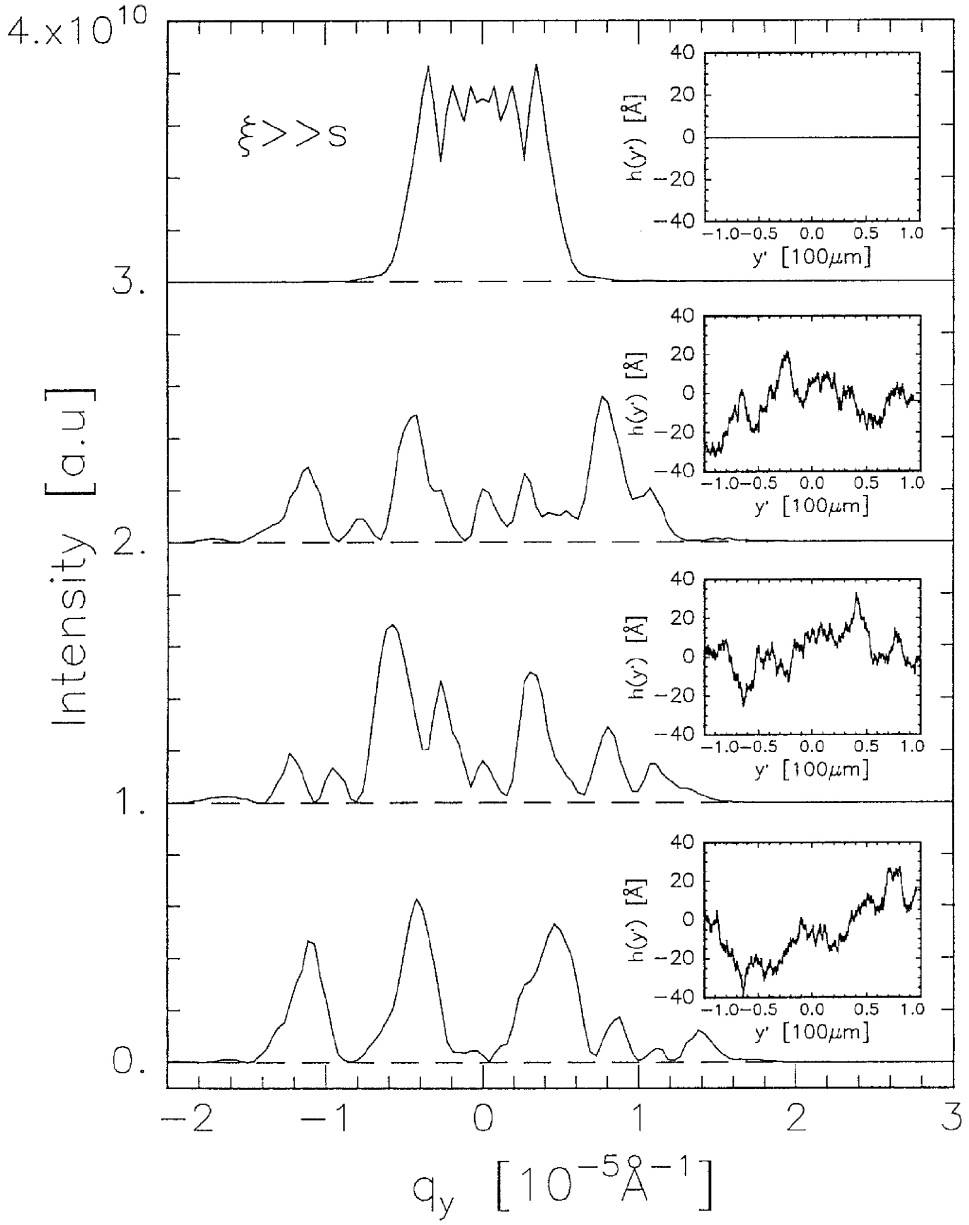

Figure 4.10: Calculations of the transverse q_y-scans of the specularly diffracted intensity distribution from a surface. The topmost curve is calculated for a smooth surface. The curve below show the speckle-like intensity distributions for different random surface morphologies. All four curves were obtained for an X-ray wavelength of $\lambda = 1$Å and the same source/sample and sample/detector distance of 0.5 m. The linear dimensions of the source size is $s = 50\,\mu$m and the transverse coherence length ξ is considered to be much larger than the source size [100, 99].

(top curve) and for three random surface structures. The surface morphologies are shown in the insets of each plot. All four curves were obtained for an X-ray wavelength of $\lambda = 1$Å and the same source/sample and sample/detector distance of 0.5 m. The linear dimensions of the source is $s = 50\,\mu$m and the transverse coherence length ξ is considered to be much larger than the source extent. Furthermore, the finite monochromaticity of source and the finite detector resolution are ignored in the simulation.

The curves in Fig.4.10 provide two useful information. First, a smooth surface yields an intensity distribution which essentially shows a reduction of the intensity at $q_y = 0$Å^{-1}. The reduction at the diffractions center resembles the well-known formation of the Poisson Spot in near field diffraction experiments from slits. By analogy we may conclude that a qualitative indication for Fresnel conditions in surface scattering experiments could be found from the verification of a reduced intensity distribution at the diffraction center. However, this useful and intuitive criterium appears to fail for diffraction patterns from rough surfaces, as shown in Fig.4.10. It is therefore worth noting that a far field (Fraunhofer) and near field (Fresnel) random speckle pattern may not reveal any characteristic differences. Secondly, the simulation indicates that different surface morphologies with identical statistical properties yield quite different speckle patterns. Conclusively, the example demonstrates that a qualitative interpretation or a precise calculation of speckle patterns is very difficult, which, therefore, makes it very unlikely to reconstruct the surface morphology from a measured speckle pattern [99].

4.3.3 Surface Scattering with Partially Coherent X-rays

In this section we will apply the propagation formulas (4.63) and (4.71) to derive an intensity for surface scattering experiments including the conditions of partially spatial and temporal source coherent. We discuss this matter in two steps. First, we will specify the source model and evaluate the general form of the incident mutual coherent function by making use of (4.63). The resulting incident mutual coherent will then be substituted into eq. (4.71), which leads to a coordinate-free representation of a propagation formula for scattering. The scattering situation and notation for this formal approach is illustrated in Fig.4.11. In a second step, we will specify the coordinate system and X-ray path length differences, which may apply to surface scattering experiments. In section 4.3.4 will further discuss the X-ray path length differences for the particular case of surface sensitive scattering conditions, i.e. for incident angles below the critical angle of the scattering medium. The coordinate system and notation for surface scattering is shown Fig.4.12.

The incident mutual coherence function may simplest be specified with

propagation formula (4.63) in combination with the Wiener-Khintchine theorem (4.67). Hence, eq. (4.73) can be written as

$$\begin{aligned}\Gamma_i\left(\mathbf{r}_1', \mathbf{r}_2', \tau - (R_{b_2} - R_{b_1})/c\right) &= \iint_{\mathcal{A}} d^2a_1 d^2a_2 \; \frac{\Gamma_a\left(\boldsymbol{a}_1, \boldsymbol{a}_2, \tau - \triangle l/c\right)}{R_{a_1} R_{a_2}} \; \bar{\Lambda}_1^* \bar{\Lambda}_2 \;, \\ &= \frac{1}{2\pi} \iint_{\mathcal{A}} d^2a_1 d^2a_2 \; \frac{\bar{\Lambda}_1^* \bar{\Lambda}_2}{R_{a_1} R_{a_2}} \\ &\quad \times \int_0^\infty d\omega_0 \; W_a(\boldsymbol{a}_1, \boldsymbol{a}_2, \omega_0) \, e^{-i\omega_0(\tau - \triangle l/c)}, \quad (4.87)\end{aligned}$$

with

$$\triangle l = (R_{a_2} - R_{a_1}) + (R_{b_2} - R_{b_1}) = (R_{a_2} + R_{b_2}) - (R_{a_1} + R_{b_1}) \qquad (4.88)$$

being the total path length difference between two X-rays, which radiate from a finite source area A, and propagate after a scattering process towards a detection point. To clarify the differences between the X-ray paths the subscribe a is used for pre-sample path lengths R_{a_1}, R_{a_2} and distances from the scatterer to the detection position are denoted by R_{b_1}, R_{b_2} in place of R_1, R_2, see Fig.4.11.

If the outgoing fields at the source plane A have for all frequencies ω_0 approximately the same spatial coherence properties, then one may write the cross-spectral density function as

$$W_a(\boldsymbol{a}_1, \boldsymbol{a}_2, \omega_0) = J_a(\boldsymbol{a}_1, \boldsymbol{a}_2) S(\omega_0) \,, \qquad (4.89)$$

where $J_a(\boldsymbol{a}_1, \boldsymbol{a}_2)$ is the mutual intensity function and $S(\omega_0)$ represents the *spectral density function* of the source [58]. The separation ansatz (4.89) states, that the transverse and longitudinal coherence properties of the source are independent from each other. Next, we assume a Gaussian distribution for the spectral density function, which shall has a HWFM of $\triangle\omega = c/\xi_l$, and be centered at the mean frequency $\bar{\omega}_0$. With the above source model one finds, after evaluating the integration over ω_0, the following expression for the incident mutual coherence function

$$\begin{aligned}\Gamma_i(\mathbf{r}_1', \mathbf{r}_2', \tau - (R_{b_2} - R_{b_1})/c) &= \frac{\triangle\omega}{\sqrt{2\pi}} \iint_{\mathcal{A}} d^2a_1 d^2a_2 \; J_a(\boldsymbol{a}_1, \boldsymbol{a}_2) \\ &\quad \times \frac{e^{-i\bar{\omega}_0(\tau - \triangle l/c)} \, e^{-\triangle\omega^2(\tau - \triangle l/c)^2/2}}{R_{a_1} R_{a_2}} \; \bar{\Lambda}_1^* \bar{\Lambda}_2 \;. \quad (4.90)\end{aligned}$$

Eq. (4.90) holds for $\bar{k}_0 \xi_l \gg 1$ and $\triangle l/(\bar{k}_0 \xi_l^2) \ll 1$. An expression for the intensity $I_s(\mathbf{r}) = \Gamma_s(\mathbf{r}, \mathbf{r}, 0)$ can finally be found by substituting eq. (4.90) into

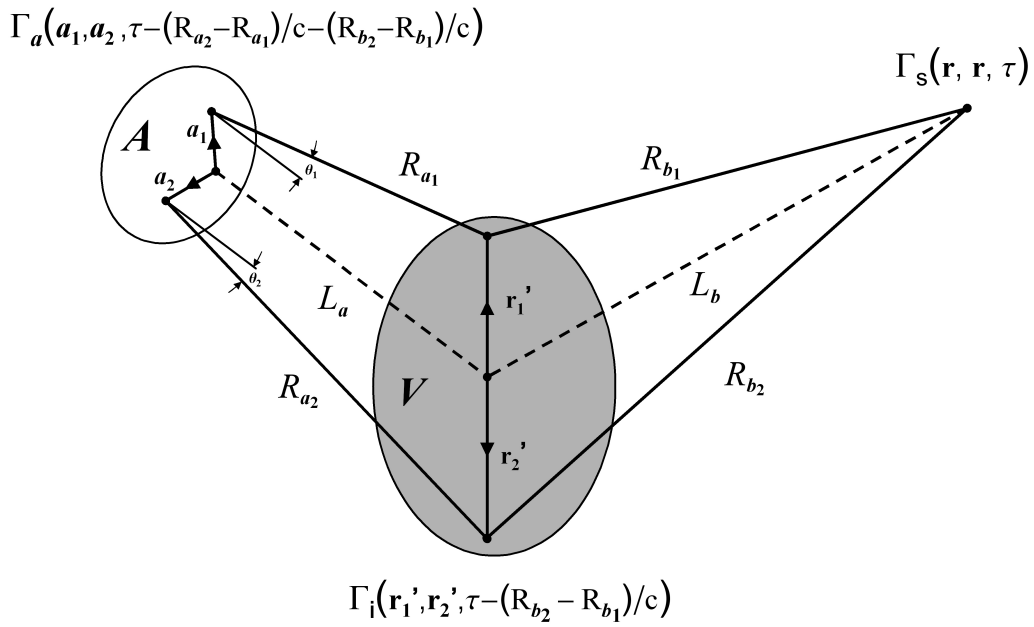

Figure 4.11: Illustration of the propagating mutual coherence function and the used notation. A radiating point on the source area A is defined by the position vector $\boldsymbol{a}$. The angular spread at each source position is describes by θ, where θ is the angle between the normal vector on the source plane and the propagation direction of the outgoing field at $\boldsymbol{a}$. The distance from source to scatterer is given by R_{a_1} and R_{a_2}. The optical axis for a bunch of X-rays is represented by the mean source/sample distance L_a and sample/detector distance L_b. To avoid confusion between the path lengths, we use the notation R_a for pre-sample distances and R_b for after-sample path lengths. The detection position $\mathbf{r} = L_b\hat{\mathbf{k}}_\mathrm{f}$ is specified by the distance L_b and the mean normal wave vector $\hat{\mathbf{k}}_\mathrm{f}$.

(4.71), hence

$$\begin{aligned} I_s(\mathbf{r}) &= \Gamma_s(\mathbf{r},\mathbf{r},0) \\ &= \frac{c}{\sqrt{2\pi}\xi_l}\iint_V d^3\mathrm{r}_1' d^3\mathrm{r}_2'\ \rho(\mathbf{r}_1')\rho(\mathbf{r}_2') \\ &\quad\times \iint_A d^2a_1 d^2a_2\ J_a(\boldsymbol{a}_1,\boldsymbol{a}_2)\ \frac{e^{i\bar{k}_0\triangle l}\, e^{-(\triangle l/\xi_l)^2/2}}{R_{a_1}R_{a_2}R_{b_1}R_{b_2}}\ \bar{\Lambda}_1^*\bar{\Lambda}_2\ . \end{aligned} \tag{4.91}$$

A further uncritical simplified of eq. (4.91) and (4.71) can be obtained by replacing the path lengths in the denominates by their mean distances L_a and L_b, respectively. In combination with the small angle approximation for the inclination factor (i.e. $\Lambda \approx i/\bar{\lambda}_0$) and the representation $\mathbf{r} = L_b\hat{\mathbf{k}}_\mathrm{f}$, one arrives

at the following expression for eq. (4.91):

$$I_s\big(L_b\hat{\mathbf{k}}_\mathrm{f}\big) = \frac{c}{\sqrt{2\pi}\xi_l}\left(\frac{r_e}{\bar{\lambda}_0 L_a L_b}\right)^2 \iint_V d^3\mathrm{r}_1' d^3\mathrm{r}_2'\ \rho(\mathbf{r}_1')\rho(\mathbf{r}_2') \times \iint_A d^2a_1 d^2a_2\ J_a(\boldsymbol{a}_1,\boldsymbol{a}_2)\ e^{i\bar{k}_0\triangle l}\, e^{-(\triangle l/\xi_l)^2/2}\ . \tag{4.92}$$

Up to this stage we have not defined the path length difference $\triangle l$ and the coordinate system in eq. (4.92). In the ongoing discussion we will remove these ambiguity, and specify first the path length difference. The choice for $\triangle l$ will obviously determine the complexity of computing the above formula, it is therefore worth recognizing, that one arrives at a greatly simplified expression in the quasi-monochromatic limit, i.e. if path length difference is small compared to the longitudinal coherence length ($\triangle l/\xi_l \ll 1$). In the quasi-monochromatic limit we can remove the second exponential function in (4.92) independently from the Fraunhofer or the Fresnel path length approximation. In the following we will, however, assume that quasi-monochromatic conditions are not necessarily fulfilled. Instead, we will seek for less restricting approximation, which can be based on the explicit form for the path length difference.

To account for Fresnel conditions in the path length difference, we expand $\triangle l$ to the second order in $\mathbf{r}_1'/L_a$, $\mathbf{r}_2'/L_a$, $\mathbf{r}_1'/L_b$ and $\mathbf{r}_2'/L_b$. With the definitions $\mathbf{L}_a = L_a\hat{\mathbf{k}}_\mathrm{i}$ and $\mathbf{L}_b = L_b\hat{\mathbf{k}}_\mathrm{f}$ $(=\mathbf{r})$, we obtain from

$$\begin{aligned}\triangle l &= (R_{a_2} - R_{a_1}) + (R_{b_2} - R_{b_1}) \\ &= \left(|\mathbf{L}_a + \mathbf{r}_2' - \boldsymbol{a}_2| - |\mathbf{L}_a + \mathbf{r}_1' - \boldsymbol{a}_1|\right) + \left(|\mathbf{L}_b - \mathbf{r}_2'| - |\mathbf{L}_b - \mathbf{r}_1'|\right),\end{aligned} \tag{4.93}$$

the approximation [91]

$$\begin{aligned}\triangle l \ \approx\ & -(\hat{\mathbf{k}}_\mathrm{f} - \hat{\mathbf{k}}_\mathrm{i})\cdot(\mathbf{r}_2' - \mathbf{r}_1') \\ & -\frac{1}{L_a}(\boldsymbol{a}_2\cdot\mathbf{r}_2' - \boldsymbol{a}_1\cdot\mathbf{r}_1') + \frac{1}{2L_a}\left(\boldsymbol{a}_2^2 - \boldsymbol{a}_1^2\right) \\ & +\frac{1}{2L_a}\left[\left(\hat{\mathbf{k}}_\mathrm{i}\times\mathbf{r}_2'\right)^2 - \left(\hat{\mathbf{k}}_\mathrm{i}\times\mathbf{r}_1'\right)^2\right] \\ & +\frac{1}{2L_b}\left[\left(\hat{\mathbf{k}}_\mathrm{f}\times\mathbf{r}_2'\right)^2 - \left(\hat{\mathbf{k}}_\mathrm{f}\times\mathbf{r}_1'\right)^2\right],\end{aligned} \tag{4.94}$$

where we have, additionally, neglected third order terms of $\boldsymbol{a}_1/L_a$ and $\boldsymbol{a}_2/L_a$ in the derivation of (4.94). The first line on the ride hand side of (4.94) refers to *Fraunhofer point-source terms*, which are customarily address as Fraunhofer terms. The first two lines may then be addressed as *Fraunhofer finite-source terms*. The last two lines define pre- and after-sample Fresnel terms,

respectively. To avoid confusion, with regard to the terminology, we will henceforth distinguish the Fraunhofer/Fresnel (point-source) conditions from *Fraunhofer/Fresnel finite-source* conditions.

In the sample coordinate system, one finds the below representation for the unit wave vectors

$$\hat{\mathbf{k}}_{\mathrm{i}} = \begin{pmatrix} 0 \\ \cos\alpha_{\mathrm{i}} \\ -\sin\alpha_{\mathrm{i}} \end{pmatrix} \qquad \text{and} \qquad \hat{\mathbf{k}}_{\mathrm{f}} = \begin{pmatrix} \cos\alpha_{\mathrm{f}}\sin\varphi \\ \cos\alpha_{\mathrm{f}}\cos\varphi \\ \sin\alpha_{\mathrm{f}} \end{pmatrix}. \tag{4.95}$$

$\hat{\mathbf{k}}_{\mathrm{i}}$ and $\hat{\mathbf{k}}_{\mathrm{f}}$ point along the mean direction of the optical axis. There angular dependence is illustrated in Fig. 4.12. The source vectors $\boldsymbol{a}_1 = a_{x_1}\hat{\boldsymbol{a}}_x + a_{z_1}\hat{\boldsymbol{a}}_z$ and $\boldsymbol{a}_2 = a_{x_2}\hat{\boldsymbol{a}}_x + a_{z_2}\hat{\boldsymbol{a}}_z$ are as well described in the sample coordinate system through their unit stretch vectors

$$\hat{\boldsymbol{a}}_x = \begin{pmatrix} 1 \\ 0 \\ 0 \end{pmatrix} \qquad \text{and} \qquad \hat{\boldsymbol{a}}_z = \begin{pmatrix} 0 \\ \sin\alpha_{\mathrm{i}} \\ \cos\alpha_{\mathrm{i}} \end{pmatrix}, \tag{4.96}$$

Note that in the sample coordinate system the 2-dimensional integrals over the source plane refer to integrals over the coefficients of the vectors $\boldsymbol{a}_1$ and $\boldsymbol{a}_2$, i.e. $d^2a_1 = da_{x_1}da_{z_1}$ and $d^2a_2 = da_{x_2}da_{z_2}$.

Next, we use the substitutions

$$\kappa_a = \frac{\bar{k}_0}{2L_a} \quad \text{and} \quad \kappa_b = \frac{\bar{k}_0}{2L_b}, \tag{4.97}$$

and the definition for the mean nominal wave vector transfer

$$\mathbf{q} = \bar{k}_0\hat{\mathbf{q}} \quad \text{with} \quad \hat{\mathbf{q}} = \hat{\mathbf{k}}_{\mathrm{f}} - \hat{\mathbf{k}}_{\mathrm{i}}. \tag{4.98}$$

With the substitutions (4.97) and (4.98), one finds at once the following representations for the exponential terms in eq (4.92):

$$\begin{aligned} \bar{k}_0\triangle l \;=\; & -\mathbf{q}\cdot(\mathbf{r}_2' - \mathbf{r}_1') + \kappa_a\left[\boldsymbol{a}_2^2 - \boldsymbol{a}_1^2 - 2(\boldsymbol{a}_2\cdot\mathbf{r}_2' - \boldsymbol{a}_1\cdot\mathbf{r}_1')\right] \\ & +\kappa_a\Big[\big(\hat{\mathbf{k}}_{\mathrm{i}}\times\mathbf{r}_2'\big)^2 - \big(\hat{\mathbf{k}}_{\mathrm{i}}\times\mathbf{r}_1'\big)^2\Big] + \kappa_b\Big[\big(\hat{\mathbf{k}}_{\mathrm{f}}\times\mathbf{r}_2'\big)^2 - \big(\hat{\mathbf{k}}_{\mathrm{f}}\times\mathbf{r}_1'\big)^2\Big], \end{aligned} \tag{4.99}$$

and the quadratic term $(\triangle l/\xi_l)^2/2$ reduces to

$$\frac{\triangle l^2}{2\xi_l^2} = \frac{[\hat{\mathbf{q}}\cdot(\mathbf{r}_2' - \mathbf{r}_1')]^2}{2\xi_l^2}. \tag{4.100}$$

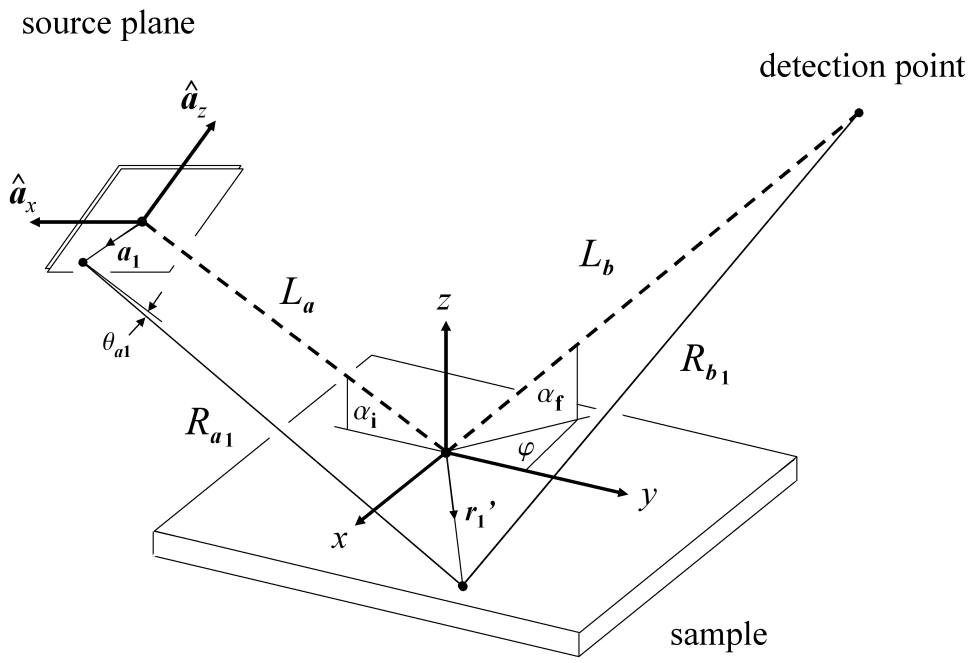

Figure 4.12: Illustration of the propagating mutual coherence function and the used notation in surface scattering geometry. The notation and the scattering geometry is for sakes of clarity illustrated for only one ray. The propagation path is described through the mean directional vectors of the optical axis, i.e. $\mathbf{k}_\mathrm{i}$ and $\mathbf{k}_\mathrm{f}$. The normalized wave vectors $\hat{\mathbf{k}}_\mathrm{i}$ and $\hat{\mathbf{k}}_\mathrm{f}$ are here identical with $\hat{\mathbf{L}}_a = \mathbf{L}_a/L_a$ and $\hat{\mathbf{L}}_b = \mathbf{L}_b/L_b$, respectively. The source vector $\boldsymbol{a}_1$ and the sample vector $\boldsymbol{r}_1'$ are both defined in the sample coordinate system (x, y, z). The z direction is chosen to be perpendicular to the mean sample surface, x and y are the surface in-plane components. The mean incident direction of the X-rays is describe by the angle α_i, and the scattering direction is defined by the angle α_f and the out of incident plane angle φ.

According to (4.100) the longitudinal coherence affects essentially the Fraunhofer terms of the path length difference. In other words, second order correction to the path length difference $\triangle l$, namely Fresnel and finite source size corrections, are negligible. After substituting eq. (4.99) and (4.100) into formula (4.92), we obtain the following solution

$$I_s(\mathbf{q}) = r_e^2 \iint_V d^3\mathrm{r}_1' d^3\mathrm{r}_2' \; \rho(\mathbf{r}_1')\rho(\mathbf{r}_2') \; \mathcal{G}(\mathbf{r}_1', \mathbf{r}_2') \; e^{-i\mathbf{q}\cdot(\mathbf{r}_2' - \mathbf{r}_1')} \; , \tag{4.101}$$

with

$$\mathcal{G}(\mathbf{r}_1', \mathbf{r}_2') = \frac{1}{L_b^2} f_a(\mathbf{r}_1', \mathbf{r}_2') f_b(\mathbf{r}_1', \mathbf{r}_2') \mathcal{G}_l(\mathbf{r}_2' - \mathbf{r}_1') J_i(\mathbf{r}_1', \mathbf{r}_2') \, , \tag{4.102}$$

where $f_a(\mathbf{r}'_1, \mathbf{r}'_2)$ and $f_b(\mathbf{r}'_1, \mathbf{r}'_2)$ respectively represent the pre- and after-sample Fresnel terms

$$f_a(\mathbf{r}'_1, \mathbf{r}'_2) = e^{i\kappa_a \left[\left(\hat{\mathbf{k}}_\mathrm{i} \times \mathbf{r}'_2\right)^2 - \left(\hat{\mathbf{k}}_\mathrm{i} \times \mathbf{r}'_1\right)^2 \right]} \tag{4.103}$$

$$f_b(\mathbf{r}'_1, \mathbf{r}'_2) = e^{i\kappa_b \left[\left(\hat{\mathbf{k}}_\mathrm{f} \times \mathbf{r}'_2\right)^2 - \left(\hat{\mathbf{k}}_\mathrm{f} \times \mathbf{r}'_1\right)^2 \right]} . \tag{4.104}$$

The function $\mathcal{G}_l(\mathbf{r}'_2 - \mathbf{r}'_1)$ and the incident mutual intensity function $J_i(\mathbf{r}'_1, \mathbf{r}'_2)$ account for the longitudinal and spatial coherence properties at the sample position, respectively. They are of the form:

$$\mathcal{G}_l(\mathbf{r}'_2 - \mathbf{r}'_1) = \frac{c}{\sqrt{2\pi}\xi_l} \, e^{-[\hat{\mathbf{q}} \cdot (\mathbf{r}'_2 - \mathbf{r}'_1)]^2 / 2\xi_l^2} \tag{4.105}$$

$$J_i(\mathbf{r}'_1, \mathbf{r}'_2) = \frac{1}{\bar{\lambda}_0^2 L_a^2} \iint_A d^2a_1 d^2a_2 \; J_a(\boldsymbol{a}_1, \boldsymbol{a}_2) \; e^{i\kappa_a \left[\boldsymbol{a}_2^2 - \boldsymbol{a}_1^2 - 2(\boldsymbol{a}_2 \cdot \mathbf{r}'_2 - \boldsymbol{a}_1 \cdot \mathbf{r}'_1) \right]} . \tag{4.106}$$

Note that the scattered intensity in eq. (4.101) is formally expressed as a function of the (mean) wave vector transfer. The function $\mathcal{G}(\mathbf{r}'_1, \mathbf{r}'_2)$ represents a generalized resolution function, which takes into account Fresnel corrections, as well as the coherence and resolution properties of the source. The above result for intensity is formally equal to eq. (4.81), however, eq. (4.101) includes the non-monochromatic - but nonetheless narrow-band - power spectrum of the source. Furthermore, we have avoided using the concept of Fresnel electron densities. [1]

To arrive at an intensity formula in form of a convolution integral, one can systematically evaluate eq. (4.102) for different conditions of spatial coherence, see discussion in section 4.3.2. In the case of a random electron density distribution, which obeys the statistical condition of spatial homogeneity, we finds at once

$$I_s(\mathbf{q}) = r_e^2 \int_{-\infty}^{\infty} d^3\mathrm{R} \; C_{\rho\rho}(\mathbf{R}) \, \mathcal{G}'(\mathbf{R}) \; e^{-i\mathbf{q}\cdot\mathbf{R}} , \qquad \text{with } \; \mathbf{R} = \mathbf{r}'_2 - \mathbf{r}'_1 , \tag{4.107}$$

$$= r_e^2 \int_{-\infty}^{\infty} d^3\mathrm{Q} \; \widetilde{C}_{\rho\rho}(\mathbf{Q}) \, \widetilde{\mathcal{G}}'(\mathbf{q} - \mathbf{Q}) , \tag{4.108}$$

where

$$\mathcal{G}'(\mathbf{R}) = \int_{-\infty}^{\infty} d^3\mathrm{r}'_1 \; \mathcal{G}(\mathbf{r}'_1, \mathbf{r}'_1 + \mathbf{R}) . \tag{4.109}$$

[1] The concept of Fresnel electron densities is only beneficial, if the electron density distribution $\rho(\mathbf{r})$ is fully known, i.e. not the subject of experimental investigation. Whether the Fresnel terms should be combined with the resolution function or the electron density, is eventually a question of the experimental purpose.

The tilde is used to denote the Fourier transform of the corresponding function without the tilde. In eq. (4.107) we have extended the integral limits to infinity. This treatment is always justified, if the scattering volume is effectively truncated by the incident X-ray field, i.e. eventually by $\mathcal{G}'(\mathbf{R})$. The actual sample size should, however, be incorporated if a spatially unlimited plane wave is incident on the sample, i.e. in the quasi-monochromatic Fraunhofer point source limit.

Eq. (4.108) resembles a convolution formula which is conventionally used to incorporate only resolution effects in scattering experiments [91, 99]. It is worth recognizing that the structure of the convolution integral (4.108) holds independently from Fresnel corrections, as well as the partial coherence and finite resolution of the source.

4.3.4 Surface Sensitive Scattering Conditions

In the previous section we have derived intensity expressions, which can be used to describe the scattering of partially coherent X-rays from deterministic and random surfaces structures. We will next specify the function $\mathcal{G}(\mathbf{r}'_1, \mathbf{r}'_2)$ for a particular case, which is of interest in this work.

In the case of surface sensitive scattering geometries the incident angle α_i is set to be below the critical angle α_c of the scattering material, which leads to the phenomenon of total external reflection. Furthermore, the X-ray penetration depth into the medium is then restricted to only a few tens of Ångstroms in the z'-direction [99]. Within this surface sensitive experimental arrangement, the maximum path length difference $\triangle l$ between the X-rays is substantially limited by the extent of the illuminated sample surface and the source size. Conclusively, the quadratic z'-terms of the sample vectors yield a negligible contribution in eq. (4.94) and can, therefore, be ignored. If we require, in addition, that the maximum source size is only few tens of microns, then the z'-components of the vector products $\boldsymbol{a}_1 \cdot \mathbf{r}'_1$ and $\boldsymbol{a}_2 \cdot \mathbf{r}'_2$ give equally an insignificant contribution to the path length difference in (4.94). Under these conditions, we may consider a reduced surface restricted path length difference, which is in great parts independent from the z'-components. Since this approximation will not affect the Fraunhofer point source term in $\triangle l$, we can restrict the following discussion on finding an approximated expression for $\mathcal{G}(\mathbf{r}'_1, \mathbf{r}'_2)$.

The approximated formula for $\mathcal{G}(\mathbf{r}'_1, \mathbf{r}'_2)$ can be simplest expressed by using the following set of two-dimensional vector representations:

$$\hat{\boldsymbol{k}}_\mathrm{i} = \begin{pmatrix} 0 \\ \cos\alpha_\mathrm{i} \end{pmatrix} \qquad \text{and} \qquad \hat{\boldsymbol{k}}_\mathrm{f} = \begin{pmatrix} \cos\alpha_\mathrm{f} \sin\varphi \\ \cos\alpha_\mathrm{f} \cos\varphi \end{pmatrix}. \tag{4.110}$$

For notational convenience, we will equally use cursive letters for the surface in-plane components of $\mathbf{r}' = (\boldsymbol{r}', z')$ and $\mathbf{q} = (\boldsymbol{q}, q_z)$ where $\boldsymbol{q} = \bar{k}_0\hat{\boldsymbol{q}} = \bar{k}_0(\hat{\boldsymbol{k}}_\mathrm{f} - \hat{\boldsymbol{k}}_\mathrm{i})$. Two-dimensional source vectors are represented as $\mathbf{a}_1 = a_{x_1}\hat{\mathbf{a}}_x + a_{z_1}\hat{\mathbf{a}}_z$ and $\mathbf{a}_2 = a_{x_2}\hat{\mathbf{a}}_x + a_{z_2}\hat{\mathbf{a}}_z$, where

$$\hat{\mathbf{a}}_x = \begin{pmatrix} 1 \\ 0 \end{pmatrix} \qquad \text{and} \qquad \hat{\mathbf{a}}_z = \begin{pmatrix} 0 \\ \sin\alpha_\mathrm{i} \end{pmatrix}. \tag{4.111}$$

With the above vector definitions, we can write the incident mutual intensity function as

$$\begin{aligned} J_i(\boldsymbol{r}_1', \boldsymbol{r}_2') &= \frac{1}{\bar{\lambda}_0^2 L_a^2} \iint_A d^2a_1 d^2a_2\, J_a(\boldsymbol{a}_1, \boldsymbol{a}_2) e^{i\kappa_a\left[\boldsymbol{a}_2^2 - \boldsymbol{a}_1^2 - 2(\mathbf{a}_2\cdot\boldsymbol{r}_2' - \mathbf{a}_1\cdot\boldsymbol{r}_1')\right]}, \\ &= \frac{1}{\bar{\lambda}_0^2 L_a^2} \iint_{-\infty}^{\infty} d^2a_1 d^2a_2\, \mathcal{A}(\boldsymbol{a}_1)\mathcal{A}(\boldsymbol{a}_2) J_a(\boldsymbol{a}_1, \boldsymbol{a}_2) e^{i\kappa_a\left[\boldsymbol{a}_2^2 - \boldsymbol{a}_1^2 - 2(\mathbf{a}_2\cdot\boldsymbol{r}_2' - \mathbf{a}_1\cdot\boldsymbol{r}_1')\right]}, \end{aligned} \tag{4.112}$$

where $\mathcal{A}(\boldsymbol{a})$ represents an aperture function. The above approximation holds for

$$\left.\left|\frac{\bar{k}_0}{2L_a} a_z z' \cos\alpha_\mathrm{i}\right|\right|_{max} \ll 1\ . \tag{4.113}$$

Note that the maximum value for z' is tens of Ångstroms and the maximum extend for a_z is determined by the linear extent the source. Let us next consider a homogenous intensity distribution across the aperture A, and a Gaussian shaped aperture opening, i.e. $\mathcal{A}(\boldsymbol{a}) = e^{-a_{x_1}^2/2\triangle a_x^2} e^{-a_{z_1}^2/2\triangle a_z^2}$. If, furthermore, the spatial correlation properties are also characterized by a Gaussian function, one obtains essentially a Gaussian-Schell model source for $\mathcal{A}(\boldsymbol{a}_1)\mathcal{A}(\boldsymbol{a}_2)J_a(\boldsymbol{a}_1, \boldsymbol{a}_2)$. Hence, the integrand in eq. (4.112) yields

$$\begin{aligned} \mathcal{A}(\boldsymbol{a}_1)\mathcal{A}(\boldsymbol{a}_2)J_a(\boldsymbol{a}_1, \boldsymbol{a}_2) = I_0 &\left(e^{-a_{x_1}^2/2\triangle a_x^2} e^{-a_{z_1}^2/2\triangle a_z^2}\right)\left(e^{-a_{x_2}^2/2\triangle a_x^2} e^{-a_{z_2}^2/2\triangle a_z^2}\right) \\ &\times \left(e^{-(a_{x_2}-a_{x_1})^2/2\xi_{tx}^2} e^{-(a_{z_2}-a_{z_1})^2/2\xi_{tz}^2}\right), \end{aligned} \tag{4.114}$$

where the width $\triangle a_z$ defines $|a_z|_{max}$ and, similarly, $\triangle a_x$ determines $|a_x|_{max}$. ξ_{tx} and ξ_{tz} represent the transverse coherence lengths in the $\hat{\boldsymbol{a}}_x$ and $\hat{\boldsymbol{a}}_z$ direction, respectively. After evaluating the above Gaussian-Schell model source, one finds for eq. (4.112):

$$J_i(\boldsymbol{r}_1', \boldsymbol{r}_2') = \mathcal{A}_i(\boldsymbol{r}_1')\mathcal{A}_i(\boldsymbol{r}_2')\ j_i(\boldsymbol{r}_2' - \boldsymbol{r}_1')\ \phi(\boldsymbol{r}_1', \boldsymbol{r}_2'). \tag{4.115}$$

with

$$\mathcal{A}_i(\boldsymbol{r}'_1) = \sqrt{I_0 \, \frac{\triangle a_x \triangle a_y}{\sin\alpha_{\rm i} \; \Sigma_x \Sigma_y}} \; e^{-x'^2_1/2\Sigma^2_x} \; e^{-y'^2_1/2\Sigma^2_y} \; , \tag{4.116a}$$

$$\mathcal{A}_i(\boldsymbol{r}'_2) = \sqrt{I_0 \, \frac{\triangle a_x \triangle a_y}{\sin\alpha_{\rm i} \; \Sigma_x \Sigma_y}} \; e^{-x'^2_2/2\Sigma^2_x} \; e^{-y'^2_2/2\Sigma^2_y} \; , \tag{4.116b}$$

$$j_i(\boldsymbol{r}'_2 - \boldsymbol{r}'_1) = e^{-(x'_2 - x'_1)^2/2\Xi^2_{tx}} \; e^{-(y'_2 - y'_1)^2/2\Xi^2_{ty}} \; , \tag{4.116c}$$

$$\phi(\boldsymbol{r}'_1, \boldsymbol{r}'_2) = e^{-i\kappa_a \frac{\triangle a^2_x}{\Sigma^2_x}(x'^2_2 - x'^2_1)} \; e^{-i\kappa_a \frac{\triangle a^2_y}{\Sigma^2_y}(y'^2_2 - y'^2_1)} . \tag{4.116d}$$

The transverse coherence length $\Xi_{tx,ty}$ and the width $\Sigma_{x,y}$ on the sample surface plane are

$$\Sigma_x = \sqrt{\triangle a^2_x + 2\left(\frac{L_a}{\bar{k}_0}\right)^2 \left(\frac{1}{2\triangle a^2_x} + \frac{1}{\xi^2_{tx}}\right)} \; , \tag{4.117a}$$

$$\Sigma_y = \frac{1}{\sin\alpha_{\rm i}} \sqrt{\triangle a^2_z + 2\left(\frac{L_a}{\bar{k}_0}\right)^2 \left(\frac{1}{2\triangle a^2_z} + \frac{1}{\xi^2_{tz}}\right)} \; , \tag{4.117b}$$

$$\Xi_{tx} = \sqrt{\xi^2_{tx}\left[1 + \left(\frac{L_a}{\bar{k}_0 \triangle a^2_x}\right)^2\right] + 2\left(\frac{L_a}{\bar{k}_0 \triangle a_x}\right)^2} \; , \tag{4.117c}$$

$$\Xi_{ty} = \frac{1}{\sin\alpha_{\rm i}} \sqrt{\xi^2_{tz}\left[1 + \left(\frac{L_a}{\bar{k}_0 \triangle a^2_z}\right)^2\right] + 2\left(\frac{L_a}{\bar{k}_0 \triangle a_z}\right)^2} \; , \tag{4.117d}$$

The solution for the incident mutual intensity function may be interpreted as a partially coherence beam footprint on the sample surface. This beam footprint is only stretch in the y' direction as $\alpha_{\rm i}$ decreases, thus the $(\sin\alpha_{\rm i})$-term in (4.117b) and (4.117d) appears only in the y' direction. Next, we give the surface sensitive approximated expression for the longitudinal resolution function, namely

$$\mathcal{G}_l(\boldsymbol{r}'_2 - \boldsymbol{r}'_1) = \frac{c}{\sqrt{2\pi}\xi_l} \; e^{-[\hat{\boldsymbol{q}}\cdot(\boldsymbol{r}'_2 - \boldsymbol{r}'_1)]^2/2\xi^2_l} \; , \tag{4.118}$$

which holds for

$$\left| \frac{x'z'}{\xi^2_l} \cos\alpha_{\rm f} \sin\varphi(\sin\alpha_{\rm i} + \sin\alpha_{\rm f}) \right|_{max} \ll 1 \; , \tag{4.119a}$$

$$\left| \frac{y'z'}{\xi^2_l} (\cos\alpha_{\rm i} - \cos\alpha_{\rm f}\cos\varphi)(\sin\alpha_{\rm i} + \sin\alpha_{\rm f}) \right|_{max} \ll 1, \tag{4.119b}$$

$$\left| \frac{z'^2}{2\xi^2_l} (\sin\alpha_{\rm i} + \sin\alpha_{\rm f})^2 \right|_{max} \ll 1 \; . \tag{4.119c}$$

The maximum values for x' and y' can be estimated with help of the Gaussian-Schell source model. For instance, the maximum illuminated sample area can be estimated by Σ_x and Σ_y, which therefore also define the maximum values for the surface in-plane coordinates. A reasonable estimate may be obtained from the half width of the Gaussian function $\mathcal{A}_i(\boldsymbol{r}')$ at $1/e$, hence $|x'|_{max} \approx \sqrt{2}\Sigma_x$ and $|y'|_{max} \approx \sqrt{2}\Sigma_y$.

Finally, one finds for the surface sensitive pre-sample Fresnel factor:

$$f_a(\boldsymbol{r}'_1, \boldsymbol{r}'_2) = e^{i\kappa_a\left[\left(\boldsymbol{r}'^2_2-(\boldsymbol{r}'_2\cdot\hat{\boldsymbol{k}}_\mathrm{i})^2\right)-\left(\boldsymbol{r}'^2_1-(\boldsymbol{r}'_1\cdot\hat{\boldsymbol{k}}_\mathrm{i})^2\right)\right]}\,, \tag{4.120}$$

for

$$\left|\frac{\bar{k}_0}{L_a}y'z'\sin\alpha_\mathrm{i}\cos\alpha_\mathrm{i}\right|_{max} \ll 1\,, \tag{4.121a}$$

$$\left|\frac{\bar{k}_0}{2L_a}z'^2\cos^2\alpha_\mathrm{i}\right|_{max} \ll 1\,, \tag{4.121b}$$

and the after-sample Fresnel factor can be reduced to

$$f_b(\boldsymbol{r}'_1, \boldsymbol{r}'_2) = e^{i\kappa_b\left[\left(\boldsymbol{r}'^2_2-(\boldsymbol{r}'_2\cdot\hat{\boldsymbol{k}}_\mathrm{f})^2\right)-\left(\boldsymbol{r}'^2_1-(\boldsymbol{r}'_1\cdot\hat{\boldsymbol{k}}_\mathrm{f})^2\right)\right]}\,, \tag{4.122}$$

for

$$\left|\frac{\bar{k}_0}{L_b}x'z'\sin\alpha_\mathrm{f}\cos\alpha_\mathrm{f}\sin\varphi\right|_{max} \ll 1\,, \tag{4.123a}$$

$$\left|\frac{\bar{k}_0}{L_b}y'z'\sin\alpha_\mathrm{f}\cos\alpha_\mathrm{f}\cos\varphi\right|_{max} \ll 1\,, \tag{4.123b}$$

$$\left|\frac{\bar{k}_0}{2L_b}z'^2\cos^2\alpha_\mathrm{f}\right|_{max} \ll 1\,. \tag{4.123c}$$

With the above approximations we can replace eq. (4.102) by the following reduces resolution function

$$\mathcal{G}(\boldsymbol{r}'_1, \boldsymbol{r}'_2) = \frac{1}{L_b^2}f_a(\boldsymbol{r}'_1, \boldsymbol{r}'_2)f_b(\boldsymbol{r}'_1, \boldsymbol{r}'_2)\mathcal{G}_l(\boldsymbol{r}'_2 - \boldsymbol{r}'_1)J_i(\boldsymbol{r}'_1, \boldsymbol{r}'_2)\,, \tag{4.124}$$

which affects only the surface in-plane coordinates, i.e. $\boldsymbol{r}' = (x', y')$.

We will finally illustrate the above approximations with experimental parameters which are relatively common in XICS measurements, see Tab.4.1. To evaluate the validity of the above inequalities, we will consider a maximum z'-value of 100Å. The maximum values for a_x and a_z are based on the relations $|a_x|_{max} \approx \sqrt{2}\triangle a_x \approx \sqrt{2}(w_x/\sqrt{8})$ and $|a_z|_{max} \approx \sqrt{2}\triangle a_z \approx \sqrt{2}(w_z/\sqrt{8})$, where $w_x = w_z = 20\mu$m defines the width of a square slit with a symmetrical opening of 20μm. The maximum surface in-plane coordinates are deduced from$|x'|_{max} \approx \sqrt{2}\Sigma_x$ and $|y'|_{max} \approx \sqrt{2}\Sigma_y$.

Table 4.1: Verification of the surface sensitive approximations with an ordinary set of experimental parameters.

(secondary) source parameters & scattering geometry	incident beam conditions	inequalities & numerical results	
$\bar{\lambda}_0$=1.55Å^{-1}		(4.113)	$4.05 \cdot 10^{-3}$
$\xi_l = (0.01 - 1)\mu$m			
$\xi_{tx} = 10\mu$m	$\Xi_{tx} \approx 10.6\mu$m	(4.119a)	0
$\xi_{tz} = 100\mu$m	$\Xi_{ty} \approx 59.0$mm	(4.119b)	$(253. - 2.53) \cdot 10^{-15}$
$\triangle a_x \approx w_x/\sqrt{8} \approx 7.1\mu$m	$\Sigma_x \approx 7.5\mu$m	(4.119c)	$(13707. - 1.37) \cdot 10^{-9}$
$\triangle a_z \approx w_z/\sqrt{8} \approx 7.1\mu$m	$\Sigma_y \approx 4.2$mm		
		(4.121a)	$8.35 \cdot 10^{-3}$
$L_a = 0.5$m		(4.121b)	$4.05 \cdot 10^{-6}$
$L_b = 1.5$m			
$\alpha_{\mathrm{i}} = 0.1^\circ$		(4.123a)	0
$\alpha_{\mathrm{f}} = 0.2^\circ$		(4.123b)	$5.57 \cdot 10^{-3}$
$\varphi = 0^\circ$		(4.123c)	$1.35 \cdot 10^{-6}$

Chapter 5

X-ray Intensity Correlation Spectroscopy from Fluid Surfaces

In the previous chapters we have discussed the diffraction of partially coherent X-rays from arbitrary static structures. The resulting interference pattern from static objects is evidently also static and can, in general, reveal information about the static properties of the scatterer. We will next consider dynamic scatterers such as fluctuating charge distributions. In analogy to a static diffraction experiment, one obtains again an interference pattern, which will, however, vary in time as the sample undergoes different states in time. An example for such a diffraction pattern would be a fluctuating random speckle pattern, which is considered in the following discussion. The analysis of such time dependent diffraction patterns can reveal dynamic properties of the scattering medium, provided the irregular fluctuations of the optical field play a minor role, or if they are properly taken into account in the analysis.

The theoretical understanding of such random interference patterns is based on statistical methods, that consider the coherence of the X-ray field, as well as the fluctuations associated with the scatterer. In general, the observation and analysis of random speckle-like interference pattern, from a rough surface or an inhomogeneous medium, belongs to the subject of photon correlation spectroscopy (PCS). With the 3rd generation of synchrotron sources a sufficiently coherent X-ray beam is produced, that enriches this technique with X-ray intensity correlation spectroscopy (XICS) which is also known as X-ray photon correlation spectroscopy (XPCS). Since the first observations of speckle pattern, obtained with X-ray beams [97, 51, 16], XICS has become a field of growing interest. The principal idea of these experiments is, that a sample is illuminated with coherent X-rays which yield a dynamic speckle-

like interference pattern. It is then assumed, that the time autocorrelation of the scattered intensity at points in the fluctuating speckle pattern refers to the characteristic time scale of the sample. In comparison to a well stabilized laser, synchrotron sources generate poorly coherent beams [74, 96] and it may, therefore, be expected that this speckle pattern is somehow affected by the coherence properties of the X-ray beam.

However, the interesting advantage of X-ray intensity correlation spectroscopy lies in the possibility of observing slow dynamic properties of the scattering medium on sub-micron length scales [79]. The accessible experimental length and time scales in XICS experiments is illustrated and compared to other scattering methods in Fig.5.1. By combining XICS with grazing incident scattering geometries, such as grazing incident diffraction (GID), one of the most advanced technique is available to investigate fluctuating soft-matter surfaces, which provides an enhanced sensitivity to the surface fluctuations rather than to the bulk dynamics [68]. Due to these promising advantages, surface sensitive XICS has become an increasingly used technique in soft-matter surface science [85, 44, 88, 36, 55].

At this stage, it is worth recapitulating the commonly observable quantity in X-ray intensity correlation experiments, which is the correlation of the X-ray intensity $I(\mathbf{r}_1, t_1)$ at time t_1 and position $\mathbf{r}_1$ with the intensity $I(\mathbf{r}_2, t_2)$ at a later time t_2 and different position $\mathbf{r}_2$. The positions $\mathbf{r}_1$ and $\mathbf{r}_2$ represent two detection points in the speckle pattern. Hence, the measured quantity is the intensity correlation function

$$G_2(\mathbf{r}_1, \mathbf{r}_2, \tau) = \langle I(\mathbf{r}_1, t_1) I(\mathbf{r}_2, t_2) \rangle \,, \tag{5.1}$$

integrated over all possible positions $\mathbf{r}_1$ and $\mathbf{r}_2$ within the finite detector area. Here $\tau = t_2 - t_1$ is the time delay between the observations and the angular brackets denote a time average over the measured intensities. Alternatively, one can represent the intensity correlation function $G_2(\mathbf{r}_1, \mathbf{r}_2, \tau)$ with the aid of the scattered fields, as

$$G_2(\mathbf{r}_1, \mathbf{r}_2, \tau) = \langle U^*(\mathbf{r}_1, t_1) U(\mathbf{r}_1, t_1) U^*(\mathbf{r}_2, t_2) U(\mathbf{r}_2, t_2) \rangle \,, \tag{5.2}$$

in which $U(\mathbf{r}, t)$ is a complex scalar representation of the electric field and the asterisk symbol denotes the complex conjugated field. In expression (5.1) and (5.2) it has been implicity assumed that the fluctuations of the fields are statistically stationary in time, hence the $G_2(\mathbf{r}_1, \mathbf{r}_2, \tau)$ function depends only on time differences.

In the following sections we will discuss the theoretical description of surface sensitive X-ray intensity correlation spectroscopy from gaussian fluctuating liquid surfaces. The rigorous incorporation of the fluctuating surface properties

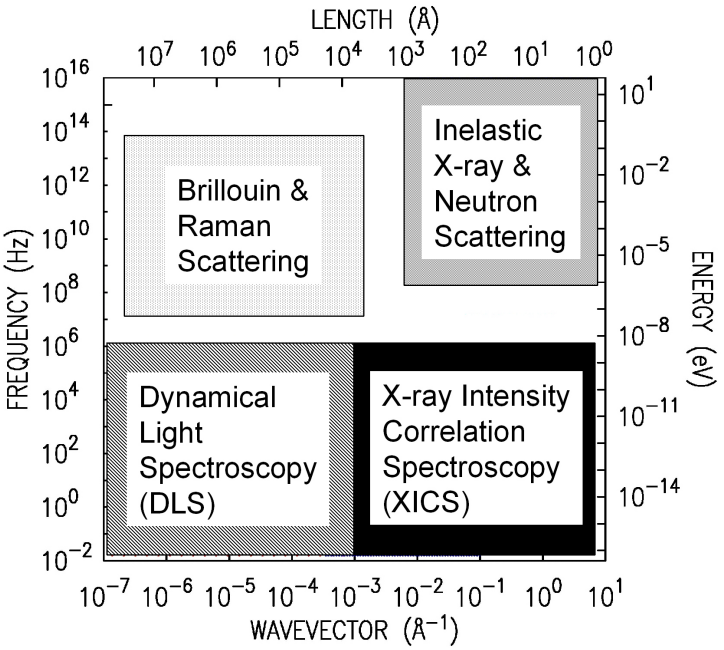

Figure 5.1: The accessible experimental length and time scales in XICS experiments is illustrated in comparison to other inelastic and quasi-elastic scattering methods (figure taken from G. Grübel [35]). The methods distinguish from another in energy and wave vector transfers and, therefore, in the detectable time and length scales of the sample under study. Due to the short wave length of X-rays, XICS yields naturally a larger wave vector transfer than DLS, hence it allows the study on shorter length scales. The small energy transfer in XICS and DLS results from quasi-elastic scattering, thus the detectable time scales are typically larger compared to inelastic scattering methods.

and the influences due to the partial coherence of the synchrotron source are the main subject of this chapter. To avoid further complications in this chapter, we will discuss this matter in the first Born approximation and consider the Siegert relation, in form of eq. (5.25), to be a priori true. At a later stage we will provide an intensity correlation function which will not be based on Siegert's relation. In section 5.1 we will first derive the scattered X-ray field from inhomogeneous media, which enables us to construct the intensity or field correlation function. The derivation of the field expression will be based on field equations obtained from Maxwell's equations. In section 5.2.1 we will derive a general form for the field correlation function that includes the spatial coherence of the X-ray source and instrumental resolution. These effects are

taken into account within the second-order coherence theory of classical scalar wave fields [58]. The subsection 5.2.2 to 5.2.4 are dedicated to surface sensitive XICS experiments, where we will specify the field correlation function from Gaussian fluctuating surfaces. In subsection 5.2.5 we illustrate the numerical results for the intensity correlation function from liquid surfaces (water and glycerol) for different spatial coherence and resolution conditions. Although, the discussions in the subsections of 5.2 are entirely based on Siegert's relation, we will find an intensity correlation expression, which provides a constructive physical interpretation for surface sensitive XICS experiments from fluid surfaces. The last section **??** eventually deals in detail with the derivation of intensity correlation functions, which will not be based the Siegert relation.

5.1 Scattering from Non-Static Media

The theoretical problem of determining intensity or field correlation functions lies, at the first stage, in the specifications of the fluctuating scattered electric field. For this purpose, one relies on the appropriate macroscopic Maxwell equations, which can provide a solution for the deterministic scattered electric field. At a later stage, one may still incorporate the statistical nature of the field into the deterministic formulas and consider adapted scalar expressions. In the following proceeding we will largely make use of the analysis that is given by Wolf and Foley [107] and also Carter [17].

Let us recall the source-free macroscopic Maxwell equations for nonmagnetic media. The deterministic (real) electric field $\mathbf{E}(\mathbf{r},t)$ and magnetic field $\mathbf{H}(\mathbf{r},t)$ then satisfy the following equations

$$\nabla\times\mathbf{E}(\mathbf{r},t) = -\frac{1}{c}\frac{\partial\mathbf{H}(\mathbf{r},t)}{\partial t}\,, \tag{5.3a}$$

$$\nabla\times\mathbf{H}(\mathbf{r},t) = \frac{1}{c}\frac{\partial\mathbf{E}(\mathbf{r},t)}{\partial t} + \frac{4\pi}{c}\frac{\partial\mathbf{P}(\mathbf{r},t)}{\partial t}\,, \tag{5.3b}$$

$$\nabla\cdot\mathbf{E}(\mathbf{r},t) = -4\pi\nabla\cdot\mathbf{P}(\mathbf{r},t)\,, \tag{5.3c}$$

$$\nabla\cdot\mathbf{H}(\mathbf{r},t) = 0\,, \tag{5.3d}$$

where $\mathbf{P}(\mathbf{r},t)$ is the induced polarization of the medium. In order to obtain a familiar wave equation from the Maxwell equations (5.3a-d), with respect to the electric field, one can proceed to apply the curl of (5.3a) and substitute its result in (5.3b). After eliminating the field $\mathbf{H}(\mathbf{r},t)$ in (5.3b) and using the vector identity $\nabla\times(\nabla\times\mathbf{E}) = \nabla\cdot(\nabla\cdot\mathbf{E}) - \Delta\mathbf{E}$ including (5.3c), one obtains the following inhomogeneous wave equation

$$\Delta\mathbf{E}(\mathbf{r},t) - \frac{1}{c^2}\frac{\partial^2\mathbf{E}(\mathbf{r},t)}{\partial t^2} = -4\pi\left[\nabla\cdot(\nabla\cdot\mathbf{P}(\mathbf{r},t)) - \frac{1}{c^2}\frac{\partial^2\mathbf{P}(\mathbf{r},t)}{\partial t^2}\right]. \tag{5.4}$$

If the total strength of the electric field $\mathbf{E}(\mathbf{r},t)$ is expressed as the sum of the incident field $\mathbf{E}_i(\mathbf{r},t)$ plus the scattered field $\mathbf{E}_s(\mathbf{r},t)$ and if, furthermore, the scattering from the medium is sufficiently weak, then eq. (5.4) becomes [17]

$$\Delta\mathbf{E}_s(\mathbf{r},t) - \frac{1}{c^2}\frac{\partial^2\mathbf{E}_s(\mathbf{r},t)}{\partial t^2} = -4\pi\left[\nabla\cdot(\nabla\cdot\mathbf{P}_1(\mathbf{r},t)) - \frac{1}{c^2}\frac{\partial^2\mathbf{P}_1(\mathbf{r},t)}{\partial t^2}\right]. \quad (5.5)$$

where $\mathbf{P}_1(\mathbf{r},t)$ refers to the induced polarization with respect to the incident field $\mathbf{E}_i(\mathbf{r},t)$. Solutions of eq. (5.5) provide a scattered field which is of the accuracy of the well-know first Born approximation. The explicit form of the polarization vector, for a causally responding isotropic media, is given as [107, 58]

$$\mathbf{P}_1(\mathbf{r},t) = \frac{1}{2\pi}\int_0^\infty \chi(\mathbf{r},t;t_0)\mathbf{E}_i(\mathbf{r},t-t_0)\,dt_0\,, \quad (5.6)$$

where $\chi(\mathbf{r},t;t_0)$ is, with regard to the time dependence, a two-parameter dielectric susceptibility function. The first time argument t of the generalized dielectric susceptibility refers to deterministic or random changes of the local macroscopic properties, such as the electron density distribution. While the second time variable t_0 is related to the optical transition times between atomic states, hence t_0 depends on the frequency ω_0 of the incident field. It should be borne in mind, that the response of $\chi(\mathbf{r},t;t_0)$ to the incident field will be, in general, on a much shorter time-scale for the second time variable in comparison to the first one. By taking advantage of the Fourier relation between $\chi(\mathbf{r},t;t_0)$ and $\widehat{\chi}(\mathbf{r},t;\omega_0)$ with regard to the second time variable

$$\widehat{\chi}(\mathbf{r},t;\omega_0) = \frac{1}{2\pi}\int_0^\infty \chi(\mathbf{r},t;t_0)\,e^{i\omega_0 t_0}\,dt_0\,, \quad (5.7)$$

we can express eq. (5.6) in a practicable alternative form, which is

$$\mathbf{P}_1(\mathbf{r},t) = \int_{-\infty}^\infty \widehat{\chi}(\mathbf{r},t;\omega_0)\widetilde{\mathbf{E}}_i(\mathbf{r},\omega_0)\,e^{-i\omega_0 t}\,d\omega_0\,. \quad (5.8)$$

Let us next use (5.8) to simplify the right-hand side of eq. (5.5), one then finds for the first term

$$\nabla\cdot(\nabla\cdot\mathbf{P}_1(\mathbf{r},t)) = \nabla\cdot\int_{-\infty}^\infty d\omega_0\,e^{-i\omega_0 t} \times\left[\nabla\widehat{\chi}(\mathbf{r},t;\omega_0)\cdot\widetilde{\mathbf{E}}_i(\mathbf{r},\omega_0) + \widehat{\chi}(\mathbf{r},t;\omega_0)\nabla\cdot\widetilde{\mathbf{E}}_i(\mathbf{r},\omega_0)\right]. \quad (5.9)$$

Since the incident field is source free, i.e. $\nabla\cdot\mathbf{E}_i(\mathbf{r},t) = 0$, the second term in the integrand of eq. (5.9) vanishes. For the two times derivative of the polarization

vector, we obtain

$$\frac{\partial^2 \mathbf{P}_1(\mathbf{r},t)}{\partial t^2} = \int_{-\infty}^{\infty} d\omega_0 \; e^{-i\omega_0 t}\, \widetilde{\mathbf{E}}_i(\mathbf{r},\omega_0) \times \left[\frac{\partial^2 \widehat{\chi}(\mathbf{r},t;\omega_0)}{\partial t^2} - i2\omega_0 \frac{\partial \widehat{\chi}(\mathbf{r},t;\omega_0)}{\partial t} - \omega_0^2 \widehat{\chi}(\mathbf{r},t;\omega_0) \right]. \quad (5.10)$$

At next we consider in (5.10) an incident field with a restricted bandwidth of high frequencies. If, within this frequency band, the local properties of the dielectric susceptibility change slowly in time, then the third term, i.e. $\omega_0^2 \widehat{\chi}(\mathbf{r},t;\omega_0)$, will increasingly dominate in the integrant of eq. (5.11) for high frequencies of the incident field [17]. This quasi-static condition for the scattering medium, requirement only that the frequencies ω of the (fluctuating) medium are small relatively to the electric field frequencies ω_0. By substituting (5.9) and (5.10) into eq. (5.5) and making use of the source free and quasi-static requirements, we find the following wave equation

$$\Delta \mathbf{E}_s(\mathbf{r},t) - \frac{1}{c^2}\frac{\partial^2 \mathbf{E}_s(\mathbf{r},t)}{\partial t^2} = -4\pi \int_{-\infty}^{\infty} d\omega_0 \; e^{-i\omega_0 t}\, \widetilde{\mathbf{E}}_i(\mathbf{r},\omega_0) \times \left[\Delta \widehat{\chi}(\mathbf{r},t;\omega_0) + \frac{\omega_0^2}{c^2} \widehat{\chi}(\mathbf{r},t;\omega_0) \right], \quad (5.11)$$

If we assume, in addition, that the spatial properties of the dielectric susceptibility change also slowly in space, then the dominating term in the integrant of eq. (5.11) will conclusively be again $\omega_0^2 \widehat{\chi}(\mathbf{r},t;\omega_0)$. We address the above requirements with regard to incident field spectrum and scatterer as the quasi-static and quasi-homogeneous conditions. It is worth noting that for a narrow band X-ray field the above requirements are for all practical purposes sufficiently well realized. With the above arguments we may eventually approximate eq. (5.5) by

$$\Delta \mathbf{E}_s(\mathbf{r},t) - \frac{1}{c^2}\frac{\partial^2 \mathbf{E}_s(\mathbf{r},t)}{\partial t^2} = -4\pi \mathbf{f}(\mathbf{r},t)\,, \quad (5.12a)$$

where

$$\mathbf{f}(\mathbf{r},t) = \int_{-\infty}^{\infty} d\omega_0 \; \frac{\omega_0^2}{c^2}\, \widehat{\chi}(\mathbf{r},t;\omega_0) \widetilde{\mathbf{E}}_i(\mathbf{r},\omega_0)\, e^{-i\omega_0 t}\,. \quad (5.12b)$$

Alternatively, one can express eq. (5.12a,b) in the frequency-time domain by taking its Fourier transform, hence

$$\Delta \widetilde{\mathbf{E}}_s(\mathbf{r},\omega) + k^2 \widetilde{\mathbf{E}}_s(\mathbf{r},\omega) = -4\pi \widetilde{\mathbf{f}}(\mathbf{r},\omega)\,, \quad (5.13a)$$

with

$$\widetilde{\mathbf{f}}(\mathbf{r},\omega) = \int_{-\infty}^{\infty} d\omega_0 \; \frac{\omega_0^2}{c^2}\, \widetilde{\chi}(\mathbf{r},\omega-\omega_0;\omega_0) \widetilde{\mathbf{E}}_i(\mathbf{r},\omega_0)\,, \quad (5.13b)$$

and

$$k = \omega/c\,. \tag{5.14}$$

The wave equations (5.12a) and (5.13a) hold for narrow-band incident electric fields, that are scattered weakly by a nonmagnetic, isotopical, quasi-homogenous and quasi-static medium. The conditions of weak scattering are incorporated in terms of the first order Born approximation. Due to the assumption of an isotopic and quasi-homogenous dielectric susceptibility we may further ignore the vectorial character of the electric field and use the scalar representation $\widetilde{U}(\mathbf{r},\omega)$ in place of the electric fields $\widetilde{\mathbf{E}}(\mathbf{r},\omega)$ [34]. By using the scalar field representation $\widetilde{U}(\mathbf{r},\omega)$, we finally obtain from eq. (5.13a,b) the following scalar wave equation

$$\Delta\widetilde{U}_s(\mathbf{r},\omega) + k^2\widetilde{U}_s(\mathbf{r},\omega) = -4\pi\int_{-\infty}^{\infty} d\omega_0\,\widetilde{F}(\mathbf{r},\omega-\omega_0;\omega_0)\,\widetilde{U}_i(\mathbf{r},\omega_0)\,, \tag{5.15}$$

where

$$\widetilde{F}(\mathbf{r},\omega-\omega_0;\omega_0) = \frac{\omega_0^2}{c^2}\,\widetilde{\chi}(\mathbf{r},\omega-\omega_0;\omega_0)\,, \tag{5.16}$$

is a generalized optical potential. The above wave equation (5.15) comprises, in comparison to the well-know Helmholtz equation, the time dependent local properties of the scatterer. In the following analysis, we will use equation (5.15) to determine the time depending scattered field from deterministic fluctuating media in the first Born approximation. [1]

5.1.1 The Scattered Field in the First Born Approximation

To provide a solution for the scattered field $\widetilde{U}_s(\mathbf{r},\omega)$ one can apply the Green's method for inhomogeneous differential equations and use, in the case of eq. (5.15), the outgoing free-space Green's function of the Helmholtz operator [9]. By using this method, the solution in the space-frequency domain can be expressed in the following integral form

$$\widetilde{U}_s(\mathbf{r},\omega) = \int_V d^3\mathrm{r}'\,\frac{e^{ikR}}{R}\int_{-\infty}^{\infty} d\omega_0\;\widetilde{F}(\mathbf{r}',\omega-\omega_0;\omega_0)\,\widetilde{U}_i(\mathbf{r}',\omega_0)\,, \tag{5.17}$$

where the distance $R = |\mathbf{r}-\mathbf{r}'|$ is illustrated in Fig. 4.9. The solution for the scattered field in the space-time domain may be readily obtained, by taking the

[1] One can easily derive a wave equation which is structural wise of the same form as (5.15), but in dependent from the assumption of weak scattering.

Fourier transform of eq. (5.17) with respect to ω and using the shift theorem for Fourier transforms [13], this yields

$$U_s(\mathbf{r},t) = \int_V d^3\mathrm{r}' \; \frac{1}{R} \int_{-\infty}^{\infty} d\omega_0 \; e^{-i\omega_0(t-R/c)} \, \widehat{F}(\mathbf{r}', t - R/c; \omega_0) \, \widetilde{U}_i(\mathbf{r}', \omega_0) \, . \quad (5.18)$$

In order to obtain the scattered field for X-ray wavelengths it is necessary to specify the optical potential in eq. (5.18). For this purpose, it will be useful to recall the static relation between the index of refraction $\widehat{n}(\mathbf{r}', 0; \omega_0)$ and the dielectric susceptibility, namely

$$\widehat{\chi}(\mathbf{r}', 0; \omega_0) = [\widehat{n}^2(\mathbf{r}', 0; \omega_0) - 1]/4\pi \, . \quad (5.19)$$

The static index of refraction, for X-ray frequencies far above the highest resonance frequencies of the scattering medium, takes the form [42]

$$\widehat{n}^2(\mathbf{r}', 0; \omega_0) = 1 - 4\pi r_e \rho(\mathbf{r}') \, \frac{c^2}{\omega_0^2} \, , \quad (5.20)$$

where r_e represents the classical electron radius and $\rho(\mathbf{r})$ the electron density of the scatterer. In case of a time depending electron density we may simple re-write relation (5.20) as

$$\widehat{n}^2(\mathbf{r}', t; \omega_0) = 1 - 4\pi r_e \rho(\mathbf{r}', t) \, \frac{c^2}{\omega_0^2} \, , \quad (5.21)$$

where $\rho(\mathbf{r}', t) = \bar{\rho} + \triangle\rho(\mathbf{r}', t)$ is essentially determined by its mean equilibrium value $\bar{\rho}$ and the deviation $\triangle\rho(\mathbf{r}', t)$ from it. On substituting from eq. (5.21) into eq. (5.19) and using the relation (5.16), one can deduce the following expression for the generalized optical potential

$$\widehat{F}(\mathbf{r}', t; \omega_0) = -r_e \, \rho(\mathbf{r}', t) \, , \quad (5.22)$$

which becomes independent of the X-ray frequency. With eq. (5.22) and (5.18) we finally find the time depending scattered field for X-ray wavelengths, which is

$$U_s(\mathbf{r},t) = -r_e \int_V d^3\mathrm{r}' \; \frac{1}{R} \; \rho(\mathbf{r}', t - R/c) \int_{-\infty}^{\infty} d\omega_0 \; \widetilde{U}_i(\mathbf{r}', \omega_0) \, e^{-i\omega_0(t-R/c)} \, , \quad (5.23)$$

or equally

$$U_s(\mathbf{r},t) = -r_e \int_V d^3\mathrm{r}' \; \rho(\mathbf{r}', t - R/c) \, \frac{U_i(\mathbf{r}', t - R/c)}{R} \, . \quad (5.24)$$

As a result of eq. (5.22) the scattered field in (5.24) is temporally determined by an unfolded product of the electron density and the magnitude of the incident field at the retarded time $t-R/c$. The above equation is the main results in this section. It provides an explicit form for the time depending scattered field and enables one to formulate field or intensity correlation functions in the X-ray region. Although we have consider up to now real fields, it can readily be shown that a complex analytic representation of the real scalar electric field also obeys the above expression (5.24). Hence, we will treat in the following sections the incident and the scattered fields as complex analytical representations of the real fields.

5.2 Intensity Correlation Function Based on Siegert's Relation

The rigorous evaluation of eq. (5.2) in combination with the field expression (5.24) is, in general, a nontrivial task. One way to approach a solution for the intensity autocorrelation function eq. (5.2) is based on the statistical properties of the scattered electric field $U(\mathbf{r}, t)$. Within this popular approach one finds a relatively simple expressions for eq. (5.2). In the following sections, we will make use of this theoretical approach in order to describe surface sensitive XICS experiments.

The central assumption is here that the scattered electric fields are of zero mean and obey Gaussian statistics. Hence, one can apply the Gaussian moment theorem and describe the intensity correlation by field correlations [58]. Conclusively, eq. (5.2) transforms to

$$G_2(\mathbf{r}_1, \mathbf{r}_2, \tau) = \langle I(\mathbf{r}_1, t_1)\rangle\langle I(\mathbf{r}_2, t_2)\rangle + |G_1(\mathbf{r}_1, \mathbf{r}_2, \tau)|^2 \,, \tag{5.25}$$

where

$$G_1(\mathbf{r}_1, \mathbf{r}_2, \tau) = \langle U^*(\mathbf{r}_1, t_1)U(\mathbf{r}_2, t_2)\rangle \,, \tag{5.26}$$

represents the field correlation function. Due to the assumption of statistical stationarity, the average value of the intensity $\langle I(\mathbf{r}, t)\rangle = \langle U^*(\mathbf{r}, t)U(\mathbf{r}, t)\rangle$ is obviously independent of time and, therefore, identical with the static intensity. The above relation reduces, in the limit situation of a point detector, i.e $\mathbf{r}_1 \approx \mathbf{r}_2 = \mathbf{r}$, to the widely used (homodyne) Siegert relation [21, 18]

$$G_2(\mathbf{r}, \tau) = \langle I(\mathbf{r}, t)\rangle^2 + |G_1(\mathbf{r}, \tau)|^2 \,. \tag{5.27}$$

It should be noted that the validity of eq. (5.25) and (5.27) is based only on the Gaussian statistical properties of the scattered field. This assumption might

be justified, if the scatterer itself undergoes Gaussian fluctuations, however, in general it cannot be taken for granted that the scattered field is a Gaussian fluctuating quantity [56, 98, 21].

5.2.1 Propagation of Scattered Field Correlations From Fluctuating Media

In the following section we will discuss the scattering of partially coherent X-rays from media, whose physical properties are randomly fluctuating in space and time. For this purpose the electron density $\rho(\mathbf{r}', t)$ and the incident field $U_i(\mathbf{r}', t)$ in eq. (5.24) will be treated as two statistically independent and stationary fluctuating quantities of time. Since it is known, that the effects of partial coherence and instrumental resolution play a significant role in XICS measurements [36], we will primarily discuss below a formal generalization of the intensity correlation function, in order to take these effects into account. For sakes of simplicity, we will discuss this matter in terms of field correlation functions and demand here that the Siegert relation is fulfilled. However, the utilization of Siegert's relation yields only meaningful intensity correlation expression, if the incident field is treated as an ideal monochromatic field [56]. For that reason we will constraint the following discussion to the influences of spatial coherence and resolution effects on the intensity correlation function. A rigorous treatment of eq. (5.2) including the finite monochromaticity of X-ray beam will be discussed later.

Based on the requirement of statistical stationarity for the electron density and the incident field it can be deduced that the random fluctuations of the scattered field are equally stationary and, moreover, the scattered mutual coherence function, defined as

$$\Gamma_s(\mathbf{r}_1, \mathbf{r}_2, \tau) = \langle U_s^*(\mathbf{r}_1, t_1) U_s(\mathbf{r}_2, t_2) \rangle \,, \tag{5.28}$$

will consequently depend only on the time difference $\tau = t_2 - t_1$. Furthermore, the angular brackets can now denote either a time average or an ensemble average. If we make use of the right hand side of eq. (5.24) and the definition of the scattered mutual coherence function eq. (5.28), we find the following formula

$$\begin{aligned} \Gamma_s(\mathbf{r}_1, \mathbf{r}_2, \tau) = r_e^2 \iint_V d^3\mathrm{r}_1' d^3\mathrm{r}_2' \; & C_{\rho\rho}(\mathbf{r}_2', \mathbf{r}_1', \tau - (R_2 - R_1)/c) \\ & \times \frac{\Gamma_i(\mathbf{r}_1', \mathbf{r}_2', \tau - (R_2 - R_1)/c)}{R_1 R_2} \,, \end{aligned} \tag{5.29}$$

where

$$C_{\rho\rho}(\mathrm{r}_2', \mathrm{r}_1', \tau - (R_2 - R_1)/c) = \langle \rho(\mathrm{r}_1', t_1 - R_1/c) \rho(\mathrm{r}_2', t_2 - R_2/c) \rangle \,, \tag{5.30}$$

is the correlation function of the electron densities and $\Gamma_i(\mathrm{r}_1', \mathrm{r}_2', \tau-(R_2-R_1)/c)$ represents the retarded mutual coherence function of the incident fields. Formula (5.29) expresses the propagation of scattered field correlations in the space-time domain within the framework of the first Born approximation. The time behavior of the scattered field correlations depends, in comparison to the static propagation formula (4.74), on the temporal electron density fluctuations, as well as the incident field fluctuations. It should be clear that the scattered mutual coherence function can only reveal the sample dynamics, if the correlation time of the electron density fluctuations is much larger in comparison to the incident field correlation time. Since this condition is practically not fulfilled, we will consider below the idealized situation of a strictly monochromatic beam. (A useful discussion on the Siegert relation and the intrinsic difficulty of including the finite coherence time of the incident electric field can be found in Ref.[56].) Hence, eq. (5.29) reduces to [58, 9]

$$\Gamma_s(\mathrm{r}_1, \mathrm{r}_2, \tau) = r_e^2 \iint_V d^3\mathrm{r}_1' d^3\mathrm{r}_2' \; C_{\rho\rho}(\mathrm{r}_2', \mathrm{r}_1', \tau - (R_2 - R_1)/c) \times \frac{J_i(\mathrm{r}_1', \mathrm{r}_2')}{R_1 R_2} \, e^{-i\omega_0(\tau-(R_2-R_1)/c)} \,, \tag{5.31}$$

where $J_i(\mathrm{r}_1', \mathrm{r}_2')$ is the incident mutual intensity function. Note that eq. (5.31) still takes the the spatial coherence properties of the incident field into account. In order to specify the incident field properties at the sample, it will be useful to deduced their coherence characteristics from the field conditions at a pre-sample slit, which may be considered as a (secondary) radiation source.

Let the function $J_i(\mathrm{r}_1', \mathrm{r}_2')$, itself, be the resulting mutual intensity function of two fields, which radiate from a finite aperture A towards the scatterer. To describe the field correlations on the planar aperture area A, one may equally introduce a mutual intensity function $J_a(\boldsymbol{a}_1, \boldsymbol{a}_2)$, where $\boldsymbol{a}_1$ and $\boldsymbol{a}_2$ are the position vectors on the aperture plane A. The relation between the mutual intensity functions at the aperture and sample position can then be deduced from the Cittert-Zernike propagation law [58], viz.

$$J_i(\mathrm{r}_1', \mathrm{r}_2') = \iint_A d^2a_1 d^2a_2 \; J_a(\boldsymbol{a}_1, \boldsymbol{a}_2) \frac{e^{ik_0(R_2-R_1)}}{R_1 R_2} \Lambda_1^* \Lambda_2 \,, \tag{5.32}$$

where the inclination factors $\Lambda_{1,2}$ are of the form

$$\Lambda_{1,2} = i\frac{k_0}{2\pi} \cos\theta_{1,2} \,, \tag{5.33}$$

and $k_0 = \omega_0/c$ denotes the magnitude of the wave vector. On substituting

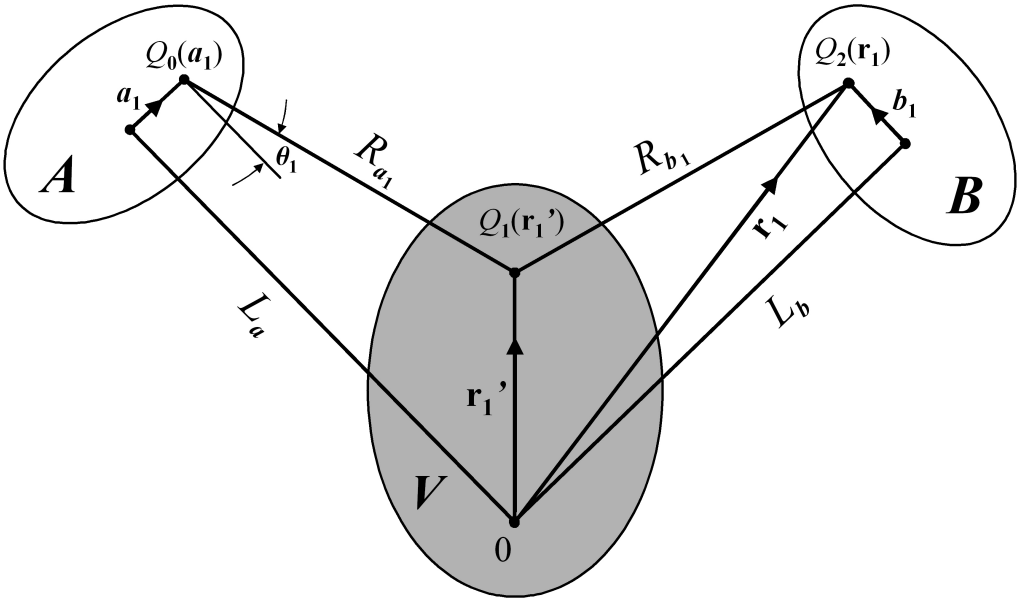

Figure 5.2: Illustration of the scattering geometry for a single ray. $Q_0(\boldsymbol{a}_1)$ represents a point on the planar aperture area A from where radiation spreads out under an angle θ_1, with regard to normal vector of the aperture plane. The distance from aperture to scatterer is given by R_{a_1}. The optical axis for a bunch of X-rays is represented by the mean incoming distance L_a and outgoing distance L_b. To emphasize the differences between pre-sample and after-sample paths, we use the notation R_{a_1} and R_{b_1}, respectively.

next the propagation law (5.32) into eq. (5.31) we obtain

$$\Gamma_s(\mathrm{r}_1,\mathrm{r}_2,\tau) = r_e^2\, e^{-i\omega_0\tau} \iint_V d^3\mathrm{r}_1' d^3\mathrm{r}_2'\; C_{\rho\rho}(\mathrm{r}_2',\mathrm{r}_1',\tau-(R_{b_2}-R_{b_1})/c)\,\frac{e^{ik_0(R_{b_2}-R_{b_1})}}{R_{b_1}R_{b_2}}$$
$$\times \iint_A d^2a_1 d^2a_2\; J_a(\boldsymbol{a}_1,\boldsymbol{a}_2)\,\frac{e^{ik_0(R_{a_2}-R_{a_1})}}{R_{a_1}R_{a_2}}\,\Lambda_1^*\Lambda_2\,. \tag{5.34}$$

To clarify the difference between the paths we have introduced the subscribe a for pre-sample path lengths R_{a_1}, R_{a_2} and distances from the scatterer to the detection positions are denoted by R_{b_1}, R_{b_2} in place of R_1, R_2. The exit angle θ_1 and the notation for one X-ray path is illustrated in Fig. 5.2.

We will next examine eq. (5.34) for some simplified considerations. Let us first replace the path lengths in the denominates of eq. (5.34) by their mean distances L_a and L_b, respectively. Furthermore, we neglect the short retardation times, i.e $(R_{2b}-R_{1b})/c$, in the electron density correlation function. To emphasize the connection to the Siegert relation we will, from now on, express the mutual coherence function $\Gamma_s(\mathrm{r}_1,\mathrm{r}_2,\tau)$ with the corresponding field

correlation function $G_1(\mathrm{r}_1, \mathrm{r}_2, \tau)$, hence eq. (5.34) yields

$$G_1(\mathrm{r}_1, \mathrm{r}_2, \tau)) = \left(\frac{r_e}{L_a L_b}\right)^2 e^{-i\omega_0\tau} \iint_V d^3\mathrm{r}_1' d^3\mathrm{r}_2'\, C_{\rho\rho}(\mathrm{r}_2', \mathrm{r}_1', \tau) \times \iint_A d^2a_1 d^2a_2\, J_a(\boldsymbol{a}_1, \boldsymbol{a}_2)\Lambda_1^*\Lambda_2 e^{ik_0\triangle l}, \tag{5.35}$$

with

$$\triangle l = (R_{a_2} - R_{a_1}) + (R_{b_2} - R_{b_1}) \tag{5.36}$$

being the total path difference between two X-rays, which are propagating from a finite slit area A via a scattering process towards different points on the detection plane B. With the field correlation function eq. (5.35) and the Siegert relation (5.25) we have finally obtained a formula for the intensity correlation function, which comprises the spatial coherency of the incident field and resolution effect due to the pre-sample aperture. It should be noted that the static intensity term in Siegert's relation (5.25) is nothing else than the field correlation function for identical detection points $\mathrm{r}_1 = \mathrm{r}_2 = \mathrm{r}$ and zero delay time $\tau = 0$. Accordingly $\langle I(\mathrm{r}, t)\rangle = G_1(\mathrm{r}, \mathrm{r}, 0)$ and eq. (5.25) can be fully determined from expression (5.35). Additional instrumental resolution effects due to a finite detector area B will be discussed at a later stage.

In the following sections we will specify the general form of eq. (5.35) and apply in particular the surface sensitive approximations of section 4.3.4.

5.2.2 Surface Sensitive XICS in first Born Approximation

Next, we will specify the scattering geometry and the electron density correlation function to describe XICS experiments from fluctuating surfaces, as it is schematically illustrated in Fig. 5.3. For a feasible use of eq. (5.35) one has to consider the X-ray path differences (5.36) in the Fraunhofer or Fresnel limit. Due to the short wavelength of X-rays the Fraunhofer requirements are experimentally difficult to accomplish and, for that reason, present XICS experiments are performed under Fresnel conditions. To account for the Fresnel limit we expand the total path length difference $\triangle l$ to the second order in $\mathbf{r}_1'/L_a$, $\mathbf{r}_2'/L_a$, $\mathbf{r}_1'/L_b$ and $\mathbf{r}_2'/L_b$, we then obtain from

$$\begin{aligned}\triangle l &= (R_{a_2} - R_{a_1}) + (R_{b_2} - R_{b_1}) \\ &= (|\mathbf{L}_a + \mathbf{r}_2' - \boldsymbol{a}_2| - |\mathbf{L}_a + \mathbf{r}_1' - \boldsymbol{a}_1|) + (|\mathbf{L}_b + \boldsymbol{b}_2 - \mathbf{r}_2'| - |\mathbf{L}_b + \boldsymbol{b}_1 - \mathbf{r}_1'|)\,,\end{aligned} \tag{5.37}$$

the approximation [91]

$$\begin{aligned}\triangle l \approx & -(\hat{\mathbf{k}}_\mathrm{f} - \hat{\mathbf{k}}_\mathrm{i}) \cdot (\mathbf{r}'_2 - \mathbf{r}'_1) \\ & -\frac{1}{L_a}(\boldsymbol{a}_2 \cdot \mathbf{r}'_2 - \boldsymbol{a}_1 \cdot \mathbf{r}'_1) + \frac{1}{2L_a}\left(\boldsymbol{a}_2^2 - \boldsymbol{a}_1^2\right) \\ & -\frac{1}{L_b}(\boldsymbol{b}_2 \cdot \mathbf{r}'_2 - \boldsymbol{b}_1 \cdot \mathbf{r}'_1) + \frac{1}{2L_b}\left(\boldsymbol{b}_2^2 - \boldsymbol{b}_1^2\right) \\ & +\frac{1}{2L_a}\Big[\left(\mathbf{r}_2'^2 - (\mathbf{r}'_2 \cdot \hat{\mathbf{k}}_\mathrm{i})^2\right) - \left(\mathbf{r}_1'^2 - (\mathbf{r}'_1 \cdot \hat{\mathbf{k}}_\mathrm{i})^2\right)\Big] \\ & +\frac{1}{2L_b}\Big[\left(\mathbf{r}_2'^2 - (\mathbf{r}'_2 \cdot \hat{\mathbf{k}}_\mathrm{f})^2\right) - \left(\mathbf{r}_1'^2 - (\mathbf{r}'_1 \cdot \hat{\mathbf{k}}_\mathrm{f})^2\right)\Big]\,, \end{aligned} \tag{5.38}$$

where we have neglected third order terms of $\boldsymbol{a}_1/L_a$, $\boldsymbol{a}_2/L_a$, $\boldsymbol{b}_1/L_b$ and $\boldsymbol{b}_2/L_b$. The notation and the explicit representations for the vectors are given in section 4.3.3. The path difference (5.38) is in comparison to expression (4.94) slightly generalized by the detector vector $\boldsymbol{b}$. To describe the detector vector $\boldsymbol{b}_1$ (and equally $\boldsymbol{b}_2$) in the sample coordinate system, we will use the following vector representation

$$\boldsymbol{b}_1 = b_{x_1}\hat{\boldsymbol{b}}_x + b_{z_1}\hat{\boldsymbol{b}}_z\ , \tag{5.39}$$

where

$$\hat{\boldsymbol{b}}_x = \begin{pmatrix} \cos\varphi \\ -\sin\varphi \\ 0 \end{pmatrix} \qquad \text{and} \qquad \hat{\boldsymbol{b}}_z = \begin{pmatrix} \sin\alpha_\mathrm{f}\sin\varphi \\ -\sin\alpha_\mathrm{f}\cos\varphi \\ \cos\alpha_\mathrm{f} \end{pmatrix} \tag{5.40}$$

are unit stretch vectors. The vectorial relations between the vectors $\boldsymbol{a}_1$, $\boldsymbol{b}_1$ and sample vector $\mathbf{r}'_1$ are explicitly clarified in Fig. 5.3. On using the relation between the frequency and the magnitude of the wave vector and also the nominal wave vector transfer $\mathbf{q} = k_0(\hat{\mathbf{k}}_\mathrm{f} - \hat{\mathbf{k}}_\mathrm{i})$, one readily finds

$$\begin{aligned} k_0\triangle l = & -\mathbf{q} \cdot (\mathbf{r}'_2 - \mathbf{r}'_1) \\ & -2\kappa_a(\boldsymbol{a}_2 \cdot \mathbf{r}'_2 - \boldsymbol{a}_1 \cdot \mathbf{r}'_1) + \kappa_a\left(\boldsymbol{a}_2^2 - \boldsymbol{a}_1^2\right) \\ & -2\kappa_b(\boldsymbol{b}_2 \cdot \mathbf{r}'_2 - \boldsymbol{b}_1 \cdot \mathbf{r}'_1) + \kappa_b\left(\boldsymbol{b}_2^2 - \boldsymbol{b}_1^2\right) \\ & +\kappa_a\Big[\left(\mathbf{r}_2'^2 - (\mathbf{r}'_2 \cdot \hat{\mathbf{k}}_\mathrm{i})^2\right) - \left(\mathbf{r}_1'^2 - (\mathbf{r}'_1 \cdot \hat{\mathbf{k}}_\mathrm{i})^2\right)\Big] \\ & +\kappa_b\Big[\left(\mathbf{r}_2'^2 - (\mathbf{r}'_2 \cdot \hat{\mathbf{k}}_\mathrm{f})^2\right) - \left(\mathbf{r}_1'^2 - (\mathbf{r}'_1 \cdot \hat{\mathbf{k}}_\mathrm{f})^2\right)\Big]\,, \end{aligned} \tag{5.41}$$

where we have used the definitions

$$\kappa_a = \frac{k_0}{2L_a} \qquad \text{and} \qquad \kappa_b = \frac{k_0}{2L_b}\,. \tag{5.42}$$

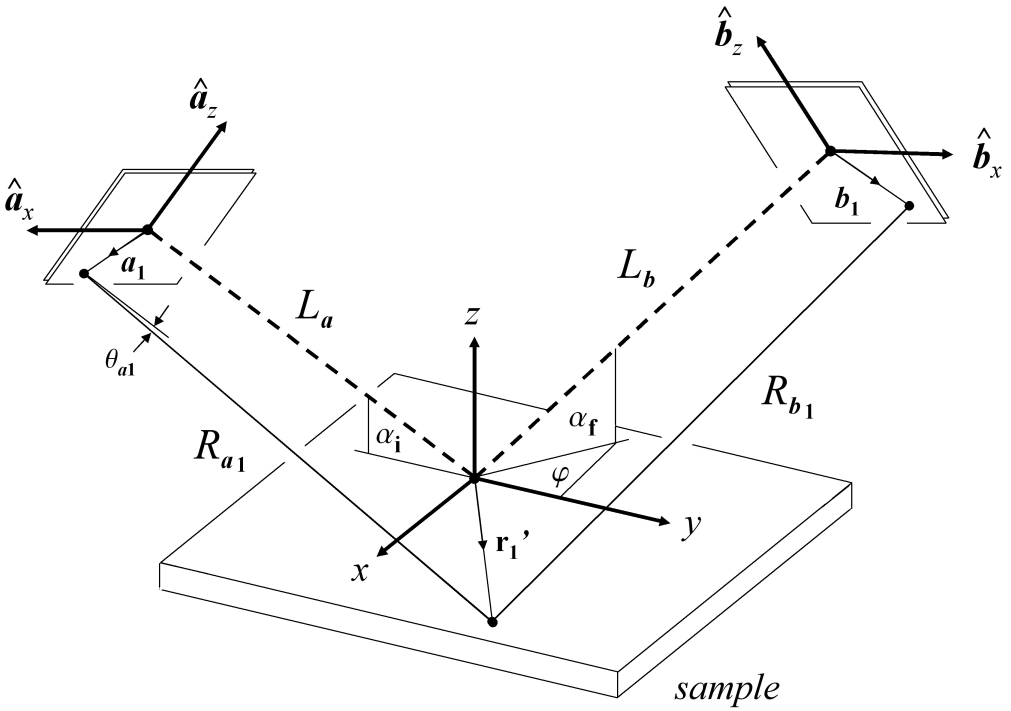

Figure 5.3: Illustration of the surface scattering geometry and notation for a single ray. The propagation path is described through the mean directional vectors $\mathbf{k}_\mathrm{i}$ and $\mathbf{k}_\mathrm{f}$. The aperture vectors $\boldsymbol{a}_1$, $\boldsymbol{b}_1$ and sample vector $\mathbf{r}'_1$ are all defined in the sample coordinate system (x, y, z). The z direction is chosen to be perpendicular to the mean sample surface, x and y are the surface in-plane components. The mean incident direction of the X-rays is describe by the angle α_i and the scattering direction is given by the angle α_f and the out of incident plane angle φ.

In the case of surface sensitive scattering geometries (see section 4.3.4) one may consider a surface restricted path length difference $\triangle l$, which is to a great extant independent from z'-components. According to the discussion in section 4.3.4, one may neglect the z'-components of the vector products $\boldsymbol{a}_1 \cdot \mathbf{r}'_1$ and $\boldsymbol{a}_2 \cdot \mathbf{r}'_2$ if the pre-sample aperture vectors are sufficiently small. Similarly, we may neglect the z'-components of the vector products $\boldsymbol{b}_1 \cdot \mathbf{r}'_1$ and $\boldsymbol{b}_2 \cdot \mathbf{r}'_2$, if the following condition holds

$$\left| \frac{k_0}{2L_b} b_z z' \cos\alpha_\mathrm{f} \right|_{max} \ll 1 \ . \tag{5.43}$$

Since the above requirements describe sufficiently the conditions for present surface sensitive XICS experiments, we can replace eq. (5.41) by

$$\begin{aligned} k_0 \triangle l = & -\boldsymbol{q}\cdot(\boldsymbol{r}_2' - \boldsymbol{r}_1') - q_z(z_2' - z_1') \\ & - 2\kappa_a(\mathbf{a}_2\cdot\boldsymbol{r}_2' - \mathbf{a}_1\cdot\mathbf{r}_1') + \kappa_a\left(\boldsymbol{a}_2^2 - \boldsymbol{a}_1^2\right) \\ & - 2\kappa_b(\mathbf{b}_2\cdot\boldsymbol{r}_2' - \mathbf{b}_1\cdot\mathbf{r}_1') + \kappa_b\left(\boldsymbol{b}_2^2 - \boldsymbol{b}_1^2\right) \\ & + \kappa_a\Big[\left(\boldsymbol{r}_2'^2 - (\boldsymbol{r}_2'\cdot\hat{\boldsymbol{k}}_\mathrm{i})^2\right) - \left(\boldsymbol{r}_1'^2 - (\boldsymbol{r}_1'\cdot\hat{\boldsymbol{k}}_\mathrm{i})^2\right)\Big] \\ & + \kappa_b\Big[\left(\boldsymbol{r}_2'^2 - (\boldsymbol{r}_2'\cdot\hat{\boldsymbol{k}}_\mathrm{f})^2\right) - \left(\boldsymbol{r}_1'^2 - (\boldsymbol{r}_1'\cdot\hat{\boldsymbol{k}}_\mathrm{f})^2\right)\Big], \end{aligned} \tag{5.44}$$

where $\mathbf{b}_1 = b_{x_1}\hat{\mathbf{b}}_x + b_{z_1}\hat{\mathbf{b}}_z$ and $\mathbf{b}_2 = b_{x_2}\hat{\mathbf{b}}_x + b_{z_2}\hat{\mathbf{b}}_z$ denote two-dimensional vector representation. The two-dimensional unit vectors $\hat{\mathbf{b}}_x$ and $\hat{\mathbf{b}}_z$ are defined as

$$\hat{\mathbf{b}}_x = \begin{pmatrix} \cos\varphi \\ -\sin\varphi \end{pmatrix} \qquad \text{and} \qquad \hat{\mathbf{b}}_z = \begin{pmatrix} \sin\alpha_\mathrm{f}\sin\varphi \\ -\sin\alpha_\mathrm{f}\cos\varphi \end{pmatrix}. \tag{5.45}$$

By substituting (5.44) into eq. (5.35) and using the the relations $\mathbf{r} = \mathbf{L}_b + \boldsymbol{b}$, we can express the surface sensitive field correlation function for Fresnel conditions in the following form

$$\begin{aligned} G_1(\mathbf{L}_b + \boldsymbol{b}_1, \mathbf{L}_b + \boldsymbol{b}_2, \tau) = & \left(\frac{r_e}{L_a L_b}\right)^2 e^{-i\omega\tau} e^{i\kappa_b\left(\boldsymbol{b}_2^2 - \boldsymbol{b}_1^2\right)} \\ & \times \iint_V d^2r_1' d^2r_2' dz_1' dz_2'\; C_{\rho\rho}(\boldsymbol{r}_2', \boldsymbol{r}_1', z_2', z_1', \tau)\, e^{-i\boldsymbol{q}\cdot(\boldsymbol{r}_2' - \boldsymbol{r}_1')} e^{-iq_z(z_2' - z_1')} \\ & \times \iint_A d^2a_1 d^2a_2\; J_a(\boldsymbol{a}_1, \boldsymbol{a}_2)\Lambda_1^*\Lambda_2\, e^{i\kappa_a\left[\boldsymbol{a}_2^2 - \boldsymbol{a}_1^2 - 2(\mathbf{a}_2\cdot\boldsymbol{r}_2' - \mathbf{a}_1\cdot\boldsymbol{r}_1')\right]} \\ & \times e^{i\kappa_a\left[\left(\boldsymbol{r}_2'^2 - (\boldsymbol{r}_2'\cdot\hat{\boldsymbol{k}}_\mathrm{i})^2\right) - \left(\boldsymbol{r}_1'^2 - (\boldsymbol{r}_1'\cdot\hat{\boldsymbol{k}}_\mathrm{i})^2\right)\right]} e^{i\kappa_b\left[\left(\boldsymbol{r}_2'^2 - (\boldsymbol{r}_2'\cdot\hat{\boldsymbol{k}}_\mathrm{f})^2\right) - \left(\boldsymbol{r}_1'^2 - (\boldsymbol{r}_1'\cdot\hat{\boldsymbol{k}}_\mathrm{f})^2\right)\right]} \\ & \times e^{-i2\kappa_b(\mathbf{b}_2\cdot\boldsymbol{r}_2' - \mathbf{b}_1\cdot\boldsymbol{r}_1')}. \end{aligned} \tag{5.46}$$

Note, that the phase terms $\exp(-i\omega\tau)$ and $\exp\left(i\kappa_b\left(\boldsymbol{b}_2^2 - \boldsymbol{b}_1^2\right)\right)$ in eq. (5.46) vanish after utilizing the Siegert relation (5.25), hence we can ignored it in the following. For the continuing discussion it will useful to introduce a general resolution function, which incorporates all optical effects, namely the pre- and after-sample Fresnel corrections and spatial coherence, as well as resolution effects. If, in addition, the (mean) detector position $\mathbf{L}_b = L_b\hat{\boldsymbol{k}}_\mathrm{f}$ is fixed in space, we can drop the formal $\mathbf{L}_b$-dependence in $G_1(\mathbf{L}_b + \boldsymbol{b}_1, \mathbf{L}_b + \boldsymbol{b}_2, \tau)$ and express eq. (5.46) as

$$\begin{aligned} G_1(\mathbf{q}, \mathbf{b}_1, \mathbf{b}_2, \tau) = & \; r_e^2 \iint_V d^2r_1' d^2r_2' dz_1' dz_2'\; C_{\rho\rho}(\boldsymbol{r}_2', \boldsymbol{r}_1', z_2', z_1', \tau)\; e^{-iq_z(z_2' - z_1')} \\ & \times \mathcal{G}(\boldsymbol{r}_1', \boldsymbol{r}_2', \mathbf{b}_1, \mathbf{b}_2)\; e^{-i\boldsymbol{q}\cdot(\boldsymbol{r}_2' - \boldsymbol{r}_1')}, \end{aligned} \tag{5.47}$$

where $\mathbf{q}$ formally denotes the $\mathbf{q}$-dependence of the field correlation function. Here the function $\mathcal{G}(\boldsymbol{r}_1', \boldsymbol{r}_2', \mathbf{b}_1, \mathbf{b}_2)$ represents a general resolution function. From formula (5.47) it becomes evident, that the z-dependence appears only in the electron density correlation function and linearly in an exponential function, which leads us to the conclusion, that the q_z-dependence of the correlation function may, even under Fresnel conditions, not be influenced by resolution and spatial coherence effects. The q_x- and q_y-dependence of the correlation signal is, however, convoluted with the function $\mathcal{G}(\boldsymbol{r}_1', \boldsymbol{r}_2', \mathbf{b}_1, \mathbf{b}_2)$. On a second note it may be recognized, that the mathematical treatment of eq. (5.47) is substantially simplified as a consequence of the surface limited conditions for the X-ray paths. This is in particular the case for the z-integrations over the electron density correlation function. We will from now address the function $\mathcal{G}(\boldsymbol{r}_1', \boldsymbol{r}_2', \mathbf{b}_1, \mathbf{b}_2)$ as the generalized resolution function. Its explicit functional form is defined as

$$\begin{aligned}\mathcal{G}(\boldsymbol{r}_1', \boldsymbol{r}_2', \mathbf{b}_1, \mathbf{b}_2) = {} & e^{i\kappa_a\left[\left(\boldsymbol{r}_2'^2-(\boldsymbol{r}_2'\cdot\hat{\boldsymbol{k}}_\mathrm{i})^2\right)-\left(\boldsymbol{r}_1'^2-(\boldsymbol{r}_1'\cdot\hat{\boldsymbol{k}}_\mathrm{i})^2\right)\right]} \\ & \times \frac{1}{L_a^2}\iint_A d^2a_1 d^2a_2 \; J_a(\boldsymbol{a}_1, \boldsymbol{a}_2)\,\Lambda_1^*\Lambda_2\, e^{i\kappa_a\left[\boldsymbol{a}_2^2-\boldsymbol{a}_1^2-2\left(\mathbf{a}_2\cdot\boldsymbol{r}_2'-\mathbf{a}_1\cdot\boldsymbol{r}_1'\right)\right]} \\ & \times e^{i\kappa_b\left[\left(\boldsymbol{r}_2'^2-(\boldsymbol{r}_2'\cdot\hat{\boldsymbol{k}}_b)^2\right)-\left(\boldsymbol{r}_1'^2-(\boldsymbol{r}_1'\cdot\hat{\boldsymbol{k}}_b)^2\right)\right]} \\ & \times \frac{1}{L_b^2}\, e^{-i2\kappa_b\left(\mathbf{b}_2\cdot\boldsymbol{r}_2'-\mathbf{b}_1\cdot\boldsymbol{r}_1'\right)}\,. \end{aligned} \tag{5.48}$$

Next, we will discuss some specific representations for the generalized resolution function.

5.2.3 The General Resolution Function

The physical meaning of the general resolution function might be best examined in terms of pre-sample and after-sample conditions. For this purpose we will arrange eq. (5.48) as

$$\mathcal{G}(\boldsymbol{r}_1', \boldsymbol{r}_2', \mathbf{b}_1, \mathbf{b}_2) = \mathcal{G}_a(\boldsymbol{r}_1', \boldsymbol{r}_2')\mathcal{G}_b(\boldsymbol{r}_1', \boldsymbol{r}_2', \mathbf{b}_1, \mathbf{b}_2)\,, \tag{5.49}$$

where $\mathcal{G}_a(\boldsymbol{r}_1', \boldsymbol{r}_2')$ represents the first two lines on the right hand side of eq. (5.48) and $\mathcal{G}_b(\boldsymbol{r}_1', \boldsymbol{r}_2', \mathbf{b}_1, \mathbf{b}_2)$ the last two lines.

With the use of (5.49) and (5.48) we can now represent the pre-sample general resolution function $\mathcal{G}_a(\boldsymbol{r}_1', \boldsymbol{r}_2')$ by essentially two characterizing functions as

$$\mathcal{G}_a(\boldsymbol{r}_1', \boldsymbol{r}_2') = f_a(\boldsymbol{r}_1', \boldsymbol{r}_2')J_i(\boldsymbol{r}_1', \boldsymbol{r}_2'), \tag{5.50}$$

where the functions on the right hand side of (5.50) regard to different scattering situation and source properties. We will next discuss a variate of pre-sample

conditions by specifying the representation of these functions. The first term in eq. (5.50) refers to the Fresnel correction to the X-ray path length. Depending on the near or far field conditions one may use one of the following two cases

$$f_a(\boldsymbol{r}'_1,\boldsymbol{r}'_2)=\begin{cases} e^{i\kappa_a\left[\left(\boldsymbol{r}'^2_2-(\boldsymbol{r}'_2\cdot\hat{\boldsymbol{k}}_{\rm i})^2\right)-\left(\boldsymbol{r}'^2_1-(\boldsymbol{r}'_1\cdot\hat{\boldsymbol{k}}_{\rm i})^2\right)\right]}\,, & \text{in the } \textit{Fresnel limit},\\ 1\,, & \text{in the } \textit{Fraunhofer limit}. \end{cases} \tag{5.51}$$

The Fraunhofer limit for $f_a(\boldsymbol{r}'_1,\boldsymbol{r}'_2)$ holds if

$$\left|\frac{(x'^2_2-x'^2_1)+(y'^2_2-y'^2_1)\sin^2\alpha_{\rm i}}{2L_a}\right|_{max}\ll\lambda_0\,, \tag{5.52}$$

where the subscribe max denotes the maximum value for the numerator. In order to satisfy the condition (5.52) for X-ray wavelength with 1Å and a distance $L_a=1m$ the linear dimensions of the sample surface need to be of the order of $10\mu m$ or smaller. Another way to satisfy Fraunhofer limit can be achieved, if the incident beam is highly directional, so that the maximum values of the numerator in eq. (5.52) are effectively restricted by the illuminated sample area.

The remaining function in (5.50) is determined by the field properties at the aperture plane A, which is henceforth treated as a secondary planar source. The function $J_i(\boldsymbol{r}'_1,\boldsymbol{r}'_2)$ defines the term

$$J_i(\boldsymbol{r}'_1,\boldsymbol{r}'_2)=\frac{1}{L_a^2}\iint_A d^2a_1d^2a_2\;J_a(\boldsymbol{a}_1,\boldsymbol{a}_2)\,\Lambda_1^*\Lambda_2\,e^{i\kappa_a\left[\boldsymbol{a}_2^2-\boldsymbol{a}_1^2-2\left(\mathbf{a}_2\cdot\boldsymbol{r}'_2-\mathbf{a}_1\cdot\boldsymbol{r}'_1\right)\right]}\,, \tag{5.53}$$

which is nothing else than a specific representation of the van Cittert-Zernike theorem [58]. The solution for eq. (5.53) yields the incident mutual intensity function $J_i(\boldsymbol{r}'_1,\boldsymbol{r}'_2)$ at the sample position for a particular. For sufficiently large samples we may interpret $J_i(\boldsymbol{r}'_1,\boldsymbol{r}'_2)$ as a partially coherent intensity footprint on the sample surface, which depends on the source-sample distance, the source divergence θ, the spatial coherence and the extent of the secondary source plane. For a convenient characterization of the spatial properties at the source plane A it will be useful to extend the integration limits in (5.53) from $-\infty$ to $+\infty$ and introduce a pupil function $\mathcal{A}(\boldsymbol{a})$ which defines the aperture shape. If, in addition, the exit angles θ_1 and θ_2 have for all positions on the source plane the same angular divergence θ, we find with

$$\Lambda_1=\Lambda_2=\frac{i}{\lambda_0}\cos\theta\,, \tag{5.54}$$

the following form for (5.53)

$$J_i(\boldsymbol{r}'_1,\boldsymbol{r}'_2,\Omega) = \left(\frac{\cos\theta}{\lambda_0 L_a}\right)^2 \iint_{-\infty}^{\infty} d^2a_1 d^2a_2 \; \mathcal{A}(\boldsymbol{a}_1)\mathcal{A}(\boldsymbol{a}_2) \times J_a(\boldsymbol{a}_1,\boldsymbol{a}_2)\, e^{i\kappa_a\left[\boldsymbol{a}_2^2-\boldsymbol{a}_1^2-2(\mathbf{a}_2\cdot\boldsymbol{r}'_2-\mathbf{a}_1\cdot\boldsymbol{r}'_1)\right]}. \tag{5.55}$$

At next we will consider secondary sources with a constant intensity I_0 across the aperture opening. Furthermore, the spatial coherence of the intensities shall be characterized by a Gaussian function, so that

$$J_a(\boldsymbol{a}_1,\boldsymbol{a}_2) = I_0 j_a(\boldsymbol{a}_2-\boldsymbol{a}_1)\,, \tag{5.56}$$

with

$$j_a(\boldsymbol{a}_2-\boldsymbol{a}_1) = e^{-(a_{x_2}-a_{x_1})^2/2\xi_{tx}^2}\; e^{-(a_{z_2}-a_{z_1})^2/2\xi_{tz}^2}\,, \tag{5.57}$$

where ξ_{tx} and ξ_{tz} represent the transverse coherence length along the $\hat{\boldsymbol{a}}_x$ and $\hat{\boldsymbol{a}}_z$ direction of the aperture. With the aid of the aperture function $\mathcal{A}(\boldsymbol{a})$ and the mutual intensity function $J_a(\boldsymbol{a}_1,\boldsymbol{a}_2)$ we can next model different source types by using the following mathematical representations

$$\mathcal{A}(\boldsymbol{a}_1)\mathcal{A}(\boldsymbol{a}_2)J_a(\boldsymbol{a}_1,\boldsymbol{a}_2) = I_0 \begin{cases} \delta^2(\boldsymbol{a}_1)\delta^2(\boldsymbol{a}_2)j_a(\boldsymbol{a}_2-\boldsymbol{a}_1), & \textit{point source model,} \\ \mathcal{A}(\boldsymbol{a}_1)\mathcal{A}(\boldsymbol{a}_2), & \textit{fully coherent source model,} \\ \mathcal{A}(\boldsymbol{a}_1)\mathcal{A}(\boldsymbol{a}_2)j_a(\boldsymbol{a}_2-\boldsymbol{a}_1), & \textit{partially coherent source model,} \\ \mathcal{A}(\boldsymbol{a}_1)\mathcal{A}(\boldsymbol{a}_2)\delta^2(\boldsymbol{a}_2-\boldsymbol{a}_1), & \textit{fully incoherent source model.} \end{cases} \tag{5.58}$$

where $\delta^2(\boldsymbol{a}) = \delta(a_x)\delta(a_z)$ and $\delta^2(\boldsymbol{a}_2-\boldsymbol{a}_1) = \delta(a_{x_2}-a_{x_1})\delta(a_{z_2}-a_{z_1})$ represent two dimensional delta functions. With the functional representations (5.51), (5.55) and eq. (5.58) we are eventually able to construct systematical the pre-sample general resolution function.

A similar treatment for the after-sample general resolution function can be used by representing $\mathcal{G}_b(\boldsymbol{r}'_1,\boldsymbol{r}'_2,\mathbf{b}_1,\mathbf{b}_2)$ as

$$\mathcal{G}_b(\boldsymbol{r}'_1,\boldsymbol{r}'_2,\mathbf{b}_1,\mathbf{b}_2) = f_b(\boldsymbol{r}'_1,\boldsymbol{r}'_2)D(\boldsymbol{r}'_1,\boldsymbol{r}'_2,\mathbf{b}_1,\mathbf{b}_2)\,, \tag{5.59}$$

where $f_b(\boldsymbol{r}'_1,\boldsymbol{r}'_2)$ is the after-sample Fresnel correlation term. In analogy to eq. (5.51) we define $f_b(\boldsymbol{r}'_1,\boldsymbol{r}'_2)$ as

$$f_b(\boldsymbol{r}'_1,\boldsymbol{r}'_2) = e^{i\kappa_b\left[\left(\boldsymbol{r}_2'^2-(\boldsymbol{r}'_2\cdot\hat{\boldsymbol{k}}_{\mathrm{f}})^2\right)-\left(\boldsymbol{r}_1'^2-(\boldsymbol{r}'_1\cdot\hat{\boldsymbol{k}}_{\mathrm{f}})^2\right)\right]}\,, \tag{5.60}$$

in the Fresnel limit. In the Fraunhofer limit one can replace the after-sample Fresnel term by one, if the following condition is satisfied

$$\left| \frac{(x_2'^2 - x_1'^2) + (y_2'^2 - y_1'^2)\sin^2\alpha_{\rm f}}{2L_b} \right|_{max} \ll \lambda_0 \,. \tag{5.61}$$

The second term in (5.59) defines the detection scheme

$$D(\boldsymbol{r}_1', \boldsymbol{r}_2', \mathbf{b}_1, \mathbf{b}_2) = \frac{1}{L_b^2} \begin{cases} e^{-i2\kappa_b\left(\mathbf{b}_2\cdot\boldsymbol{r}_2' - \mathbf{b}_1\cdot\boldsymbol{r}_1'\right)} & \textit{two point detection,} \\ e^{-i2\kappa_b \mathbf{b}\cdot(\boldsymbol{r}_2' - \boldsymbol{r}_1')} & \textit{single point detection.} \end{cases} \tag{5.62}$$

The vector $\mathbf{b}$ stands for the vectors $\mathbf{b}_1$ or $\mathbf{b}_2$ if the single point detection scheme is fulfilled.

By using the above definitions one may construct a general resolution function which adequately describes the pre and after scattering conditions in surface sensitive XICS experiments. The incorporation of detector resolution effects is separately discussed in the next paragraph.

A. Finite Detector Resolution

In order to consider detector resolution effects in the intensity correlation function $G_2(\mathbf{r}_1, \mathbf{r}_2, \tau)$, we make use of the Siegert relation in its representation eq. (5.25). The finite detector opening can then be taken into account by integrating both sides of eq. (5.25) over all detection points $\mathbf{r}_1 = \mathbf{L}_b + \boldsymbol{b}_1$ and $\mathbf{r}_2 = \mathbf{L}_b + \boldsymbol{b}_2$ on the plane B. For a fixed (mean) detector position $\mathbf{L}_b = L_b\hat{\mathbf{k}}_b$, we can reduces the integration over the detector plane to integrals over the vectors $\boldsymbol{b}_1 = b_{x_1}\hat{\boldsymbol{b}}_x + b_{z_1}\hat{\boldsymbol{b}}_z$ and $\boldsymbol{b}_2 = b_{x_2}\hat{\boldsymbol{b}}_x + b_{z_2}\hat{\boldsymbol{b}}_z$, i.e. in practice over the coefficients $d^2b_1 d^2b_2 = db_{x_1} db_{z_1} db_{x_2} db_{z_2}$. Hence, after interchanging the order of averaging and detector integration, we find (for surface sensitive conditions)

$$\begin{aligned} G_2(\mathbf{q}, \tau) &= \iint_B d^2b_1 d^2b_2 \; G_2(\mathbf{r}_1, \mathbf{r}_2, \tau) \\ &= \iint_B d^2b_1 d^2b_2 \; \langle I(\mathbf{q}, \mathbf{b}_1, t_1)\rangle \langle I(\mathbf{q}, \mathbf{b}_2, t_2)\rangle \\ &\quad + \iint_B d^2b_1 d^2b_2 \; |G_1(\mathbf{q}, \mathbf{b}_1, \mathbf{b}_2, \tau)|^2 \,, \end{aligned} \tag{5.63}$$

where we have formally expressed the averaged intensity correlation function $G_2(\mathbf{q}, \tau)$ on the detector plane as a function of the (mean) wave vector transfer.

The second term in (5.63) can be evaluated with the general field correlation formula (5.47). The first term in (5.63) can be calculated by making use of the conditions $\mathbf{b}_1 = \mathbf{b}_2$ and $\tau = 0$. The explicit forms for the intensity term

$\langle I(\mathbf{q}, \mathbf{b}_1, t_1)\rangle$ and its integrated value $\bar{I}(\mathbf{q})$, over the detector area, are given here for clarity

$$\bar{I}(\mathbf{q}) = \int_B d^2b_1 \, \langle I(\mathbf{q}, \mathbf{b}_1, t_1)\rangle \,, \tag{5.64}$$

with

$$\begin{aligned} \langle I(\mathbf{q}, \mathbf{b}_1, t_1)\rangle &= G_1(\mathbf{q}, \mathbf{b}_1, \mathbf{b}_1, 0) \\ &= r_e^2 \iint_V d^2r_1' d^2r_2' dz_1' dz_2' \; C_{\rho\rho}(\boldsymbol{r}_2', \boldsymbol{r}_1', z_2', z_1', 0)\, e^{-iq_z(z_2'-z_1')} \\ &\quad \times \mathcal{G}(\boldsymbol{r}_1', \boldsymbol{r}_2', \mathbf{b}_1, \mathbf{b}_1)\, e^{-i\boldsymbol{q}\cdot(\boldsymbol{r}_2'-\boldsymbol{r}_1')} \,, \end{aligned} \tag{5.65}$$

where the $\mathbf{b}_1$-dependence of $\mathcal{G}(\boldsymbol{r}_1', \boldsymbol{r}_2', \mathbf{b}_1, \mathbf{b}_1)$ is determined by the single point detector function eq. (5.62). A mathematically identical expression can be obtained for $\langle I(\mathbf{q}, \mathbf{b}_2, t_2)\rangle$, if $\mathbf{b}_1$ is replacing by $\mathbf{b}_2$ in eq. (5.65). Conclusively, we can replace the first term in eq. (5.63) by the static intensity $\bar{I}^2(\mathbf{q})$ and express eq. (5.63) as

$$G_2(\mathbf{q}, \tau) = \bar{I}^2(\mathbf{q}) + \iint_B d^2b_1 d^2b_2 \; |G_1(\mathbf{q}, \mathbf{b}_1, \mathbf{b}_2, \tau)|^2 \,. \tag{5.66}$$

The above formula represents the Siegert relation including the effects of finite detector resolution.

5.2.4 The Field Correlation Function for Gaussian Fluctuating Surfaces

We will next specify the electron density correlation function $C_{\rho\rho}(\mathbf{r}_2', \mathbf{r}_1', \tau)$ for a rather simple liquid model and evaluate the integration over the z-coordinates in eq. (5.47). By means of this liquid model we will later on examine the influences of the detector resolution and the general resolution function on the field correlation function. The model, that we propose here is based on some statistical conditions for the electron density fluctuations, as well as its spatial distribution. In according with our previews assumptions, see section 2, we demand that the time fluctuations of the liquid are statistically stationary. The distribution of the liquid is, for simplicity, considered to be of infinite depth but truncated in the positive z-direction at the height h, where $h = h(\boldsymbol{r}', t)$ is a randomly changing function of the surface position $\boldsymbol{r}'$ and time t. The electron density distribution along the $\boldsymbol{r}' = (x', y')$ coordinates are considered to be of finite extent in both directions, which will be denoted in the following by a limited integration over the surface area $\mathcal{S}$, see expression (5.72). In addition to the condition of statistical stationarity we demand that the electron density fluctuations are statistically homogeneous in the $\boldsymbol{r}'$-plane.

On top of the liquid surface we will think of a vapor atmosphere, which is similarly extended to a infinite height. The influences of the vapor atmosphere on the height displacements $h(\boldsymbol{r}', t)$ is assumed to be negligible, so that the spatial and temporal properties of the height function are essentially determined by the liquid, i.e. the statistical conditions of homogeneity and stationarity are equally applied to $h(\boldsymbol{r}', t)$.

For a convenient formulation of the electron density $\rho(\boldsymbol{r}', z', t)$, in terms of its mean equilibrium value $\bar{\rho}$ plus the deviation $\triangle\rho(\boldsymbol{r}', z', t)$ from it, we will treat $\rho(\boldsymbol{r}', z', t)$ as the electron density function of the entire z-space. Hence, $\bar{\rho}$ represents the arithmetical average of the mean equilibrium values from the liquid and the vapor atmosphere, which are represented by $\bar{\rho}_l$ and $\bar{\rho}_v$, respectively. The deviation of the electron density $\triangle\rho(\boldsymbol{r}', z', t)$ from its mean value $\bar{\rho}$ is assumed to be maximal at the liquid-vapor interface region. In other words, the inherent bulk electron density fluctuations in the liquid and vapor atmosphere are neglected in this model. The mathematical formulation for the electron density distribution is then

$$\begin{aligned} \rho(\boldsymbol{r}', z', t) &= \bar{\rho} + \triangle\rho(\boldsymbol{r}', z', t), \\ &= \bar{\rho} + \triangle\bar{\rho}\left[\frac{1}{2} - \mathrm{H}(z' - h(\boldsymbol{r}', t))\right], \\ &= \bar{\rho}_l\big[1 - \mathrm{H}(z - h(\boldsymbol{r}', t))\big], \qquad \text{for } \bar{\rho}_l \gg \bar{\rho}_v\,, \end{aligned} \tag{5.67}$$

where $\bar{\rho} = (\bar{\rho}_l + \bar{\rho}_v)/2$, $\triangle\bar{\rho} = \bar{\rho}_l - \bar{\rho}_v$ and $\mathrm{H}(z' - h(\boldsymbol{r}', t))$ stands for the Heaviside function. Eq. (5.67) states that the deviations from the mean electron density appear at the height position $h(\boldsymbol{r}', t)$ with a magnitude of $\pm\triangle\bar{\rho}/2$ or approximately $\bar{\rho}_l$.

By using the electron density model (5.67) for the entire z-space, which yet comprises the finite distribution of the liquid, one can readily extent the z-integrations in expression (5.47) from minus to plus infinity. With eq. (5.67) and (5.30) the z-integrations in expression (5.47) yield

$$\iint_{-\infty}^{\infty} dz_1' dz_2'\; C_{\rho\rho}(\boldsymbol{r}_2' - \boldsymbol{r}_1', z_2', z_1', \tau)\, e^{-iq_z(z_2' - z_1')} = \frac{\bar{\rho}_l^2}{q_z^2}\left\langle e^{-iq_z(h_2 - h_1)}\right\rangle, \tag{5.68}$$

where $h_1 = h(\boldsymbol{r}_1', t_1)$ and $h_2 = h(\boldsymbol{r}_2', t_2)$. Eq. (5.68) has been evaluated by interchanging the order of integration with the averaging.

Next, we demand that the random realizations of the height displacements are, in the ensemble average, symmetrically distributed above and below the mean equilibrium $\bar{h}$, which shall be located at the origin $z = 0$. This symmetrical distribution of the height displacements is explicitly characterized by a Gaussian probability function. In addition, we assume that $h_1 = h(\boldsymbol{r}_1', t_1)$

and $h_2 = h(\boldsymbol{r}'_2, t_2)$ are statistically dependent from each other for arbitrary spatial and temporal differences. Conclusively, the ensemble average on right hand side of eq. (5.68) can be evaluated with the bivariate Gaussian probability function [58], which leads to the relation (see Appendix A1)

$$\begin{aligned}\left\langle e^{-iq_z(h_2-h_1)}\right\rangle &= e^{-q_z^2\left(\langle h_1^2\rangle+\langle h_2^2\rangle-\langle h_1h_2\rangle-\langle h_2h_1\rangle\right)/2} \\ &= e^{-q_z^2\left(\sigma^2-C_{zz}(\boldsymbol{r}'_2-\boldsymbol{r}'_1,\tau)\right)}\end{aligned} \tag{5.69}$$

In the second line of (5.69) we have made use of statistical properties of the height function, viz. spatial homogeneity and temporal stationary, which states that $\langle h^2(\boldsymbol{r}'_1, t_1)\rangle = \langle h^2(\boldsymbol{r}'_2, t_2)\rangle = \sigma^2$, where the constant σ is root-mean-squared roughness of the interface. Similarly, we have used the equality of $\langle h(\boldsymbol{r}'_1, t_1)h(\boldsymbol{r}'_2, t_2)\rangle = \langle h(\boldsymbol{r}'_2, t_2)h(\boldsymbol{r}'_1, t_1)\rangle$ and expressed both terms through the height correlation function $C_{zz}(\boldsymbol{r}'_2 - \boldsymbol{r}'_1, \tau)$. It is important to note that the maximum value of the height correlation function is equal to σ^2. This necessary condition has been often ignored in the analysis of correlation functions for liquid surfaces. A detail discussion on this matter is given in section 2 and 3.

A useful approximation for eq. (5.69) is obtained, if we restrict the outgoing angle α_f to values which satisfy the condition $1 \gg q_z^2\sigma^2$. We can then replace (5.69) by

$$\left\langle e^{-iq_z(h_2-h_1)}\right\rangle \approx e^{-q_z^2\sigma^2}\left(1 + q_z^2 C_{zz}(\boldsymbol{r}'_2 - \boldsymbol{r}'_1, \tau)\right) \tag{5.70}$$

for

$$q_z^2\sigma^2 \ll 1 \qquad \text{and} \qquad \alpha_\mathrm{i} < \alpha_c\,, \tag{5.71}$$

where the second relation just recalls the surface sensitive condition. By using the approximation (5.70) at $\varphi = 0$ including the limitation in α_i and α_f we have effectively restricts all components of the wave vector transfer $\mathbf{q} = (q_x, q_y, q_z)$ and, therefore, the applicable range of therefrom derived field autocorrelation function. However, the accessibly $\mathbf{q}$-range is still sufficiently large to describe present surface sensitive XICS experiments from numerous liquids with low surface roughness.

Combining the equations (5.70) and (5.68) gives after substitution into (5.47) the field autocorrelation function for a Gaussian fluctuating surface in the following form

$$\begin{aligned}G_1(\mathbf{q}, \mathbf{b}_1, \mathbf{b}_2, \tau) = (\bar{\rho}_l\, r_e)^2\, e^{-q_z^2\sigma^2}\Bigg[&\frac{1}{q_z^2}\iint_{\mathcal{S}} d^2\boldsymbol{r}'_1 d^2\boldsymbol{r}'_2\; \mathcal{G}(\boldsymbol{r}'_1, \boldsymbol{r}'_2, \mathbf{b}_1, \mathbf{b}_2)\, e^{-i\mathbf{q}\cdot(\boldsymbol{r}'_2-\boldsymbol{r}'_1)} \\ &+ \iint_{\mathcal{S}} d^2r'_1 d^2r'_2\; C_{zz}(\boldsymbol{r}'_2 - \boldsymbol{r}'_1, \tau)\, \mathcal{G}(\boldsymbol{r}'_1, \boldsymbol{r}'_2, \mathbf{b}_1, \mathbf{b}_2)\, e^{-i\mathbf{q}\cdot(\boldsymbol{r}'_2-\boldsymbol{r}'_1)}\Bigg].\end{aligned} \tag{5.72}$$

The integration limit $\mathcal{S}$ denotes the finite surface area of the scatterer. Eq. (5.72) is for a static smooth surface, where $\sigma = C_{zz}(\boldsymbol{r}'_2 - \boldsymbol{r}'_1, \tau) = 0$, determined by the first term in the rectangular parenthesis, which refers to the static specular component of the scattered beam. For a fluctuating rough surface, we may then interpret the second term in the parenthesis as the field autocorrelation part due to the diffusely scattered beam. It be should noted that the above interpretation is in agreement with the treatment of the static scattering function from rough surfaces [90].

By introducing in eq. (5.72) a truncation function $\mathcal{T}(\boldsymbol{r})$ for the sample size, we can extend the real space integration limits from minus to plus infinity. This leads to the representation

$$\begin{aligned} G_1(\mathbf{q}, \mathbf{b}_1, \mathbf{b}_2, \tau) = {} & (\bar{\rho}_l\, r_e)^2 e^{-q_z^2\sigma^2} \\ & \times \left[\frac{1}{q_z^2} \iint_{-\infty}^{\infty} d^2r'_1 d^2r'_2\, \mathcal{T}(\boldsymbol{r}'_1)\mathcal{T}(\boldsymbol{r}'_2)\mathcal{G}(\boldsymbol{r}'_1, \boldsymbol{r}'_2, \mathbf{b}_1, \mathbf{b}_2) e^{-i\boldsymbol{q}\cdot(\boldsymbol{r}'_2 - \boldsymbol{r}'_1)} \right. \\ & \left. + \iint_{-\infty}^{\infty} d^2r'_1 d^2r'_2 C_{zz}(\boldsymbol{r}'_2 - \boldsymbol{r}'_1, \tau)\mathcal{T}(\boldsymbol{r}'_1)\mathcal{T}(\boldsymbol{r}'_2)\mathcal{G}(\boldsymbol{r}'_1, \boldsymbol{r}'_2, \mathbf{b}_1, \mathbf{b}_2) e^{-i\boldsymbol{q}\cdot(\boldsymbol{r}'_2 - \boldsymbol{r}'_1)} \right], \end{aligned} \tag{5.73}$$

which is more preferable, since it enables us to treat the integrals in terms of conventional Fourier transformations. For a practical use of eq. (5.73) one needs to construct the general resolution function of the experimental conditions including the sample truncation function.

The height correlation function in the space-time domain may finally be modeled based on the hydrodynamical theory of liquid surfaces. Alternatively, we can apply the convolution theorem in (5.73) and specify the height correlation function of the reciprocal space-time domain, i.e. the function $\widetilde{C}_{zz}(\boldsymbol{q}, \tau)$. Both approaches eventually yield to the same result for the field autocorrelation function and distinguish from another only in the mathematical effort. In the following proceeding we will demonstrate the latter treatment.

A. Reciprocal Space Discussion

In order to apply the convolution theorem in eq. (5.73) we make use of the spatial homogeneity of the height correlation function and by introducing the relative coordinates $\boldsymbol{R} = \boldsymbol{r}'_2 - \boldsymbol{r}'_1$, as well as the substitution

$$\begin{aligned} \mathcal{G}_t(\boldsymbol{R}, \mathbf{b}_1, \mathbf{b}_2) &= \int_{-\infty}^{\infty} d^2r'_1\, \mathcal{T}(\boldsymbol{r}'_1)\mathcal{T}(\boldsymbol{r}'_2)\mathcal{G}(\boldsymbol{r}'_1, \boldsymbol{r}'_2, \mathbf{b}_1, \mathbf{b}_2) \\ &= \int_{-\infty}^{\infty} d^2r'_1\, \mathcal{T}(\boldsymbol{r}'_1)\mathcal{T}(\boldsymbol{r}'_1 + \boldsymbol{R})\mathcal{G}(\boldsymbol{r}'_1, \boldsymbol{r}'_1 + \boldsymbol{R}, \mathbf{b}_1, \mathbf{b}_2). \end{aligned} \tag{5.74}$$

The new function $\mathcal{G}_t(\boldsymbol{R}, \mathbf{b}_1, \mathbf{b}_2)$ takes additional resolution effects into account, which result from the finite sample size. For actual XICS measurements from liquids the finite surface area may often be larger than the illuminated sample surface, under these conditions the sample truncation functions can be replace by one and $\mathcal{G}_t(\boldsymbol{R}, \mathbf{b}_1, \mathbf{b}_2)$ is essentially defined by the general resolution function. With the above definition eq. (5.73) can be rewritten as

$$G_1(\mathbf{q}, \mathbf{b}_1, \mathbf{b}_2, \tau) = (\bar{\rho}_l\, r_e)^2\, e^{-q_z^2\sigma^2} \left[\frac{1}{q_z^2} \int_{-\infty}^{\infty} d^2R\; \mathcal{G}_t(\boldsymbol{R}, \mathbf{b}_1, \mathbf{b}_2)\, e^{-i\boldsymbol{q}\cdot\boldsymbol{R}} + \int_{-\infty}^{\infty} d^2R\; C_{zz}(\boldsymbol{R}, \tau) \mathcal{G}_t(\boldsymbol{R}, \mathbf{b}_1, \mathbf{b}_2)\, e^{-i\boldsymbol{q}\cdot\boldsymbol{R}} \right], \tag{5.75}$$

which then yields with the convolution theorem in the reciprocal space representation of equation (5.73). Hence,

$$G_1(\mathbf{q}, \mathbf{b}_1, \mathbf{b}_2, \tau) = (\bar{\rho}_l\, r_e)^2\, e^{-q_z^2\sigma^2} \times \left[\frac{1}{q_z^2}\, \widetilde{\mathcal{G}}_t(\boldsymbol{q}, \mathbf{b}_1, \mathbf{b}_2) + \int_{-\infty}^{\infty} d^2q'\; \widetilde{C}_{zz}(\boldsymbol{q}', \tau) \widetilde{\mathcal{G}}_t(\boldsymbol{q} - \boldsymbol{q}', \mathbf{b}_1, \mathbf{b}_2) \right], \tag{5.76}$$

where the tilde symbol denotes the Fourier transformation of each function.

The height correlation function given in the reciprocal space-time domain can next be determined from the surface spectrum $S_{zz}(\boldsymbol{q}, \omega)$ of thermal excited capillary waves. By preforming the inverse Fourier transform of the surface spectrum we find the following expression for the height correlation function (see section 2.2.2)

$$\widetilde{C}_{zz}(\boldsymbol{q}, \tau) = \frac{k_B T}{\gamma}\, \widetilde{c}_{zz}(\boldsymbol{q}, \tau)\,, \tag{5.77}$$

where $\widetilde{c}_{zz}(\boldsymbol{q}, \tau)$ is in the high viscosity limit equal to

$$\widetilde{c}_{zz}(\boldsymbol{q}, \tau) = \frac{1}{\boldsymbol{q}^2 + q_g^2}\, e^{-\Gamma_h(q)\tau(1+q_g^2/\boldsymbol{q}^2)}\,, \tag{5.78}$$

and for low viscous liquids

$$\widetilde{c}_{zz}(\boldsymbol{q}, \tau) \approx \frac{1}{\boldsymbol{q}^2 + q_g^2} \cos\left(\omega_s(\boldsymbol{q})\tau\right)\, e^{-\Gamma_l(\boldsymbol{q})\tau}\,. \tag{5.79}$$

Let us finally substituting (5.77) into eq. (5.76) and us the following representation for the field correlation function

$$G_1(\mathbf{q}, \mathbf{b}_1, \mathbf{b}_2, \tau) = G_{\mathrm{S}}(\mathbf{q}, \mathbf{b}_1, \mathbf{b}_2) + \frac{k_B T}{\gamma}\, G_{\mathrm{D}}(\mathbf{q}, \mathbf{b}_1, \mathbf{b}_2, \tau)\,, \tag{5.80}$$

where

$$G_{\mathrm{S}}(\mathbf{q}, \mathbf{b}_1, \mathbf{b}_2) = (\bar{\rho}_l \, r_e)^2 e^{-q_z^2 \sigma^2} \frac{1}{q_z^2} \, \widetilde{\mathcal{G}}_t(\boldsymbol{q}, \mathbf{b}_1, \mathbf{b}_2) \,, \tag{5.81}$$

and

$$G_{\mathrm{D}}(\mathbf{q}, \mathbf{b}_1, \mathbf{b}_2, \tau) = (\bar{\rho}_l \, r_e)^2 e^{-q_z^2 \sigma^2} \int_{-\infty}^{\infty} d^2 q' \; \widetilde{c}_{zz}(\boldsymbol{q}', \tau) \widetilde{\mathcal{G}}_t(\boldsymbol{q} - \boldsymbol{q}', \mathbf{b}_1, \mathbf{b}_2). \tag{5.82}$$

Here eq. (5.81) regards to the specular reflected field correlation function and (5.82) refers to the diffusely scattered component of the field correlation function.

5.2.5 Examples

In the following section we will illustrate the application of (5.80) in combination with eq. (5.78) and (5.79). Eq. (5.78) and (5.79) will be respectively specified with the material constants of glycerol and water at room temperature. To simulate the effects of resolution and spatial coherence on the intensity autocorrelation function we will first discuss the Fraunhofer and then Fresnel limit. The intensity autocorrelation function $G_2(\mathbf{r}_1, \mathbf{r}_2, \tau)$, which was presented in the introduction will be replaced here by the representation $G_2(\mathbf{q}, \tau)$, which explicitly includes the integration over the finite detection area B, see section 5.2.3. The Siegert relation is then given by eq. (5.66). However, for the examples given in this section, we will use a further modified Siegert relation by dividing both of sides of eq. (5.63) by $\bar{I}^2(\mathbf{q})$. This leads to the following normalized representation of Siegert's relation

$$\begin{aligned} g_2(\mathbf{q}, \tau) &= \frac{G_2(\mathbf{q}, \tau)}{\bar{I}^2(\mathbf{q})} \\ &= 1 + \frac{1}{\bar{I}^2(\mathbf{q})} \iint_B d^2 b_1 d^2 b_2 \; |G_1(\mathbf{q}, \mathbf{b}_1, \mathbf{b}_2, \tau)|^2 \,. \end{aligned} \tag{5.83}$$

If, we next substitute (5.80) into (5.83) and express the mean static intensity $\bar{I}(\mathbf{q})$ as the sum of the specular intensity $\bar{I}_{\mathrm{S}}(\mathbf{q})$ and diffuse component $\bar{I}_{\mathrm{D}}(\mathbf{q})$,

then eq. (5.83) yields

$$
\begin{aligned}
g_2(\mathbf{q},\tau) &= 1 + \frac{1}{[\bar{I}_{\mathrm{S}}(\mathbf{q}) + \bar{I}_{\mathrm{D}}(\mathbf{q})]^2} \iint_B d^2b_1 d^2b_2 \\
&\quad \times \left| G_{\mathrm{S}}(\mathbf{q},\mathbf{b}_1,\mathbf{b}_2) + \frac{k_B T}{\gamma} G_{\mathrm{D}}(\mathbf{q},\mathbf{b}_1,\mathbf{b}_2,\tau) \right|^2 , \\
&= 1 + \frac{1}{[\bar{I}_{\mathrm{S}}(\mathbf{q}) + \bar{I}_{\mathrm{D}}(\mathbf{q})]^2} \iint_B d^2b_1 d^2b_2 \\
&\quad \times \Bigg[|G_{\mathrm{S}}(\mathbf{q},\mathbf{b}_1,\mathbf{b}_2)|^2 + \frac{2k_B T}{\gamma} \mathrm{Re}[G^*_{\mathrm{S}}(\mathbf{q},\mathbf{b}_1,\mathbf{b}_2) G_{\mathrm{D}}(\mathbf{q},\mathbf{b}_1,\mathbf{b}_2,\tau)] \\
&\quad + \left(\frac{k_B T}{\gamma}\right)^2 |G_{\mathrm{D}}(\mathbf{q},\mathbf{b}_1,\mathbf{b}_2,\tau)|^2 \Bigg],
\end{aligned}
\tag{5.84}
$$

where the mean static intensity terms are given by

$$
\bar{I}_{\mathrm{S}}(\mathbf{q}) = \int_B d^2b \; G_{\mathrm{S}}(\mathbf{q},\mathbf{b},\mathbf{b}) \,, \tag{5.85a}
$$

$$
\bar{I}_{\mathrm{D}}(\mathbf{q}) = \frac{k_B T}{\gamma} \int_B d^2b \; G_{\mathrm{D}}(\mathbf{q},\mathbf{b},\mathbf{b},0) \,. \tag{5.85b}
$$

The Fraunhofer and Fresnel examples presented in this section will be based on formula (5.84). Independent from these to limit cases, we can conclude from the general form of eq. (5.84) that the dynamic properties of the surface fluctuations are integrated in the $g_2(\mathbf{q},\tau)$ function by a linear and quadratic term of $G_{\mathrm{D}}(\mathbf{q},\mathbf{b}_1,\mathbf{b}_2,\tau)$. The linear term and quadratic terms refer, in the contents of photon correlation spectroscopy, to the heterodyne and homodyne correlation signal. With eq. (5.84) one can expect, that the observation of a strong heterodyne or homodyne signal depends, regardless of Fraunhofer or Fresnel conditions, on the following inequality

$$
\frac{k_B T}{2\gamma} \frac{\left| \frac{G_{\mathrm{D}}(\mathbf{q},\mathbf{b}_1,\mathbf{b}_2,\tau)}{G_{\mathrm{S}}(\mathbf{q},\mathbf{b},\mathbf{b})} \right|^2}{\mathrm{Re}\left[\frac{G_{\mathrm{D}}(\mathbf{q},\mathbf{b}_1,\mathbf{b}_2,\tau)}{G_{\mathrm{S}}(\mathbf{q},\mathbf{b},\mathbf{b})} \right]} \begin{cases} \ll 1 & \textit{strong heterodyne signal}, \\ \gg 1 & \textit{strong homodyne signal}. \end{cases} \tag{5.86}
$$

With the explicit form of the time dependent height correlation function, see section 2, the only remaining unknown quantity in eq. (5.84) is the function $\widetilde{\mathcal{G}}_t(\boldsymbol{q}-\boldsymbol{q}',\mathbf{b}_1,\mathbf{b}_2)$, which is apart from the sample truncation function essential determined by the general resolution function $\mathcal{G}(\boldsymbol{r}'_1,\boldsymbol{r}'_2,\mathbf{b}_1,\mathbf{b}_2)$. For the modeling of the truncation function $\mathcal{T}(\boldsymbol{r}')$ we will consider, for simplicity sakes, a Gaussian function

$$
\mathcal{T}(\boldsymbol{r}') = \exp\left(-\frac{\boldsymbol{r}'^2}{2\triangle r^2} \right), \tag{5.87}
$$

where $\boldsymbol{r}'^2 = x'^2 + y'^2$ and the full width of the Gaussian functions at $1/\exp$ defines the extend of the sample surface, i.e. $\mathcal{S} \simeq 8\triangle r^2$. With the above model (5.87), we will next discuss the evaluation of eq. (5.84) for numerous conditions in surface sensitive XICS experimental from liquids surface.

A. Fraunhofer point-source/point-detector conditions

In order to derive the function $\widetilde{\mathcal{G}}_t(\boldsymbol{q}-\boldsymbol{q}', \mathbf{b}_1, \mathbf{b}_2)$ in the Fraunhofer limit, we start with the construction of the general resolution function $\mathcal{G}(\boldsymbol{r}'_1, \boldsymbol{r}'_2, \mathbf{b}_1, \mathbf{b}_2)$. On using the Fraunhofer representations for $f_a(\boldsymbol{r}'_1, \boldsymbol{r}'_2)$ and $f_b(\boldsymbol{r}'_1, \boldsymbol{r}'_2)$ (see section 5.2.3), one finds for the far-field general resolution function:

$$\mathcal{G}(\boldsymbol{r}'_1, \boldsymbol{r}'_2, \mathbf{b}_1, \mathbf{b}_2) = J_i(\boldsymbol{r}'_1, \boldsymbol{r}'_2) D(\boldsymbol{r}'_1, \boldsymbol{r}'_2, \mathbf{b}_1, \mathbf{b}_2)\,. \tag{5.88}$$

Note that the incident and scattered field are regarded as plane waves in this example. Hence, the maximum value for $\boldsymbol{r}'$ is only determined by the truncation function (5.87) and the Fraunhofer conditions (5.52) and (5.61) refer here to the inequalities

$$\left|\frac{\triangle r^2(1+\sin\alpha_{\rm i})^2}{L_a}\right|_{max}, \quad \left|\frac{\triangle r^2(1+\sin\alpha_{\rm f})^2}{L_b}\right|_{max} \ll \lambda_0\,. \tag{5.89}$$

On using the point source presentation in eq. (5.58), one finds for eq. (5.88)

$$\mathcal{G}(\boldsymbol{r}'_1, \boldsymbol{r}'_2, \mathbf{b}_1, \mathbf{b}_2) = I_0 \left(\frac{\cos\theta}{\lambda_0 L_a}\right)^2 D(\boldsymbol{r}'_1, \boldsymbol{r}'_2, \mathbf{b}_1, \mathbf{b}_2)\,. \tag{5.90}$$

In order to derive next the function $\widetilde{\mathcal{G}}_t(\mathbf{q}-\mathbf{q}', \mathbf{b}_1, \mathbf{b}_2)$, we will first recall the real-space representation eq. (5.74) in combination with (5.90), hence

$$\mathcal{G}_t(\boldsymbol{R}, \mathbf{b}_1, \mathbf{b}_2) = I_0 \left(\frac{\cos\theta}{\lambda_0 L_a}\right)^2 \int_{-\infty}^{\infty} d^2 r'_1\; \mathcal{T}(\boldsymbol{r}'_1)\mathcal{T}(\boldsymbol{r}'_1+\boldsymbol{R}) D(\boldsymbol{r}'_1, \boldsymbol{r}'_1+\boldsymbol{R}, \mathbf{b}_1, \mathbf{b}_2)\,. \tag{5.91}$$

With the definition for the detector function (5.62) and the truncation function (5.87), one finds the expression

$$\mathcal{G}_t(\boldsymbol{R}, \mathbf{b}_1, \mathbf{b}_2) = I_0 \pi \left(\frac{\triangle r\, \cos\theta}{\lambda_0 L_a L_b}\right)^2 e^{-(\triangle r \kappa_b)^2(\mathbf{b}_2-\mathbf{b}_1)^2} e^{-\boldsymbol{R}^2/4\triangle r^2} e^{-i\kappa_b \boldsymbol{R}\cdot(\mathbf{b}_1+\mathbf{b}_2)}\,. \tag{5.92}$$

After performing the 2-dimensional Fourier transformation of eq. (5.92) we obtain the following reciprocal-space representation

$$\widetilde{\mathcal{G}}_t(\boldsymbol{q}, \mathbf{b}_1, \mathbf{b}_2) = I_0 \left(\frac{\cos\theta}{\lambda_0 L_a L_b}\right)^2 \widetilde{\mathcal{T}}^2(\boldsymbol{q}) e^{-2\kappa_b[\boldsymbol{q}\cdot(\mathbf{b}_1+\mathbf{b}_2)+\kappa_b(\mathbf{b}_1^2+\mathbf{b}_2^2)]/\triangle q^2}\,, \tag{5.93}$$

where the reciprocal-space sample truncation function $\widetilde{\mathcal{T}}(\boldsymbol{q})$ is

$$\widetilde{\mathcal{T}}(\boldsymbol{q}) = \frac{2\pi}{\triangle q^2} \exp\left(-\frac{\boldsymbol{q}^2}{2\triangle q^2}\right), \tag{5.94}$$

and $\triangle q = 1/\triangle r$ defines the spread in the wave vector transfer $\boldsymbol{q}$. After substituting (5.93) into eq. (5.81) one finds the specular field correlation function for the above experimental situation, namely

$$G_{\mathrm{S}}(\mathbf{q}, \mathbf{b}_1, \mathbf{b}_2) = I_0 \left(\frac{\bar{\rho}_l \, r_e \cos\theta}{\lambda_0 L_a L_b}\right)^2 e^{-q_z^2\sigma^2} \, e^{-2\kappa_b[\boldsymbol{q}\cdot(\mathbf{b}_1+\mathbf{b}_2)+\kappa_b(\mathbf{b}_1^2+\mathbf{b}_2^2)]/\triangle q^2} \, \frac{\widetilde{\mathcal{T}}^2(\boldsymbol{q})}{q_z^2}, \tag{5.95}$$

and similarly, one finds for the diffuse counterpart

$$\begin{aligned} G_{\mathrm{D}}(\mathbf{q}, \mathbf{b}_1, \mathbf{b}_2, \tau) = I_0 &\left(\frac{\bar{\rho}_l \, r_e \cos\theta}{\lambda_0 L_a L_b}\right)^2 e^{-q_z^2\sigma^2} \, e^{-2\kappa_b^2(\mathbf{b}_1^2+\mathbf{b}_2^2)/\triangle q^2} \\ &\times \int_{-\infty}^{\infty} d^2\boldsymbol{q}' \; \widetilde{c}_{zz}(\boldsymbol{q}', \tau) \widetilde{\mathcal{T}}^2(\boldsymbol{q} - \boldsymbol{q}') \, e^{-2\kappa_b(\boldsymbol{q}+\boldsymbol{q}')\cdot(\mathbf{b}_1+\mathbf{b}_2)/\triangle q^2} . \end{aligned} \tag{5.96}$$

The above representations can be used to evaluate eq. (5.84). To perform the integration over the detector area we will first consider a point detector plane. The point detection scheme can be modeled by extending the integration limits in (5.84) from $-\infty$ to ∞ and by introducing a pupil function, which is defined by the 2-dimensional delta functions $\delta^2(\boldsymbol{b}_1) = \delta(b_{x_1})\delta(b_{z_1})$ and $\delta^2(\boldsymbol{b}_2) = \delta(b_{x_2})\delta(b_{z_2})$. It is then straight forward to show that the integration over $d^2b_1 d^2b_2$ yields a solution, which can simply be constructed from expression (5.95) and (5.96) at $\mathbf{b}_1 = \mathbf{b}_2 = 0$. Hence, for a point detector one finds, after integrating over $d^2b_1 d^2b_2$, the following identities

$$|G_{\mathrm{S}}(\mathbf{q}, 0, 0)| = \bar{I}_{\mathrm{S}}(\mathbf{q}) , \tag{5.97a}$$

$$\mathrm{Re}[G_{\mathrm{S}}^*(\mathbf{q}, 0, 0) G_{\mathrm{D}}(\mathbf{q}, 0, 0, \tau)] = \bar{I}_{\mathrm{S}}(\mathbf{q}) G_{\mathrm{D}}(\mathbf{q}, \tau) , \tag{5.97b}$$

where

$$G_{\mathrm{D}}(\mathbf{q}, \tau) \equiv G_{\mathrm{D}}(\mathbf{q}, 0, 0, \tau) . \tag{5.97c}$$

With the above relations we can finally express eq. (5.84) as

$$g_2(\mathbf{q}, \tau) = 1 + \frac{1}{[1 + \bar{I}_{\mathrm{D}}(\mathbf{q})/\bar{I}_{\mathrm{S}}(\mathbf{q})]^2} \left[1 + \frac{2k_BT}{\gamma} \frac{G_{\mathrm{D}}(\mathbf{q}, \tau)}{\bar{I}_{\mathrm{S}}(\mathbf{q})} + \left(\frac{k_BT}{\gamma} \frac{|G_{\mathrm{D}}(\mathbf{q}, \tau)|}{\bar{I}_{\mathrm{S}}(\mathbf{q})}\right)^2\right], \tag{5.98}$$

or explicitly as

$$g_2(\mathbf{q},\tau) = 1 + \frac{1}{\left[1 + \left(2\pi\eta/\bar{I}_{\rm S}(\boldsymbol{q},q_z)\right)\int_{-\infty}^{\infty} d^2q'\ \widetilde{c}_{zz}(\boldsymbol{q}')\bar{I}_{\rm S}(\boldsymbol{q}-\boldsymbol{q}',q_z)\right]^2} \times\left[1 + \frac{4\pi\eta}{\bar{I}_{\rm S}(\boldsymbol{q},q_z)}\int_{-\infty}^{\infty} d^2q'\ \widetilde{c}_{zz}(\boldsymbol{q}',\tau)\bar{I}_{\rm S}(\boldsymbol{q}-\boldsymbol{q}',q_z) + \left(\frac{2\pi\eta}{\bar{I}_{\rm S}(\boldsymbol{q},q_z)}\left|\int_{-\infty}^{\infty} d^2\boldsymbol{q}'\ \widetilde{c}_{zz}(\boldsymbol{q}',\tau)\bar{I}_{\rm S}(\boldsymbol{q}-\boldsymbol{q}',q_z)\right|\right)^2\right], \tag{5.99}$$

$$= 1 + \frac{1}{\left[1 + \left(2\pi\eta/\widetilde{\mathcal{T}}^2(\boldsymbol{q})\right)\int_{-\infty}^{\infty} d^2q'\ \widetilde{c}_{zz}(\boldsymbol{q}')\widetilde{\mathcal{T}}^2(\boldsymbol{q}-\boldsymbol{q}')\right]^2} \times\left[1 + \frac{4\pi\eta}{\widetilde{\mathcal{T}}^2(\boldsymbol{q})}\int_{-\infty}^{\infty} d^2q'\ \widetilde{c}_{zz}(\boldsymbol{q}',\tau)\widetilde{\mathcal{T}}^2(\boldsymbol{q}-\boldsymbol{q}') + \left(\frac{2\pi\eta}{\widetilde{\mathcal{T}}^2(\boldsymbol{q})}\left|\int_{-\infty}^{\infty} d^2\boldsymbol{q}'\ \widetilde{c}_{zz}(\boldsymbol{q}',\tau)\widetilde{\mathcal{T}}^2(\boldsymbol{q}-\boldsymbol{q}')\right|\right)^2\right], \tag{5.100}$$

where $\eta = (k_BT/2\pi\gamma)q_z^2$. Let us next examine the results eq. (5.98) and (5.99), which already reveal some constitutive properties of the intensity correlation function for surface sensitive XICS conditions.

If the specular intensity term $\bar{I}_{\rm S}(\boldsymbol{q},q_z)$ has a sufficiently small the wave vector spread $\triangle q$, then $\bar{I}_{\rm S}(\boldsymbol{q},q_z)$ tends to have a $\boldsymbol{q} = (q_x,q_y)$ dependence which acts as delta function. Hence, in that case eq. (5.98) may readily be approximated by

$$g_2(\mathbf{q},\tau) \approx 1 + \left(\frac{k_BT}{\gamma}\frac{|G_{\rm D}(\mathbf{q},\tau)|}{\bar{I}_{\rm D}(\mathbf{q})}\right)^2 \tag{5.101a}$$

$$= 1 + \left(\frac{|\widetilde{c}_{zz}(\boldsymbol{q},\tau)|}{\widetilde{c}_{zz}(\boldsymbol{q})}\right)^2 \tag{5.101b}$$

$$= 1 + \begin{cases} e^{-2\Gamma_h(q)\tau(1+q_g^2/\boldsymbol{q}^2)}, & \text{with eq. (5.78)},\\ \cos^2(\omega_s(\boldsymbol{q})\tau)\, e^{-2\Gamma_l(\boldsymbol{q})\tau}, & \text{with eq. (5.79)}, \end{cases} \tag{5.101c}$$

for all $\boldsymbol{q} \neq 0$. Note that the above normalized intensity correlation function is fully determined by the normalized height correlation function $\widetilde{c}_{zz}(\boldsymbol{q},\tau)$. Eqs. (5.101b,c) are, apart from a contrast factor β in front the second term, the conventional formulas to interpret PCS and XICS data from simple fluid

surfaces. The principle idea in such experiments is to record intensity correlation function at different $\boldsymbol{q}$-values and, consequentially, probe the dispersion and damping of surface fluctuation at different $\boldsymbol{q}$-values or respectively different length scales.

Due to eq. (5.101c), one expects for high viscosity liquids an intensity correlation function which decays as the correlation time τ increases. The data analysis is mainly focus on determining the damping constant $\Gamma_h(q)$ and its dependence on the kinetic liquid viscosity ν and surface tension γ. If the term $(q_g/\boldsymbol{q})^2$ is negligible in the investigated experimental $\boldsymbol{q}$-range, one can readily omit it in eq. (5.101c). It is worth recognizing that the regular ansatz for the normalized intensity correlation function from high viscous liquids is

$$g_2(q_x, q_y) = 1 + \beta \exp(-2\Gamma(q_x, q_y)\tau)\,. \tag{5.102}$$

Hence, it is apart from the contrast factor β equal with eq. (5.101c). In this naive approach, it is believed that all optical effects - such as partial coherence, finite instrumental resolution and near field conditions - are sufficiently described by the pre-factor β (see section 5.3 for details discussion of eq. 5.102). Even though the standard ansatz (5.102) appears to has provided a reasonable understanding of XICS experiments from complex fluids, such as polymers [66], it has however failed to explain intensity correlation data from a relatively well understood glycerol sample [85]. It is worth recognizing that the XICS data analysis in Ref.[85] did only provide resealable fluid constants, i.e. values for the ratio $\gamma/(\nu\varrho_l)$, if the factor 2 was omitted in the exponential function of eq. (5.102).

In the low viscosity case of eq. (5.101c), one expects an oscillating intensity correlation function, which decays as the correlation time τ increases. The data analysis of $g_2(\mathbf{q}, \tau)$ from low viscous liquids can, in general, be used to study the dispersion relation $\omega_s(\boldsymbol{q})$ of propagating capillary wave. Similarly, to the high viscosity liquid case one can, for instances, deduce from such intensity correlation experiments the kinetic viscosity and surface tension. The simulation of eq. (5.101c) is shown for a set of q_y-values in Fig. 5.4. The q_x-component is set to be zero in the simulation. The normalized intensity correlation for low viscous liquids is illustrated with the material constants of water at room temperature. The high viscosity case is generated with the liquids constants of glycerol at room temperature.

Note that according to (5.101c), the intensity correlation function $g_2(\mathbf{q}, \tau)$ oscillates twice as fast as the actual surface frequency $\omega_s(\boldsymbol{q})$ of propagating capillary waves. Furthermore, the time decay of $g_2(\mathbf{q}, \tau)$ is twice as fast compared to the normalized surface correlation function $\widetilde{c}_{zz}(\boldsymbol{q}, \tau)$. This feature is obviously due the exponent of 2 in eq. (5.101c), which is, in general, a characteristic feature for homodyne detection schemes [21, 20]. If, however, the

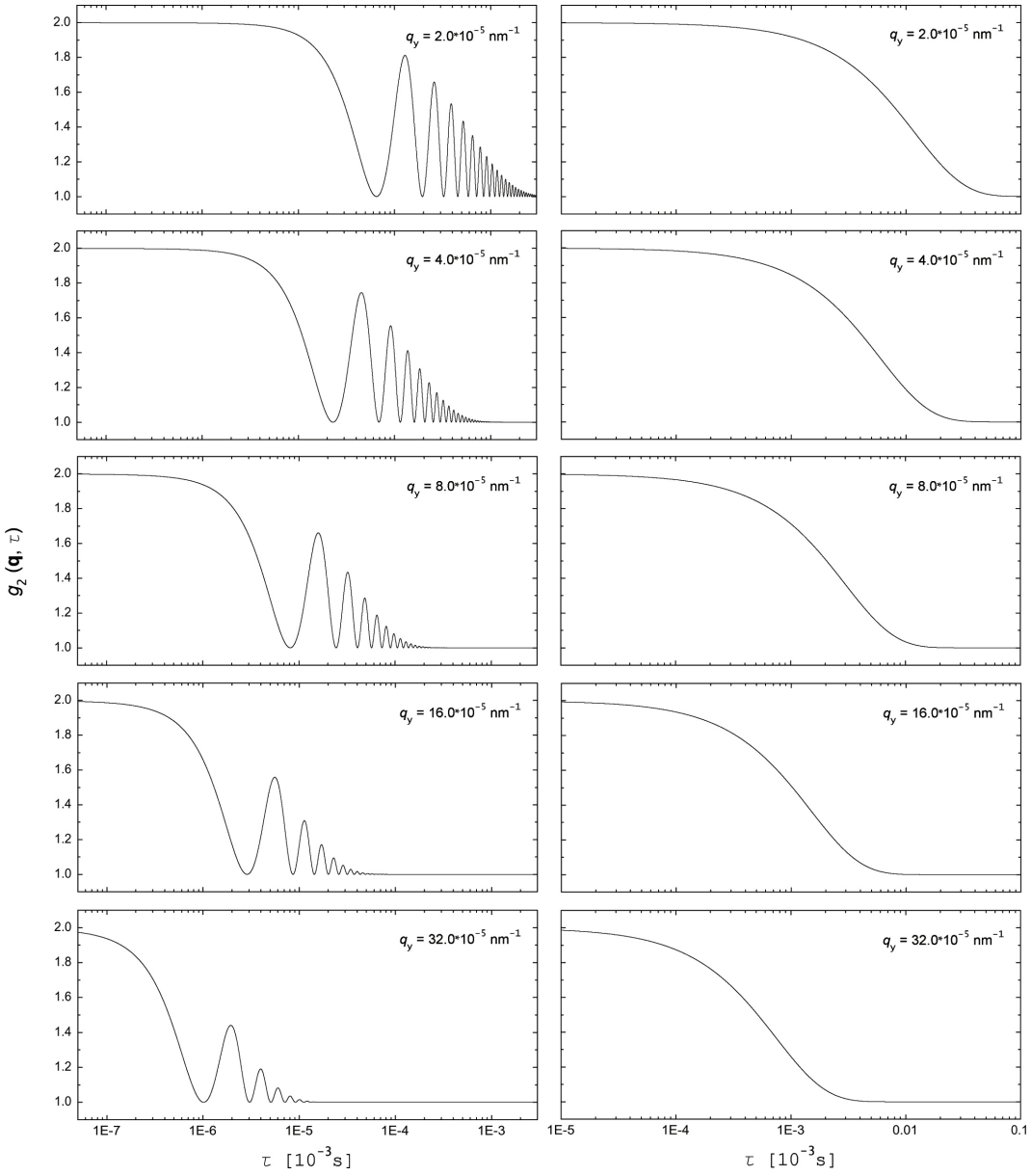

Figure 5.4: Simulations of intensity correlation functions for water and glycerol. Left side plots: Normalized intensity correlation function (5.101c) for low viscous liquids with the material constants of water at temperature $T = 20°\mathrm{C}$ ($\varrho_l = 1000\,\mathrm{kg/m^3}$, $\gamma = 0.073\,\mathrm{N/m}$ and $\nu = 1.0055 \cdot 10^{-6}\,\mathrm{m^2\,s}$). Right side plots: Normalized intensity correlation function (5.101c) for high viscous liquids with the material constants of glycerol at temperature $T = 20°\mathrm{C}$ ($\varrho_l = 1261\,\mathrm{kg/m^3}$, $\gamma = 0.062\,\mathrm{Nm^{-1}}$ and $\nu = 0.0117\,\mathrm{m^2\,s}$). The q_x-component of the wave vector transfer is set to be zero and the q_y-dependence is illustrated for both liquids at $q_y = 2.0, 4.0, 8.0, 16.0$ and $32.0 \cdot 10^{-5}\mathrm{nm}$.

scattered field is correlated with a reference beam at the detector plane, then one observes a so-called heterodyne $g_2(\mathbf{q},\tau)$ signal, which essentially refers to eq. (5.101c) with an exponent of one. Note that in Ref.[85], a heterodyne signal was observed in the XICS experiment on glycerol. Moreover, a similar correlation experiment on water provided as well a heterodyne signal [36]. These two experimental result can obviously not be explained by the simple structure of eq. (5.101c). However, eq. (5.98) is able to generate a homodyne as well as heterodyne correlation signal. The origin for the heterodyne signal can be recognized from eq. (5.99), which accounts for an optical mixing between of the static specular intensity and the dynamical diffuse field correlation function, in terms of convoluting $\bar{I}_{\mathrm{S}}(\boldsymbol{q},q_z)$ with $\widetilde{c}_{zz}(\boldsymbol{q},\tau)$. The heterodyne term becomes significant for small wave vector transfers $\boldsymbol{q}$ or for broad specular beams, i.e. large wave vector spread $\triangle q$. The transition from a homodyne to a heterodyne intensity correlation function is illustrated for different ratios of $\triangle q/\boldsymbol{q}$ in Fig. 5.5 and Fig. 5.6 for water and glycerol at room temperature, respectively. The transition comes along with an addition damping of $g_2(\mathbf{q},\tau)$, which is due to resolution effects. Another condition which could case the observation of a heterodyne signal for water and glycerol might be the relatively high surface tension or, in principle, a small $\eta = (k_B T/2\pi\gamma)q_z^2$ value (see condition (5.86) or eq. (5.99)). This interpretation is also in agreement with the observation of homodyne intensity correlation signals from liquids with low surface tension (i.e. $\gamma = (0.02 - 0.04)\,\mathrm{Nm}^{-1}$), such as hexane and polystyrene [44].

Next, we will define a measure for the visibility of the normalized intensity correlation function as

$$\mathcal{V}(\mathbf{q}) \equiv g_2(\mathbf{q},0) - \lim_{\tau\to\infty} g_2(\mathbf{q},\tau)\,. \tag{5.103}$$

In the Fraunhofer point-source/detector condition, one easily obtains finds with eq. (5.103) and (5.98) the visibility

$$\mathcal{V}(\mathbf{q}) = 1 - \frac{1}{\left[1 + \bar{I}_{\mathrm{D}}(\mathbf{q})/\bar{I}_{\mathrm{S}}(\mathbf{q})\right]^2}\,. \tag{5.104}$$

According to (5.104), the visibility yields one for $\triangle q/\boldsymbol{q} \to 0$ and tends to zero in the limit $\triangle q/\boldsymbol{q} \to \infty$. It is worth noting, that the $g_2(\mathbf{q},\tau)$ function is a constant at $\tau = 0$, which therefore explains why the origin of $g_2(\mathbf{q},\tau=0)$ is independent from $\triangle q/\boldsymbol{q}$ ratios, see Fig. 5.5 and Fig. 5.6.

B. Fraunhofer finite-source/point-detector conditions

The resolution effect in the previous example was based on the finite sample area and therefore on the sample truncation function $\widetilde{\mathcal{T}}(\boldsymbol{q})$. A more realistic

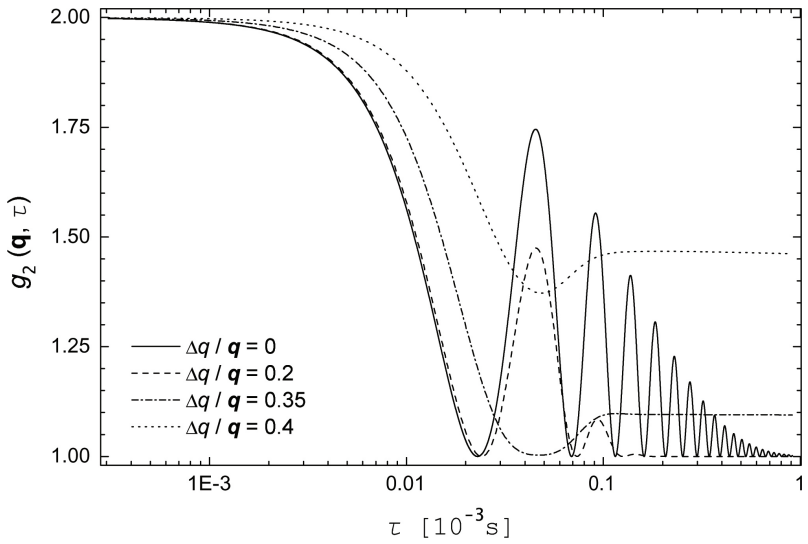

Figure 5.5: The transition from a homodyne to a heterodyne signal is illustrated for water. The resolution dependent normalized intensity correlation function $g_2(\mathbf{q}, \tau)$ is plotted for water at room temperature. The scattering angles are $\alpha_\mathrm{i} = 0.1°$, $\alpha_\mathrm{f} \approx 0.128°$ and $\varphi = 0°$. The corresponding wave vector transfer is $\mathbf{q} = (q_x = 0, q_y = 4 \cdot 10^{-5}\mathrm{nm}^{-1}, 16160 \cdot 10^{-5}\mathrm{nm}^{-1})$. The solid line represent the case with no uncertainty in the wave vector transfer (see eq. (5.101c)). The transition from a homodyne to a heterodyne signal occurs as $\triangle q$ increases. This transition comes along with an addition damping of $g_2(\mathbf{q}, \tau)$, which is due to resolution effects (see the convolution integrals in eq. (5.99) or (5.100)).

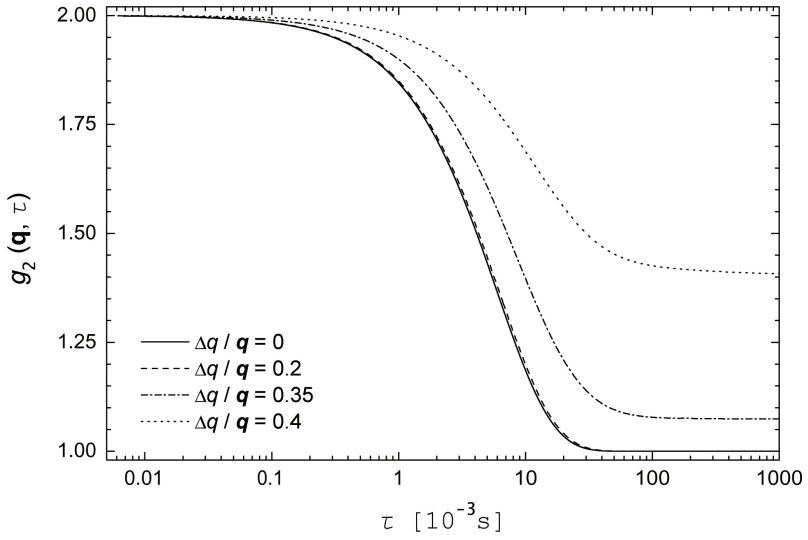

Figure 5.6: The transition from a homodyne to a heterodyne signal is illustrated for glycerol at room temperature. The wave vector transfer $\mathbf{q}$ is the same as in Fig. 5.5.

truncation effect occurs, however, due to the finite beam footprint on the sample surface, which is ordinarily smaller than the sample surface and thus it is the effective truncation of the scattering area in conventional surface sensitive XICS experiments. To illustrate this situation, we will consider here a finite source with symmetrical linear dimensions in the a_x and a_z directions, hence $\triangle a_x = \triangle a_z = \triangle a$. Furthermore, we will assume that the source is partially coherence with asymmetric spatial coherence conditions across the source plane, i.e $\xi_{tx} \neq \xi_{tz}$. The above source conditions will be modeled here with the Gaussian-Schell source model. Hence, if the actual sample size is irrelevant in an XICS experiment, one can express eq. (5.91) as

$$\mathcal{G}_t(\boldsymbol{R}, \mathbf{b}_1, \mathbf{b}_2) = \int_{-\infty}^{\infty} d^2 r_1' \; J_i(\boldsymbol{r}_1', \boldsymbol{r}_1' + \boldsymbol{R}) D(\boldsymbol{r}_1', \boldsymbol{r}_1' + \boldsymbol{R}, \mathbf{b}_1, \mathbf{b}_2)\,, \tag{5.105}$$

where the incident mutual intensity function $J_i(\boldsymbol{r}_1', \boldsymbol{r}_1' + \boldsymbol{R})$ is given by (4.115). The evaluation of eq. (5.105) is relatively simple and therefore omitted. In the point detection scheme, one finds the following $g_2(\mathbf{q}, \tau)$ expression

$$\begin{aligned} g_2(\mathbf{q}, \tau) = 1 + & \frac{1}{\left[1 + \left(2\pi\eta / \widetilde{\mathcal{T}}_B^2(\boldsymbol{q})\right) \int_{-\infty}^{\infty} d^2 q' \; \widetilde{c}_{zz}(\boldsymbol{q}') \widetilde{\mathcal{T}}_B^2(\boldsymbol{q} - \boldsymbol{q}')\right]^2} \\ & \times \left[1 + \frac{4\pi\eta}{\widetilde{\mathcal{T}}_B^2(\boldsymbol{q})} \int_{-\infty}^{\infty} d^2 q' \; \widetilde{c}_{zz}(\boldsymbol{q}', \tau) \widetilde{\mathcal{T}}_B^2(\boldsymbol{q} - \boldsymbol{q}') \right. \\ & \left. + \left(\frac{2\pi\eta}{\widetilde{\mathcal{T}}_B^2(\boldsymbol{q})} \left| \int_{-\infty}^{\infty} d^2 \boldsymbol{q}' \; \widetilde{c}_{zz}(\boldsymbol{q}', \tau) \widetilde{\mathcal{T}}_B^2(\boldsymbol{q} - \boldsymbol{q}') \right| \right)^2 \right], \end{aligned} \tag{5.106}$$

where

$$\widetilde{\mathcal{T}}_B(\boldsymbol{q}) = \left(\frac{\sqrt{2\pi}}{\triangle q_x} \; e^{-q_x^2 / 2\triangle q_x^2} \right) \left(\frac{\sqrt{2\pi}}{\triangle q_y} \; e^{-q_y^2 / 2\triangle q_y^2} \right). \tag{5.107}$$

The above formula (5.106) is structural wise identical with our previous solution eq. (5.100). However, the new beam truncation function $\widetilde{\mathcal{T}}_B(\boldsymbol{q})$ results from the finite beam footprint on the sample, and the wave vector spreads $\triangle q_x$ and $\triangle q_y$ are determined by the source size and spatial coherence. Their explicit representations are

$$\triangle q_x = \sqrt{\frac{2}{\Xi_{tx}^2} + \frac{1}{\Sigma_x^2}\Big(1 + (k_0 \triangle a^2 / L_a)^2\Big)}\,, \tag{5.108a}$$

$$\triangle q_y = \sqrt{\frac{2}{\Xi_{ty}^2} + \frac{1}{\Sigma_y^2}\Big(1 + (k_0 \triangle a^2 / L_a)^2\Big)}\,, \tag{5.108b}$$

where Ξ_{tx} and Ξ_{ty} are the incident transverse coherence lengths on the sample surface, see eq. (4.117c) and (4.117d). The size of beam footprint is determined by the beam waists Σ_x and Σ_y, which are defined in eq. (4.117a) and (4.117b). In order to justify the above Fraunhofer approximation, the following two conditions should be satisfied

$$\left|\frac{\Sigma_x^2+\Sigma_y^2\sin^2\alpha_{\rm i}}{L_a}\right|_{max}, \quad \left|\frac{\Sigma_x^2+\Sigma_y^2\sin^2\alpha_{\rm f}}{L_b}\right|_{max} \ll \lambda_0\,. \tag{5.109}$$

For symmetrical transverse source coherence, i.e. $\xi_{tz}=\xi_{tx}=\xi_t$, one finds the relation $\triangle q_y = \triangle q_x \sin\alpha_{\rm i}$, which clearly reveals the asymmetric resolution effects of the beam footprint.

C. Fraunhofer point-source/finite-detector conditions

To illustrated the effect of finite detector resolution, we will model the detection plane with a Gaussian function, which shall have a symmetric width $\triangle b$ in the b_x and b_z direction. We consider again an in-plane scattering geometry with $\varphi=0$, hence $q_x=0$. The $g_2(\mathbf{q},\tau)$ function takes then the form

$$\begin{aligned} g_2(\mathbf{q},\tau) = 1 + \frac{1}{(1+\bar{I}_{\rm D}(\mathbf{q})/\bar{I}_{\rm S}(\mathbf{q}))^2}\iint_{-\infty}^{\infty} d^2b_1 d^2b_2\; e^{-(\boldsymbol{b}_1^2+\boldsymbol{b}_2^2)/2\triangle b^2} \\ \times\left[\frac{|G_{\rm S}(\mathbf{q},\mathbf{b}_1,\mathbf{b}_2)|^2}{\bar{I}_{\rm S}^2(\mathbf{q})} + \left(\frac{2k_BT}{\gamma}\right)\frac{{\rm Re}[G_{\rm S}^*(\mathbf{q},\mathbf{b}_1,\mathbf{b}_2)G_{\rm D}(\mathbf{q},\mathbf{b}_1,\mathbf{b}_2,\tau)]}{\bar{I}_{\rm S}^2(\mathbf{q})}\right. \\ \left. + \left(\frac{k_BT}{\gamma}\right)^2\frac{|G_{\rm D}(\mathbf{q},\mathbf{b}_1,\mathbf{b}_2,\tau)|^2}{\bar{I}_{\rm S}^2(\mathbf{q})}\right], \end{aligned} \tag{5.110}$$

where $\boldsymbol{b}^2 = b_x^2+b_z^2$, $\mathbf{b}^2 = b_x^2+b_z^2\sin^2\alpha_{\rm f}$ and $\boldsymbol{q}\cdot\mathbf{b} = -q_y b_z \sin\alpha_{\rm f}$. On using these relations and expressions (5.95) and (5.96), we obtain after a straight forward

calculation the following $g_2(\boldsymbol{q},\tau)$ formula

$$g_2(\mathbf{q},\tau) = 1 + \frac{1}{\left[1+\frac{2\pi\eta}{\widetilde{\mathcal{T}}^2(\boldsymbol{q})\widetilde{\mathcal{T}}_D(\boldsymbol{q})}\int_{-\infty}^{\infty} d^2q'\ \widetilde{c}_{zz}(\boldsymbol{q}')\widetilde{\mathcal{T}}^2(\boldsymbol{q}-\boldsymbol{q}')\widetilde{\mathcal{T}}_D(\boldsymbol{q}-\boldsymbol{q}')\right]^2}$$
$$\times\Bigg[1+\frac{4\pi\eta}{\widetilde{\mathcal{T}}^2(\boldsymbol{q})\widetilde{\mathcal{T}}_D^2(\boldsymbol{q})}\int_{-\infty}^{\infty} d^2q'\,\widetilde{c}_{zz}(\boldsymbol{q}',\tau)\widetilde{\mathcal{T}}^2(\boldsymbol{q}-\boldsymbol{q}')\widetilde{\mathcal{T}}_D^2(\boldsymbol{q}-\boldsymbol{q}'/2)$$
$$+\left(\frac{2\pi\eta}{\widetilde{\mathcal{T}}^2(\boldsymbol{q})\widetilde{\mathcal{T}}_D^2(\boldsymbol{q})}\right)^2$$
$$\times\iint_{-\infty}^{\infty} d^2q_1'd^2q_2'\,\widetilde{c}_{zz}(\boldsymbol{q}_1',\tau)\widetilde{c}_{zz}(\boldsymbol{q}_2',\tau)\widetilde{\mathcal{T}}^2(\boldsymbol{q}-\boldsymbol{q}_1')\widetilde{\mathcal{T}}^2(\boldsymbol{q}-\boldsymbol{q}_2')\widetilde{\mathcal{T}}_D^2(\boldsymbol{q}-(\boldsymbol{q}_1'+\boldsymbol{q}_2')/2)\Bigg], \tag{5.111}$$

where

$$\widetilde{\mathcal{T}}_D(\boldsymbol{q}-\boldsymbol{q}') = \exp\left\{\frac{q_x'^2}{2\triangle q^2}\frac{\left(\frac{k_0\triangle b}{L_b\triangle q}\right)^2}{1/2+\left(\frac{k_0\triangle b}{L_b\triangle q}\right)^2}\right\}$$
$$\times\exp\left\{\frac{(q_y-q_y')^2}{2\triangle q^2}\frac{\left(\sin\alpha_{\mathrm{f}}\frac{k_0\triangle b}{L_b\triangle q}\right)^2}{1/2+\left(\sin\alpha_{\mathrm{f}}\frac{k_0\triangle b}{L_b\triangle q}\right)^2}\right\}. \tag{5.112}$$

The structural form of the above formula holds also for *Fraunhofer finite-source/detector conditions*, if the sample truncation function is replaced by a beam truncation function, see previous section. An interesting consequence of the finite detector plane is that the contrast of the normalized intensity correlation function is reduced at $\tau = 0$. This contrast reduction is shown in Fig. 5.7 and Fig. 5.8 for a homodyne dominated correlation signal of water and glycerol, respectively. It appears, that the effect of finite detector resolution on $g_2(\mathbf{q},\tau)$ could be taken into account by simply introducing a weighting factor in eq. (5.106) or eq. (5.100). Such simplified treatments may only be useful in the analysis of XICS data if the relatively small frequency shift, which can be seen in Fig. 5.7, is negligible.

D. Fresnel finite-source/point-detector conditions

The calculation of Fresnel case is to a large extent identical to the Fraunhofer examples and will therefore be omitted. If $\varphi = 0$ and $\triangle a = \triangle a_x = \triangle a_z$, one finds in the Fresnel finite-source/point-detector case an identical formula

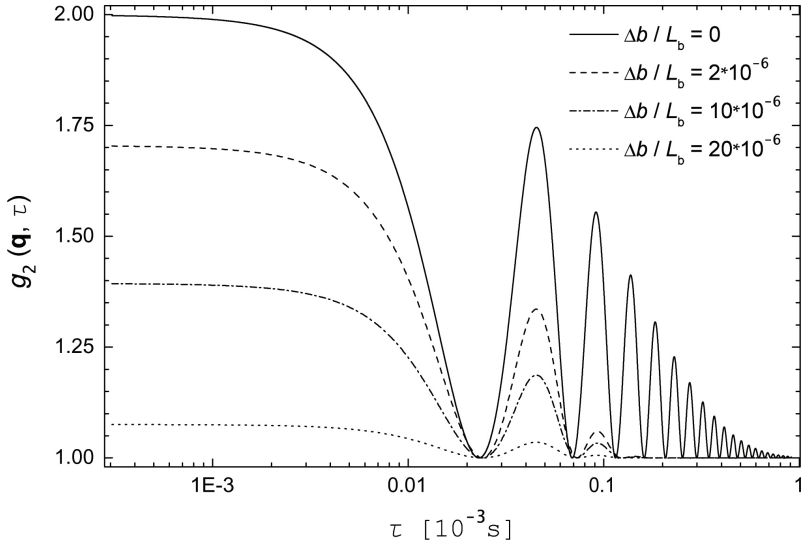

Figure 5.7: The effect of finite detector resolution is illustrated for a homodyne dominated $g_2(\mathbf{q}, \tau)$ function for water at room temperature. The solid line represent the case with no uncertainty in the wave vector transfer and detector resolution (see eq. (5.101c)). The parameter for the other curves are $\triangle q/\boldsymbol{q} = 0.2$ and different ratios of $\triangle b/L_b$. All other parameters are the same as in Fig. 5.5. The simulation yields with increasing detector opening $\triangle b$ a reduces visibility of the $g_2(\mathbf{q}, \tau)$ function.

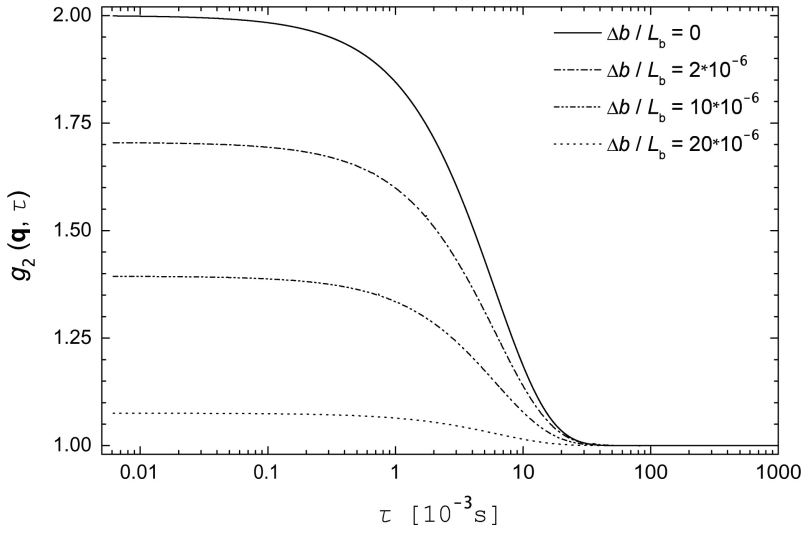

Figure 5.8: The effect of finite detector resolution is illustrated for a homodyne dominated $g_2(\mathbf{q}, \tau)$ function for glycerol at room temperature. The solid line represent the case with no uncertainty in the wave vector transfer and detector resolution (see eq. (5.101c)). The scattering parameters are the same as in Fig. 5.7.

as eq. (5.106). However, the wave vector spreads in eq. (5.108a) and (5.108b) transform in Fresnel limit to

$$\triangle q_x = \sqrt{\frac{2}{\Xi_{tx}^2} + \frac{1}{\Sigma_x^2}\left(1 + (k_0 \triangle a^2/L_a)^2 \left(1 - \frac{\Sigma_x^2}{\triangle a^2}\frac{L_a + L_b}{L_b}\right)^2\right)}\,, \tag{5.113a}$$

$$\triangle q_y = \sqrt{\frac{2}{\Xi_{ty}^2} + \frac{1}{\Sigma_y^2}\left(1 + (k_0 \triangle a^2/L_a)^2 \left(1 - \frac{\Sigma_y^2}{\triangle a^2}\frac{L_a \sin^2\alpha_\mathrm{f} + L_b \sin^2\alpha_\mathrm{i}}{L_b}\right)^2\right)}\,, \tag{5.113b}$$

where the incident transverse coherence lengths and the beam widths are defined in subsection 4.3.4. In comparison to eq. (5.108b) and (5.108b), we find a reduced uncertainty in the wave spread. Furthermore, $\triangle q_y$ depends here on the scattering angle α_f.

D. Fresnel finite-source/detector conditions

We consider again in-plane scattering conditions, i.e. $\varphi = 0$, and a symmetric source and detector shape, hence $\triangle a = \triangle a_x = \triangle a_z$ and $\triangle b = \triangle b_x = \triangle b_z$. The calculation of this Fresnel case yields the following $g_2(\boldsymbol{q}, \tau)$ formula

$$\begin{aligned} g_2(\mathbf{q},\tau) = 1 &+ \frac{1}{\left[1 + \frac{2\pi\eta}{\widetilde{\mathcal{T}}_B^2(\boldsymbol{q})\widetilde{\mathcal{T}}_D(\boldsymbol{q})}\int_{-\infty}^{\infty} d^2q'\; \widetilde{c}_{zz}(\boldsymbol{q}')\widetilde{\mathcal{T}}_B^2(\boldsymbol{q}-\boldsymbol{q}')\widetilde{\mathcal{T}}_D(\boldsymbol{q}-\boldsymbol{q}')\right]^2} \\ &\times \Bigg[1 + \frac{4\pi\eta}{\widetilde{\mathcal{T}}_B^2(\boldsymbol{q})\widetilde{\mathcal{T}}_D^2(\boldsymbol{q})}\int_{-\infty}^{\infty} d^2q'\, \widetilde{c}_{zz}(\boldsymbol{q}',\tau)\widetilde{\mathcal{T}}_B^2(\boldsymbol{q}-\boldsymbol{q}')\widetilde{\mathcal{T}}_D^2(\boldsymbol{q}-\boldsymbol{q}'/2) \\ &+ \left(\frac{2\pi\eta}{\widetilde{\mathcal{T}}_B^2(\boldsymbol{q})\widetilde{\mathcal{T}}_D^2(\boldsymbol{q})}\right)^2 \\ &\times \iint_{-\infty}^{\infty} d^2q_1' d^2q_2'\, \widetilde{c}_{zz}(\boldsymbol{q}_1',\tau)\widetilde{c}_{zz}(\boldsymbol{q}_2',\tau)\widetilde{\mathcal{T}}_B^2(\boldsymbol{q}-\boldsymbol{q}_1')\widetilde{\mathcal{T}}_B^2(\boldsymbol{q}-\boldsymbol{q}_2')\widetilde{\mathcal{T}}_D^2(\boldsymbol{q}-(\boldsymbol{q}_1'+\boldsymbol{q}_2')/2)\Bigg], \end{aligned} \tag{5.114}$$

where

$$\widetilde{\mathcal{T}}_B(\boldsymbol{q}-\boldsymbol{q}') = \left(\frac{\sqrt{2\pi}}{\triangle q_x} e^{-q_x'^2/2\triangle q_x^2}\right)\left(\frac{\sqrt{2\pi}}{\triangle q_y} e^{-(q_y-q_y')^2/2\triangle q_y^2}\right), \tag{5.115}$$

$$\widetilde{\mathcal{T}}_D(\boldsymbol{q}-\boldsymbol{q}') = \exp\left\{\frac{q_x'^2}{2\triangle q_x^2}\frac{\left(\frac{k_0\triangle b}{L_b\triangle q_x}\right)^2}{1/2+\left(\frac{k_0\triangle b}{L_b\triangle q_x}\right)^2(1+\triangle q_x^2\Sigma_x^2)}\right\}$$
$$\times\exp\left\{\frac{(q_y-q_y')^2}{2\triangle q_y^2}\frac{\left(\sin\alpha_{\mathrm{f}}\frac{k_0\triangle b}{L_b\triangle q_y}\right)^2}{1/2+\left(\sin\alpha_{\mathrm{f}}\frac{k_0\triangle b}{L_b\triangle q_y}\right)^2(1+\triangle q_y^2\Sigma_y^2)}\right\}. \quad (5.116)$$

The wave vector spreads $\triangle q_x$ and $\triangle q_y$ are respectively defined in eq. (5.113a) and (5.113b). The above solution for $g_2(\boldsymbol{q},\tau)$ is closely related to the Fraunhofer result. The only difference between the Fraunhofer and the Fresnel limit yields to be the different definitions of the wave vector spreads.

5.3 Pusey's Formulation of the Intensity Correlation Function

The intensity correlation function in the previous sections was based on the Siegert relation, hence on the Gaussian statistics of the scattered fields. The main problem of this approach is that the finite longitudinal coherence length of the X-ray beam can not be included [56].

An alternative approach to derive the intensity correlation function was provided by P. N. Pusey [77]. Pusey's derivation of the intensity correlation function is essentially based on the statistical properties of the electron density rather than the scattered fields. Although, this approach appears to be more reasonable it is mainly based on assumptions which only hold for XICS measurements that are sensitive to short range density fluctuations. Furthermore, it should be realized that Pusey's derivation is entirely funded on conditions which are met in laser light scattering experiments, e.g. Fraunhofer conditions and excellent coherence properties of the light beam.

We will briefly illustrate the central assumption and approximation made in Pusey's calculation. For this purpose we will first construct the G_2-function by making use of the right-hand side of eq. (5.24), hence

$$G_2(\mathbf{r}_1,\mathbf{r}_2,\tau) = \left(\frac{r_e}{L_b}\right)^4\iiiint_V d^3\mathrm{r}_1' d^3\mathrm{r}_2' d^3\mathrm{r}_3' d^3\mathrm{r}_4'$$
$$\times\langle\rho(\mathbf{r}_1',t_1-R_1/c)\rho(\mathbf{r}_2',t_1-R_2/c)\rho(\mathbf{r}_3',t_2-R_3/c)\rho(\mathbf{r}_4',t_2-R_4/c)\rangle$$
$$\times\langle U_i^*(\mathbf{r}_1',t_1-R_1/c)U_i(\mathbf{r}_2',t_1-R_2/c)U_i^*(\mathbf{r}_3',t_2-R_3/c)U_i(\mathbf{r}_4',t_2-R_4/c)\rangle\,. \quad (5.117)$$

If the incident fields are Gaussian random variable and obey the condition of statistical stationary, we can use the below statistical identity [58]

$$\langle U_i^*(\mathbf{r}_1,t_1)U_i(\mathbf{r}_2,t_1)U_i^*(\mathbf{r}_3,t_2)U_i(\mathbf{r}_4,t_2)\rangle = \Gamma_i(\mathbf{r}_1,\mathbf{r}_2,0)\Gamma_i(\mathbf{r}_3,\mathbf{r}_4,0) + \Gamma_i^*(\mathbf{r}_2,\mathbf{r}_3,\tau)\Gamma_i(\mathbf{r}_1,\mathbf{r}_4,\tau)\,, \quad (5.118)$$

where $\tau = t_2 - t_1$. Since the correlation time of the incident fields is typically of the order of 10^{-14}s, we will neglect the time dependent mutual coherence functions in (5.118). These terms contribute only on extremely short time scales at which the sample typically relies no dynamics. Hence, the incident field correlations in eq. (5.117) may be approximated by

$$\langle U_i^*(\mathbf{r}_1',t_1-R_1/c)U_i(\mathbf{r}_2',t_1-R_2/c)U_i^*(\mathbf{r}_3',t_2-R_3/c)U_i(\mathbf{r}_4',t_2-R_4/c)\rangle \approx \Gamma_i(\mathbf{r}_1',\mathbf{r}_2',(R_2-R_1)/c)\Gamma_i(\mathbf{r}_3',\mathbf{r}_4',(R_4-R_3)/c)\,. \quad (5.119)$$

If we next use (5.119) in eq. (5.117) and ignore the retardation term R/c in the electron density, we find

$$G_2(\mathbf{r}_1,\mathbf{r}_2,\tau) = \left(\frac{r_e}{L_b}\right)^4 \iiiint_V d^3\mathrm{r}_1' d^3\mathrm{r}_2' d^3\mathrm{r}_3' d^3\mathrm{r}_4' \times\langle\rho(\mathbf{r}_1',t_1)\rho(\mathbf{r}_2',t_1)\rho(\mathbf{r}_3',t_2)\rho(\mathbf{r}_4',t_2)\rangle \times\Gamma_i(\mathbf{r}_1',\mathbf{r}_2',(R_2-R_1)/c)\Gamma_i(\mathbf{r}_3',\mathbf{r}_4',(R_4-R_3)/c)\,. \quad (5.120)$$

On using the envelop representation for the incident fields, i.e. $U_i(\mathbf{r}',t) = U(\mathbf{r}',t)e^{i(\mathbf{k}_\mathrm{i}\cdot\mathbf{r}'-\omega_0 t)}$, one readily finds in the Fraunhofer limit the below representation for (5.120):

$$G_2(\mathbf{r}_1,\mathbf{r}_2,\tau) = \left(\frac{r_e}{L_b}\right)^4 \iiiint_V d^3\mathrm{r}_1' d^3\mathrm{r}_2' d^3\mathrm{r}_3' d^3\mathrm{r}_4' \times\langle\rho(\mathbf{r}_1',t_1)\rho(\mathbf{r}_2',t_1)\rho(\mathbf{r}_3',t_2)\rho(\mathbf{r}_4',t_2)\rangle \times\Gamma(\mathbf{r}_1',\mathbf{r}_2',(R_2-R_1)/c)\Gamma(\mathbf{r}_3',\mathbf{r}_4',(R_4-R_3)/c)\; e^{-i\mathbf{q}\cdot(\mathbf{r}_1'-\mathbf{r}_2'+\mathbf{r}_3'-\mathbf{r}_4')}\,, \quad (5.121)$$

where the above mutual coherence function refer to incident field amplitudes. Next, let the electron density be a Gaussian random variable. We can then use the Gaussian moment theorem to reduce the fourth-order correlation term into a sum of second-order correlations terms [58], hence

$$\langle\rho(\mathbf{r}_1',t_1)\rho(\mathbf{r}_2',t_1)\rho(\mathbf{r}_3',t_2)\rho(\mathbf{r}_4',t_2)\rangle = \langle\rho(\mathbf{r}_1',t_1)\rho(\mathbf{r}_2',t_1)\rangle\langle\rho(\mathbf{r}_3',t_2)\rho(\mathbf{r}_4',t_2)\rangle + \langle\rho(\mathbf{r}_1',t_1)\rho(\mathbf{r}_3',t_2)\rangle\langle\rho(\mathbf{r}_2',t_1)\rho(\mathbf{r}_4',t_2)\rangle + \langle\rho(\mathbf{r}_1',t_1)\rho(\mathbf{r}_4',t_2)\rangle\langle\rho(\mathbf{r}_2',t_1)\rho(\mathbf{r}_3',t_2)\rangle\,. \quad (5.122)$$

Introducing this expansion into eq. (5.121) yields a sum of three correlation terms, which can be expressed as $G_2(\mathbf{r}_1, \mathbf{r}_2, \tau) = G_2^{(1)}(\mathbf{r}_1, \mathbf{r}_2) + G_2^{(2)}(\mathbf{r}_1, \mathbf{r}_2, \tau) + G_2^{(3)}(\mathbf{r}_1, \mathbf{r}_2, \tau)$. If the electron density fluctuations are statistically stationary, then the first term $G_2^{(1)}(\mathbf{r}_1, \mathbf{r}_2)$ simply refers to the mean static intensity at the positions $\mathbf{r}_1$ and $\mathbf{r}_2$, i.e $\langle I(\mathbf{r}_1, t_1)\rangle\langle I(\mathbf{r}_2, t_2)\rangle$. The second term $G_2^{(2)}(\mathbf{r}_1, \mathbf{r}_2, \tau)$ depends on the correlation terms $\langle\rho(\mathbf{r}_1', t_1)\rho(\mathbf{r}_3', t_1)\rangle$ and $\langle\rho(\mathbf{r}_2', t_2)\rho(\mathbf{r}_4', t_2)\rangle$. These terms are ignored in Pusey's derivation, based on the argument that their contribution is only significant for small vector differences $\mathbf{r}_3' - \mathbf{r}_1'$ and $\mathbf{r}_4' - \mathbf{r}_2'$, which only occurs if the scattering angle is zero [77, 96]. With the condition of statistical homogeneity for electron density fluctuations, as well as the above approximations, one can reduce eq. (5.121) to

$$\begin{aligned} G_2(\mathbf{r}_1, \mathbf{r}_2, \tau) = \langle I(\mathbf{r}_1, t_1)\rangle\langle I(\mathbf{r}_2, t_2)\rangle + \left(\frac{r_e}{L_b}\right)^4 \iiiint_V d^3\mathrm{r}_1' d^3\mathrm{r}_2' d^3\mathrm{r}_3' d^3\mathrm{r}_4' \\ \times\langle\rho(0,0)\rho(\mathbf{r}_4' - \mathbf{r}_1', \tau)\rangle\langle\rho(0,0)\rho(\mathbf{r}_3' - \mathbf{r}_2', \tau)\rangle \\ \times\Gamma(\mathbf{r}_1', \mathbf{r}_2', (R_2 - R_1)/c)\Gamma(\mathbf{r}_3', \mathbf{r}_4', (R_4 - R_3)/c)\, e^{-i\mathbf{q}\cdot(\mathbf{r}_1' - \mathbf{r}_2' + \mathbf{r}_3' - \mathbf{r}_4')}\,. \end{aligned} \tag{5.123}$$

The above formula can be substantially simplified by assuming that the incident fields have a large longitudinal and transverse coherence length compared to the bulk correlation length of the scatterer, i.e. $\xi_l, \xi_t \gg \ell_b$. If this condition, as well as $V \gg \ell_b$, is satisfied within the scattering volume V, then one can treat the mutual coherence functions as constant factors in the integrand of eq. (5.123), thus they can be pulled out of the integral and evaluated separately. Conclusively, one finds after some algebra the below normalized intensity correlation function

$$\begin{aligned} g_2(\mathbf{r}_1, \mathbf{r}_2, \tau) &= \frac{G_2(\mathbf{r}_1, \mathbf{r}_2, \tau)}{\langle I(\mathbf{r}_1, t_1)\rangle\langle I(\mathbf{r}_2, t_2)\rangle} \\ &= 1 + \beta(\mathbf{r}_1, \mathbf{r}_2)\left|\int_V d^3\mathrm{r}'\,\langle\rho(0,0)\rho(\mathbf{r}', \tau)\rangle\; e^{i\mathbf{q}\cdot\mathbf{r}'}\right|^2, \end{aligned} \tag{5.124}$$

where $\beta(\mathbf{r}_1, \mathbf{r}_2)$ depends on the static intensity terms, as well as the mutual coherence functions. Note that a formally equivalent expression can be found even if the finite detector resolution is considers. Hence, even with detector resolution one may arrive at the below result

$$g_2(\mathbf{q}, \tau) = 1 + \beta\left|\int_V d^3\mathrm{r}'\,\langle\rho(0,0)\rho(\mathbf{r}', \tau)\rangle\; e^{i\mathbf{q}\cdot\mathbf{r}'}\right|^2, \tag{5.125}$$

where the normalized intensity correlation function is formally expressed as a function of the wave vector transfer. Eq. (5.125) is essentially the $g_2(\mathbf{q}, \tau)$

representation which was first derived by Pusey [77]. Alternatively, one can represent Pusey's $g_2(\mathbf{q},\tau)$ function in terms of the intermediate scattering function $S(\mathbf{q},\tau)$ [54], hence

$$g_2(\mathbf{q},\tau) = 1 + \beta \left| \frac{S(\mathbf{q},\tau)}{S(\mathbf{q})} \right|^2 , \tag{5.126}$$

with

$$S(\mathbf{q},\tau) = \int_V d^3\mathrm{r}'\, C_{\rho\rho}(\mathbf{r}',\tau)\; e^{i\mathbf{q}\cdot\mathbf{r}'} . \tag{5.127}$$

and $C_{\rho\rho}(\mathbf{r}',\tau) = \langle \rho(0,0)\rho(\mathbf{r}',\tau)\rangle$ denotes the density correlation function. The normalization with static intermediate scattering function $S(\mathbf{q}) = S(\mathbf{q},0)$ results form the normalization with the static intensity terms, see eq. (5.124). Hence, in the above formulation of $g_2(\mathbf{q},\tau)$, the optical contrast factor β account only for effects of partial coherence and detector resolution. A further approximation of eq. (5.126) can be obtained if the scattering volume is the sufficiently large. With this approximation one finally finds the $g_2(\mathbf{q},\tau)$ expression which is conventionally used to interpret DLS experiments from density fluctuations, viz.

$$g_2(\mathbf{q},\tau) \approx 1 + \beta \left| \frac{\widetilde{C}_{\rho\rho}(\mathbf{q},\tau)}{\widetilde{C}_{\rho\rho}(\mathbf{q})} \right|^2 . \tag{5.128}$$

Based on the above formula, it is customarily assumed that the $g_2(\mathbf{q},\tau)$ expression for surface sensitive XICS experiments is of a similar form, namely

$$g_2(\boldsymbol{q},\tau) = 1 + \beta \left| \frac{\widetilde{C}_{zz}(\boldsymbol{q},\tau)}{\widetilde{C}_{zz}(\boldsymbol{q})} \right|^2 , \tag{5.129}$$

where $\widetilde{C}_{zz}(\boldsymbol{q},\tau)$ is the time dependent surface height correlation function in reciprocal space, see chapter 2.

It is important to realize that the ordinarily used $g_2(\mathbf{q},\tau)$ expression for surface sensitive XICS experiments is only based on plausibility arguments. Eq. (5.129) can not be derived from (5.128). Note that the most fruitful assumption in Pusey's derivation is based on the comparison between the coherence length of the incident light beam and the bulk correlation length of the sample, i.e. $\xi_l, \xi_t \gg \ell_b$. It is obvious that the condition $\xi_l, \xi_t \gg \ell_b$ is allows fulfilled for DLS experiments from inhomogeneous media, however for surface sensitive XICS experiments the condition $\xi_l, \xi_t \gg \ell_s$ has to be satisfied, where ℓ_s is the surface correlation length. Since, $\ell_b \ll \ell_s \sim (1-4)mm$ and

$\xi_l, \xi_t \sim (1 - 100)\mu$m the condition $\xi_l, \xi_t \gg \ell_s$ is clearly not fulfilled in surface sensitive XICS experiments. Accordingly, one can not describe the influences of the partially coherent X-ray beam by a trivial contrast factor β. In summary, the conventionally used $g_2(\mathbf{q}, \tau)$ expression (5.129) for surface sensitive XICS experiments has no theoretical foundation and it has clearly failed to provide a reasonable explanation for surface sensitive XICS data from water and glycerol [36, 85].

Chapter 6

Experimental Part

In the chapters we will present and analyze XICS experiments from water and hexane surfaces. Both measurements were carried out with partially coherent X-rays at beamline ID10A (Troïka) at the European Synchrotron Radiation Facility (ESRF) in Grenoble (France). Detailed descriptions of this beamline devices including the used diffractometer can be found in the published descriptions of this institution. Here we will only discuss briefly the experimental conditions.

6.1 ID10A Beamline Description

The experimental requirements for successful XICS measurements are very specialized with respect to X-ray source, beam optics, and detection. Several technological advances made in the last two decades have made scattering experiments with (partially) coherent X-ray beams possible. The most important technical improvement is the insertion of undulators in synchrotrons radiation facilities. Beamlines that are equipped with undulator provide the small source size and high brilliance which is necessary to produce a usable partially coherence X-ray beam. Developed alongside such sources have been high-precision slits and pinhole apertures of only a few micrometers. These optical elements are necessary for achieving spatial coherence in X-ray beam incident on the sample. Temporal coherence is obtained by monochromator crystals in the beamline. Finally, fast avalanche photodiodes have become available and convenient to use.

At beamline ID10A the X-ray radiation arises from three undulators placed in series in the storage ring, giving an effective source with full width at half maximum (FWHM) dimensions of $928 \times 23 \mu m^2$ (H×V). Preliminary collimation is done by a set of preliminary apertures of $300 \times 300\,\mu m^2$ and

$200 \times 200\,\mu\text{m}^2$ at 33m and 43m from the source, respectively. A single-bounce Si(111) monochromator operating in a horizontal scattering geometry selects energies of 8 or 13.4 keV, corresponding to the third and fifth harmonic of the undulator radiation, leading to a wavelength λ of 1.55 or 9.25 Å, respectively. Subsequently, the beam is reflected by a Si mirror to suppress higher order harmonics. The sample position is at a distance of 45 m from the source. The transverse coherence length at this beamline is estimated with $\lambda R/s$, in which R is the source/sample distance and s the source size. The relation yields for $\approx 10\mu$m in the horizontal direction and $\approx 100\mu$m in the vertical direction. A compound refractive beryllium lens is used to increase the incident intensity by focusing the beam in the vertical direction. Focusing reduces the vertical coherence length, matching it to the coherence length in the horizontal direction. The longitudinal coherence length ξ_l of about 1.5μm is determined by the bandpass of the monochromator $\triangle\lambda/\lambda\mu \approx 10^{-4}$ (pink beam conditions yield $\xi_l \approx 10$nm). We used 10μm and 20μm pinholes in front of the sample to select the spatially coherent part of the beam. The beam incident on the sample was observed to be structured. These distortions are attributed to speckles occurring from imperfections in the windows and other optical elements in the beam path, and cause some uncertainty in the spatial coherence lengths of the beam. Guard slits were placed after the pinhole to remove parasitic scattering. A fast avalanche photodiode (Perkin Elmer C30703) [4] with an intrinsic time resolution $\leq 4ns$ was used as detector at a distance of $(1.2 - 1.4)$m from the sample, with pre-detector slit gaps varying from 0.01 to 0.2 mm. The intensity correlation function was measured in real time using a hardware multiple-tau digital auto-correlator FLEX01-8D (correlator.com, sampling time down to 8 ns) [87, 85].

6.2 Measurement and Analysis of XICS data from Hexane

In this section we will discuss a surface sensitive XICS experiment in which the surface dynamics from a low viscosity liquid were measured. The fluid of study was liquid hexane. For liquid surfaces the roughness is caused by thermally excited capillary waves, and the changes in the related speckle distribution is on the same time scale as the surface fluctuations. The measurement of the temporal correlation function of the intensity gives access to information about the dynamic surface properties. For highly viscous liquids the thermally excited waves are over-damped and the corresponding intensity correlation signal shows a steady decay with increasing time [85, 44]. The situation is different

for liquids with low viscosity, such as hexane. The capillary waves propagate and thus the intensity correlation signal shows an oscillatory behavior [36, 55]. This characteristic feature was clearly revealed in the XICS measurement on hexane surface, see Fig.6.1. Furthermore, the data exhibits intensity oscillations on the top of a baseline which is refers to a homodyne detection scheme.

In previous (DLS) experiments, it was observed that the experimentally obtained intensity correlation signal suggested an unreasonable large liquid viscosity constant [61, 15, 19]. The discrepancies were in particular significant for liquids with low viscous. This issue, which was first addressed by D. Langevin [48], can be related to the finite instrumental resolution of the experimental setup. Hence, the necessary to consider resolution effects in the data analysis is even required in DLS experiments and, moreover, it is vital for the interpretation of the intensity correlation signal. Similar corrections can be expected to be required for all XICS experiments on low viscosity materials. We will show in following that such corrections are in deed required in analysis of the XICS data from hexane.

In order to analyze the intensity correlation data we have applied the conventionally used g_2-function eq. (5.129), as well as eq. (5.114). Both formulas were modified by two fitting parameters, which account for the efficiency of the experimental setup. Hence, we rewrite eq. (5.129) as

$$g_2(\boldsymbol{q},\tau) = A + B'\beta \left| \frac{\widetilde{C}_{zz}(\boldsymbol{q},\tau)}{\widetilde{C}_{zz}(\boldsymbol{q})} \right|^2 , \tag{6.1}$$

where A and B' respectively account for an arbitrary shift and contrast reduction. On substituting eq. (2.54) into (6.1) and using the trivial substitution $B = B'\beta$, one finds

$$g_2(\boldsymbol{q},\tau) = A + B \left| \cos\left(\omega_s(q)\tau\right)\, e^{-\Gamma_l(\boldsymbol{q})\tau} \right|^2 \tag{6.2}$$

where $\Gamma_l(\boldsymbol{q})$ defines the damping of capillary waves and $\omega_s(q)$ the frequency (for details see chapter 2). Formula (6.2) was used to fit the intensity correlation data from hexane.

The second fit formula was deduced from eq. (5.114). On using similar

arguments as above and some trivial substitutions, we obtain

$$
\begin{aligned}
g_2(\boldsymbol{q}, q_z, \tau) = \mathcal{A} + \mathcal{B}\Bigg[& \\
& \times \left(\frac{k_B T}{\gamma} \frac{q_z^2}{\widetilde{\mathcal{T}}_B^2(\boldsymbol{q}) \widetilde{\mathcal{T}}_D^2(\boldsymbol{q})} \right) \int_{-\infty}^{\infty} d^2 q' \, \widetilde{c}_{zz}(\boldsymbol{q}', \tau) \widetilde{\mathcal{T}}_B^2(\boldsymbol{q} - \boldsymbol{q}') \widetilde{\mathcal{T}}_D^2(\boldsymbol{q} - \boldsymbol{q}'/2) \\
& + \frac{1}{2} \left(\frac{k_B T}{\gamma} \frac{q_z^2}{\widetilde{\mathcal{T}}_B^2(\boldsymbol{q}) \widetilde{\mathcal{T}}_D^2(\boldsymbol{q})} \right)^2 \\
& \times \iint_{-\infty}^{\infty} d^2 q_1' d^2 q_2' \, \widetilde{c}_{zz}(\boldsymbol{q}_1', \tau) \widetilde{c}_{zz}(\boldsymbol{q}_2', \tau) \widetilde{\mathcal{T}}_B^2(\boldsymbol{q} - \boldsymbol{q}_1') \widetilde{\mathcal{T}}_B^2(\boldsymbol{q} - \boldsymbol{q}_2') \widetilde{\mathcal{T}}_D^2(\boldsymbol{q} - (\boldsymbol{q}_1' + \boldsymbol{q}_2')/2) \Bigg],
\end{aligned}
\tag{6.3}
$$

where are $\mathcal{A}$ and $\mathcal{B}$ are addition fitting parameters. The fit formulas (6.2) and (6.3) are used to analyze experimentally measured intensity correlation functions arising from propagating capillary waves. The fit results for both formulas are compared in section 6.2.2.

6.2.1 Experimental Setup

The double chamber sample environment used in the experiment has been described in detail elsewhere [84]. Liquid hexane was filled in a reservoir, which was connected to the evacuated inner cell. The hexane was then condensed from the vapor phase into an aluminum trough of approximately 0.2 mm depth and 100 mm diameter. The outer cell was evacuated and used to isolate the inner cell from thermal fluctuations of the environment. The temperature of the inner cell was cooled by a gas flow from evaporating liquid nitrogen. Within these surroundings the hexane sample was cooled down to $T = (2 \pm 0.05)^\circ$C. At this temperature the mass density is $\varrho = 675.64\,\mathrm{kg/m^3}$ and the kinetic viscosity of hexane is $\nu = 5.661 \times 10^{-7}\,\mathrm{m^2/s}$ [73], which is in comparison to water nearly four times smaller. The surface tension is $\gamma = 0.021\,\mathrm{N/m}$ [92].

The XICS measurements were performed at the ID10A station of the TROIKA beamline at the European Synchrotron Radiation Facility (ESRF) with an incident X-ray beam of energy 8.53 keV ($\lambda = 1.45\,$Å). The measurements were carried out in the uniform filling mode of the storage ring (992 electron bunches are equally distributed around the whole circumference of the storage ring). A pinhole aperture with a diameter of 20 μm was situated at $L_a = 380\,$mm upstream of the sample and was used to obtain a collimated and partially coherent beam with an angular divergence of $\Delta\alpha = 2 \times 10^{-5}\,$rad

in the vertical direction. Irregular scattering from the pinhole were suppressed by a guard slit behind the pinhole. In order to increase the intensity the experiment was performed using the so-called "pink beam mode", where the full 3rd harmonic of the undulator source is used. This yields a coherent intensity of 1×10^{11} ph/sec through the $20\,\mu$m pinhole at a distance of $\sim 60\,$m from the source. To suppress higher order harmonics of the undulator the beam was deflected in the vertical direction by a double bounce reflection from two Silicon mirrors separated by 1 m. The double mirror assembly is located $\sim 36\,$m downstream from the source in an UHV-vessel mounted on a hexapode table in the optics hutch of the beamline. The first mirror deflects the beam upwards by 0.366° and the second mirror makes the beam path horizontal by a similar deflection downwards. The critical energy of total external reflection for Si is around 9.7 keV for an incidence angle of 0.183°. This means that the 3rd order harmonic at 8.53 keV is almost 100% reflected by the mirrors while the 4th (11.37 keV) and 5th (14.22 keV) orders are suppressed by factors of 1×10^{-2} and 6×10^{-4} respectively. In addition to the harmonic rejection the double mirror can also be used to focus the beam in the vertical direction. This is achieved by cooling the top part of the first mirror and by heating the bottom part, thus creating a thermal gradient ΔT that will curve the mirror [60]. In this way the beam can be focussed down to a vertical size of approximately $30\,\mu$m at the position of the pinholes, 24 m from the mirror and during our experiment ΔT was kept constantly at 2.25°. The bandwidth of the 3rd harmonic is $\Delta E/E \approx 1.3\%$ yielding a longitudinal coherence length of approximately 11 nm. Right before the pinhole the pink beam was deflected downwards by a smaller steering mirror to obtain a grazing angle of incidence $\alpha_{\mathrm{i}} = 0.10°$ of incoming radiation onto the sample surface. This angle is below the critical angle of total external reflection which is $\alpha_{\mathrm{c}} = 0.122°$ for liquid hexane at 8.53 keV. The grazing incident angle provided highly surface sensitive conditions since the penetration depth X-ray radiation was only ca. 110 Å.

By detecting the in-plane scattered intensity (i.e $\varphi = 0$) for different exit angles α_{f}, the investigated wave vector transfers q_y parallel to the surface varies according to $q_y = k(\cos\alpha_{\mathrm{f}} - \cos\alpha_{\mathrm{i}})$, where $k = 2\pi/\lambda$. Within a range of wave vectors, spanning from $4 \times 10^{-5}\,\mathrm{nm}^{-1}$ to $1.6 \times 10^{-4}\,\mathrm{nm}^{-1}$ the analyzed length scales $r_x = 2\pi/q_x$ on the surface ranged from $158\,\mu$m to $40\,\mu$m. The scattered intensity was detected at the distance $L_b = 1280\,$mm behind the sample by a fast avalanche photo diode (APD) and a digital correlator [2], which calculated the time correlation function signal at a given $\boldsymbol{q}$ value. In front of the APD an adjustable slit was used with $50 \times 50\,\mu\mathrm{m}^2$ opening to define the solid angle of detection.

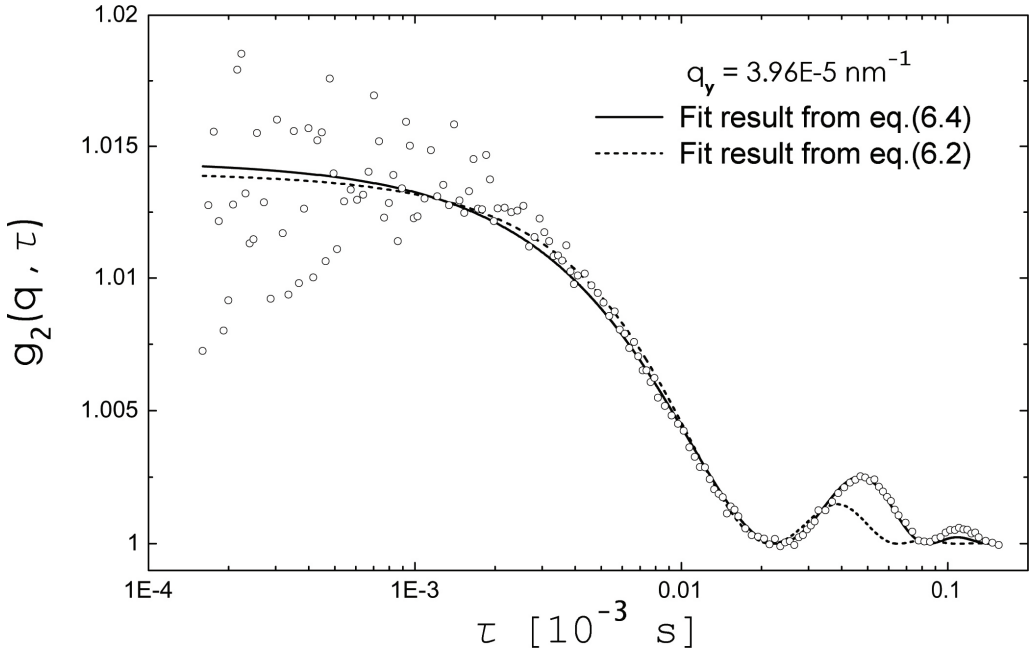

Figure 6.1: Measured autocorrelation data (circles) at an in-plane wave vector transfers of $q_y = 3.96 \times 10^{-5}\,\mathrm{nm}^{-1}$ from a liquid hexane surface at temperature $T = (2 \pm 0.05)°\mathrm{C}$. The dotted curve presents a fit with a homodyne correlation function eq. (6.2). The solid line shows the best fit result for eq. (6.4).

6.2.2 Results and Discussion

In a first attempt we tried to fit the experimental data with the fit formula (6.2). This equation is, with regard to the used height correlation function, valid within the range of our measured wave vector transfers, since the necessary condition $\Gamma_l/\omega_s \ll 1$ is completely satisfied with Γ_l/ω_s values from 0.04 up to 0.08. (For more details on this approximation see chapter 2.) A typical result of these fits is shown in Fig.6.1. Obviously, it is not possible to describe the data with this g_2-function. In a second attempt to analyze the data the cosine term in eq. (6.2) was generalized by a phase term ϕ, namely

$$g_2(\boldsymbol{q},\tau) = A + B\left|\cos\left(\omega_s(q)\tau + \phi\right)\, e^{-\Gamma_l(\boldsymbol{q})\tau}\right|^2 \quad . \tag{6.4}$$

Such modifications were used in DLS in order to account for deviations from a Lorentzian shape of the surface spectrum $S_{zz}(\boldsymbol{q},\omega)$ [19]. The solid line in Fig.6.1 represents a fit with eq. (6.4), which provided a better description of the data compared to the fit with eq. (6.2). The fit results for $\omega_s(q)$ are reasonable as can be seen in Fig.6.3. However, the results for the damping constant $\Gamma_l(\boldsymbol{q})$ yield values considerably larger than expected. This exhibits that even devi-

Table 6.1: Theoretical values for frequency and damping of capillary waves on hexane surface are compared to fit results from equation (6.4).

experimental wave vector transfer	theoretical values		fit values		
q_y	ω	Γ	ω	Γ	φ
$[10^{-5}\mathrm{nm}^{-1}]$	$[10^3\mathrm{s}^{-1}]$	$[10^3\mathrm{s}^{-1}]$	$[10^3\mathrm{s}^{-1}]$	$[10^3\mathrm{s}^{-1}]$	[rad]
3.96	43.90	1.77	47.08	20.71	0.49
5.49	71.69	3.41	81.23	24.51	0.28
7.11	105.90	5.73	103.00	36.94	0.39
9.72	169.94	10.77	201.50	48.04	0.14
11.64	221.58	15.34	249.50	54.09	0.12
15.72	347.88	27.98	358.40	79.20	0.16

ations from the surface spectrum in eq. (2.51) do not fully explain the experimental data (see Table 6.1 and Fig.6.4). Additionally, the q-dependence also deviated significantly from the expected behavior $\Gamma_l(\boldsymbol{q}) = 2\nu\boldsymbol{q}^2$. In Table 6.1 the fit results are summarized and compared with the theoretical values[1].

These above discrepancies are similar to the ones encountered in DLS experiments and indicate the influence of limited resolution, which should be especially important for small wave vector transfers [19, 36]. In order to take such effects into account, we considered an experimental uncertainty for the wave vector transfer Δq_x and Δq_y. Next we will present fit results which are based on formula (6.3). In this formula the wave vector spread is implicitly considered by the truncation function $\mathcal{T}_B(\boldsymbol{q})$ and $\mathcal{T}_B(\boldsymbol{q})$. The explicit expression for Δq_x and Δq_y has been derived in chapter 5, hence

$$\triangle q_x = \sqrt{\frac{2}{\Xi_{tx}^2} + \frac{1}{\Sigma_x^2}\left(1 + (k\triangle a^2/L_a)^2\left(1 - \frac{\Sigma_x^2}{\triangle a^2}\frac{L_a + L_b}{L_b}\right)^2\right)}\,, \tag{6.5a}$$

$$\triangle q_y = \sqrt{\frac{2}{\Xi_{ty}^2} + \frac{1}{\Sigma_y^2}\left(1 + (k\triangle a^2/L_a)^2\left(1 - \frac{\Sigma_y^2}{\triangle a^2}\frac{L_a \sin^2\alpha_\mathrm{f} + L_b \sin^2\alpha_\mathrm{i}}{L_b}\right)^2\right)}\,. \tag{6.5b}$$

In order to fit the XICS data with the relatively complicated formula (6.3), we have used the following fitting strategy: 1. The number of fitting parameters were reduced by using the given experimental values for L_a, L_b, α_i,

[1]The theoretical values are calculated from literature values of the material constants of hexane at $T = 2°\mathrm{C}$.

α_f and k (see section 6.2.1). Furthermore, we have used the approximation $\triangle a \approx$ (pinhole opening)$/\sqrt{8}$ and $\triangle b \approx$ (detector opening)$/\sqrt{8}$. Hence, the only fitting parameters in eq. (6.3) are $\mathcal{A}$, $\mathcal{B}$, Σ_x, Σ_y, Ξ_x, Ξ_y, γ, ν and ϱ. For the mass density of hexane we used the the literature value at $T = 2 \circ \mathrm{C}$ [73]. 2. Since the discrepancies in the previous fits (see Tab. 6.1)) are stronger pronounced at small wave vector transfers, we have therefore fitted all fitting parameters only at $q_x = 3.96 \times 10^{-5}\,\mathrm{nm}^{-1}$. The obtained fitting parameters for $\Sigma_x = 6\mu$m, $\Sigma_y = 12.5$mm, $\Xi_x = 13\mu$m and $\Xi_y = 50$mm were reused for all other fits. Note that the strong asymmetry between the x and the y-direction is predicted by the gracing incidence scattering geometry (see for more details chapter 4). 3. On using the above fitting results from the correlation data at $q_y = 3.96 \times 10^{-5}\,\mathrm{nm}^{-1}$, we have calculated with (6.5a,b) the wave vector spreads for all other curve. The results for the calculated uncertainties $\triangle q_x$ and $\triangle q_y$ were finally used to fit the remanding data, see Tab. 6.2). Hence, apart from the correlation data at $q_x = 3.96 \times 10^{-5}\,\mathrm{nm}^{-1}$, we have reduced the set of fitting parameters to $\mathcal{A}$, $\mathcal{B}$, γ and ν. The fitting results for γ, ν, $\triangle q_x$ and $\triangle q_y$ are summarized in Tab. 6.2). Representative fits are shown in Fig.6.2.

Table 6.2: The fluid constants γ and ν of a hexane surface are fitted by equation (6.3). Known table values at $T = 2°\mathrm{C}$ are $\gamma = 0.021\,\mathrm{N/m}$ and $\nu = 5.661 \times 10^{-7}\,\mathrm{m}^2/\mathrm{s}$.

experimental wave vector transfer	fit values			
q_y $[10^{-5}\mathrm{nm}^{-1}]$	Δq_x $[10^{-6}\mathrm{nm}^{-1}]$	Δq_y $[10^{-6}\mathrm{nm}^{-1}]$	γ $[10^{-2}\mathrm{N/m}]$	ν $[10^{-7}\mathrm{m}^2/\mathrm{s}]$
3.96	20.94	5.91	2.69	5.74
5.49	20.94	6.21	2.21	5.78
7.11	20.94	6.52	1.99	5.76
9.75	20.94	7.04	2.25	5.81
11.64	20.94	7.39	2.15	5.31
15.72	20.94	8.18	2.03	5.72

It should be noted that the data are well described by eq. (6.3) in combination with the calculated uncertainties eq. (6.5a,b). Furthermore, no arbitrary phase ϕ term was needed, which is in good agreement with the fact that the surface spectrum in eq. (2.51) takes a Lorentzian form for liquids with low viscosity.

The resulting frequencies $\omega_s(\boldsymbol{q})$ and damping constants $\Gamma_l(q)$ for capillary

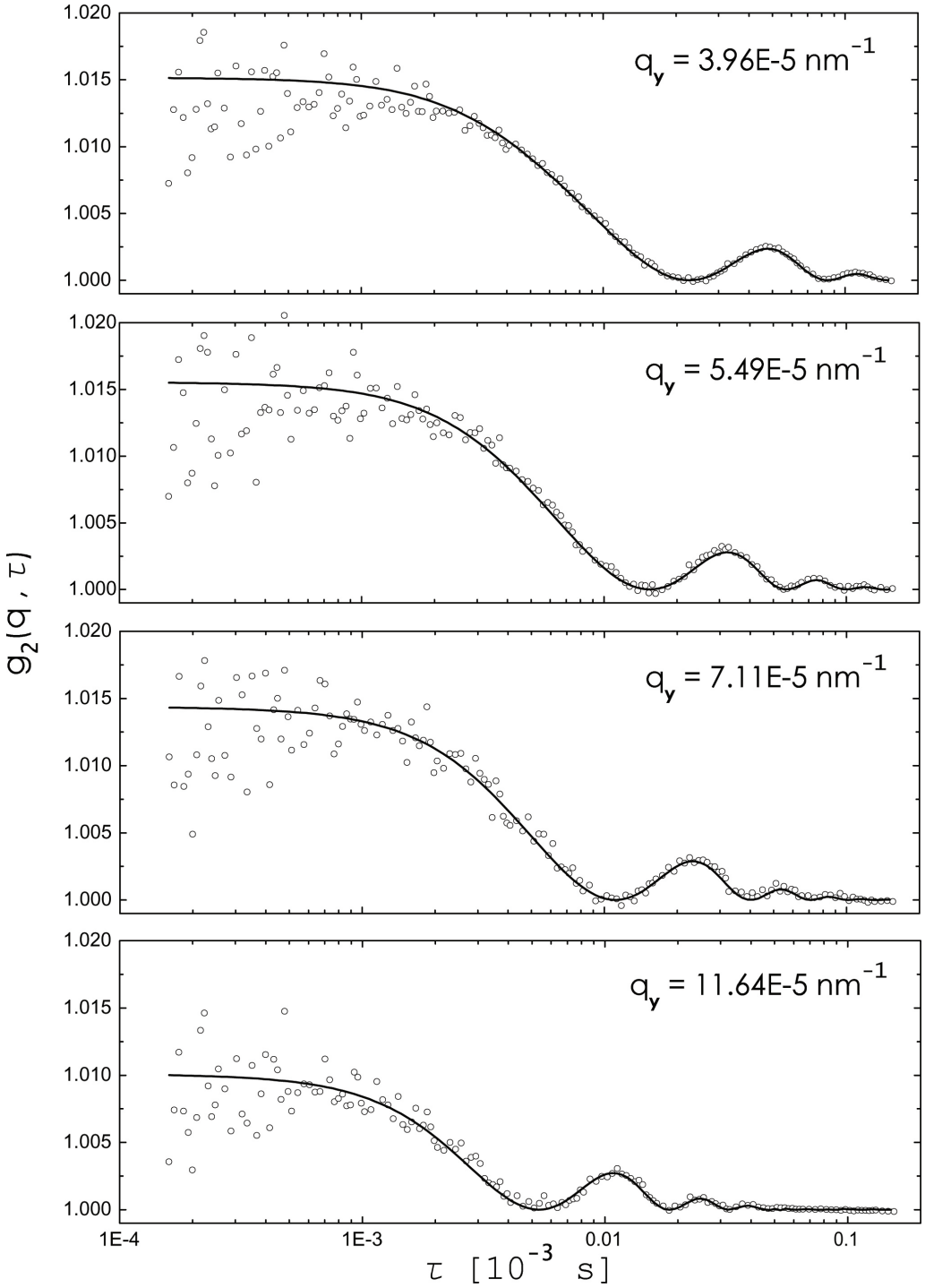

Figure 6.2: Measured autocorrelation data (circles) obtained at four different in-plane wave vector transfers from a liquid hexane surface at temperature $T = (2 \pm 0.05)$°C. The solid line represents a fit with a correlation function eq. (6.3).

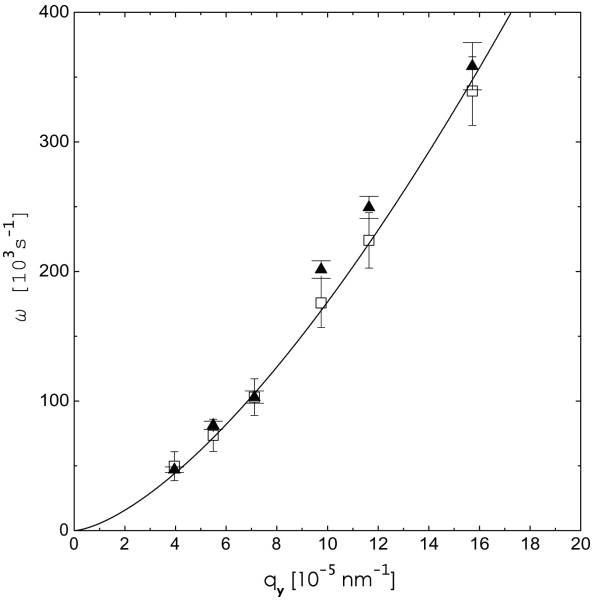

Figure 6.3: Theoretical dispersion relation (solid line) of propagating capillary waves on a liquid hexane surface at $T = 2\,^{\circ}\mathrm{C}$, compared to the fitting results (squares) from eq. (6.3) and eq. (6.4) (triangle). The displayed dispersion curve given by $\omega_s(q_x = 0, q_y) = (q_y^3\gamma/\varrho)^{1/2}$ is calculated with the known mass density ϱ and surface tension γ of liquid hexane.

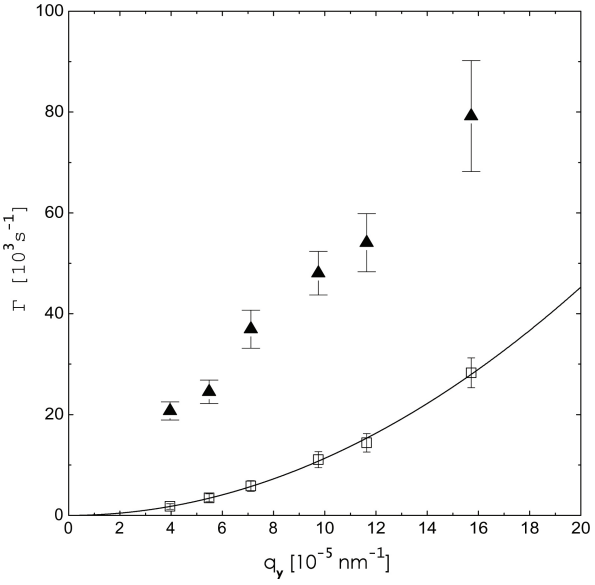

Figure 6.4: The fitted damping constants, with (squares) and without (triangle) considering a wave vector spread. The solid line shows the predicted capillary wave damping according to $\Gamma_l(q_x = 0, q_y) = 2\nu q_y^2$, where the bulk viscosity value $\nu = 5.661 \times 10^{-7}\,\mathrm{m}^2/\mathrm{s}$ has been used.

waves on a hexane surface are calculated from the fitting results for γ and ν. A good agreement of experiment and theory is obtained (see Fig. 6.4 and Fig. 6.3). The need to account for the an uncertainties in $\triangle \boldsymbol{q}$ is especially obvious in Fig. 6.4.

In summary, temporal intensity autocorrelation data from a hexane surface have been measured using pink beam XICS. We have shown that for low viscosity liquids the effects due to the uncertainties in $\triangle \boldsymbol{q}$ need to be included in the data analysis. It is worth recognizing that the conventionally used g_2-function (5.129) does account for partial coherence, finite detector resolution and thus for the uncertainty in $\triangle \boldsymbol{q}$, see chapter 5. However, eq.(5.129) clearly failed to explain the hexane data and yielded systematic errors. These errors appear in a considerable larger damping constant $\Gamma_l(\boldsymbol{q})$ and a small shift in the capillary wave frequency. Both effects become less pronounced with increasing wave vector transfer. In order to resolve these errors we have considered the uncertainty in the experimental wave vector transfers Δq_x and Δq_y, which we have related to the spatial coherence properties of the X-ray beam and the finite detector resolution. It was only possible to reach a good agreement between the experimentally and theoretically determined damping constants and frequencies after including the uncertainties in Δq_x and Δq_y.

6.3 Measurement and Analysis of XICS data from Water

We discuss next the measurement of propagating capillary waves on a liquid water surface at $T = (5 \pm 0.05)°\mathrm{C}$ with XICS. The experiment has been performed under grazing incidence conditions with an incoming X-ray beam below the critical angle of total external reflection. The experimental conditions were quite similar to the hexane experiment. However, the measured intensity correlation functions of the liquid water surface were found to be heterodyne signals, i.e. in contrast to previous XICS experiments we observed intensity oscillations around a baseline, see Fig.6.5.

Due to this circumstance one can obviously not apply fit formula (6.4), which can only yield an oscillations on top of a baseline. In order to account for the heterodyne feature, we will further modified eq. (6.4). The proposed fit formula is

$$g_2(\boldsymbol{q},\tau) = A + B\left(\cos\left(\omega_s(q)\tau+\phi\right)\, e^{-\Gamma_l(\boldsymbol{q})\tau}\right) + C\left|\cos\left(\omega_s(q)\tau+\phi\right)\, e^{-\Gamma_l(\boldsymbol{q})\tau}\right|^2 \tag{6.6}$$

where A, B, C and ϕ are fitting parameter. A similar equation is conventionally used in DLS experiments, if the experimental conditions are setup for the heterodyne detection scheme [18, 21, 20].

It is worth recognizing that the first term in the square bracket of eq. (6.3) does account for a heterodyne signals of the g_2-function. From expression (6.3) we can propose to possible origins for the observation of the heterodyne signal: 1. The surface tension of water is, with $\gamma = 0.075\,\mathrm{N/m}$, approximately 3.6 times larger compared to hexane. Since the heterodyne term is weighted by $1/\gamma$ and the homodyne by $1/\gamma^2$, it appears reasonable to assume, that the larger surface tension of water has caused the dominantly heterodyne signal. 2. An addition enhancement of the heterodyne term may have been caused by the smaller $\boldsymbol{q}$ values in the water experiment. Accordingly, the measurements were performed closer to specularly reflected beam which could have caused an optical mixing with the diffuse counterpart of the scattered beam [36]. This effect is accounted for in (6.3) by the weighting factor $1/(\widetilde{\mathcal{T}}_B^2(\boldsymbol{q})\mathcal{T}_D^2(\boldsymbol{q}))$, which is essentially proportional to one over the specularly reflected beam, see the more detailed discussion in chapter 5.

6.3.1 Experimental Setup

For the sample environment a setup very similar to the one described in Ref.[84] was used. The water sample was filled into an aluminum trough with approximately 0.5 mm depth and 100 mm diameter, which itself was placed inside

an inner sample cell. The outer cell was evacuated and used to isolate the inner cell from thermal fluctuations of the environment. Within this setup the temperature of the inner cell was electronically stabilized by high power Peltier elements at the temperature $T = (5 \pm 0.05)°\mathrm{C}$. Under these conditions the mass density is $\varrho = 999\,\mathrm{kg/m^3}$ and the kinetic viscosity of water becomes $\nu = 1.519 \times 10^{-6}\,\mathrm{m^2/s}$ [73]. The surface tension is $\gamma = 0.075\,\mathrm{N/m}$ [73]. In comparison to the hexane experiment, water has a surface tension which is larger by a factor of 3.6.

The XICS measurements were performed at the ID10A station of the TROIKA beamline at the European Synchrotron Radiation Facility (ESRF) with an incident X-ray beam of energy 8.03 keV ($\lambda = 1.54\,\text{Å}$). The measurements were carried out in the $2 \times 1/3$ filling mode of the storage ring (330 electron bunches spaced by a gap of 1/6th of the ring). The incident X-ray beam of energy 8.03 keV was selected by a Si(111) crystal monochromator, which provided a bandpass of $\triangle\lambda/\lambda \approx 10^{-4}$. This yields a longitudinal coherence length of approximately $1\,\mu$m. A pinhole aperture with a diameter of $12\,\mu$m was situated at $L_a = 380\,$mm upstream of the sample and was used to obtain a collimated and partially coherent beam. A guard slit in front of the sample was used to suppress the parasitic scattering from the first pinhole. Right before the pinhole the beam was deflected downwards by a smaller steering mirror to obtain a grazing angle of $\alpha_\mathrm{i} = 0.10°$ of incoming radiation onto the sample surface. This angle is below the critical angle of water, which is for 8.03 keV at $\alpha_\mathrm{c} = 0.153°$. The penetration depth of the radiation was approximatively 100 Å, thus the experiment was highly surface sensitive.

The scattered radiation was detected under different exit angles α_f in the scattering plane, i.e. $\varphi = 0$. From the incident and exit angles we have obtained the wave vector transfer parallel to the surface, hence $q_x = 0$ and $q_y = k(\cos\alpha_\mathrm{f} - \cos\alpha_\mathrm{i})$. Within a range of wave vectors, spanning from $2.2 \times 10^{-5}\,\mathrm{nm^{-1}}$ to $6.1 \times 10^{-4}\,\mathrm{nm^{-1}}$ the analyzed length scales $r_x = 2\pi/q_x$ on the surface ranged from $285\,\mu$m to $103\,\mu$m. The scattered intensity was detected at the distance $L_b = 1403\,$mm behind the sample by a fast avalanche photo diode (APD) and a digital correlator [2], which calculated the time correlation function signal at a given $\boldsymbol{q}$ value. In front of the detector a slit with a $50 \times 50\,\mu\mathrm{m^2}$ opening was used in order define the solid angle of detection.

6.3.2 Results and Discussion

In order to analyze the experimental data it is essential to know whether optical mixing with a reference beam is performed or not in the experiment. In contrast to previous XICS experiments we observed a g_2-function which oscillated around a baseline. A representative experimental correlation functions

is shown in Fig.6.5. This finding points towards a detection scheme without a beam interference, i.e. the intensity autocorrelation function is dominated by the heterodyne signal rather than by homodyne signal.

Table 6.3: Theoretical values for frequency and damping of capillary waves on water surface are compared to fit results from equation (6.4).

experimental wave vector transfer	theoretical values		fit values		
q_y $[10^{-5}\mathrm{nm}^{-1}]$	ω $[10^3\mathrm{s}^{-1}]$	Γ $[10^3\mathrm{s}^{-1}]$	ω $[10^3\mathrm{s}^{-1}]$	Γ $[10^3\mathrm{s}^{-1}]$	φ [rad]
2.2	28.23	1.47	22.16	7.51	0.47
2.8	40.53	2.38	31.68	9.29	0.47
3.4	54.73	3.55	43.65	12.92	0.48
4.1	70.82	5.01	60.48	16.59	0.38
4.7	88.82	6.77	76.69	20.32	0.38

Due to this circumstance fits with eq. (6.4) failed to describe the water data. Better fit were obtained by using eq. (6.6). In Fig.6.5 a representative fit with eq. (6.4) and eq. (6.6) is illustrated. Better description of the data are obtained by eq. (6.6). With eq. (6.6) the fit results for $\omega_s(q)$ are systematically shifted to smaller values, but still within a reasonable range, as can be seen in Fig. 6.6. The results for the damping constant $\Gamma_l(\boldsymbol{q})$ yield values substantially larger than expected. In analogy to the hexane result, we have found a much larger discrepancies with the theory for $\Gamma_l(\boldsymbol{q})$ than for $\omega_s(q)$. In Table 6.3 the fit results are summarized and compared with the theoretical values[2].

In conclusion, we measured capillary waves on a liquid water surface with XPCS under grazing incidence. From the oscillating character of the correlation functions and from the measured wave frequencies we conclude that heterodyne mixing was observed in the experiment. We have shown that the conventionally used g_2-function (5.129) clearly failed to explain the water data or at least the heterodyne character of the correlation signal. Similarly to the hexane data, we have obtained from eq. (5.129) (and modifications of this formula) systematic errors, appearing in a considerable larger damping constant $\Gamma_l(\boldsymbol{q})$ and a small shift in the capillary wave frequency. We showed by including the coherence properties of the X-ray radiation into the scattering function, as well as the surface tension, that heterodyne mixing can be explained as an interference effect between the static specularly reflected beam and the

[2]The theoretical values are calculated from literature values of the material constants of water at $T = 5°\mathrm{C}$.

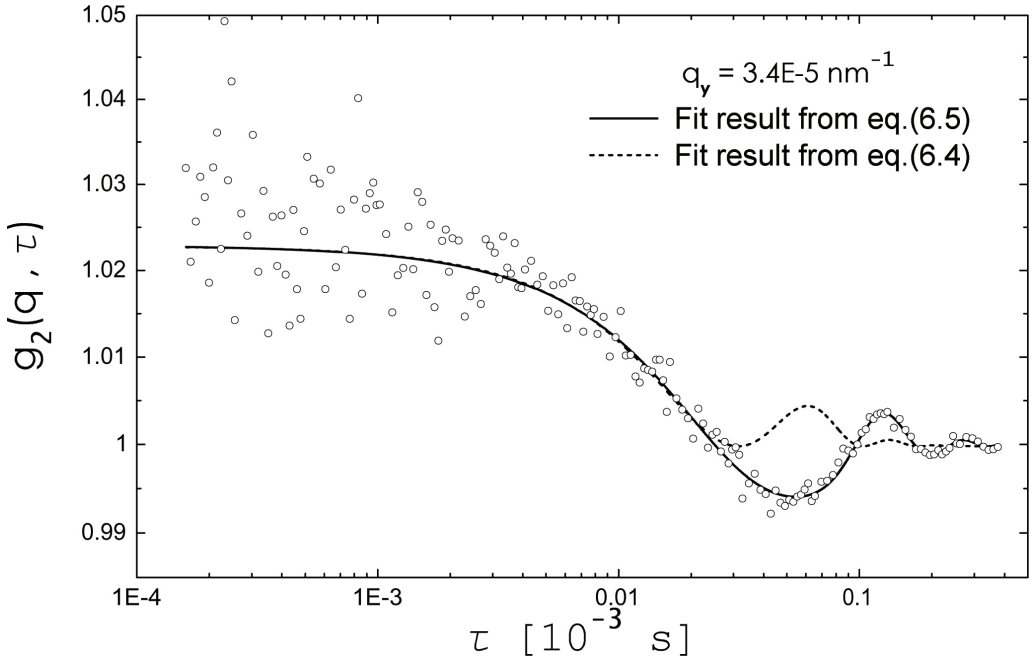

Figure 6.5: Measured autocorrelation data (circles) at an in-plane wave vector transfers of $q_x = 3.96 \times 10^{-5}\,\mathrm{nm}^{-1}$ from a liquid water surface at temperature $T = (5 \pm 0.05)°\mathrm{C}$. The dotted curve presents a fit with a homodyne correlation function eq. (6.4). The solid line shows the best fit result for eq. (6.6).

diffusely scattered signal containing the dynamic information, see section 6.3 and chapter 5. The observation of heterodyne mixing in an XICS signal is fundamental for all future applications of this technique since the scattering signal is in general very weak for large in-plane momentum transfers. Thus, the possibility of heterodyne mixing with a strong reference beam may open in the future the way to the observation of surface dynamics down to lateral length scales in the nanometer range [36].

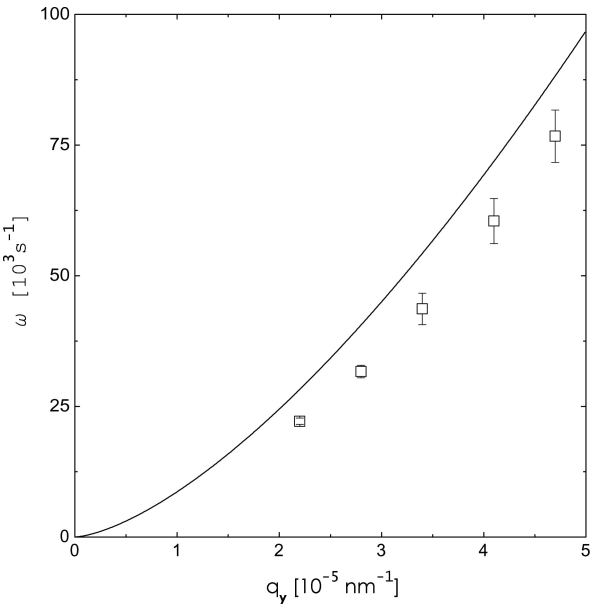

Figure 6.6: Theoretical dispersion relation (solid line) of propagating capillary waves on a liquid water surface at $T = 5\,^{\circ}\mathrm{C}$, compared to the fitting results (squares) from eq. (6.6). The displayed dispersion curve given by $\omega_s(q_x = 0, q_y) = (q_y^3\gamma/\varrho)^{1/2}$ is calculated with the known mass density ϱ and surface tension γ of liquid water.

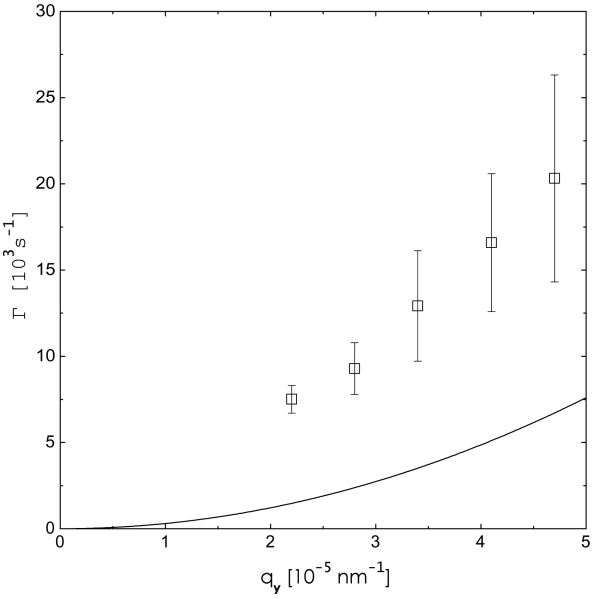

Figure 6.7: The fitted damping constants (squares) are compared with the predicted capillary wave damping (solid line).

Chapter 7

Conclusions and Future Research

7.1 Conclusions

The main contributions of this thesis are numerous theoretical approaches that provide better interpretations of surface sensitive X-ray scattering experiments from fluid surfaces.

One of the important contributions of this thesis is a detailed mathematical discussion on surface height correlation functions from high and low viscous liquids. It was shown conclusively that present representations of the static height correlation function contain a non-physical singularity. We have further demonstrated that, due to this singularity, present theoretical intensity formulas for surface X-ray scattering equally contain a singularity, which result from a Gamma function term. In chapter 3, we have provided a number of original calculations on elastic X-ray scattering from rough surfaces. It is shown, in particular, how the singularity can be removed from the present theory of elastic surface X-ray scattering. The given derivation and arguments are independent from the first Born approximation and thus hold in the first order distorted wave Born approximation.

In chapter 4, we have generalized our theoretical analysis on elastic X-ray scattering from static media by considering effects of partial coherence, instrumental resolution and Fresnel conditions. The necessary of considering these effects in X-ray scattering experiments was initiated and chiefly discussed by S. K. Sinha and M. Tolan [91, 100, 101, 99]. We contributed to this subject by describing the scattering process in terms of propagation formulas for the mutual coherence function. The main achievement consist here in the comprehensible formulation of pre-sample mutual coherence function and scattered mutual co-

herence function, which were related by propagation formulas. Based on these propagation formulas, we have provided an analysis on surface scattering with partially coherent X-rays under Fresnel condition. Within this discussion, we have demonstrated that Fresnel corrections can be neglected to some extent, if the angle of the incident X-ray beam is smaller than the critical angle of the sample surface under study. Furthermore, a details study is given on propagating partially coherent X-rays, as well as their Fresnel diffraction by a square slit.

In chapter 5, the considerations of partial coherence, instrumental resolution and Fresnel conditions are introduced in the theoretical treatment of surface sensitive X-ray scattering from temporally fluctuation media. We have given a detailed theoretical description of surface sensitive X-ray intensity correlation spectroscopy experiments. Based on the statistical properties of the fluid surface and the scattered fields, we have derived an intensity correlation formula which accounts for finite spatial coherence, instrumental resolution and Fresnel conditions. The predictions of this intensity correlation function are compared with the conventionally used formula in XICS, which is deduced from bulk sensitive DLS theories. One of the more general contributions in this chapter is the formulation of a wave equation for the scalar field. The wave equation applies to quasi-elastic X-ray scattering and is formally similar to the Helmholtz equation. The usefulness of such field equations may become apparent if one attempt to use the distorted wave Born approximation for the theoretical description of XICS.

We contributed to the understanding of surface sensitive XICS experiments by theoretical analyses, as well as experiments on hexane surface and water surface. These measurements are some of the first experiments using surface sensitive XICS techniques on low viscous fluids. The analysis of the XICS experiments has clearly revealed that the conventionally used intensity correlation formula can not explain our experimental data. A reasonable understanding of the data was only possible, if the above mentioned resolution effects were considered.

7.2 Future Research

There are several areas where future research may be directed in the field of XICS. On the experimental side more principle experiments may be needed in order to understand and specify the conditions of partial coherence in XICS experiments. For instance, relatively simple slit experiments could be performed in order to analysis and, eventually, specify the coherence properties of the X-ray at a beam line.

On the theoretical side, one should consider the use of the distorted wave Born approximation for the interpretation of surface sensitive XICS experiments. Independent from this point, present theories on XICS are founded on some questionable assumptions referring to the statistical properties of the sample and the electric field. In particular, the statistical assumptions regarding the scattered fields (based on Siegert) and the bulk electron density (based on Pusey) should be avoided in the theoretical treatment of surface sensitive XICS. Hence, statistical assumption should be restricted to the sample surface and the X-ray source, in other words the incident fields. We have briefly outlined a calculation in appendix B, which is based only the Gaussian statistical properties of the sample surface and incident field fluctuations.

Appendix A

Gaussian Statistics

The following definitions and statistical theorems are frequently used in this work. For a comprehensive introduction on probability theory see Ref[58, 32].

A.1 Definitions

Expectation value for random variables

Let $\langle x \rangle$ be the *mean* or *average* or *expectation value* of the random variable x. The mean is obtained by weighting each value of x by the associated probability $p(x)\,dx$ for that value and integrating over the allowed range of x. Thus

$$\langle x \rangle = \int x\, p(x)\, dx \ , \tag{A.1}$$

provided that the integral exists.

Expectation value for functions of random variables

More generally, if x is a random variable, any function $f(x)$ of x is itself a random variable, and its mean or expectation, if it exists, is given by

$$\langle f(x) \rangle = \int f(x) p(x)\, dx \ . \tag{A.2}$$

Note that the probability density $p(f(x))$ of a function depending of a random variable can differ from the probability density $p(x)$ of its random variable.

Gaussian distribution

Let x be a continuous random variable defined on the infinite interval

from $-\infty$ to ∞. The variable x is known as a Gaussian random variable if its probability density $p(x)$ is of the form

$$p(x) = \frac{1}{\sqrt{2\pi}\sigma} e^{-\Delta x^2/2\sigma^2} \ , \tag{A.3}$$

where $\sigma = \sqrt{\langle (x - \langle x \rangle)^2 \rangle}$ is called the *root-mean-squared deviation* or *standard deviation* and $\Delta x = x - \langle x \rangle$ is the *deviation*.

Multivariate Gaussian distribution

Let us consider two Gaussian variates A and B with standard deviations σ_A and σ_B, respectively. Then each variate has a probability distribution of the form (A.3). If the variates are statistically dependent the joint probability distribution $p(A, B)$ takes the form

$$\begin{aligned} p(A,B) = & \frac{1}{2\pi\sigma_{_A}\sigma_{_B}\sqrt{1-\rho_{_{AB}}^2}} \\ & \times \exp\left[-\frac{1}{2\left(1-\rho_{_{AB}}^2\right)} \left(\frac{\Delta A^2}{\sigma_{_A}^2} - \frac{2\rho_{_{AB}}\Delta A \Delta B}{\sigma_{_A}\sigma_{_B}} + \frac{\Delta B^2}{\sigma_{_B}^2} \right) \right], \end{aligned} \tag{A.4}$$

where $\Delta A = A - \langle A \rangle$, $\Delta B = B - \langle B \rangle$ and

$$\rho_{_{AB}} = \frac{\langle \Delta A \Delta B \rangle}{\sigma_{_A}\sigma_{_B}} \tag{A.5}$$

is the so-called *correlation coefficient*. The expectation value for a function $f(A, B)$ takes the form

$$\langle f(A,B) \rangle = \iint f(A,B) p(A,B)\, dA dB \ . \tag{A.6}$$

Gaussian moment theorem

Gaussian variates have the property that all higher-order correlations among them are expressible in terms of second-order correlations between pairs of variates. Let $x_1, x_2, ...$ be a set of Gaussian variates. Then for any set of N indices $i_1, i_2, ..., i_N$,

$$\begin{aligned} & \langle \Delta x_{i_1} \Delta x_{i_2} ... \Delta x_{i_N} \rangle \\ & \quad = \begin{cases} 0, & \text{if } N \text{ is odd}, \\ \sum_{(N-1)!!} \langle \Delta x_{i_1} \Delta x_{i_2} \rangle \langle \Delta x_{i_3} \Delta x_{i_4} \rangle ... \langle \Delta x_{i_{N-1}} \Delta x_{i_N} \rangle, & \text{if } N \text{ is even}, \end{cases} \end{aligned} \tag{A.7}$$

where $\sum$ denotes the summation over all $(N-1)!!$ pair combinations and $\Delta x_{i_N} = x_{i_N} - \langle x_{i_N} \rangle$ represents the deviation.

The Gaussian moment theorem for complex variables $z_1, z_2, ...$ states the below conditions

$$\langle \Delta z_{i_1}^* ... \Delta z_{i_N}^* \Delta z_{j_1} ... \Delta z_{j_M} \rangle = \begin{cases} 0, & \text{if } N \neq M, \\ \sum_{N!} \langle \Delta z_{i_1}^* \Delta z_{j_1} \rangle \langle \Delta z_{i_2}^* \Delta z_{j_2} \rangle ... \langle \Delta z_{i_N}^* \Delta z_{j_N} \rangle, & \text{if } N = M, \end{cases} \tag{A.8}$$

We will next use the above definitions to provide some statistical relations, which are frequently used in this work.

A.2 Bloch Theorem

Let a function of random variable x be definite by

$$f(x) = e^{iqx} \ . \tag{A.9}$$

And let the mean value $\langle x \rangle$ be at the origin, so that $\langle x \rangle = 0$ and $\sigma = \sqrt{\langle x^2 \rangle}$. Including (A.9) in (A.2) gives

$$\left\langle e^{iqx} \right\rangle = \frac{1}{\sqrt{2\pi}\sigma} \int_{-\infty}^{\infty} e^{-x^2/2\sigma^2} e^{iqx} = e^{-q^2\sigma^2/2}$$

which yields with $\sigma = \sqrt{\langle x^2 \rangle}$

$$\left\langle e^{iqx} \right\rangle = e^{-q^2\langle x^2 \rangle/2} \ . \tag{A.10}$$

A.3 Classical Baker-Hausdorff Theorem

Let a function of the random variables A and B be definite by

$$f(A, B) = e^{iq(A+B)} \ . \tag{A.11}$$

And let the mean values be $\langle A\rangle = \langle B\rangle = 0$, so that $\sigma_A = \sqrt{\langle A^2\rangle}$ and $\sigma_A = \sqrt{\langle B^2\rangle}$, respectively. With (A.6) and (A.4) the expectation value for (A.11) is

$$\begin{aligned}\left\langle e^{iq(A+B)}\right\rangle &= \frac{1}{2\pi\sigma_{_A}\sigma_{_B}\sqrt{1-\rho_{_{AB}}^2}} \\ &\quad\times \iint_{-\infty}^{\infty} dA dB\; e^{-\frac{1}{2\left(1-\rho_{_{AB}}^2\right)}\left(\frac{A^2}{\sigma_{_A}^2}-\frac{2\rho_{_{AB}}AB}{\sigma_{_A}\sigma_{_B}}+\frac{B^2}{\sigma_{_B}^2}\right)}\; e^{iq(A+B)} \\ &= \frac{1}{2\pi\sigma_{_A}\sigma_{_B}\sqrt{1-\rho_{_{AB}}^2}} \int_{-\infty}^{\infty} dB\; e^{-\frac{1}{2\left(1-\rho_{_{AB}}^2\right)}\frac{B^2}{\sigma_{_B}^2}}\; e^{iqB} \\ &\quad\times \int_{-\infty}^{\infty} dA\; e^{-\frac{1}{2\left(1-\rho_{_{AB}}^2\right)}\left(\frac{A^2}{\sigma_{_A}^2}-\frac{2\rho_{_{AB}}AB}{\sigma_{_A}\sigma_{_B}}\right)}\; e^{iqA}\;. \end{aligned} \tag{A.12}$$

Preforming the integration over A yields

$$\begin{aligned}\int_{-\infty}^{\infty} dA\; e^{-\frac{1}{2\left(1-\rho_{_{AB}}^2\right)}\left(\frac{A^2}{\sigma_{_A}^2}-\frac{2\rho_{_{AB}}AB}{\sigma_{_A}\sigma_{_B}}\right)}\; e^{iqA} &= \sqrt{2\pi\left(1-\rho_{_{AB}}^2\right)}\;\sigma_{_A}\; e^{-\frac{1}{2}q^2\left(1-\rho_{_{AB}}^2\right)\sigma_{_A}^2} \\ &\quad\times e^{\frac{\rho_{_{AB}}^2}{2\left(1-\rho_{_{AB}}^2\right)\sigma_{_B}^2}B^2}\; e^{iqB\rho_{_{AB}}\frac{\sigma_{_A}}{\sigma_{_B}}}. \end{aligned} \tag{A.13}$$

Including (A.13) in (A.12) gives

$$\begin{aligned}\left\langle e^{iq(A+B)}\right\rangle &= \frac{e^{-\frac{1}{2}q^2\left(1-\rho_{_{AB}}^2\right)\sigma_{_A}^2}}{\sqrt{2\pi}\sigma_{_B}} \int_{-\infty}^{\infty} dB\; e^{\frac{\rho_{_{AB}}^2-1}{2\left(1-\rho_{_{AB}}^2\right)}\frac{B^2}{\sigma_{_B}^2}}\; e^{iqB\left(1+\rho_{_{AB}}\frac{\sigma_{_A}}{\sigma_{_B}}\right)} \\ &\quad\times \frac{e^{-\frac{1}{2}q^2\left(1-\rho_{_{AB}}^2\right)\sigma_{_A}^2}}{\sqrt{2\pi}\sigma_{_B}}\;\sqrt{2\pi}\sigma_{_B}\; e^{-\frac{1}{2}q^2\left(1+\rho_{_{AB}}\frac{\sigma_{_A}}{\sigma_{_B}}\right)^2\sigma_{_B}^2} \\ &= \exp\left[-\frac{1}{2}q^2\left\{\left(1-\rho_{_{AB}}^2\right)\sigma_{_A}^2+\left(1+\rho_{_{AB}}\frac{\sigma_{_A}}{\sigma_{_B}}\right)^2\sigma_{_B}^2\right\}\right] \\ &= e^{-\frac{1}{2}q^2\left[\sigma_{_A}^2+\sigma_{_B}^2+2\rho_{_{AB}}\sigma_{_A}\sigma_{_B}\right]} \end{aligned} \tag{A.14}$$

With $\sigma_A = \sqrt{\langle A^2\rangle}$, $\sigma_A = \sqrt{\langle B^2\rangle}$ and (A.5) we finally obtain the classical Baker-Hausdorff theorem

$$\left\langle e^{iq(A+B)}\right\rangle = e^{-q^2[\langle A^2\rangle+\langle B^2\rangle+2\langle AB\rangle]/2}\;. \tag{A.15}$$

By generalizing the multivariate Gaussian distribution (A.4) for $x_1, x_2, ..., x_N$ Gaussian variates one can proof the following general relation [58]

$$\left\langle \exp\left(i\sum_{j=1}^{N}\xi_j x_j\right)\right\rangle = \exp\left(i\sum_{j=1}^{N}\xi_j\langle x_j\rangle\right)\exp\left(-\frac{1}{2}\sum_{j=1}^{N}\sum_{k=1}^{N}\xi_j\xi_k\langle\Delta x_j\Delta x_k\rangle\right), \tag{A.16}$$

and with $\langle x_j \rangle = 0$

$$\left\langle \exp\left(i \sum_{j=1}^{N} \xi_j x_j \right) \right\rangle = \exp\left(-\frac{1}{2} \sum_{j=1}^{N} \sum_{k=1}^{N} \xi_j \xi_k \langle x_j x_k \rangle \right). \tag{A.17}$$

A.4 Siegert's Relation for (real) random variables

Let a function of the random variables A and B be definite by

$$f(A,B) = A^2 B^2 \ . \tag{A.18}$$

And let the mean values be $\langle A \rangle = \langle B \rangle = 0$, so that $\sigma_A = \sqrt{\langle A^2 \rangle}$ and $\sigma_A = \sqrt{\langle B^2 \rangle}$, respectively. With (A.6) and (A.4) the expectation value for (A.18) is

$$\begin{aligned}
\left\langle A^2 B^2 \right\rangle &= \frac{1}{2\pi\sigma_{_A}\sigma_{_B}\sqrt{1-\rho_{_{AB}}^2}} \iint_{-\infty}^{\infty} dA dB \ A^2 B^2 \ e^{-\frac{1}{2\left(1-\rho_{_{AB}}^2\right)}\left(\frac{A^2}{\sigma_{_A}^2} - \frac{2\rho_{_{AB}} AB}{\sigma_{_A}\sigma_{_B}} + \frac{B^2}{\sigma_{_B}^2}\right)}, \\
&= \frac{1}{2\pi\sigma_{_A}\sigma_{_B}\sqrt{1-\rho_{_{AB}}^2}} \int_{-\infty}^{\infty} dB \ e^{-\frac{1}{2\left(1-\rho_{_{AB}}^2\right)}\frac{B^2}{\sigma_{_B}^2}} \ B^2 \\
&\quad \times \int_{-\infty}^{\infty} dA \ e^{-\frac{1}{2\left(1-\rho_{_{AB}}^2\right)}\left(\frac{A^2}{\sigma_{_A}^2} - \frac{2\rho_{_{AB}} AB}{\sigma_{_A}\sigma_{_B}}\right)} \ A^2 \ , \\
&= \frac{1}{2\pi\sigma_{_A}\sigma_{_B}\sqrt{1-\rho_{_{AB}}^2}} \int_{-\infty}^{\infty} dB \ e^{-\frac{1}{2\left(1-\rho_{_{AB}}^2\right)}\frac{B^2}{\sigma_{_B}^2}} \ B^2 \\
&\quad \times \sqrt{2\pi\left(1-\rho_{_{AB}}^2\right)^3}\sigma_{_A}^3 \left(1 + \frac{\rho_{_{AB}}^2}{1-\rho_{_{AB}}^2}\frac{B^2}{\sigma_{_B}^2}\right) \ e^{\frac{\rho_{_{AB}}^2}{2\left(1-\rho_{_{AB}}^2\right)}\frac{B^2}{\sigma_{_B}^2}} \ , \\
&= \frac{\left(1-\rho_{_{AB}}^2\right)\sigma_{_A}^2}{\sqrt{2\pi}\sigma_{_B}} \int_{-\infty}^{\infty} dB \ \left(1 + \frac{\rho_{_{AB}}^2}{1-\rho_{_{AB}}^2}\frac{B^2}{\sigma_{_B}^2}\right) B^2 \ e^{\frac{\rho_{_{AB}}^2 - 1}{2\left(1-\rho_{_{AB}}^2\right)\sigma_{_B}^2}B^2} \ .
\end{aligned} \tag{A.19}$$

Preforming the integration over B yields

$$\int_{-\infty}^{\infty} dB \ \left(1 + \frac{\rho_{_{AB}}^2}{1-\rho_{_{AB}}^2}\frac{B^2}{\sigma_{_B}^2}\right) B^2 \ e^{\frac{\rho_{_{AB}}^2 - 1}{2\left(1-\rho_{_{AB}}^2\right)\sigma_{_B}^2}B^2} = \sqrt{2\pi} \ \sigma_{_B}^3 \frac{1+2\rho_{_{AB}}^2}{1-\rho_{_{AB}}^2}. \tag{A.20}$$

Including (A.20) in (A.19) gives

$$\left\langle A^2 B^2 \right\rangle = \sigma_{_A}^2 \sigma_{_B}^2 \left(1 + 2\rho_{_{AB}}^2\right). \tag{A.21}$$

With $\sigma_A = \sqrt{\langle A^2 \rangle}$, $\sigma_A = \sqrt{\langle B^2 \rangle}$ and $\rho_{AB} = \langle AB \rangle / \sigma_A \sigma_B$ we finally proofed the relation

$$\langle A^2 B^2 \rangle = \langle A^2 \rangle \langle B^2 \rangle + \langle AB \rangle^2 \ . \tag{A.22}$$

Normalizing (A.22) by $\langle A^2 \rangle \langle B^2 \rangle$ yields *Siegert's relation* for (real) Gaussian variables

$$\frac{\langle A^2 B^2 \rangle}{\langle A^2 \rangle \langle B^2 \rangle} = 1 + \frac{\langle AB \rangle^2}{\langle A^2 \rangle \langle B^2 \rangle} \ . \tag{A.23}$$

Similarly one can proof the Siegert relation for complex Gaussian variables Z_1 and Z_2

$$\frac{\langle |Z_1|^2 |Z_2|^2 \rangle}{\langle |Z_1|^2 \rangle \langle |Z_2|^2 \rangle} = 1 + \frac{|\langle Z_1 Z_2^* \rangle|^2}{\langle |Z_1|^2 \rangle \langle |Z_2|^2 \rangle} \ . \tag{A.24}$$

Result (A.22) can be obtained at once from the Gaussian moment theorem.

A.5 Applications to Surface Fluctuations

Let $h_1 = h(x_1, y_1)$ and $h_2 = h(x_2, y_2)$ be surface height functions located at the lateral positions (x_1, y_1) and (x_2, y_2), respectively. The Expectation value of interest is definition by

$$\left\langle e^{-iq_z(h_1 - h_2)} \right\rangle \ , \tag{A.25}$$

and can easily be solve with the assumption that the surface height functions are Gaussian variates. If furthermore, h_1 and h_2 are correlated and their expectation values are $\langle h_1 \rangle = \langle h_2 \rangle = 0$, one can use (A.17), which leads to

$$\left\langle e^{-iq_z(h_1 - h_2)} \right\rangle = \exp\left(-\frac{1}{2} \sum_{j=1}^{2} \sum_{k=1}^{2} \xi_j \xi_k \langle h_j h_k \rangle \right) \ , \tag{A.26}$$

with $\xi_1 = -q_z$ and $\xi_2 = q_z$. Evaluating the sum yields

$$\begin{aligned} \left\langle e^{-iq_z(h_1 - h_2)} \right\rangle &= e^{-[(-q)^2 \langle h_1 h_1 \rangle + (-q) q \langle h_1 h_2 \rangle + q(-q) \langle h_2 h_1 \rangle + q^2 \langle h_2 h_2 \rangle]/2} \\ &= e^{-q_z^2 [\langle h_1^2 \rangle + \langle h_1^2 \rangle - 2\langle h_1 h_2 \rangle]/2} \ , \end{aligned} \tag{A.27}$$

where the equality of $\langle h_2 h_1 \rangle = \langle h_1 h_2 \rangle$ was used. The above relation is frequently used to describe the statistical properties of rough surfaces.

Appendix B

Alternative Calculation of the Intensity Correlation Function

The intensity correlation formulas in chapter 5.2 were based on the Gaussian statistical properties of the scattered fields (Siegert relation) and the surface fluctuations. In chapter 5.3 an intensity correlation formula was derived founded on the assumptions that the incident fields and the electron density obeys Gaussian statistics (Pusey's approach). Both approaches could be combined to arrive at more justified description of surface sensitive XICS. The following calculation makes use of the conditions that the incident fields and the sample surface obey Gaussian statistical. The notation is the same as in chapter 4 and 5. The below formula can be deduced from eq. (5.120):

$$\begin{aligned} G(\mathbf{q},\tau) &= \langle I(\mathbf{q},0)I(\mathbf{q},\tau)\rangle \\ &= r_e^4 \iiiint_V d^3\mathrm{r}_1 d^3\mathrm{r}_2 d^3\mathrm{r}_3 d^3\mathrm{r}'_4 \ \langle \rho(\mathbf{r}_1,0)\rho(\mathbf{r}_2,0)\rho(\mathbf{r}_3,\tau)\rho(\mathbf{r}_4,\tau)\rangle \\ &\quad \times \mathcal{G}(\boldsymbol{r}_1,\boldsymbol{r}_2)\mathcal{G}(\boldsymbol{r}_3,\boldsymbol{r}_4) e^{-iq_z(z_2-z_1+z_4-z_3)} e^{-i\boldsymbol{q}\cdot(\boldsymbol{r}_2-\boldsymbol{r}_1+\boldsymbol{r}_4-\boldsymbol{r}_3)}, \end{aligned} \tag{B.1}$$

with

$$\mathcal{G}(\boldsymbol{r}_1,\boldsymbol{r}_2) = f_a(\boldsymbol{r}_1,\boldsymbol{r}_2) f_b(\boldsymbol{r}_1,\boldsymbol{r}_2) \mathcal{G}_l(\boldsymbol{r}_2-\boldsymbol{r}_1) J_i(\boldsymbol{r}_1,\boldsymbol{r}_2) D(\boldsymbol{r}_2-\boldsymbol{r}_1)\,, \tag{B.2}$$

where (holds for in-plane scattering geometry i.e. $\varphi = 0$)

$$\begin{aligned} f_a(\boldsymbol{r}_1,\boldsymbol{r}_2) f_b(\boldsymbol{r}_1,\boldsymbol{r}_2) &= e^{i\kappa_a[(\boldsymbol{r}_2^2-(\boldsymbol{r}_2\cdot\hat{\boldsymbol{k}}_\mathrm{i})^2)-(\boldsymbol{r}_1^2-(\boldsymbol{r}_1\cdot\hat{\boldsymbol{k}}_\mathrm{i})^2)]} e^{i\kappa_b[(\boldsymbol{r}_2^2-(\boldsymbol{r}_2\cdot\hat{\boldsymbol{k}}_\mathrm{f})^2)-(\boldsymbol{r}_1^2-(\boldsymbol{r}_1\cdot\hat{\boldsymbol{k}}_\mathrm{f})^2)]} \\ &= \left(e^{i(\kappa_a+\kappa_b)(x_2^2-x_1^2)}\right)\left(e^{i(\kappa_a \sin^2\alpha_\mathrm{i}+\kappa_b\sin^2\alpha_\mathrm{f})(y_2^2-y_1^2)}\right) \end{aligned} \tag{B.3}$$

$$\begin{aligned} \mathcal{G}_l(\boldsymbol{r}_2-\boldsymbol{r}_1) &= \frac{c}{\sqrt{2\pi}\xi_l}\ e^{-[\hat{\boldsymbol{q}}\cdot(\boldsymbol{r}_2-\boldsymbol{r}_1)]^2/2\xi_l^2} \\ &= \left(\frac{c}{\sqrt{2\pi}\xi_l}\ e^{-(\cos\alpha_\mathrm{i}-\cos\alpha_\mathrm{f})^2(y_2-y_1)^2/2\xi_l^2}\right) \end{aligned} \tag{B.4}$$

$$
\begin{aligned}
J_i(\boldsymbol{r}_1,\boldsymbol{r}_2) &= \sqrt{I_i(\boldsymbol{r}_1)}\sqrt{I_i(\boldsymbol{r}_2)}j_i(\boldsymbol{r}_2-\boldsymbol{r}_1)\phi(\boldsymbol{r}_1,\boldsymbol{r}_2) \\
&= \left(\sqrt{I_0\frac{\triangle a^2}{\sin\alpha_{\mathrm{i}}\Sigma_x\Sigma_y}}\; e^{-(x_1^2+x_2^2)/2\Sigma_x^2}\; e^{-(x_2-x_1)^2/2\Xi_{tx}^2}\; e^{-i\kappa_a\frac{\triangle a^2}{\Sigma_x^2}(x_2^2-x_1^2)}\right) \\
&\quad\times\left(\sqrt{I_0\frac{\triangle a^2}{\sin\alpha_{\mathrm{i}}\Sigma_x\Sigma_y}}\; e^{-(y_1^2+y_2^2)/2\Sigma_y^2}\; e^{-(y_2-y_1)^2/2\Xi_{ty}^2}\; e^{-i\kappa_a\frac{\triangle a^2}{\Sigma_y^2}(y_2^2-y_1^2)}\right),
\end{aligned}
\tag{B.5}
$$

$$
\begin{aligned}
D(\boldsymbol{r}_2-\boldsymbol{r}_1) &= \left(\frac{\sqrt{2\pi}\triangle b}{L_b}\right)^2\; e^{-2\kappa_b^2\triangle b^2[\hat{\boldsymbol{b}}\cdot(\boldsymbol{r}_2-\boldsymbol{r}_1)]^2} \\
&= \left(\frac{\sqrt{2\pi}\triangle b}{L_b}\; e^{-2\kappa_b^2\triangle b^2(x_2-x_1)^2}\right)\left(\frac{\sqrt{2\pi}\triangle b}{L_b}\; e^{-2\kappa_b^2\triangle b^2\sin^2\alpha_{\mathrm{f}}(y_2-y_1)^2}\right).
\end{aligned}
\tag{B.6}
$$

We finally find for $\mathcal{G}(\boldsymbol{r}_1,\boldsymbol{r}_2)$ a bivariate Gaussian representation:

$$
\begin{aligned}
\mathcal{G}(\boldsymbol{r}_1,\boldsymbol{r}_2) = I_0&\frac{\sqrt{2\pi}c\triangle a^2\triangle b^2}{\sin\alpha_{\mathrm{i}}L_b^2\Sigma_x\Sigma_y\xi_l} \\
&\times\Bigg(e^{-\frac{x_1^2}{2}\left[\frac{1}{\Xi_{tx}^2}+(2\kappa_b\triangle b)^2+\frac{1}{\Sigma_x^2}+i(2\kappa_b+2\kappa_a(1-(\triangle a/\Sigma_x)^2))\right]}e^{x_1x_2\left[\frac{1}{\Xi_{tx}^2}+(2\kappa_b\triangle b)^2\right]} \\
&\times e^{-\frac{x_2^2}{2}\left[\frac{1}{\Xi_{tx}^2}+(2\kappa_b\triangle b)^2+\frac{1}{\Sigma_x^2}-i(2\kappa_b+2\kappa_a(1-(\triangle a/\Sigma_x)^2))\right]}\Bigg) \\
&\times\Bigg(e^{-\frac{y_1^2}{2}\left[\frac{1}{\Xi_{ty}^2}+(2\kappa_b\triangle b\sin\alpha_{\mathrm{f}})^2+(\cos\alpha_{\mathrm{i}}-\cos\alpha_{\mathrm{f}})^2/\xi_l^2\right]} \\
&\times e^{-\frac{y_1^2}{2}\left[\frac{1}{\Sigma_y^2}+i(2\kappa_b\sin^2\alpha_{\mathrm{f}}+2\kappa_a(\sin^2\alpha_{\mathrm{i}}-(\triangle a/\Sigma_y)^2))\right]} \\
&\times e^{y_1y_2\left[\frac{1}{\Xi_{ty}^2}+(2\kappa_b\triangle b\sin\alpha_{\mathrm{f}})^2+(\cos\alpha_{\mathrm{i}}-\cos\alpha_{\mathrm{f}})^2/\xi_l^2\right]} \\
&\times e^{-\frac{y_2^2}{2}\left[\frac{1}{\Xi_{ty}^2}+(2\kappa_b\triangle b\sin\alpha_{\mathrm{f}})^2+(\cos\alpha_{\mathrm{i}}-\cos\alpha_{\mathrm{f}})^2/\xi_l^2\right]} \\
&\times e^{-\frac{y_2^2}{2}\left[\frac{1}{\Sigma_y^2}-i(2\kappa_b\sin^2\alpha_{\mathrm{f}}+2\kappa_a(\sin^2\alpha_{\mathrm{i}}-(\triangle a/\Sigma_y)^2))\right]}\Bigg).
\end{aligned}
\tag{B.7}
$$

After evaluating the z-integrations in eq. (B.2), one finds

$$
\begin{aligned}
G(\mathbf{q},\tau) = &\left(\frac{\rho_l\, r_e}{q_z}\right)^4\iiiint_S d^2r_1d^2r_2d^2r_3d^2r_4\left\langle e^{-iq_z(h_2-h_1+h_4-h_3)}\right\rangle \\
&\times\mathcal{G}(\boldsymbol{r}_1,\boldsymbol{r}_2)\mathcal{G}(\boldsymbol{r}_3,\boldsymbol{r}_4)\, e^{-i\boldsymbol{q}\cdot(\boldsymbol{r}_2-\boldsymbol{r}_1+\boldsymbol{r}_4-\boldsymbol{r}_3)},
\end{aligned}
\tag{B.8}
$$

where $h_1 = h(\boldsymbol{r}_1, 0)$, $h_2 = h(\boldsymbol{r}_2, 0)$, $h_3 = h(\boldsymbol{r}_3, \tau)$ and $h_4 = h(\boldsymbol{r}_4, \tau)$ represent the surface height displacement functions.

EVALUATING THE AVERAGE TERM

If the height functions are gaussian random variables the average term can be evaluated as follows:

$$\left\langle \exp\left(i \sum_{j=1}^{4} c_j h_j \right) \right\rangle = \exp\left(-\frac{1}{2} \sum_{j=1}^{4} \sum_{k=1}^{4} c_j c_k \langle h_j h_k \rangle \right) , \tag{B.9}$$

where the coefficients $c_j = (q_z, -q_z, q_{z2}, -q_{z2})$ for $j = 1, 2, 3, 4$. Relation (B.9) yields

$$\begin{aligned} \left\langle \exp\left(i \sum_{j=1}^{4} c_j h_j \right) \right\rangle = {} & e^{-q_z^2 \left[\langle h_1^2 \rangle + \langle h_2^2 \rangle - 2\langle h_1 h_2 \rangle \right]/2} \; e^{-q_z^2 \left[\langle h_3^2 \rangle + \langle h_4^2 \rangle - 2\langle h_3 h_4 \rangle \right]/2} \\ & \times e^{-q_z^2 [\langle h_1 h_3 \rangle - \langle h_1 h_4 \rangle - \langle h_2 h_3 \rangle + \langle h_2 h_4 \rangle]} . \end{aligned} \tag{B.10}$$

With the substitutions $\langle h(\boldsymbol{r}, 0) h(\boldsymbol{r'}, \tau) \rangle = C(\boldsymbol{r} - \boldsymbol{r'}, \tau)$ and $\langle h(\boldsymbol{r}, \tau) h(\boldsymbol{r}, \tau) \rangle = \sigma^2$, one finds for eq. (B.10)

$$\begin{aligned} \left\langle \exp\left(i \sum_{j=1}^{4} c_j h_j \right) \right\rangle = {} & e^{-2q_z^2\sigma^2} e^{q_z^2 C(\boldsymbol{r}_2 - \boldsymbol{r}_1)} e^{q_z^2 C(\boldsymbol{r}_4 - \boldsymbol{r}_3)} \\ & \times e^{-q_z^2 [C(\boldsymbol{r}_1 - \boldsymbol{r}_3, \tau) + C(\boldsymbol{r}_2 - \boldsymbol{r}_4, \tau) - C(\boldsymbol{r}_1 - \boldsymbol{r}_4, \tau) - C(\boldsymbol{r}_2 - \boldsymbol{r}_3, \tau)]} . \end{aligned} \tag{B.11}$$

After expansion up to the second order, one finds

$$\begin{aligned} \left\langle \exp\left(i \sum_{j=1}^{4} c_j h_j \right) \right\rangle = e^{-2q_z^2\sigma^2} \Bigg\{ & 1 + \\ & + q_z^2 \Big[C(\boldsymbol{r}_2 - \boldsymbol{r}_1) + C(\boldsymbol{r}_4 - \boldsymbol{r}_3) + C(\boldsymbol{r}_2 - \boldsymbol{r}_3, \tau) \\ & + C(\boldsymbol{r}_1 - \boldsymbol{r}_4, \tau) - C(\boldsymbol{r}_2 - \boldsymbol{r}_4, \tau) - C(\boldsymbol{r}_1 - \boldsymbol{r}_3, \tau) \Big] \\ & + \frac{q_z^4}{2} \Big[C(\boldsymbol{r}_2 - \boldsymbol{r}_1) + C(\boldsymbol{r}_4 - \boldsymbol{r}_3) + C(\boldsymbol{r}_2 - \boldsymbol{r}_3, \tau) \\ & + C(\boldsymbol{r}_1 - \boldsymbol{r}_4, \tau) - C(\boldsymbol{r}_2 - \boldsymbol{r}_4, \tau) - C(\boldsymbol{r}_1 - \boldsymbol{r}_3, \tau) \Big]^2 \Bigg\} . \end{aligned} \tag{B.12}$$

Using (B.12) in (B.8) yields

$$
\begin{aligned}
G(\mathbf{q},\tau) = \left(\frac{\rho_l\, r_e}{q_z}\right)^4 \iiiint_S d^2r_1 d^2r_2 d^2r_3 d^2r_4 \; \mathcal{G}(\boldsymbol{r}_1,\boldsymbol{r}_2)\mathcal{G}(\boldsymbol{r}_3,\boldsymbol{r}_4)\, e^{-i\boldsymbol{q}\cdot(\boldsymbol{r}_2-\boldsymbol{r}_1+\boldsymbol{r}_4-\boldsymbol{r}_3)} \\
\times e^{-2q_z^2\sigma^2} \Bigg\{ 1 + q_z^2\left[C(\boldsymbol{r}_2-\boldsymbol{r}_1)+C(\boldsymbol{r}_4-\boldsymbol{r}_3)\right] \\
+\frac{q_z^4}{2}\left[C(\boldsymbol{r}_2-\boldsymbol{r}_1)+C(\boldsymbol{r}_4-\boldsymbol{r}_3)\right]^2 \\
+q_z^2\left[C(\boldsymbol{r}_2-\boldsymbol{r}_3,\tau)+C(\boldsymbol{r}_1-\boldsymbol{r}_4,\tau)-C(\boldsymbol{r}_2-\boldsymbol{r}_4,\tau)-C(\boldsymbol{r}_1-\boldsymbol{r}_3,\tau)\right] \\
+\frac{q_z^4}{2}\big[C(\boldsymbol{r}_2-\boldsymbol{r}_3,\tau)+C(\boldsymbol{r}_1-\boldsymbol{r}_4,\tau)-C(\boldsymbol{r}_2-\boldsymbol{r}_4,\tau)-C(\boldsymbol{r}_1-\boldsymbol{r}_3,\tau)\big]^2 \\
+q_z^4\big[C(\boldsymbol{r}_2-\boldsymbol{r}_1)+C(\boldsymbol{r}_4-\boldsymbol{r}_3)\big] \\
\times\big[C(\boldsymbol{r}_2-\boldsymbol{r}_3,\tau)+C(\boldsymbol{r}_1-\boldsymbol{r}_4,\tau)-C(\boldsymbol{r}_2-\boldsymbol{r}_4,\tau)-C(\boldsymbol{r}_1-\boldsymbol{r}_3,\tau)\big] \Bigg\}.
\end{aligned}
\tag{B.13}
$$

The normalized intensity correlation function is finally

$$
\begin{aligned}
g(\mathbf{q},\tau) = \frac{\langle I(\mathbf{q},0)I(\mathbf{q},\tau)\rangle}{\langle I(\mathbf{q},0)\rangle^2} = \frac{\langle I(\mathbf{q},0)I(\mathbf{q},\tau)\rangle}{(\bar{I}_S(\mathbf{q})+\bar{I}_D(\mathbf{q}))^2} \\
= 1 + \frac{q_z^2\, e^{-2q_z^2\sigma^2}}{(\bar{I}_S(\mathbf{q})+\bar{I}_D(\mathbf{q}))^2}\left(\frac{\rho_l\, r_e}{q_z}\right)^4 \\
\times \iiiint_S d^2r_1 d^2r_2 d^2r_3 d^2r_4 \; \mathcal{G}(\boldsymbol{r}_1,\boldsymbol{r}_2)\mathcal{G}(\boldsymbol{r}_3,\boldsymbol{r}_4)\, e^{-i\boldsymbol{q}\cdot(\boldsymbol{r}_2-\boldsymbol{r}_1+\boldsymbol{r}_4-\boldsymbol{r}_3)} \\
\times \Bigg\{ \big[1 + q_z^2(C(\boldsymbol{r}_2-\boldsymbol{r}_1)+C(\boldsymbol{r}_4-\boldsymbol{r}_3))\big] \\
\times\big[C(\boldsymbol{r}_2-\boldsymbol{r}_3,\tau)+C(\boldsymbol{r}_1-\boldsymbol{r}_4,\tau)-C(\boldsymbol{r}_2-\boldsymbol{r}_4,\tau)-C(\boldsymbol{r}_1-\boldsymbol{r}_3,\tau)\big] \\
+\frac{q_z^2}{2}\big[C(\boldsymbol{r}_2-\boldsymbol{r}_3,\tau)+C(\boldsymbol{r}_1-\boldsymbol{r}_4,\tau)-C(\boldsymbol{r}_2-\boldsymbol{r}_4,\tau)-C(\boldsymbol{r}_1-\boldsymbol{r}_3,\tau)\big]^2 \Bigg\}.
\end{aligned}
\tag{B.14}
$$

where

$$
\bar{I}_S(\mathbf{q}) = \left(\frac{\rho_l\, r_e}{q_z}\right)^2 e^{-q_z^2\sigma^2} \iint_S d^2r_1 d^2r_2 \; \mathcal{G}(\boldsymbol{r}_1',\boldsymbol{r}_2')\, e^{-i\boldsymbol{q}\cdot(\boldsymbol{r}_2'-\boldsymbol{r}_1')} \;, \tag{B.15}
$$

refers to the static specular intensify and

$$\bar{I}_D(\mathbf{q}) = \left(\frac{\rho_l\, r_e}{q_z}\right)^2 e^{-q_z^2\sigma^2} \iint_S d^2r_1 d^2r_2\; \mathcal{G}(\boldsymbol{r}_1', \boldsymbol{r}_2')\, e^{-i\boldsymbol{q}\cdot(\boldsymbol{r}_2'-\boldsymbol{r}_1')} \times \left[q_z^2 C(\boldsymbol{r}_2-\boldsymbol{r}_1) + \frac{q_z^4}{2} C(\boldsymbol{r}_2-\boldsymbol{r}_1)^2\right], \tag{B.16}$$

represents the static diffuse intensify. Eq. (B.14) is next written as

$$\begin{aligned} g(\mathbf{q},\tau) &= 1 + (T_{23}+T_{14}-T_{24}-T_{13}) + (T_{21,23}+T_{21,14}-T_{21,24}-T_{21,13}) \\ &\quad +(T_{43,23}+T_{43,14}-T_{43,24}-T_{43,13}) \\ &\quad +(T_{23}+T_{14}-T_{24}-T_{13})^2 \\ &= 1 + (T_{23}+T_{14}-T_{24}-T_{13}) + (T_{21,23}+T_{21,14}-T_{21,24}-T_{21,13}) \\ &\quad +(T_{43,23}+T_{43,14}-T_{43,24}-T_{43,13}) + (T_{23,23}+T_{14,14}+T_{24,24} \\ &\quad +T_{13,13}) - 2(T_{23,24}+T_{23,13}+T_{14,24}+T_{14,13}) + 2(T_{14,23}+T_{13,24}) \end{aligned} \tag{B.17}$$

where $\frac{q_z^2\, e^{-2q_z^2\sigma^2}}{(\bar{I}_S(\mathbf{q})+\bar{I}_D(\mathbf{q}))^2}\left(\frac{\rho_l\, r_e}{q_z}\right)^4$ is disregarded in the following. $T_{i,j}$ defines heterodyne terms depending on $C(\boldsymbol{r}_i-\boldsymbol{r}_j,\tau)$ in eq. (B.14). Similarly $T_{ij,kl}$ defines the semi-heterodyne terms $C(\boldsymbol{r}_i-\boldsymbol{r}_j)C(\boldsymbol{r}_k-\boldsymbol{r}_l,\tau)$, as well as the homodyne terms $C(\boldsymbol{r}_i-\boldsymbol{r}_j,\tau)C(\boldsymbol{r}_k-\boldsymbol{r}_l,\tau)$. Eq. (B.17) can be evaluated term-wise by using the Fourier representation

$$C(\boldsymbol{r}-\boldsymbol{r}',\tau) = \int d^2q\; \widetilde{C}(\boldsymbol{q},\tau) e^{i\boldsymbol{q}\cdot(\boldsymbol{r}-\boldsymbol{r}')}\;. \tag{B.18}$$

The bivariate Gaussian function $\mathcal{G}(\boldsymbol{r},\boldsymbol{r}')$ can be treated similarly. After a long but straight forward calculation one finds essentially three terms:

$$g_2(\mathbf{q},\tau) = 1 + g_2^{(heterto)}(\mathbf{q},\tau) + g_2^{(semi-heterto)}(\mathbf{q},\tau) + g_2^{(homo)}(\mathbf{q},\tau)\,, \tag{B.19}$$

which consist of convolution integrals between the height correlation function and the bivariate Gaussian resolution functions.

Bibliography

[1] http://functions.wolfram.com/GammaBetaErf/Erf/20/02/0002/.

[2] A digital multiple tau autocorrelator from Correlator.com has been used to generated the experimental intensity time-autocorraltion function. Autocorrelator model: Flex01-08D.

[3] J. Als-Nielsen and D. MacMorrow. *Elements of modern x-ray physics*. John Wiley & Sons, Ltd., New York, 2001.

[4] A. Q. R. Baron. *Hyperfine Interactions*, 125:29, 2000.

[5] F. G. Bass and I. M. Fuks. *Wave Scattering from Statistically Rough Surfaces*. Pergamon Press Ltd., Oxford, 1979.

[6] J. K. Basu and M. K. Sanyal. *Phys. Rep.*, 363:1–84, 2002.

[7] P. Beckmann and A. Spizzichino. *The Scattering of Electromagnetic Waves from Rough Surfaces*. Pergamon Press Ltd., New York, 1963.

[8] D. Bedeaux and J. D. Weeks. *J. Chem. Phys.*, 82(5):972–979, 1984.

[9] M. Born and E. Wolf. *Principles of Optics*. Cambridge University Press, New York, 7th edition, 1999.

[10] M. A. Bouchiat and J. Meunier. *J. Phys. (Paris)*, 32:561, 1971.

[11] A. Braslau, P. S. Pershan, G. Swislow, B. M. Ocko., and J. ALs-Nielsen. *Phys. Rev. A*, 38(5):2457–2470, 1988.

[12] L. J. F. Broer. *Appl. Sci. Res.*, 30:430–446, 1974.

[13] I. N. Bronstein, K. A. Semendjajew, G. Musiol, and H. Mhlig. *Taschenbuch der Mathematik*. Verlag Harri Deutsch, Franfurt am Main, 1997.

[14] F. P. Buff, R. A. Lovett, and F. H. Stillinger. *Phys. Rev. Lett.*, 15:621–623, 1965.

[15] D. Byrne and J. C. Earnshaw. *J. Phys. D: Appl. Phys.*, 10:L207, 1977.

[16] Z. H. Cai, B. Lai, W. B. Yun, I. McNulty, K. G. Huang, and T. P. Russell. *Phys. Rev. Lett.*, 73(1):82–85, 1994.

[17] W. H. Carter. *Opt. Comm.*, 77(2,3):121–125, 1990.

[18] B. Chu. *Laser Light Scattering.* Academic Press, San Diego, 1991.

[19] J. F. Crilly and J. C. Earnshaw. *J. Phys. D: Appl. Phys.*, 18:609, 1985.

[20] H. Z. Cummins and E. R. Pike, editors. *Photon Correlation Spectroscopy and Light Beating Spectroscopy.* Plenum Press, New York, 1974.

[21] H. Z. Cummins and E. R. Pike, editors. *Photon Correlation Spectroscopy and Velocimetry.* Plenum Press, New York, 1977.

[22] J. Daillant. *X-Ray and Neutron Reflectivity: Principles and Applications*, chapter Reflectivity of Liquid Surfaces and Interfaces, pages 281–304. Springer-Verlag, Berlin, 1999.

[23] J. Daillant, S. Mora, C. Fradin, M. Alba, A. Braslau, and D. Luzet. *Appl. Sur. Sci.*, 182:223–230, 1901.

[24] F. David. *Statistical Mechanics of Membranes and Surfaces*, volume 5, chapter Geometry and Field Theory of Random Surfaces and Membranes, pages 45–141. Wold Scientific, Singapore, 1989.

[25] D. K. G. de Boer. *Phys. Rev. B*, 49(9):5817–5820, 1993.

[26] D. K. G. de Boer. *Phys. Rev. B*, 51(8):5297–5305, 1994.

[27] R. Evans. *Adv. Phys.*, 28(2):143–200, 1979.

[28] R. Evans. *Mol. Phys.*, 42(5):1169–1196, 1981.

[29] J. T. Foley and E. Wolf. *Rhys. Rew. A*, 40(2):588–598, 1989.

[30] C. Fradin, A. Braslau, D. Luzet, D. Smilgles, M. Alba, N. Boudet, M. Mecke, and J. Daillant. *Nature*, 403:871–874, 2000.

[31] M. P. Gelfand and M. E. Fisher. *Physica A*, 166:1–74, 1990.

[32] J. W. Goodman. *Statistical Optics.* John Wiley & Sons, Inc., New York, 2000.

[33] I. S. Gradshteyn and I. M. Ryzhik. *Table of Integrals, Series, and Products*. Academic Press, San Diego, 2000.

[34] H. S. Green and E. Wolf. *Proc. Phys. Soc*, A66:1129–1137, 1953.

[35] G. Grübel. *Phys. Bl.*, 54(11):1243–1251, 1998.

[36] C. Gutt, T. Ghaderi, V. Chamard, A. Madsen, T. Seydel, M. Tolan, M. Sprung, G. Grübel, and S. K. Sinha. *Phys. Rev. Lett.*, 91:076104, 2003.

[37] E. Hecht. *Optics*. Addison-Wesley, Massachusetts, 2 edition, 1987.

[38] W. Helfrich. *Z. Naturforsch.*, 28c:693–703, 1973.

[39] D. A. Huse, W. van Saarloos, and D. Weeks. *Phys. Rew. 5*, 32(1):233–246, 1985.

[40] J. Jäckle. *J. Phys. Condens. Matter*, 10:7121, 1998.

[41] J. Jäckle and K. Kawasaki. *J. Phys. Condens. Matter*, 7:4351, 1995.

[42] J. D. Jackson. *Classical Electrodynamics*. John Wiley & Sons, Inc., New York, 3th edition, 1999.

[43] D. Jasnow. *Rep. Prog. Phys.*, 47:1059–1132, 1984.

[44] H. Kim, A. Rühm, L. B. Lurio, J. K. Basu, J. Lal, D. Lumma, S. G. J. Mochrie, and S. K. Sinha. *Phys. Rev. Lett.*, 90(6):068302–1, 2003.

[45] V Kohn, I. Snigireva, and A. Snigirev. *Phys. Rev. Lett.*, 85(13):2745–2748, 2000.

[46] V Kohn, I. Snigireva, and A. Snigirev. *Opt. Comm.*, 198:293–309, 2001.

[47] L. D. Landau and E. M. Lifshitz. *Fluid Mechanics*, volume 6. Pergamon Press, London, 1959.

[48] D. Langevin. *J. Chem. Soc. Faraday I.*, 70:95, 1974.

[49] J. Lekner. *Theory of Reflection*. Martinus Nijhoff Publishers, Dordrecht, 1987.

[50] D. Li, B. Yang, B. Lin, M. Meron, J. Gebhardt, T. Graber, and S. A. Rice. *Phys. Rev. Lett.*, 92(13):136102–1–136102–4, 2004.

[51] J. L. Libbert, R. Pindak, S. B. Dierker, and I. K. Robinson. *Phys. Rev. B*, 56(11):6454–6457, 1997.

[52] B. Lin, M. L. Schlossman, M. Meron, S. M. Williams, Z. Huang, and P. J. Viccaro. *Phys. Rev. B*, 58(12):8025–8037, 1997.

[53] R. Loudon. *Proc. R. Soc. (London), Ser. A*, 372:275, 1980.

[54] D. Lumma, L. B. Lurio, and S. G. J. Mochrie. *Rev. Sci. Instrum.*, 71(9):3274, 2000.

[55] A. Madsen, T. Seydel, M. Sprung, C. Gutt, M. Tolan, and G. Grübel. *Phys. Rev. Lett.*, 92:096104, 2004.

[56] L. Mandel. *Phys. Rev.*, 181(1):75–84, 1969.

[57] L. Mandel and E. Wolf. *Rev. Mod. Phys.*, 37(2):231–287, 1965.

[58] L. Mandel and E. Wolf. *Optical Coherence and Quantum Optics*. Cambridge University Press, New York, 1995.

[59] A. S. Marathay. *Elements of Optical Coherence Theory*. John Wiley & Sons, Inc., New York, 1982.

[60] M. Mattenet, D. Abernathy, F. Zontone, C. Detlefs, G. Grübel, M. Facchini, and P. Jacquot. *NIM*, A 467-468:305–308, 2001.

[61] D. Mcqueen and I. Lundström. *J. C. S. Faraday I*, 69:694, 1973.

[62] K. R. Mecke. *J. Phys.: Condens. Matter*, 13:4615–4636, 2001.

[63] K. R. Mecke and S. Dietrich. *Phy. Rev. E*, 59(6):6766–6783, 1999.

[64] J. W. Miles. *J. Fluid Mech.*, 8(1):153–158, 1977.

[65] D. M. Mills, editor. *Third Generation Hard X-ray Synchrotron Radiation Sources: Source Properties, Optics, and Experimental Techniques*. John Wiley & Sons, Inc., New York, 2002.

[66] S. G. J. Mochrie. Equilibrium dynamics of complex fluids studied via x-ray photon correlation spectroscopy at 8-id at the aps. Internet source: http://8id.xor.aps.anl.gov/UserInfo/Analysis/slslecturenotes.pdf.

[67] A. S. Monin, V. M. Kamenkovich, and V. G. Kort. *Variability of the Oceans*. John Wiley & Sons, Inc., New York, 1977.

[68] S. Mora and J. Daillant. *Eur. Phys. J. B*, 27:417–428, 2002.

[69] S. Mora, J. Daillant, K. Mecke, D. Luzet, A. Braslau, M. Alba, and B. Struth. *Phys. Rev. Lett.*, 90(21):216101–1–216101–4, 2003.

[70] M. Napiorkowski and S. Dietrich. *Phy. Rev. E*, 47(3):1836–1849, 1993.

[71] M. Nieto-Vesperinas. *Scattering and Diffraction in Physical Optics*. John Wiley & Sons, Inc., New York, 1991.

[72] B. M. Ocko, X. Z. Wu, E. B. Sirota, S. K. Sinha, and M. Deutsch. *Phys. Rev. Lett.*, 72(2):242–245, 1994.

[73] NIST National Institute of Standards and Technology. www.nist.gov.

[74] D. Paterson, B. E. Allman, P. J. McMahon, J. Lin, N. Moldovan, K. A. Nugent, I. McNulty, C. T. Chantler, C. C. Retsch, and T. H. K. Irving. *Opt. Commu.*, 195:79–84, 2001.

[75] D. N. Pattanayak and E. Wolf. *Phys. Rev. D*, 13(8):2287–2290, 1976.

[76] D. N. Pattanayak and E. Wolf. *Phys. Rev. D*, 13(4):913–922, 1976.

[77] P. N. Pusey. *Photon Correlation Spectroscopy and Velocimetry*, chapter Statistical Properties of Scattered Radiation, pages 45–141. Plenum Press, New York, 1977.

[78] R. Pynn. *Phys. Rev. B*, 45(2):602–612, 1992.

[79] D. O. Riese, W. L. Vos, G. H. Wegdam, F. J. Poelwijk, D. L. Abernathy, and G. Grübel. *Phys. Rev. E*, 61(2):1676–1680, 2000.

[80] J. S. Rowlinson and B. Widom. *Molecular Theory of Capillarity*. Oxford University Press, Oxford, 1982.

[81] M. K. Sanyal, S. K. Sinha, K. G. Huang, and B. M. Ocko. *Phys. Rev. Lett.*, 66(5):628–631, 1991.

[82] A. C. Schell. *IEEE. Trans. Antennas and Progag.*, AP-15:187–188, 1967.

[83] V. F. Sears. *Phys. Rev. B*, 48(23):17477–17485, 1993.

[84] T. Seydel, A.Madsen, M. Sprung, M. Tolan, G. Grübel, and W. Press. *Rev. Sci. Instrum.*, 74:4033, 2003.

[85] T. Seydel, A. Madsen, M. Tolan, G. Grübel, and W. Press. *Phys. Rev. B*, 63:073409–1–073409–4, 2001.

[86] T. Seydel, M. Tolan, B. M. Ocko, O. H. Seeck, R. Weber, E. DiMasi, and W. Press. *Phys. Rev. B*, 65:184207–1–184207–7, 2002.

[87] I. Sikharulidze, I. P. Dolbnya, A. Fera, A. Madsen, and W. H. de Jeu. *Opt. Comm.*, 247:111–124, 2005.

[88] I. Sikharulidze, I. P. Dolbnya, A. Fera, A. Madsen, B. I. Ostrovskii, and W. H. de Jeu. *Phys. Rev. Lett.*, 88:115503, 2002.

[89] S. K. Sinha. *Liquid Crystals*, chapter 9 X-ray surface scattering studies of liquid crystals, pages 333–392. Cambridge University Press, New York, 2001.

[90] S. K. Sinha, S. Garoff, and H. B. Stanley. *Phys. Rev. B*, 38:2297, 1988.

[91] S. K. Sinha, M. Tolan, and A. Gibaud. *Phys. Rev. B*, 57(5):2740–2758, 1998.

[92] G. R. Somayajulu, M. Tolan, and A. Gibaud. *Int. J. Thermophys.*, 9(4):559–566, 1988.

[93] A. Sommerfeld. *Optics*. Academic Press, New York, 1954.

[94] A. Steyerl. *Z. Physik*, 254:169–188, 1972.

[95] A. Steyerl, S. S. Malik, and L. R. Iyengar. *Physica B*, 173:47–64, 1991.

[96] M. Sutton. *Third Generation Hard X-ray Synchrotron Radiation Sources: Source Properties, Optics, and Experimental Techniques*, chapter 3 Coherent X-ray Diffraction, pages 101–123. John Wiley & Sons, Inc., New York, 2002.

[97] M. Sutton, S. G. J. Mochrie, T. Greytak, S. E. Nagler, L. E. Berman, G. A. Held, and G. B. Stephenson. *Nature*, 352:608–610, 1991.

[98] P. Tartaglia and S. H. Chen. *J. Chem. Phys.*, 58:4389, 1973.

[99] M. Tolan. *X-Ray Scattering from Soft-Matter Thin Films: Materials Science and Basic Research*. Springer-Verlag, New York, 2000.

[100] M. Tolan and S. K. Sinha. *Physica B*, 248:399–404, 1998.

[101] M. Tolan, T.Seydel, A. Madsen, G. Grübel, W. Press, and S. K. Sinha. *Appl. Sur. Sci.*, 182:236, 2001.

[102] G. H. Vineyard. *Phys. Rev. B*, 26(8):4146–4158, 1982.

[103] T. D. Visser and E. Wolf. *Phys. Rev. B*, 59(2):2355–2360, 1999.

[104] A. G. Voronovich. *Wave Scattering from Rough Surfaces*. Springer-Verlag, Berlin, 1996.

[105] B. Widom. *Phase Transitions and Critical Phenomena*, volume 2, chapter Surface Tension of Fluids, pages 79–99. Academic, New York, 1972.

[106] E. Wolf. A generalized extinction theorem and its role in scattering theory. In L. Mandel and E. Wolf, editors, *Coherence and Quantum Optics*, page 339, New York, 1973. Plenum Press.

[107] E. Wolf and J. T. Foley. *Rhys. Rev. A*, 40(2):579–587, 1989.

[108] E. Wolf, D. F. V. James, and F. Gori. *J. Opt. Soc. Am. A*, 6(8):1142–1149, 1989.

[109] Y. Yoneda. *Phys. Rev.*, 131(5):2010–2013, 1963.

[110] V. E. Zakharov. *J. Appl. Mech. Tech.*, 9(2):86–94, 1968.

[111] X.-L. Zhou and S.-H. Chen. *Rhys. Rep.*, 257:223–348, 1995.

[112] X.-L. Zhou, S.-H. Chen, and G. P. Felcher. *Rhys. Rev. A*, 46(4):1839–1843, 1992.

[113] X.-L. Zhou, G. P. Felcher, and S.-H. Chen. *Physica B*, 173:167–179, 1991.